Research Thesis: Declaration of Authorship

Print name: Ibrahim H. Abughazaleh

Title of thesis: Advanced ultrafast thulium-doped fibre laser systems for biomedical imaging applications

I declare that this thesis and the work presented in it are my own and has been generated by me as the result of my own original research.

I confirm that:

1. This work was done wholly or mainly while in candidature for a research degree at this University;
2. Where any part of this thesis has previously been submitted for a degree or any other qualification at this University or any other institution, this has been clearly stated;
3. Where I have consulted the published work of others, this is always clearly attributed;
4. Where I have quoted from the work of others, the source is always given. With the exception of such quotations, this thesis is entirely my own work;
5. I have acknowledged all main sources of help;
6. Where the thesis is based on work done by myself jointly with others, I have made clear exactly what was done by others and what I have contributed myself;
7. None of this work has been published before submission: -

Signature: ..... Date:.....

UNIVERSITY OF SOUTHAMPTON

Advanced Ultrafast Thulium-doped Fibre Laser Systems For Biomedical Imaging Applications

by

Ibrahim Husein Abughazaleh

Supervisors: Dr. Lin Xu
Prof. David Richardson
Dr. Yongmin Jung

Thesis

In the
Faculty of Engineering and Physical Sciences
Optoelectronics Research Centre

December 2025

Acknowledgements

Bismillāh wa al-ḥamdu lillāh.

I would like to give a special thank you to my supervisor, Dr. Lin Xu. I would also like to thank my co-supervisors, Yongmin Jung and Professor David Richardson, as well as my colleagues, for their input, continuous support, and valuable insights into this research. I would also like to express my deepest gratitude to my family for their encouragement and support.

ABSTRACT

This research presents the development of a high intensity ultrafast pulsed laser in the short-wave infrared (SWIR) region for deep-tissue medical imaging. The challenge is catering for the inhomogeneous biological system. To address this and uncover deep biological tissue structure, a mode-locked (ML) laser source with an operating wavelength of 1845 nm and 20.5 MHz repetition rate (RR) was used to seed a master oscillator power amplifier (MOPA) system. In addition, an acousto-optic modulator (AOM) and a pulse picker (PP) were added before the final amplifiers for peak power scaling at lower RR without increasing the average power responsible for thermal damage. The system features chirped pulse amplification (CPA), where pulses were temporally stretched, then amplified before recompression at the output using a grating pair to increase the peak powers of the pulses. As low as ∼380 fs compressed pulse duration was attained at 2 MHz of RR, resulting in peak powers up to 410 kW. Imaging experiments were carried out using this laser *in-vitro* on human and animal bone samples. The results revealed an increase in the imaging depth up to 400 μm as RR was reduced. To improve soft tissue imaging, a carbon nanotube (CNT) based ML laser was developed with a shorter emission wavelength of 1789 nm, which minimises water attenuation and enhances penetration in soft tissue. This was combined with a nonlinear amplification and compression achieved by provoking self-phase modulation (SPM) to broaden the pulse spectrum using a highly nonlinear fibre (HNF) before applying CPA to achieve pulse durations of 180 fs. The limit of short wavelength generation from an ML thulium (Tm) fibre system was explored next by developing a tunable source from 1900 to 1725 nm and an amplifier optimised for the short wavelength with the incorporation of a bending-induced low-pass fibre filter. Finally, a gain-switched laser diode (GSLD) was used as an "off-the-shelf" alternative for generating ultrafast pulses by initially applying SPM to broaden the spectrum, a spectral filter to clean the pulse chirp and a 2-stage compression method comprising a 100 m single-mode fibre (SMF) linear compressor and a nonlinear Tm-doped fibre amplifier compressor to achieve simultaneous pulse amplification and compression from 40 ps to 560 fs. A GSLD was also used to demonstrate an adaptive approach for selective imaging of regions of interest (ROI), increasing the resolution while minimising the effects of photo-toxicity, photo-bleaching, and thermal damage to surrounding tissue. Non-uniform pulsed patterns were generated and amplified to simulate this form of imaging, and the gain saturation effects during amplification were analysed. Analytical and numerical solutions were developed to predict and shape the amplifier input pulses to compensate for uneven pulse amplification on a single 50 ns burst and adapted for a 1 ms non-uniform multi-burst signal. Various advanced ultrafast Tm fibre laser technologies were developed for deep-tissue biomedical imaging, including source and amplifier design optimisation, and pulse manipulation.

Contents

List of Figures

List of Tables

List of abbreviations

Table 1: **List of abbreviations.**

Abbreviation	Full Term
2PF	Two-photon fluorescence
3PF	Three-photon fluorescence
ACF	Autocorrelation function
AWG	Arbitrary waveform generator
AOM	Acousto-optic modulator
ASE	Amplified spontaneous emission
CNT	Carbon nanotube
CPA	Chirped pulse amplification
CMA	Chirp-managed pulse amplification
CPAN	Chirped pulse amplifier and nonlinear broadening
CS	Conventional soliton
CT	Computed tomography
CW	Continuous wave
DCF	Dispersion compensation fibre
DS	Dissipative soliton
Er	Erbium
EDFA	Erbium-doped fibre amplifier
EDFL	Erbium-doped fibre laser
EOM	Electro-optic modulator
EM	Electromagnetic
FWHM	Full width at half maximum
FWM	Four-wave mixing
GDD	Group delay dispersion
GSLD	Gain-switched laser diode
GVD	Group velocity dispersion
HNF	Highly nonlinear fibre
HR	Highly reflecting
HWP	Half-waveplate

Continued on next page

Table 1 (continued)

Abbreviation	Full Term
ISO	Isolator
ML	Mode-locked
MO	Mamyshev oscillator
MR	Mamyshev regenerator
MOPA	Master oscillator power amplifier
MPM	Multiphoton microscopy
MFA	Mode field area
MFD	Mode field diameter
MRI	Magnetic resonance imaging
NALM	Nonlinear amplifier loop mirror
NOLM	Nonlinear optical loop mirror
NPR	Nonlinear polarisation rotation
NLSE	Nonlinear Schrödinger equation
NLS	Noise-like soliton
NA	Numerical aperture
NCPA	Nonlinear broadening with chirped pulse amplification
OC	Output coupler
OSA	Optical spectrum analyser
OSNR	Optical signal-to-noise ratio
LD	Laser diode
PER	Polarisation extinction ratio
PC	Polarisation controller
PPC	Peak power clamping effect
PET	Positron emission tomography
PM	Polarisation maintaining
PMT	Photomultiplier tube
PP	Pulse picker
QWP	Quarter-waveplate
RF	Radio frequency
ROI	Regions of interest
RR	Repetition rate
SA	Saturable absorber
SESAM	Semiconductor saturable absorber mirror
SHG	Second-harmonic generation
SWIR	Short-wave infrared
SNR	Signal-to-noise ratio
SMF	Single-mode fibre
SPM	Self-phase modulation
SWNT	Single-walled carbon nanotube

Continued on next page

Table 1 (continued)

Abbreviation	Full Term
SPS	Stretch pulse solitons
Tm	Thulium
TDF	Thulium-doped fibre
TDFA	Thulium-doped fibre amplifier
TDFL	Thulium-doped fibre laser
TFL	Transform-limited
TBP	Time-bandwidth product
THG	Third-harmonic generation
UHNA	Ultra-high numerical aperture
ARHCF	Anti-resonant hollow-core fibre
WDM	Wavelength division multiplexer
Yb	Ytterbium

Chapter 1

Introduction

The PhD research presented in this thesis is part of the EPSRC-funded InlightenUS project, which aims to deliver rapid, non-invasive diagnostic technologies for the health-care needs of the future. A study was conducted throughout the project to determine the optimum laser parameters for deep-tissue multiphoton microscopy (MPM).

In this section, the biological properties as well as the best-suited laser parameters for safe operation while maximising both the measured signal and penetration depths are discussed.

1.1 Research background

Current medical imaging modalities, such as X-rays and Computer Tomography (CT), expose patients to harmful ionising radiation. Positron Emission Tomography (PET) also involves radioactive frequencies and requires the injection of radioactive chemical tracers like ^{18}F-Glucose for visualisation purposes [1]. Magnetic Resonance Imaging (MRI) does not involve radiation or tracers. However, obtaining MRI scans is time-consuming, requiring patients to remain still for extended periods to prevent image artefacts. This can cause discomfort and, in some cases, claustrophobia due to the scanner's design [2]. Additionally, MRI poses risks for patients with metallic implants or tattoos due to its strong magnetic field [3]. Both MRI and PET scanners are complex, leading to high costs for their construction and maintenance. [2].

Nonlinear MPM excitation techniques have gained significant interest for non-radiative optical deep-tissue microscopy, although further development is needed for clinical applications. Such techniques include second/third-harmonic generation (SHG, THG) and two/three-photon fluorescence (2PF, 3PF). These techniques require high-intensity pulses in the near infrared region to generate observable signals in deep-tissue [4]. They offer advantages over existing clinical technologies by being inexpensive to build and

maintain, providing rapid label-free images without imposing ionising radiation or harmful tracers to biological tissue. The disadvantages of MPM, however, arise from the limited penetration depths of up to a few hundred micrometres to a millimetre due to the absorption of light to various degrees from different tissue. There are key factors that need to be considered for deep-tissue imaging, such as tissue absorption and scattering, which limit the allowable wavelengths for deep penetration as demonstrated in Fig. 1.1. These factors vary with wavelength across the visible and infrared regions, and that minimum loss can be achieved between 1600-1850 nm; this region is known as the optical transparency window [5]. Moreover, common issues that arise from the need to use high-power pulses for deeper tissue penetration include thermal tissue damage, photo-bleaching and photo-toxicity [6, 7]. Thermal damage arises from high average powers [6]. However, photo-bleaching occurs when the tissue is exposed for extended periods and the pulse RRs surpasses the fluorescence decay time (τ_f) of the tissue [4]. The risk of photo-toxicity rises with prolonged exposures and elevated laser powers [8]. The depth and type of tissue affect the optical losses and thresholds associated with these effects. Hence, progress towards the optimisation of the laser parameters and even developing adaptive imaging mechanisms is required.

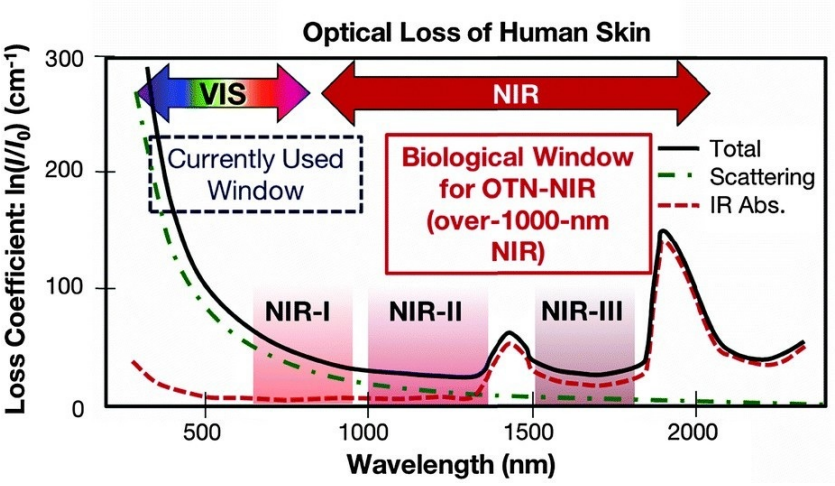

FIGURE 1.1: Optical transparency of human skin across the visible and near infrared, as a result of absorption (red) and scattering (green). This figure was adapted from *Eva Hemmer, 2016* [9].

To tailor laser systems for MPM, the optical transparency wavelength can be generated using of thulium-doped fibre (TDF), which has an emission bandwidth ranging from 1625-2100 nm. However, an operating wavelength below 1850 nm is more beneficial for deep-tissue applications. To achieve this emission, pump sources targeting the various absorption bands of Tm can be utilised. These include tandem pumping, high-power laser diodes at 790 nm, or erbium-doped fibre lasers operating between 1450-1600 nm [10, 11] (more on this chapter 2). The overlap of the emission and absorption bands in the relevant wavelength region for MPM presents a challenge for generating and amplifying a high-power signal for deep-tissue applications. High pulse energy, on the order of tens

of nanojoules, along with very short pulse durations of hundreds of femtoseconds, is essential for nonlinear imaging. This challenge becomes more significant as the power requirements increase at greater depths [12]. The pulse width requirement can be met with the use of an ML laser cavity and careful management of the net dispersion and pulse evolution [13]. The output power from these lasers is low. Therefore, an amplifier or a series of amplifiers to produce a MOPA system can be used to scale the pulse energy to meet the pulse requirement for imaging [14]. A common method to amplify ML lasers to achieve high peak powers is CPA, which involves initially stretching the pulse temporally in orders of tens of picoseconds, then amplifying before recompressing the pulses. The result is propagation of the pulse without any nonlinear distortion that affects the spectral coherence of the pulse and an increased pulse peak power at the output as a result of the reduced pulse width and amplifiers [14].

On these bases, a thulium-doped ML fibre laser and amplifier featuring CPA was built for third-order MPM at the start of my PhD. The work was carried out in collaboration with the Institute of Life Sciences (IFLS), where the laser was used for imaging. The performance of the laser was closely monitored, and limitations were discussed. My project revolved around continuing to improve and upgrade the imaging laser with novel technologies, making it a better fit for deep-tissue imaging based on the end user feedback. Traditional methods were initially adopted and pushed to their limits, and over time, a shift from conventional approaches was investigated, and the development of novel ultrafast technologies was demonstrated with ease of integration into the imaging laser in mind.

1.2 Aims and objectives

The project aimed to develop a compact, robust, high-power, ultrafast pulsed laser system for high-resolution, adaptive and efficient multiphoton imaging deep in biological tissue. The objectives set to accomplish the aims were to develop all-fibre Tm-doped fibre laser source and amplifiers, and shift the operational wavelength towards the shorter emission bandwidth of thulium, which coincides with the third optical transparency window of biological tissue. The absorption bandwidth of thulium overlaps with this wavelength region, making it challenging but necessary to achieve. Low average powers but high peak powers are needed; therefore, pedestal-free short compressed pulses in the order of hundred femtoseconds were required, increasing the efficiency by maximising the peak powers while maintaining a low average power. Additionally, the RR of the laser needs to be lowered to maximise the amplification per pulse while being high enough to avoid parasitic self-lasing in the amplifier and photon shot noise during microscopy. The RR manipulation can be achieved by the length of an ML cavity or externally via the use of optical intensity modulators such as an AOM or an electro-optic modulator (EOM). The efficiency of imaging can be further enhanced with adaptive imaging by

selective imaging of the ROI. This can be realised by firstly identifying the ROIs and secondly, encoding their spatial distribution into intensity-uniform temporal patterns. The synchronisation of the laser source with an arbitrary waveform generator (AWG) and AOM is essential for complex waveform generation.

1.3 Thesis Layout

This thesis is composed of 8 chapters.

The **first chapter** outlines the research background and defines the aims and objectives.

The **second chapter** reviews the multiphoton background and recent advancements in adaptive nonlinear imaging. It covers the relevant theoretical background, including the mechanisms of stimulated and spontaneous emission, an explanation of thulium fibre amplifiers, gain dynamics, mode-locking fundamentals, and pulse compression.

In the **third chapter**, the development and characterisation of the 1845 nm imaging laser will be presented, along with the results from a third-harmonic-generation imaging experiment.

The **fourth chapter** outlines the steps taken to create a novel fiberised imaging technology to enhance the existing imaging laser, addressing its limitations. A ML laser was constructed to test various nonlinear pulse amplification and compression techniques that enable shorter pulse durations and wavelength generation.

The **fifth chapter** explores the limitations of short wavelength generation in thulium ML fibre lasers. It discusses how a low-pass filter, induced by bending a weakly guiding dispersion compensation fibre (DCF), leads to the development of a dispersion management ML cavity with wavelength-tunable operation, dependent on the bending diameter of the low-pass filter. This chapter also introduces a novel fibre amplifier design for short wavelength amplification.

In the **sixth chapter**, methods for achieving ultra-short pulses without using ML laser systems are discussed. Techniques such as chirp cleaning and nonlinear compression are applied to the output of a GSLD, converting picosecond pulses into femtosecond pulses with output that approaches the near-transmission limit, owing to the induced soliton effect.

The **seventh chapter** features work on gain saturation compensation and burst preshaping for adaptive imaging, aimed at increasing the functionality of the imaging laser technology.

Finally, in the **eighth chapter**, I conclude with a discussion on future work and provide a comprehensive list of publications.

Chapter 2

Theoretical background

In this chapter, the relevant theories and recent research will be discussed, starting with a review of both adaptive and multiphoton imaging methods. This is followed by an examination of the theories behind amplification, ML laser development, alternative laser sources, and pulse compression, as well as specialised equipment used for both manipulating and measuring the laser output.

2.1 Multiphoton imaging

The second-order nonlinear multiphoton excitation process is depicted in Fig. 2.1. The differences between 2PF and SHG are shown. The latter is the frequency doubling of two identical frequencies, where $\omega + \omega = 2\omega$. The process requires a nonlinear medium for the phase-matching condition to be met. On the other hand, the excitation in the former process is caused by two photons of a similar wavelength that match the energy band gap of a molecule which is excited to an upper state, causing the signal to decay non-radiatively. Thus, the generated fluorescence frequency is $\omega_1 + \omega_2 > \omega_o$ where ω_1 and ω_2 are the frequencies of the incident photons and ω_o is the frequency caused by fluorescence decay [4].

The third-order nonlinearity effects, such as THG and 3PF, follow similar principles with an additional photon, and the peak power requirements scale up with the order of nonlinearity. As a result, the images show enhanced axial resolution due to the concentration of higher intensity areas within a smaller focal region, as shown in Fig. 2.2. Therefore, the higher-order nonlinearity is favourable for high-resolution imaging [16].

Moreover, 3PF and THG require longer excitation wavelengths compared to 2PF and SHG for the same electronic transition to achieve a visible signal. Whereas the absorption is wavelength-dependent, the use of the longer wavelengths benefits deep-tissue

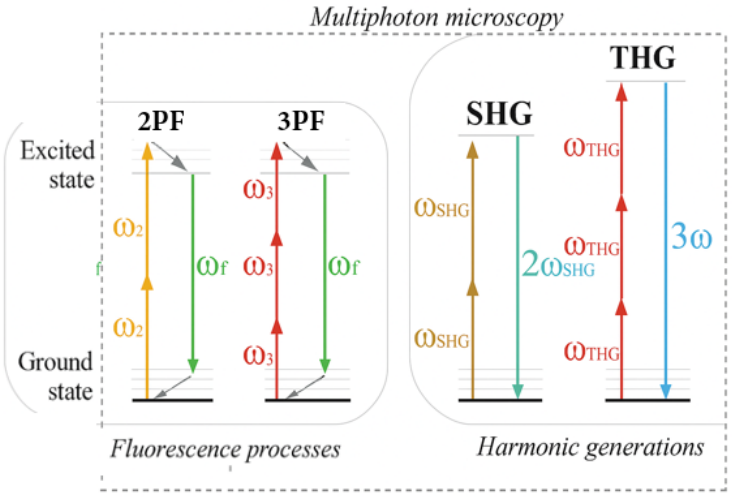

FIGURE 2.1: Two-photon fluorescence (2PF), second-harmonic generation (SHG), three-photon fluorescence (3PF) and third-harmonic generation (THG) processes. This figure was adapted from *C. Lefort, 2017* [15].

imaging, as they are less prone to scattering and reduce the effects of photo-bleaching and photo-toxicity since the energy per photon required for excitation is lower [17].

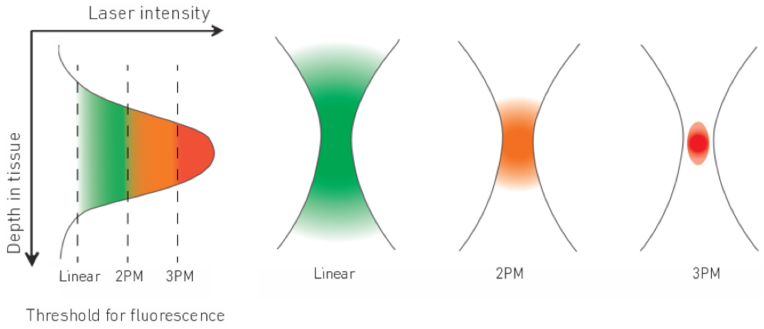

FIGURE 2.2: Single-photon (linear), two-photon (2PM) and three-photon microscopy (3PM) intensity and focal region dependence. This figure was reproduced from *Class 5 Photonics, 2025* [18].

A study by *Li et al.* compared the effectiveness of 3PF and 2PF techniques for imaging the same neurons in a mouse brain [6]. The authors found that with 3PF, they were able to reach imaging depths of up to 750 μm compared to only 680 μm when using 2PF. A high-power laser source was used to excite the nonlinear processes at these depths, which raises a fundamental limitation on the imaging of biological samples. Since high intensity pulses are required for high-resolution imaging at high penetration depths, maintaining a low average power is essential for minimising the effects of thermal damage. This trade-off is known as the "photon budget" and is a property of the biological tissue [6, 19].

2.2 Selective imaging

The fundamental limitation arising from the photon budget was addressed by *Li et al.* [6]. The authors developed an adaptive laser source with variable peak and average powers for illuminating different regions on a sample. The developed laser system, which is presented in Fig. 2.3, illustrates the involved methodology; firstly, raster scanning of the sample using low average power, then identifying the ROI with the aid of image processing. The information was then relayed to an AWG, which is a device used to produce electrical pulse signals with variable RR and amplitudes based on the desired function and input signal. The AWG output was used to generate a complex electrical pulse train to modulated the laser output by using an AOM to be "off" outside the locations of the ROI's. Since the modulator is placed before the amplifier, the peak powers are increased with a lower RR. As seen in Fig. 2.3, the AWG was used to drive the AOM based on input from the imaged samples and the output of the amplifier. Feedback from the output of the amplifier is required because with a non-uniform RR (bursts of signal), the pulses produced are amplified to different magnitudes, and the gain needs to be compensated [6]. The AWG and AOM need to be synchronised with the microscope, laser source, and identified ROI to achieve this adaptive output. An iterative method is used by *Li et al.* for gain compensation. They reported that it takes 30 iterations and up to 15 s to produce a uniform signal [6]. Control over the signal is important to ensure that the intended average power is maintained throughout the sample and damage is avoided.

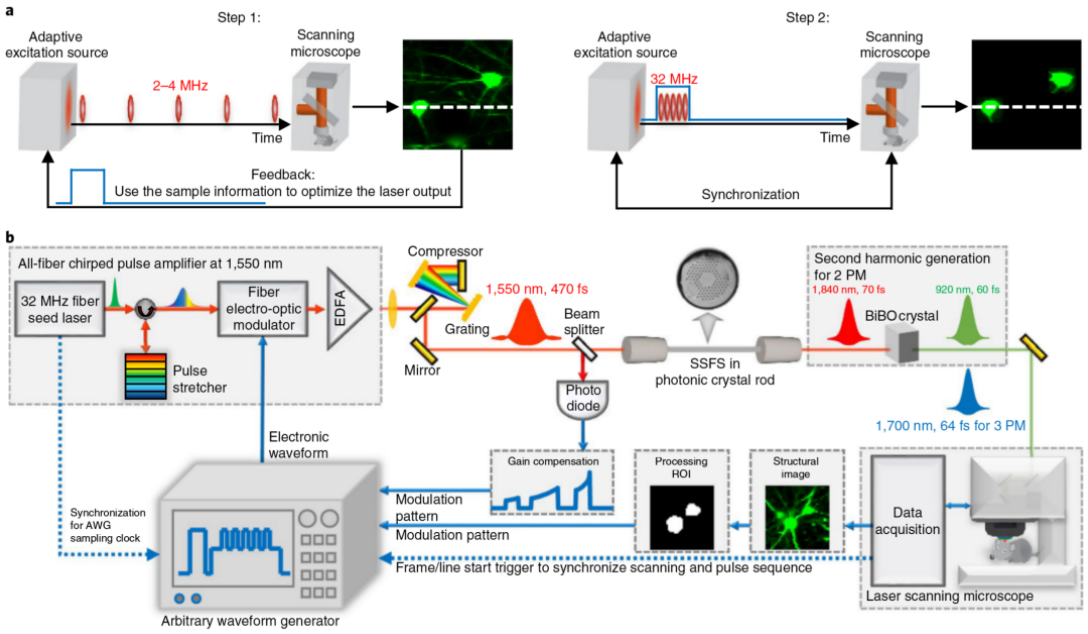

FIGURE 2.3: Adaptive multiphoton imaging laser source developed by *Li et al.*. This figure was reproduced from *Bo Li, 2020* [6].

Different biological tissues have different damage thresholds depending on the depth and the wavelength used for imaging. However, an average power in the range of 200-800 mW is needed for imaging biological samples, and a minimum RR of around 1 MHz is needed for fast imaging [6]. This power and RR combination can only be achieved with the use of adaptive imaging. The imaging speed and average power determine the pixel density, resolution, and duration of continuous sample monitoring. Using this adaptive technique, *Li et al.* tested the photon-to-noise ratio by counting the number of photons causing a signal. they found that the number of photons causing a signal per frame increased while the noise levels were decreased [6]. Therefore, it can be deduced that efficiency has been improved while using adaptive methods because the excitation is more probable when higher intensities are focused on specific areas. The laser source in Fig. 2.3 shows that *Li et al.* have converted a 1550 nm signal to 1700 nm via a soliton self-frequency shift (SSFS). In my project, thulium is proposed in an all-fibre laser system to directly generate the desired wavelength. Enhancing the method proposed by *Li et al.* creates a simpler and more efficient laser source.

Pinkard et al. have demonstrated a different approach for adaptive optical deep-tissue imaging [19]. Their approach is to minimise scattering effects depending on the sample's geometry and tissue type, since the optical path to the focus point will be affected differently. This implementation uses the 3D topology data from the sample as input for a machine-learning algorithm to predict the laser intensity needed to overcome the tissue scattering, whereas the method proposed by *Li et al.* requires the use of a feedback loop iterative model to highlight specific regions on the sample. Both allow imaging to be carried out deeper in tissue. But the former was demonstrated for providing 3D structural information, whereas the latter was demonstrated for monitoring tissue activity over time. *Pinkard et al.* have reported a significant increase in imaging depth when compared with constant illumination of the sample [19]. Specialised instruments are needed to map out the 3D structural information of the sample's surface, whereas the work carried out by *Li et al.* requires the modulation to occur in the laser system. This can be integrated with any microscope [6], making it easier to implement and test.

2.3 Laser theory

The intensity I of an electromagnetic (EM) wave propagating through an absorbing medium will be reduced with distance z as governed by the Beer-Lambert law [20].

$$\frac{dI}{dz} = -N\sigma(\omega)I(\omega) \tag{2.1}$$

By integrating equation 2.1, it becomes:

$$I = I_0 e^{-N\sigma L} \tag{2.2}$$

Where N is the number of absorbing centres per unit volume, σ is the optical cross-section, and I_0 is the initial intensity. Equation 2.2 shows an exponential decrease in the intensity. This basic concept governs many of the laser phenomena associated with emission and absorption in the gain medium of a laser and is used throughout the following sections for their derivation.

2.3.1 Laser amplification

The following equation describes the steady state behaviour, both spatially and temporally in a gain medium, and it states:

$$\frac{dN_2}{dt} = \Gamma - \frac{N_2}{\tau_f} - (N_2 - N_1)(\frac{\sigma(\omega)I(z)}{\hbar\omega}) \tag{2.3}$$

Where, $\hbar$ is the reduced planck's constant such that $\hbar = h/2\pi$, the term describing the pumping rate density (Γ) increases the population of the upper excited state, N_2/τ, which is the depletion of the upper energy state due to spontaneous emission. The last two terms show the depletion of the upper energy level via stimulated emission (negative term) and the reabsorption (positive term) of signals emitted by both stimulated and spontaneous processes. For a thin material such that z is small, the re-absorption term can be neglected and the intensity of the beam remains approximately constant [21]. The derived rate equation applies to a 4-level laser. If N_0 is the population in the ground energy level, N_3 is the pumped population from the ground state, N_2 and N_1 are the populations in the upper and lower laser transition energy levels, respectively, as indicated in Fig. 2.4. Transitions from levels 3 to 2 and 1 to 0 are transient and non-radiative [21] and describe the quantum defect q of an amplifier such that $q = (hf_{\text{pump}} - hf_{\text{signal}})/hf_{\text{pump}}$. Therefore, their temporal variation can be neglected, and population inversion can be assumed in terms of N_2.

Solving the steady state equation such that $dN_2/dt = 0$ in equation 2.3, gives an expression for the population inversion N_2 as follows:

$$\begin{aligned} N_2 &= \frac{\Gamma\tau_f}{1 + \frac{I(z)\sigma\tau_f}{\hbar\omega}} \\ Let,\ I_{sat} &= \frac{\hbar\omega}{\sigma\tau_f} \end{aligned} \tag{2.4}$$

The saturation intensity (I_{sat}) describes the value of the signal intensity where the population inversion is reduced by half. It is a limitation on the gain caused by the properties of the absorbing material as seen in equation 2.4. In confined structures such as an optical fibre, spontaneous emission can also saturate the gain as it can deplete the population inversion. The intensity of the spontaneous emission can be described

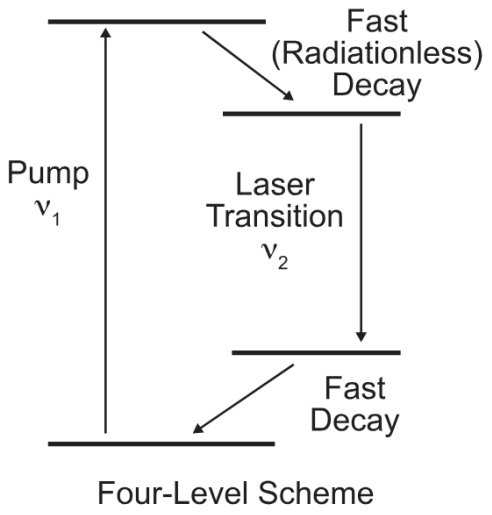

FIGURE 2.4: 4-Level laser gain medium. This figure was reproduced from *Paul McManamon, 2015* [22].

in terms of the power P of the spontaneously emitted signal, the area of the medium a, and the solid angle projection Ω as seen in equation 2.5.

$$I = \frac{P\Omega}{a4\pi} \tag{2.5}$$

The gain can be modelled by plugging the expression for N from equation 2.4 in equation 2.1 and integrating it to get an expression of the intensity I after propagating through the thickness L of an active medium.

$$N_0\sigma L = log(\frac{I(L)}{I(0)}) + \frac{I(L) - I(0)}{I_{sat}} \tag{2.6}$$

This shows an initial exponential increase in the intensity by neglecting the second term when $I(L) - I(0) << I_{sat}$. As the intensity increases such that $I(0) << I(L)$, the first term can be neglected, and a linear increase is observed.

2.3.2 Pulse gain dynamics

Another important theory to develop is the gain dynamics for a short interval (i.e. the gain function throughout a pulse). This is critical for selective imaging since amplifying non-uniform bursts results in a signal where the intra- and inter-pulse intensities vary due to the effects of gain saturation. To develop this theory, it is assumed that the effects of pumping remain constant over the burst duration, which is small relative to the period and excited-state lifetime. Therefore, the effects of amplified spontaneous emission (ASE) and additional build-up of the population inversion can be neglected across the burst duration [23]. Therefore, equation 2.3 becomes:

$$\frac{dN}{dt} = -N_2 I(z)(\frac{2 * \sigma(\omega)}{\hbar\omega}) \tag{2.7}$$

And by substituting in equation 2.1.

$$\frac{dN}{dt} = (I(t)_{out} - I(t)_{in})(\frac{2*}{\hbar\omega}) \tag{2.8}$$

Where $2*$ is a newly introduced factor that varies between 1 and 2 depending on how fast the lower excited state depletes; this is known as the "saturation factor" [23].

A term for the gain per unit length of doped fibre can be derived by slightly adjusting the terms and rearranging equation 2.2, whereby:

$$\begin{aligned} G(t) &= \frac{I(t)_{out}}{I(t)_{in}} \\ G(t) &= e^{-N_2(t)\sigma} \end{aligned} \tag{2.9}$$

From equation 2.4, the gain saturation energy per unit area becomes:

$$U_{sat} = \frac{\hbar\omega}{2 * \sigma} \tag{2.10}$$

By integrating $I(t)$ to get $U(t)$, the energy per unit area and using equation 2.8 an expression for transient gain can be developed as follows:

$$G(t) = 1 + (G_0 - 1)e^{\frac{E(t)_{out}}{E_{sat}}} \tag{2.11}$$

Where $G_0 = e^{\sigma N_0}$ is the small signal gain and $E = U * A_{eff}$, A_{eff} is the effective area given by $A_{eff} = k(\pi/4)MFD$ [24], k is the wave-number and MFD is the mode field diameter, which for an SMF (SMF28e) is calculated to be $10.4 \pm 0.4\mu m$ at 1550 nm.

By combining equation 2.9 and equation 2.11, the final mathematical term that models the pulse shape evolution through an amplifier can be attained, which is written as follows:

$$I(t)_{out} = \frac{I(t)_{in}}{1 + (G_0 - 1)e^{\frac{E(t)_{out}}{E_{sat}}}} \tag{2.12}$$

For a given amplifier (amplifier chain), equation 2.12 can be used to predict the amplifier input burst intensity profile $I(t)_{in}$ for a target output intensity shape $I(t)_{out}$. This method is used throughout the literature for pulse shaping [23, 25] and burst shaping [26, 27]. Practical limits are imposed by the speed of the optical modulators used to

shape the burst. Typical rise and fall times of AOM and EOM are in the order of $\sim$ 100 ns.

2.3.3 Emission and absorption of thulium-doped fibres

The target wavelength for deep-tissue imaging is 1600-1850 nm as mentioned in section 1. As seen in Fig. 2.5(b), Tm has an emission bandwidth that covers the desired range. Moreover, Fig. 2.5(a) shows two pumping wavelengths at 785 nm utilising the cross-relaxation between 2 Tm^{3+} ions or by pumping directly at around $\sim$ 1550 nm. Laser diodes at 785 nm tend to have high power at the cost of low brightness, making them more suitable for cladding pumping. Furthermore, as seen in Fig. 2.5(b), Tm has the highest absorption peak at 785 nm pump wavelength. However, due to cross-relaxation, this method requires a long length of high Tm density in the fibre to be an effective method of generating the required wavelength [28]. Moreover, a high doping concentration can also lead to a higher re-absorption between 1600-1800 nm, especially at increased fibre length, as shown in Fig. 2.5(b), which can limit the gain and energy in this range.

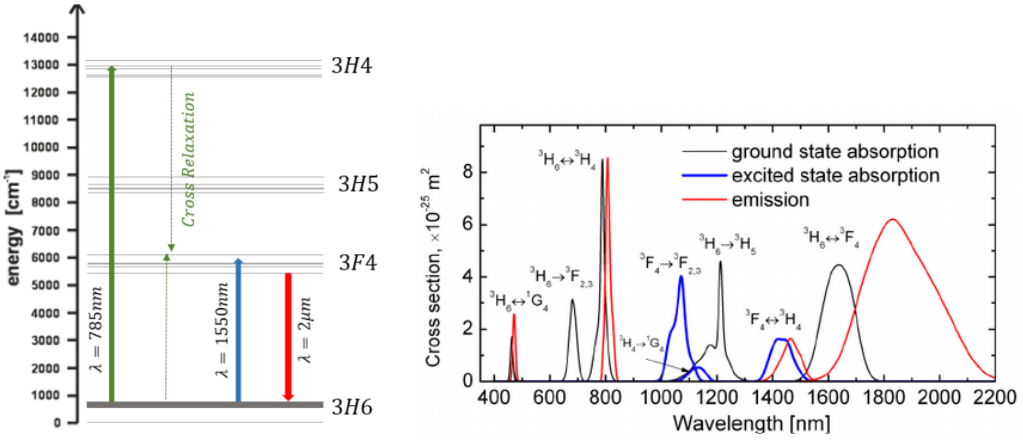

(a) Tm^{3+} energy levels showing manifolds and 2 pumping schemes. This figure was reproduced from *Eoin Russell, 2018* [28].

(b) Absorption (blue) and emission (red) spectrum of Tm^{3+}. This figure was reproduced from *Bernard Dussardier, 2012* [29].

FIGURE 2.5: Tm^{3+} energy levels corresponding to 2 μm emission and the bandwidth spectrum of emission and absorption.

On the other hand, erbium (Er) doped fibres can be used to build lasers and amplifiers capable of a broad emission band between 1450-1600 nm and an absorption wavelength at 980 nm, as shown in Fig. 2.6(a). The absorption at the pump wavelength is relatively small. Therefore, the efficiency of Er can be further enhanced by co-doping the fibres with ytterbium (Yb), as it has a higher absorption cross-sectional area as seen in Fig.

2.6(b). Thus increasing absorption of the pump wavelength before non-radiatively emitting the pump wavelength to Er dopants [30, 31]. Such pump sources can be achieved from laser diodes with SMF pigtails for ease of integration with multiple laser diodes to increase the output power of erbium-doped fibre lasers/amplifiers (EDFL/A) with the advantage of high brightness, courtesy of all single-mode operation (pump input and signal output) [32]. Pumping Tm with Er-doped lasers is known as in-band pumping, and due to the smaller shift in the wavelength of the pump and signal, the quantum defect and heat generation are reduced [33, 34]. In-band pumping is best used for core pumping of thulium laser systems. This allows the use of shorter TDF lengths, higher gain in the shorter wavelength and higher brightness at the output with near diffraction-limited beam quality essential for confocal imaging.

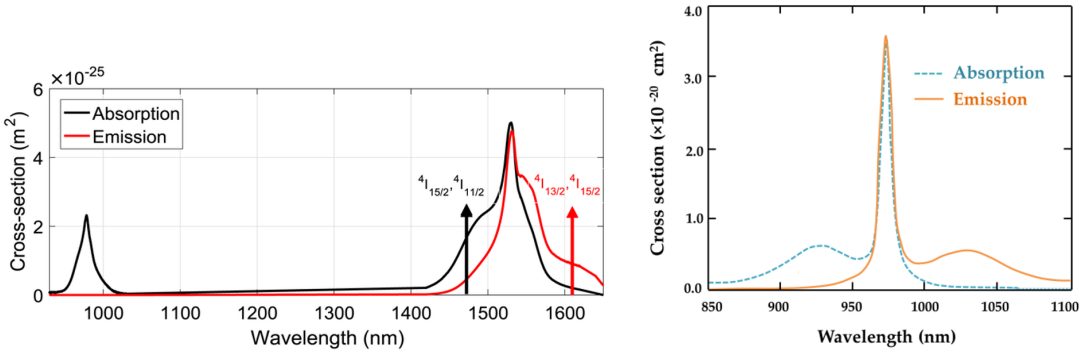

(a) Er-Doped Optical Fibre emission and absorption spectra. This figure was adapted from *Benish Kanwal, 2023* [35].

(b) Yb-Doped Silica Fiber emission and absorption spectra. This figure was adapted from *Maryam Ilchi-Ghazaani, 2016* [36].

FIGURE 2.6: Emission and absorption rare-earth dopants.

The wide emission and absorption spectral bandwidth seen in Fig. 2.5(b) can be understood by observing the energy levels in Fig. 2.5(a). Doping rare earth metal ions such as Tm^{3+} in a glass fibre distorts the electronic configuration of the material, leading to the broadening and splitting of the energy levels into manifolds. This is known as inhomogeneous broadening, and different host materials can cause deviation in the the emission and absorption spectra [11]. Finally, the parameters of interest for a single-mode TDF with a 9 μm core were calculated using the formulas previously mentioned and are shown in Table 2.1 below. These parameters were assumed for all the TDFA's used in this project.

TABLE 2.1: Relevant 9 μm diameter core single-mode TDF parameters [37].

Thulium fibre parameter	Symbol	Value
Peak emission cross section (m^2)	σ	$6.00E{-}25$
Effective mode field area (m^2)	MFA	$8.39E{-}11$
Fluorescence lifetime (s)	τ_f	0.00056
Saturation energy (J)	E_{sat}	$1.48E{-}5$

2.4 Mode-Locked fibre lasers

Mode-locking is one of the most common ways of generating ultrafast laser pulses in the range of sub-100 fs, with variable RR of up to a few hundred megahertz depending on the laser cavity length [38]. Specifically, passive mode-locking is better suited for the short-pulse generation since it relies on the relatively fast effects of a saturable absorber (SA) over the electronically driven AOM and EOM used in active mode-locking.

Nonlinearity and chromatic dispersion play an important role in attaining mode-locking; both parameters can be easily controlled with the use of fibres. Both properties are influenced by fibre design, material, and wavelength [38]. The propagation of a pulse in a passive optical fibre and how the pulse shape evolves during propagation is a result of the interplay between the nonlinearity and the dispersion. This is described by the nonlinear Schrodinger equation (NLSE), which states:

$$\frac{\delta A}{\delta z} + \frac{A\alpha}{2} + \frac{i\beta_2}{2}\frac{\delta^2 A}{\delta T^2} = i\gamma|A|^2 A \tag{2.13}$$

Where $A = \sqrt{P_0}e^{i\phi}$ is the slowly varying pulse amplitude, $\phi = k_0 nz - \omega_0 t$, n is the refractive index, z is the propagation distance, k_0 is the wavenumber in a vacuum, ω the angular frequency of the pulse, T is the time variable measured in the frame of a moving pulse, and α is the attenuation constant of the fibre due to material absorption and Rayleigh scattering caused by imperfections in fibre fabrication that lead to density fluctuation, causing wavelength dependant losses defined as $\alpha L = -10log(P/P_o)$, where the minimum loss in silica fibres is $0.2dB/km$ at 1550 nm [39]. Lastly, β_2 and γ refer to the second-order of dispersion known as group velocity dispersion (GVD) and a property of the fibre known as the nonlinear coefficient, respectively. It should be noted that the spatial mode distribution in the presumed SMF is ignored since the variation in the pulse spectrum over the effective area A_{eff} of the fibre is negligible [39].

The formation of stable pulses known as solitons in ML lasers arises from the breakup of continuous wave (CW) radiation travelling in a nonlinear anomalous dispersion medium. This effect, known as modulation instability, is spontaneous, and mathematically is described as the accumulation of power-dependent nonlinear phase shift [40] as follows:

$$\phi_{NL} = \gamma P_0 z \tag{2.14}$$

The following sections will introduce the theory behind mode-locking and the components used to achieve it, followed by the soliton pulse dynamics in a laser cavity.

2.4.1 Nonlinearity and dispersion

The effects of nonlinearity and dispersion on propagation in a passive fibre will be considered separately. This can be understood by examining the effective refractive index of the fibre, which is the sum of the linear and nonlinear components [41], such that:

$$n_{eff}(\omega, E) = n(\omega) + n_2|E|^2 \tag{2.15}$$

Where n is the linear (first-order) refractive index that depends on the material and the wavelength of radiation, and n_2 is the nonlinear refractive index mathematically defined as $n_2 = Re(\chi^3)3/8n$. Only third-order susceptibility exists in silica fibres since the molecules are centrosymmetric; thus, the second-order nonlinearity vanishes and the strength of higher-order nonlinear effects is negligible in comparison [39].

From equation 2.15 it can be observed that while the linear refractive index is influenced by the wavelength of light, the nonlinear component scales with peak power instead $|E|^2$.

Therefore, two parameters can be introduced: dispersion length L_D, and the nonlinear length L_{NL}, which help visualise mathematically the propagation distance at which each effect becomes significant on the evolution of the pulse. They can be expressed as follows:

$$\begin{aligned} L_D &= \frac{T_0^2}{|\beta_2|} \\ L_{NL} &= \frac{1}{\gamma P_0} \end{aligned} \tag{2.16}$$

Where T_0 is transform-limited (TFL) pulse width, P_0 is peak power and the nonlinear coefficient γ can be defined as,

$$\gamma = \frac{n_2\omega_0}{cA_{eff}} \tag{2.17}$$

Where the effective area is $A_{eff} = \pi r^2$. A higher peak power leads to a shorter nonlinear length L_{NL}, which enhances the impact of nonlinearity on the pulse. Conversely, a longer pulse duration represents a longer L_D, leading to weaker effects of dispersion on the pulse evolution. Equation 2.17 shows that the nonlinearity of a fibre is not only wavelength dependent but also varies depending on the material and fibre design represented by the nonlinear refractive index n_2 and A_{eff}, respectively.

The relevant parameters at 1.8 μm for the fibres used throughout the project are given in Table 2.2, based on manufacturer data sheet and reports in the literature.

TABLE 2.2: Relevant fibre parameters [42–44].

Fibre	SMF28e	OFS TDF	UHNA7	UHNA4	PM1550	PM2000D	HN1550
$\beta_2(ps^2m^{-1})$	-0.058	-0.02	0.046	0.093	0.065	0.09	0.000531
$\beta_3(ps^3m^{-1})$	0.00104	0.00096	-0.00014	0.000033	-	-	-
$A_{eff}(um^2)$	93.3	27.5	11	23	80.1	12.6	12.4
$\gamma(W^{-1}m^{-1})$	0.00074	-	-	-	-	-	0.0108

2.4.1.1 Chromatic dispersion

Variable β has been introduced in many equations as it plays an important role in describing the wave propagation vector perpendicular to the wavefronts, where $\beta(\omega) = n\omega/c$. Using Taylor's expansion gives us the following expression:

$$\beta(\omega) = \beta_0 + \beta_1(\omega - \omega_0) + 1/2\beta_2(\omega - \omega_0)^2 + 1/6\beta_3(\omega - \omega_0)^3 + ... \tag{2.18}$$

Where, $\beta_n = \frac{\delta^n\beta}{\delta\omega^n}$, β_0 is the wavenumber also denoted as $k = n\omega/c$, $v_g = \beta_1^{-1}$ is the the group velocity, which is the speed at which the pulse envelope moves through a material, β_2 is the GVD responsible for pulse broadening by inducing a linear chirp across the pulse, and β_3 is the third-order dispersion, which imposes a nonlinear chirp (temporal variation of the instantaneous frequency) on the pulse causing asymmetric pulse evolution. β_3 is negligible for pulses with a spectral width $\Delta\omega << \omega_0$ [41]. Its effects become more significant for pulse widths below 100 fs and can be detrimental to the overall pulse shape because, unlike β_2 they can't be reversed by normal means of pulse compression (more on this section 2.5). The first two terms of the Taylor expansion are defined as follows:

$$\beta_1 = 1/c(n + \omega\frac{dn}{d\omega}) = n_g/c = 1/v_g \tag{2.19}$$

$$\beta_2 = 1/c(\frac{\omega d^2n}{d\omega^2} + \frac{2dn}{d\omega}) \tag{2.20}$$

Where n_g is the group index that describes the variation in the velocity of different wavelength components of a pulse. For silica fibres, the refractive index variation with wavelength can be seen in Fig. 2.7. However, equation 2.20 does not account for the waveguide dispersion, shifting the total dispersion by manipulating different fibre parameters such as birefringence, core size, and core-cladding index [39]. The modified dispersion formula becomes:

$$D = -\frac{\beta_2 2\pi c}{\lambda^2} \tag{2.21}$$

Two key features can be seen from Fig. 2.7. D is negative and decreases in magnitude with wavelength until reaching zero dispersion at 1.284 μm for fused silica [45]. This

region is known as normal dispersion. Below-zero dispersion, D becomes positive and increases in magnitude for longer wavelengths; this region is known as anomalous dispersion, and it is where the wavelength of choice for deep-tissue imaging laser development resides. In the normal dispersion region, the shorter wavelengths travel more slowly than the longer wavelengths and for anomalous dispersion, the opposite is true. Waveguide design can shift the dispersion, as seen in fibres such as the ultra-high numerical aperture fibres e.g UNHA7 and UHNA4 (from Coherent, Inc.). As the name suggests, the increased numerical aperture allows the capability of normal dispersion at 1.8 μm by decreasing the core size and increasing the doping concentration of germanium in the core [46].

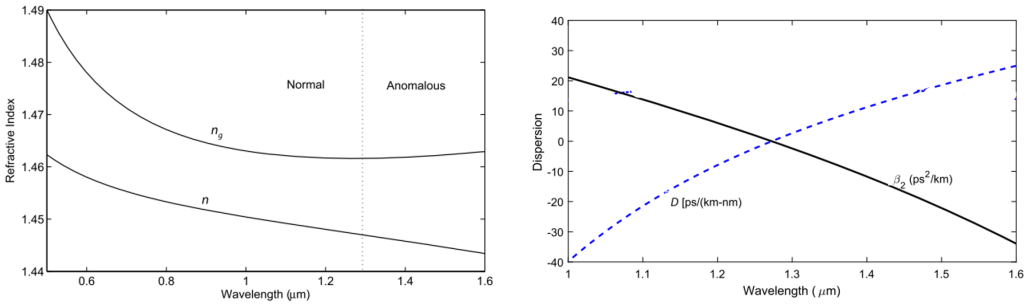

(a) Index of refraction n and group index n_g

(b) Group-velocity dispersion D and β_2

FIGURE 2.7: Dispersion wavelength dependence for fused silica (solid curves). These figures were reproduced from *Agrawal, Govind P., 2019* [47].

To investigate the effects of GVD acting on the pulse in the absence of nonlinearity and losses, equation 2.13 changes such that all α and γ terms go to zero, leaving $-idU/dz = \beta_2/2\frac{d^2U}{dT^2}$. This can be used to create an equation for the pulse shape in terms of the normalised pulse amplitude $U(z,T)$ as a function of time and distance as follows:

$$U(z,\omega) = U(0,\omega)e^{(-i\beta_2\omega^2 z/2)} \tag{2.22}$$

By applying the Fourier transform to equation 2.22,

$$U(z,T) = 1/2\pi \int_{-\infty}^{\infty} U(z,\omega)e^{(-i\omega T)}d\omega \tag{2.23}$$

Equations 2.22 and 2.23 provide spectral and temporal information about the pulse [47]. Assuming an initial Gaussian pulse shape such that:

$$U(0,T) = e^{(-T^2/2T_0^2)} \tag{2.24}$$

and spectrally,

$$U(0,\omega) = \int_{-\infty}^{\infty} U(0,T)e^{(i\omega T)}dT \tag{2.25}$$

Therefore [47],

$$U(z,T) = \frac{T_0^2}{(T_0^2 - i\beta_2 z)^{1/2}} e^{(\frac{-T^2}{2(T_0^2 - i\beta_2 z)})} \tag{2.26}$$

Where T_0 is the full width at half maximum (FWHM) of an unchirped pulse duration. A graphical representation of equation 2.26 is seen in Fig. 2.8, whereby it shows that under the influence of GVD, a pulse would maintain its shape, but the temporal width would increase by the following relationship:

$$T = T_0(1 + (z\beta_2/T_0^2)^2)^{1/2} \tag{2.27}$$

For values where $1 << (z\beta_2/T_0^2)^2$, equation 2.27 becomes $T \approx z\beta_2/T_0$, which shows that the output pulse width would be larger for longer propagation distances, higher β_2, and for a narrower initial pulse width.

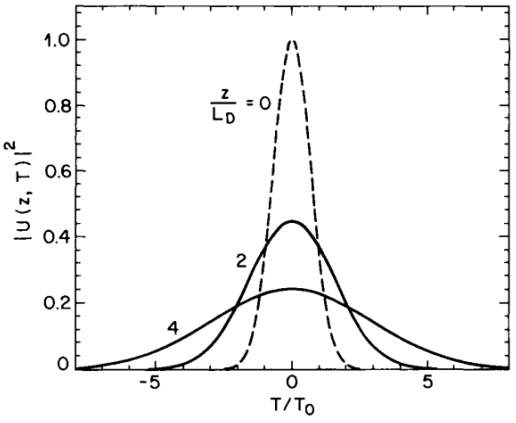

FIGURE 2.8: Dispersion-induced broadening of a Gaussian pulse inside a fibre at different propagation distances $z = 2L_D$ and $z = 4L_D$. This figure was reproduced from *Govind P. Agrawal, 1995* [48].

On the other hand, the effect on the phase shift temporally is:

$$\phi(z,T) = -\frac{sgn(\beta_2)(z\beta_2/T_0^2)T^2}{T_0^2(1 + (z\beta_2/T_0^2)^2)} + 1/2tan^{-1}((z\beta_2/T_0^2)) \tag{2.28}$$

The frequency shift can be calculated from the first derivative of phase such that $\delta\omega = -\delta\phi/\delta T$ [48].

$$\delta\omega = \frac{sgn(\beta_2)(2z\beta_2/T_0^2)T^2}{T_0^2(1+(z\beta_2/T_0^2)^2)} \tag{2.29}$$

Equation 2.29 shows that the spectral components will spread out across the pulse, causing a linear frequency shift known as a linear chirp, which is negative or positive depending on the sign of β_2.

2.4.1.2 Self-phase modulation

SPM is the manifestation of the third-order nonlinearity. It is an instantaneous effect that causes spectral broadening to occur in a pulse propagating in a nonlinear medium by generating new spectral components [49]. To understand the effect of nonlinearity on the pulse, all the dispersive and loss terms in equation 2.13 can be neglected to become,

$$\frac{\delta U}{\delta z} = i\gamma|U|^2U \tag{2.30}$$

The equation above can be solved to give the following expression for the field amplitude as a function of propagating distance z and time frame of pulse T:

$$U(z,T) = U(0,T)e^{(i\phi_{NL}(z,T))} \tag{2.31}$$

where,

$$\phi_{NL}(z,T) = |U(0,T)|^2(z\gamma P_0) \tag{2.32}$$

It should be noted that, due to the peak power dependence of the nonlinearity, the presence of losses in the distance travelled z is replaced with $z_{eff} = (1-e^{-\alpha z})/\alpha$. Equation 2.31 shows that the temporal profile of the pulse doesn't change under the influence of SPM. The maximum phase shift (ϕ_{max}) occurs at the center of the pulse where $U(0,0) = 1$ resulting in $\phi_{max} = 1 = z\gamma P_0$. The spectral effects can be understood by taking the first derivative of the phase such that:

$$-d\phi_{NL}(z,T)/dT = \delta\omega(T) = -\frac{d|U(0,T)|^2}{dT}(z\gamma P_0) \tag{2.33}$$

The time dependence of $\delta\omega$ shows a frequency chirp that is proportional to the derivative of the pulse intensity profile, suggesting that the new spectral components are being continuously generated during propagation, increasing the magnitude of the pulse chirp

[48]. Assuming a Gaussian pulse profile as shown in equation 2.24, the solution to equation 2.33 can be written as follows:

$$\delta\omega(T) = (2z\gamma P_0 T/T_0^2)e^{-(T/T_0)^2} \tag{2.34}$$

A plot visualising equation 2.34 is shown in Fig. 2.9. Equation 2.32 showed that the temporal phase shape follows the pulse intensity profile. Using these equations, three main features can be understood about the SPM-induced spectral broadening. Firstly, is zero at the centre and the chirp increases positively and linearly through central part of the pulse from negative at the leading to positive at the trailing edge. This results in the production of lower frequencies at the trailing edge, known as the red shift, and higher frequencies at the leading edge, known as the blue shift. The peak frequency chirp occurs at the steepest part of the pulse and increases with "steepness" and becomes nonlinear towards the edges.

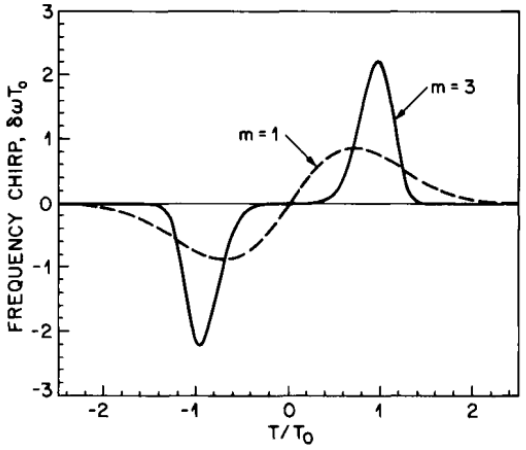

FIGURE 2.9: SPM induced frequency chirp on a Gaussian (dashed) and super-Gaussian (solid) pulses. This figure was reproduced from *Govind P. Agrawal, 1995* [49].

2.4.1.3 Four-wave mixing

Generating new spectral components is also possible through a process known as four-wave mixing (FWM). Unlike SPM, it is the manifestation of the third-order nonlinearity when a phase-matching condition is met [50]. The process occurs when photons annihilate, creating two new photons where their energy and momentum are conserved. To analyse this, four linearly polarised photons with the same or different frequencies, denoted as $(\omega_1, \omega_2, \omega_3, \omega_4)$, are considered. Their total electric field ($\mathbf{E}$) and induced nonlinear polarisation ($\mathbf{P}_{NL}$) in the fibre can be described as [50]:

$$\mathbf{E} = \hat{x}\,\frac{1}{2}\sum_{j=1}^{4} E_j\,\exp[i(k_j z - \omega_j t)] \tag{2.35}$$

$$\mathbf{P}_{NL} = \hat{x}\,\frac{1}{2}\sum_{j=1}^{4} P_j\,\exp[i(k_j z - \omega_j t)] \tag{2.36}$$

Solving the equation 2.36 shows that a single polarisation is induced as a product of three electric fields. For example, for P_4:

$$\begin{aligned} P_4 = n_2 \left\{|E_4|^2 + 2\left(|E_1|^2 + |E_2|^2 + |E_3|^2\right)\right\} E_4 \\ + 2E_1E_2E_3\exp(i\theta_+) + 2E_1E_2E_3^*\exp(i\theta_-) + \cdots, \end{aligned} \tag{2.37}$$

Where,

$$\theta_+ = (k_1 + k_2 + k_3 - k_4)z - (\omega_1 + \omega_2 + \omega_3 - \omega_4)t, \tag{2.38}$$

$$\theta_- = (k_1 + k_2 - k_3 - k_4)z - (\omega_1 + \omega_2 - \omega_3 - \omega_4)t. \tag{2.39}$$

The term proportional to $|E_4|^2$ is responsible for SPM, which has been discussed in section 2.4.1.2, whereas the rest of the terms describe FWM. Two types of FWM mixing are seen from the equations describing phase-matching conditions. The first, is THG, where $\omega_1 + \omega_2 + \omega_3 = \omega_4$ such that $\omega_1 = \omega_2 = \omega_3$ or $\omega_1 \neq \omega_2 = \omega_3$. The second is the annihilation of two photons while simultaneously generating two new photons such that $\omega_1 + \omega_2 = \omega_4 + \omega_3$. The phase-matching condition required for FWM is such that the relative phase between photons vanishes ($\Delta K = 0$). The phase matching condition is harder for THG and is how a visible signal is achieved during third-order nonlinear imaging, but it is harder to achieve in a fibre relative to the second process. Therefore, only the second case of FWM will be considered moving forward in this section. The frequency shift as a result of FWM is given by $\Omega_s = \omega_1 - \omega_2 = \omega_3 - \omega_4$; where $\omega_3 < \omega_4$ are referred to as Stokes and anti-Stokes, respectively. The process is considered degenerate if the pump photons are equal, such as $\omega_1 = \omega_2$.

Assuming a single-mode operation, degeneracy, and using the paraxial wave propagation equation, key equations can be gained from solving equations 2.35 and 2.36. For two pump photons with incident pump powers P_2 and P_1, such that $P_i = |E(0)_i|^2$:

$$g = [(4\gamma^2 P_2 P_1) - (\kappa/2)^2]^{1/2} \tag{2.40}$$

where,

$$\kappa = \Delta K_M + \Delta K_W + \Delta K_{NL} \tag{2.41}$$

$$L_{coh} = 2\pi/\Delta\kappa \tag{2.42}$$

Where g is the parametric gain, which depends on the pump power and relative photon phase, which is maximised when the net phase mismatch $\kappa = 0$. The coherence length

L_{coh} defines the length at which the phase mismatch is negligible, since it is challenging to maintain phase matching over long distances in the presence of dispersion.

There are several ways of achieving phase matching. The first thing to consider is that phase shift can be caused by material dispersion ΔK_M, waveguide dispersion ΔK_W, and nonlinear effects ΔK_{NL}. They are mathematically defined as:

$$\Delta K_M = \frac{n_3\omega_3 + n_4\omega_4 - n_1\omega_1 - n_2\omega_2}{c} \tag{2.43}$$

$$\Delta K_W = \frac{\Delta n_3\omega_3 + \Delta n_4\omega_4 - \Delta n_1\omega_1 - \Delta n_2\omega_2}{c} \tag{2.44}$$

$$\Delta K_{NL} = \gamma(P_1 + P_2) \tag{2.45}$$

Therefore, to achieve phase matching, at least one of these components needs to be negative. In a SMF, there are three possible ways to achieve this [50]:

- Reduce ΔK_M and ΔK_{NL} by using small frequency shifts and low pump powers.
- Operate near the zero-dispersion wavelength so that ΔK_W nearly cancels ΔK_M + ΔK_{NL}.
- Operate in the anomalous GVD regime so that ΔK_M is negative and can be cancelled by ΔK_{NL} + ΔK_W .

Alternatively, birefringent fibres can be used to achieve phase matching. Fibres may be strongly birefringent, as in polarisation-maintaining (PM) fibres, or weakly birefringent, as in non-PM fibres. In PM fibres, stress rods are embedded in the cladding to induce a higher refractive index along one axis compared to the other as shown in Fig. 2.10.

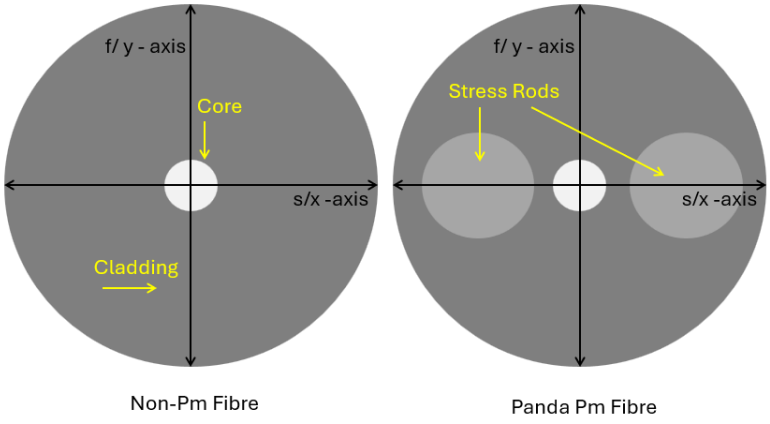

FIGURE 2.10: A cross-section comparison of pm and non-pm fibres showing the asymmetrical induced refractive index due to the addition of stress rods.

The conditions that need to be met are given in Table 2.3 [50]:

TABLE 2.3: Wave polarisation, frequency shift, and phase-matching condition for different processes. Reproduced from *Govind P. Agrawal, 1995* [50].

Process	**Wave Polarization**				**Frequency shift Ω_s**	**Condition**
	A_1	A_2	A_3	A_4		
I	s	f	s	f	$\delta n/(\lvert\beta_2\rvert\, c)$	$\beta_2 > 0$
II	s	f	f	s	$\delta n/(\lvert\beta_2\rvert\, c)$	$\beta_2 < 0$
III	s	s	f	f	$(4\pi\, \delta n/\lvert\beta_2\rvert\, \lambda_1)^{1/2}$	$\beta_2 > 0$
IV	f	f	s	s	$(4\pi\, \delta n/\lvert\beta_2\rvert\, \lambda_1)^{1/2}$	$\beta_2 < 0$

Where δn is the fibre birefringence defined as $\delta n = \Delta n_x - \Delta n_y$, and s and f refer to the slow and fast axes, respectively.

2.4.2 Saturable absorber

SAs can be either physical optical components, such as CNTs, semiconductor saturable absorber mirrors (SESAMs), or artificial ones that rely on the nonlinear properties of light. The most common types of artificial SA are nonlinear amplifier/optical loop mirror (NALM/NOLM), nonlinear polarisation rotation (NPR), and a Mamyshev regenerator (MR). Both techniques are intensity-dependent; however, the latter are known as fast SAs since the pulse regulates itself, whereas the SA carried out by the material tends to be a slower process, reshaping the pulse. Material SA have limitations in high-power applications due to their low damage thresholds [51, 52]. Both types were explored throughout the project, and the working principles behind each are discussed in this section. In classifying and evaluating SAs, several key properties are considered, as they directly determine the suitability of an absorber for mode-locking. The saturation fluence, which defines the optical power required to bleach the absorber, while the modulation depth quantifies the maximum change in transmission and therefore the strength of pulse shaping. The non-saturable loss represents residual absorption that cannot be bleached and thus limits overall laser efficiency. Another critical factor is the recovery time, which distinguishes fast absorbers (fs–ps timescales, suitable for ultrafast mode-locking) from slower ones (ns–μs, typically used for Q-switching).

2.4.2.1 Material saturable absorber

A CNT is a thin layer of transmissive material that can be embedded into the cavity. On the other hand, SESAM consists of reflective components made up of a Bragg grating mirror and quantum well absorber layer with a bandgap that determines the operating wavelength, recovery time, and modulation depth of the SESAM. Moreover, the Bragg grating structure is set up so that each layer is optically equivalent to a quarter wavelength $nd = \lambda/4$ [53]. The properties of both SAs that have been used throughout the project are shown in Fig. 2.11. The different CNT samples characterisation was carried

out by Dr.Panuwat Srisamran; however, CNT sample number 4 was used in the imaging laser for its relatively higher losses at longer wavelengths of the thulium emission.

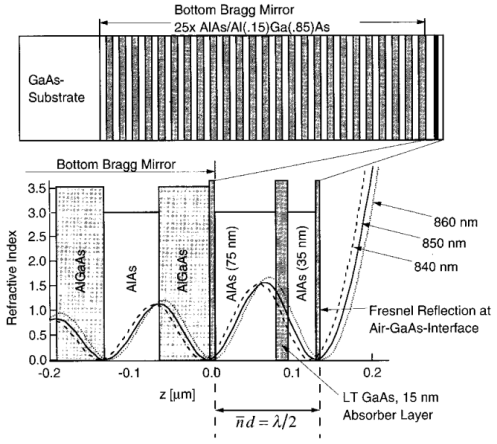

(a) SESAM structure showing quantum well layer followed by the Bragg gratings. This figure was reproduced from *D. Kopf, 1997* [53].

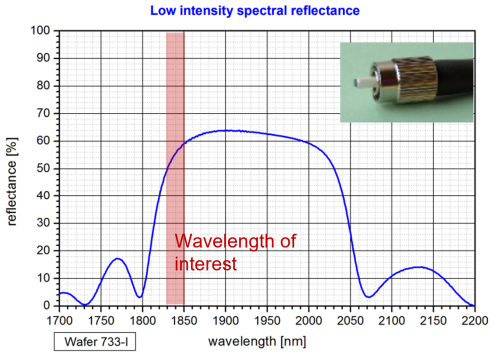

(b) Wavelength dependant reflectance of SESAM-1960 from "Batop optoelectronics". This figure was reproduced from *BATOP GmbH, 2024* [54], in accordance with their open access policy and terms of use.

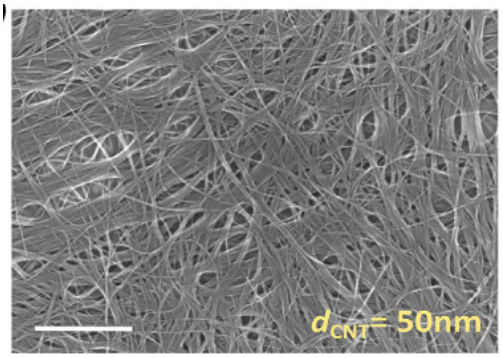

(c) CNT cross-section structure. This figure was reproduced from *Grzegorz Sobon, 2017* [55].

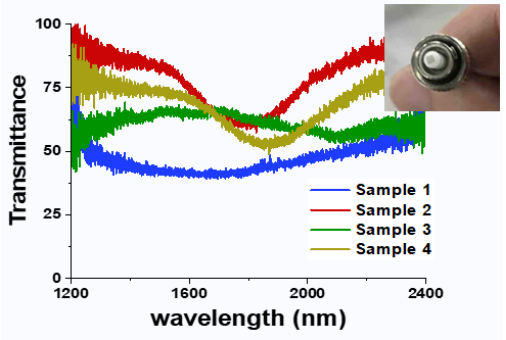

(d) Measured transmission spectrum of different CNT samples.

FIGURE 2.11: Schematics and spectral response of both the SESAMs and CNTs used in this study.

SAs are classified as either slow or fast-acting depending on the recovery time relative to the pulse duration. In the case of a fast SA, the recovery time is shorter than the pulse duration [56] and the losses follow the shape of the pulse temporally given by,

$$\alpha_{sa}(T) = \frac{\alpha_0}{1 + \frac{|U(T)|^2}{P_{sat}}} \tag{2.46}$$

Where α_0 is the unsaturated loss of the SA, P_{sat} is the saturation power of the SA, which is the power it takes to reduce the initial value to $1/e$ [57]. In the case of a slow absorber with a recovery time τ_{sa} longer than the pulse duration, the losses become,

$$\frac{d\alpha_{sa}(T,t)}{dt} = -\frac{\alpha_{sa} - \alpha_0}{\tau_{sa}} - \frac{\alpha_{sa}|U(T,t)|^2}{U_{sat}} \tag{2.47}$$

As a result of the loss-gain dynamics from the active fibre and saturable absorption, the areas of the pulse where the losses fall below the gain threshold are amplified each round-trip, thus shaping the pulse. The non-uniform slow response of the SA results in a time delay in the pulse train caused by a shift in the peak intensity of the pulse.

2.4.2.2 Artificial saturable absorber

As shown in Fig. 2.12, NPR can be set up by having two polarisers separated by a long piece of fibre and a polarisation controller (PC) in front of the input polariser. The first polariser ensures that a linear polarisation propagates in the fibre, and the polarisation controls the orientation of the linear polarisation, which evolves by the pulse experiencing an intensity-dependent nonlinear phase shift, and is filtered by the polariser at the output.

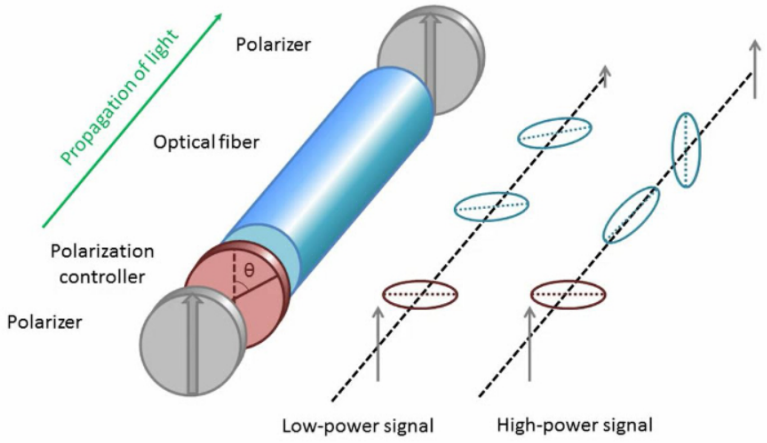

FIGURE 2.12: NPR mechanisms in fibre. This figure was reproduced from *Michel Olivier, 2016* [58].

In a MR, as the pulse propagates a nonlinear dependent phase shift manifests as SPM, causing the input spectrum to broaden, generating new spectral components that correspond to the high-intensity part of the pulse [59] as shown in Fig. 2.13. In practice, a red or blue shifted (with respect to the input spectrum) filter is added to filter the newly generated spectrum.

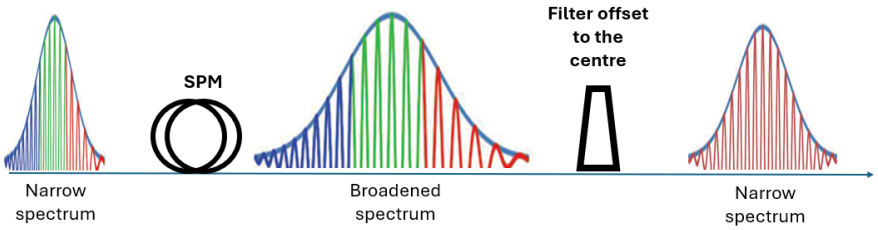

FIGURE 2.13: MR mechanisms in fibre.

An optical loop mirror can be set up as shown in Fig. 2.14. The power of an incoming pulse (input port marked in Fig. 2.14) is split as depicted by the coupler ratio to then recombine at the coupler to form the reflection (output port marked in Fig. 2.14). At low powers, the reflectance is linear and purely depends on the coupling ratio as shown in Fig. 2.15.

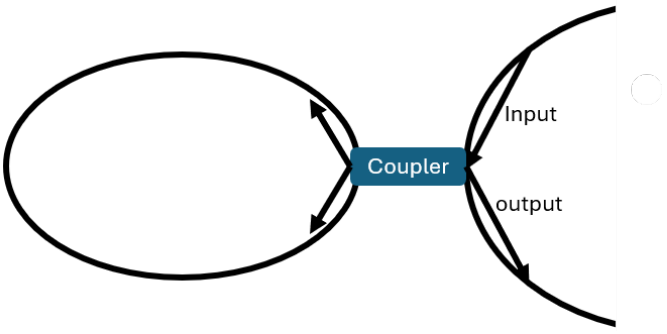

FIGURE 2.14: Optical loop mirror schematics.

At higher powers, the saturable absorption is set up by creating asymmetry in the power transmission in each port, either by a difference in the coupling ratio or by introducing a DCF into one of the ports, which forms a NOLM. A NALM, on the other hand, is set up by introducing an active fibre to create the phase change in the counter-propagating pulses, where one with higher intensity experiences a higher nonlinear phase shift than the lower-power arm [49, 60]. Therefore, the transmission (T) is given as a function of the linear and nonlinear process (power-dependent component) described as:

$$T_m = 1 - 2f(1-f)\left\{1 + \cos\left[(1-2f)\gamma P_0 L\right]\right\}, \tag{2.48}$$

where ($T = 1 - R$), and f is the fraction representing the coupling ratio.

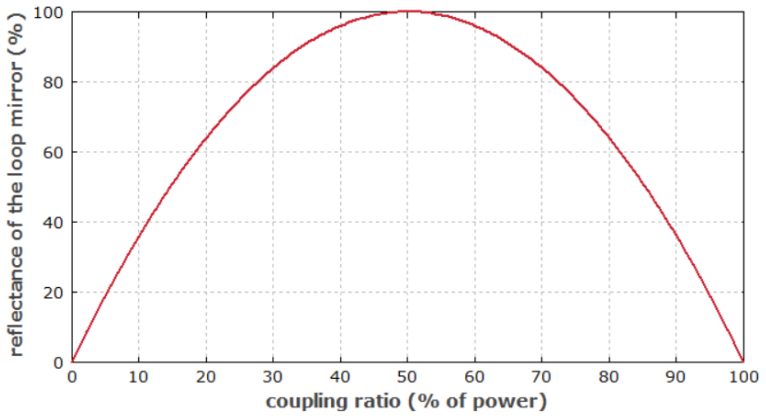

FIGURE 2.15: Reflectance of a linear fibre loop mirror based on the splitting. This figure was reproduced from *RP Photonics, 2024* [61].

2.4.3 Solitons

Thus far, the description of a soliton was developed for passive fibres where a stable pulse whose temporal and spectral features remain unchanged during propagation. However, in a laser cavity where active fibres, SAs and spectral filters are introduced that dynamically change the pulse during a round trip. Therefore, the solitons generated have to be defined by a more complex form of the NLSE [62], which is modified to include the loss-gain dynamics and higher-order effects as follows for a more accurate estimation [62]:

$$\frac{\delta A}{\delta z} + \frac{A(\alpha - g)}{2} + \frac{i(\beta_2 + ig\Omega)}{2}\frac{\delta^2 A}{\delta T^2} + \frac{i(\beta_3)}{6}\frac{\delta^3 A}{\delta T^3} = i\gamma|A|^2 A \tag{2.49}$$

Where many of the parameters have already been introduced in equation 2.13. The new parameters include third-order dispersion (β_3), the gain linewidth is given by Ω, and g the gain coefficient. Solving this equation reveals multiple converging solutions, highlighting the presence of various types of stable solitons. The primary types of stable solitons are conventional solitons (CS) and the dispersion-managed solitons, which include stretched pulse solitons (SPS) and dissipative solitons (DS) [63–66]. The type of soliton formed can be controlled by the net dispersion of the cavity. As for CS, they are formed in a cavity with a large net negative dispersion (all or partially anomalous). The order of a soliton is determined by the ratio of nonlinearity to GVD. This can be examined by introducing the following relationship [40]:

$$N^2 = L_D/L_{NL} \tag{2.50}$$

$$z_0 = \pi L_D/2 \tag{2.51}$$

Where N is an integer that refers to the order of the soliton. Ideally, a first-order soliton (fundamental soliton) is stable throughout propagation and remains unchanged. Practically however, an average (fundamental) soliton produced in a CS ML cavity, varies in both amplitude and pulse width depending on the interaction at different positions in the cavity, as shown in Fig. 2.16. Higher-order solitons will change periodically during propagation, compressing and stretching and splitting (generating multiple peaks and pulse function depending on the soliton order), alternating between a TFL state and a chirped state in a distance known as a soliton period (z_0) as shown in equation 2.51 [40]. CS propagate with a TFL pulse duration, and their intensity profile is best described as:

$$U(T) = U_0 Sech^2(T/T_0) \tag{2.52}$$

Another distinct feature of CS is Kelly's side-bands, which are discrete spectral lines that represent the amplification of the background CW radiation with excess soliton energy [67]. This manifests from the large anomalous dispersion and greatly limits the pulse energy output [68, 69]. The energy limit in an all-anomalous dispersion fibre laser system is defined as $E_p \propto \lambda\beta A_{eff}/\Delta t$, where E_p is the pulse energy, λ is the wavelength, β is the dispersion coefficient of the fibre, A_{eff}, the effective fibre area, and Δt is the pulse duration. To combat this, a normal dispersion fibre can be inserted into the cavity, which gives rise to other types of solitons.

Dispersion-managed solitons are created by adding a normal dispersive fibre into the cavity, creating breathing of the pulse as shown in Fig. 2.16. This mitigates the pulse break-up in the cavity, resolves the Kelly's sideband and enables high pulse energy generation not confined by the limits of the CS found in all-anomalous-dispersion cavities. The first of those dispersion-managed solitons is the SPS, which is formed in a cavity with a small net anomalous dispersion; it is capable of larger pulse energies than CS, and its bandwidth increases as the net dispersion tends to zero [70]. This makes it very attractive for ultrafast pulse generation.

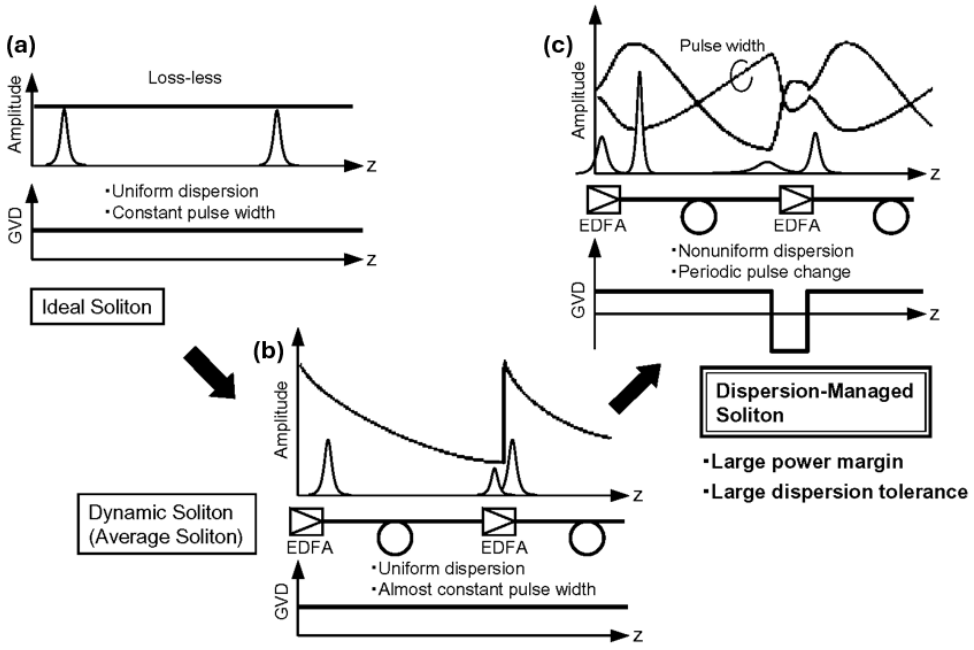

FIGURE 2.16: [The pulse evolution with distance of an (a) Ideal soliton, (b) is an avarage soltion, and (c) is dispersion managed soltion. This figure was adapted from *Tohoku University* [71].

DS, on the other hand, are formed from net normal or near-zero dispersion cavities. Unlike the SPS, the large normal dispersion and high nonlinearity required to form DS give rise to a self-similar pulse evolution and can provide even higher pulse energies [44]. Their spectrum exhibits distinctive flat edges, and as the net dispersion approaches zero, the bandwidth increases [70]. The pulses generated are chirped; thus, the ML

cavity needs to be accompanied by a compressor to generate short pulses. However, the large magnitude of nonlinearity associated with them also makes it challenging to compress these types of pulses, often resulting in a temporal pedestal [70]. Moreover, it has been reported that the output central wavelength of the pulses can be controlled by the addition of spectral filters, provided the active fibre emission spectrum covers those wavelengths, and the pump power is adjusted to compensate for the discrepancy in the gain at the desired wavelength [72].

Finally, it is worth noting the existence of noise-like solitons (NLS), which are pulses made up of much smaller wave-packets that are spread in time and are formed from ML cavities via different mechanisms depending on the net dispersion. For example, in a net anomalous dispersion cavity, the forming mechanism is based on a soliton collapse, whereas a peak power clamping effect (PPC) is the cause of NLP formation in the net normal dispersion. The change to an NLP can be abrupt from a stable soliton, indicating a switching point from a positive to a negative cavity feedback from the SA. This is when the gain no longer amplifies the pulse but amplifies the background instead in PPC, and the pulse breaks up due to high pulse energy in a soliton effect. They are used for applications where high pulse energies are required, as they are capable of generating microjoules of pulse energies [73].

2.5 Pulse compression

Pulses can be compressed either linearly or nonlinearly. In both cases, gratings, prisms, fibre gratings, or fibres are used. As mentioned in section 2.4.1.1, GVD imposes a linear chirp on the pulse during propagation inside a dispersive medium, causing the linear spectral phase shift in a pulse made up of several spectral components. However, in the latter, the pulse is propagated in a nonlinear medium (usually a fibre) before compression, allowing for spectral broadening [72]. An increase in the pulse's spectral bandwidth then allows the pulse to be compressed to an even shorter duration. Since the shortest temporal width is inversely proportional to the spectral width, as described by the time-bandwidth product (TBP), it is constant and depends on the pulse shape. For $Sech^2$ and Gaussian pulses, TBP is 0.315 and 0.44, respectively [74].

$$TBP = \Delta T \Delta \nu \tag{2.53}$$

Where ν and T are the FWHM spectral and temporal widths, respectively. Equation 2.53 also shows that a TFL pulse cannot be compressed. A comparison of two compression methods was demonstrated by *W.Jinzhang et.al* [72] where a 2 μm pulse with a 3 dB bandwidth of 103 nm was linearly compressed in a fibre UHNA4 that has a normal dispersion coefficient β_2 at 2 μm to compensate for the negative chirp of the

pulse. This generated a pulse width of 75 fs. However, 29 fs pulses were generated when nonlinearly compressing the pulse. This was realised by incorporating sections of HNF in intervals with SMF in the compressor to maintain a similar pulse shape and high peak powers throughout propagation, resulting in a more efficient nonlinear response. This was followed by UHNA4 fibre for compression as in the previous case [72]. Another method used for nonlinear pulse compression was demonstrated by *M. Gebhardt et.al* [75] where a gas-filled anti-resonant hollow-core fibre (ARHCF) was used to produce a self-compressing pulse due to the weak anomalous dispersion effects of the fibre in combination with a broadening of the spectrum caused by the nonlinear interaction with the gas molecules [75].

Figure. 2.17 shows a "Treacy configuration" grating pair, composed of 2 parallel transmission gratings and a mirror that reflects light back towards the input, doubling the effect of the dispersion of one pass used for compressing pulses. Dispersion is achieved as a result of a time delay caused by a difference in the optical paths experienced by different wavelengths (shorter wavelengths travel less than longer ones).

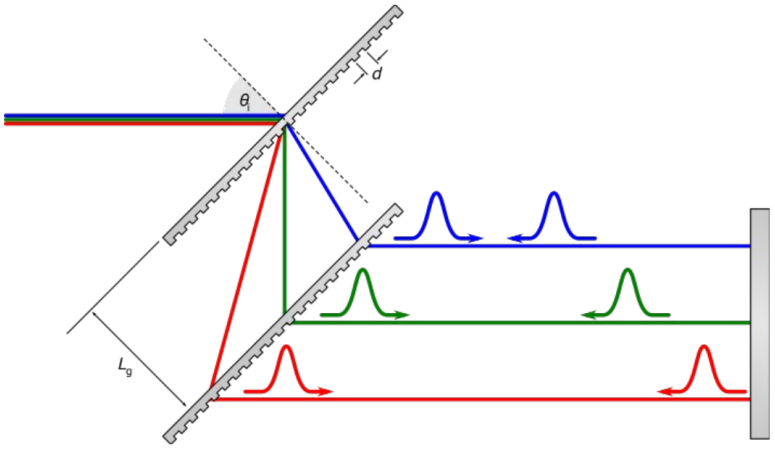

FIGURE 2.17: Diagram of "Treacy configuration" transmission grating pairs. This figure was reproduced from *A. Garza-Reyes, 2012* [76].

The frequency dependence of diffraction angle is given by [76]:

$$sin(\theta_r) = \frac{m2\pi c}{\omega\Lambda} - sin(\theta_i) \tag{2.54}$$

Where m is the order of diffraction and is 1 for the first-order diffraction, which is used to generate dispersion, θ_i and θ_r are the incident and diffracted angles to the normal to the grating plane, respectively, and Λ is the grating period. As for linear pulse compression, the GVD effect on the pulse in a fibre has been previously explained in section 2.4.1.1 to depend on the fibre refractive index. The group delay dispersion (GDD) is $GDD = GVD * L$, which describes the total dispersion experienced by the

pulse during propagation. GDD for a grating pair can be written as follows:

$$\frac{d^2\phi}{d\omega^2} = \frac{m^2\lambda^3 L_g}{2\pi c^2 \Lambda^2}(1 - (-m\frac{\lambda}{\Lambda} - sin(\theta_i)^2)^{-3/2} \tag{2.55}$$

Where L_g is the distance between the diffraction gratings. As seen from equation 2.55 θ_r is inversely proportional to ω, which means that the longer the wavelength, the larger the diffraction angle.

Grating pairs in this format are used frequently throughout this project due to their compactness while generating higher dispersion values than other methods. Two different pairs of gratings were used for separate experiments. For the imaging laser, fused silica transmission gratings with a groove density of 560 lines/mm and a roof mirror were used (see chapter 3), whereas fused silica transmission gratings with a groove density of 900 lines/mm were used for the sub-100 fs pulse generation experiment (refer to chapter 4). Grating compressors in Treacy configuration can only impose negative second-order dispersion on the pulse, which only acts to compensate for positive linear chirp components, meaning that any nonlinear chirp components (caused by higher-order dispersion or nonlinearity) are incompressible and appear as temporal side pedestals in the compressed pulse shape [77].

Chapter 3

1847 nm femtosecond thulium fibre laser for biomedical imaging

In this section, the details of the development and characterisation of the imaging laser system shown in Fig. 3.1 are discussed. This laser was constructed from a ML cavity capable of generating a few-hundred-femtosecond pulse, which is then stretched and amplified, and then compressed in CPA fashion. An optical modulator is placed before the final amplifiers in the system to control the RR of the laser and scale the peak power of the pulses while maintaining a low average power in order to achieve deep-tissue penetration without causing thermal damage to the biological sample. Finally, the results acquired from THG imaging at the different RR will be presented, and optimum experimental parameters will be discussed.

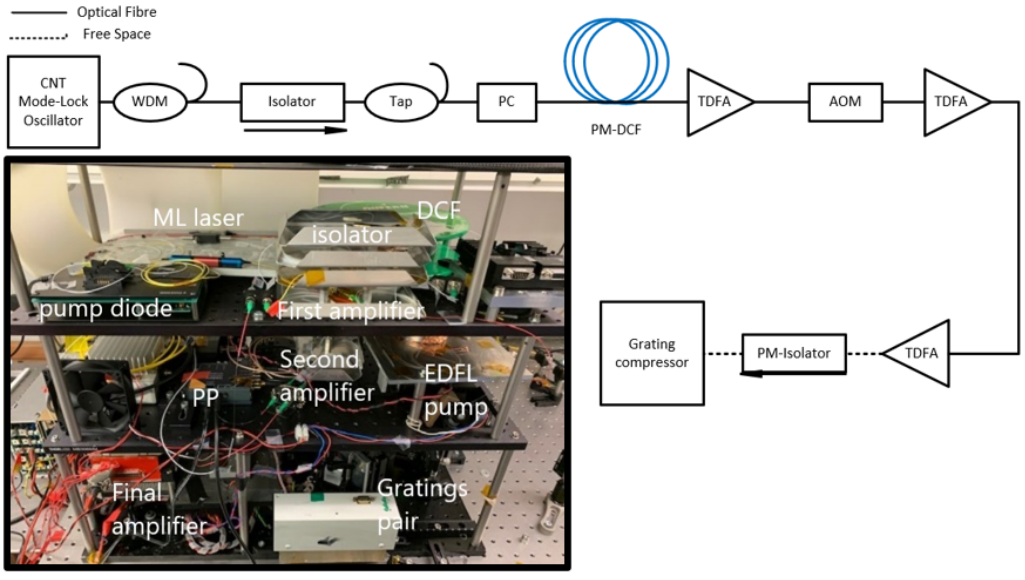

FIGURE 3.1: Imaging laser schematics; inset picture of the final laser.

The imaging laser was developed by drawing inspiration from a study by *D. Xu et al.*, where an NPR and SESAM-based ML laser cavity seeded CPA system operating at the fundamental laser RR of 16.6 MHz and capable of generating 630 fs compressed pulse duration (assuming Gaussian shape) with an average power of up to 2.5 W and a pulse energy of 150 nJ [78]. The laser was used for THG imaging, allowing up to 40 μm of penetration depth was reported in rat tail samples.

3.1 CNT Mode-locked seed laser

An all-fibrised ML cavity was built in collaboration with a former PhD student in my research group, Dr. Panuwat Srisamran, using a single-walled carbon nanotube (SWCNT) SA sample provided to our research group in collaboration with the Cambridge University graphene centre. I was involved in adapting this cavity to meet the requirements for medical imaging, then integration, development and characterisation of the whole system. The schematics of this cavity are presented in Fig. 3.2. A laser diode (Princeton Lightwave, DEI14919) operating at 1550 nm wavelength and 170 mW average output power was used to pump this cavity, delivered into the cavity with the use of a 1560/1960 wavelength division multiplexer (WDM, AFR 223005). The cavity comprised a 0.5 m Tm-doped fibre (OSF TmDF200) gain medium, a 4.5 m DCF (Nufern UHNA4) managing the dispersion in the cavity, an isolator (ISO) for unidirectional flow of light, SMF28e passive fibre between components, two PCs placed on either side of the SA to adjust the phase shift for obtaining mode-locking, and a 75/25% output coupler (OC, Thorlabs TW2000R3A2A). I adjusted the OC port from the original design, using the 75% output port for a higher output power of 14.5 mW, compared to the 1 mW reported with a 25% tap by Dr. Panuwat. This meant an increased pumping threshold to compensate for the higher losses. Due to the polarisation-insensitive nature of the SA in an all non-PM (polarisation maintaining) design, the cavity showed long-term stability under continuous use.

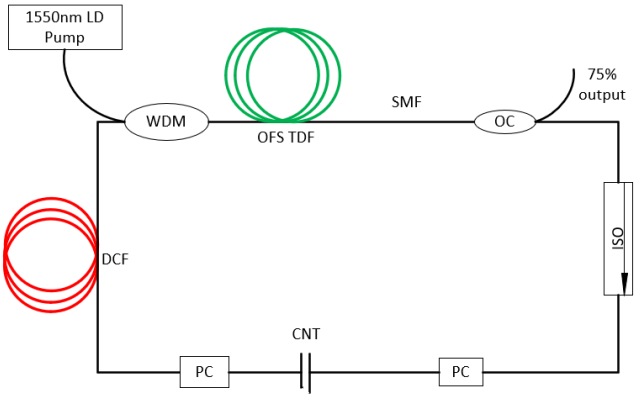

FIGURE 3.2: Mode-locked laser cavity schematics, featuring a CNT acting as a SA.

A DS pulse operation was achieved, represented by the distinctive sharp edges of the spectrum as seen in Fig. 3.3. Using an optical spectrum analyser (OSA, AQ6375), the generated pulses were measured to have a central wavelength of 1847 nm and a 3 dB bandwidth of around 30 nm. The temporal pulse duration, on the other hand, was measured using an autocorrelator and the width of the autocorrelation function (ACF) was found to be 5.4 ps. The cavity length resulted in an RR of 20.4 MHz and a net dispersion of 0.01 ps^2. It should be noted, that the ML spectrum shown in Fig. 3.3 is the final optimised output spectrum used for the imaging experiment; multiple alternate ML states were used throughout the optimisation and characterisation of the system.

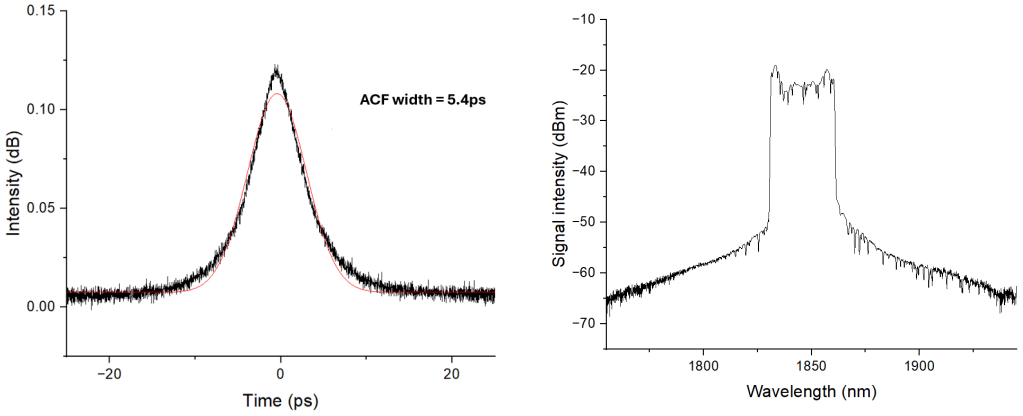

(a) Measured autocorrelation function (ACF) trace, (b) Pulse spectrum $\lambda_c = 1847\ nm$ and $\Delta\lambda = 30\ nm$. the FWHM = 5.4 ps.

FIGURE 3.3: CNT ML cavity output pulse characteristics.

3.2 Stretcher and Pre-amplifier

The first amplifier schematics are shown in Fig. 3.4. A 50 m long piece of PM-DCF (Choerent, PM2000D) was used to stretch the pulses while allowing for the preservation of the polarisation of all spectral components over long distances compared to the non-PM counterpart. This was evident by minimal distortion to the pulse spectrum caused by the wavelength-dependent phase shift passing through a fast-axis block PM-isolator as seen below in Fig. 3.5.

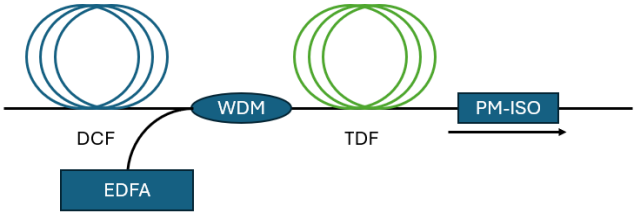

FIGURE 3.4: First amplifier and pre-stretcher schematics pumped by an EDFA, PM-ISO: polarisation maintaining isolator.

The addition of the PM-fibre increased the efficiency since less energy is lost in the ISO due to the poor alignment of the polarisation with the pass axis of certain pulse components. This was observed when measuring the maximum power attainable from the first amplifier after the PM-ISO, with the output power increased from 26.5 mW when using a non-PM DCF to 31 mW when a PM-DCF was used for an overall amplifier slope efficiency at $\approx 18.3\%$.

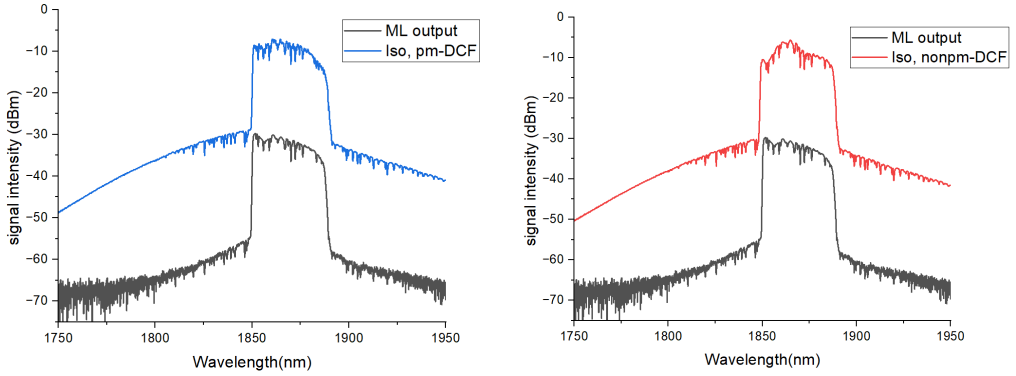

(a) Spectrum before (black) and after PM-isolator (blue) passing through a PM-DCF

(b) Spectrum before (black) and after PM-isolator (red) passing through a nonPM-DCF

FIGURE 3.5: Pulse spectrum $\lambda_c = 1869nm$ and 3 dB $\Delta\lambda = 38nm$ before and after PM-isolator using a PM and nonPM DCF fibre.

Moreover, the DCF length increased the pulse duration to 50.3 ps (assuming Gaussian shape) as shown in Fig. 3.6. The effects on the pulse compressibility pre and post PM-ISO transmission were also examined for both DCFs, and no distortion to the compressed pulse shape was observed when incorporating the PM-fibre.

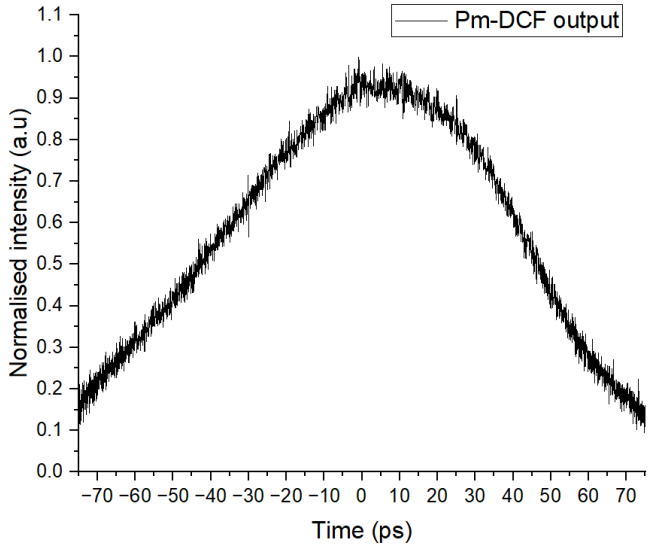

FIGURE 3.6: Pulse ACF trace at the output of the DCF; ACF width = 50.3*1.41 ps.

3.3 Pulse picker

Oscilloscope data provided in Fig. 3.7 demonstrate RR division capabilities of the optical signal of both the AOM (GOOCH & HOUSEGO T-M250-0.3C16Z-3-F2P) and the electro-optical modulator (EOM, Exail MX2000-LN-01) that were driven by a PP (TOMBAK AreoDIODE). The modulation capabilities of both modulators were tested, and the AOM was chosen for the final design due to having a 2 dB lower insertion loss than the EOM and a higher extinction ratio, as seen in Fig. 3.7.

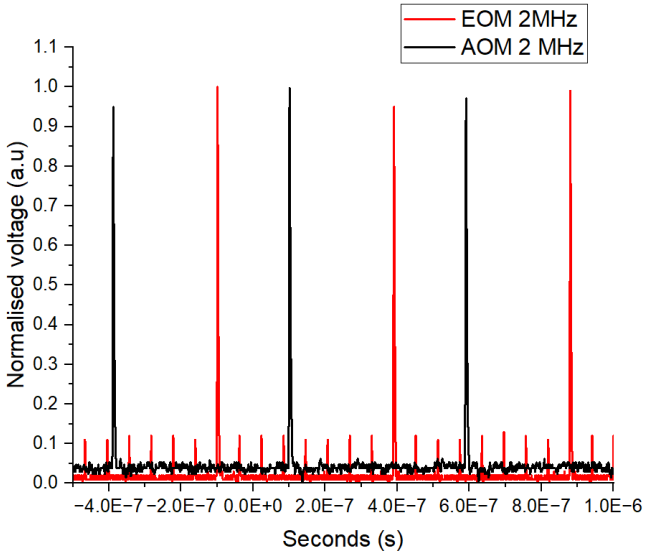

FIGURE 3.7: 2 MHz output from AOM and EOM; offset temporally for visualisation.

Next, the power was measured at the output of the AOM while incrementally dividing the fundamental optical repetition frequency from 20.4 MHz using the PP to generate outputs of 10, 5, and 2 MHz. The characterised results are presented in the Table 3.1 below:

TABLE 3.1: Optical powers and losses after the AOM.

Repetition Rate (MHz)	Av. Power(mW)	Loss(dB)
20.4	14.1	-3.4
10.2	6.9	-6.5
5.1	3.47	-9.5
2.04	1.2	-14.1
1.02	0.61	-17.1

3.4 Second amplifier

The amplifier shown in Fig. 3.8 was backwards-pumped in an attempt to reduce the number of components in the system and reduce the overall fibre length that contributes

to pulse compression. This has the advantage of using a single WDM following the TDF for joining and filtering the pump with the signal instead of two WDMs on either side of the amplifier in a forward pumping scheme. This orientation also makes use of the ISO before the AOM to prevent back-reflection of the signal to the source.

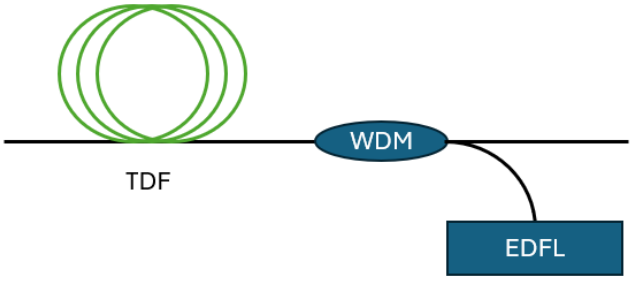

FIGURE 3.8: Second stage amplifier schematics pumped by an EDFL.

This stage was core pumped from an in-house built EDFL capable of up to 1.1 W of power. The second amplifier output power was measured and is shown in Fig. 3.9 while varying the repetition frequency and pumping power using the input powers mentioned in Table 3.1. The slope efficiency of the amplifier decreases as the RR is decreased from $\approx 10\%$ at the fundamental RR to $\approx 3.5\%$ at 2 MHz as a result of the reduced input powers. However a high gain $(9 - 12dB)$ was feasible across the different RR.

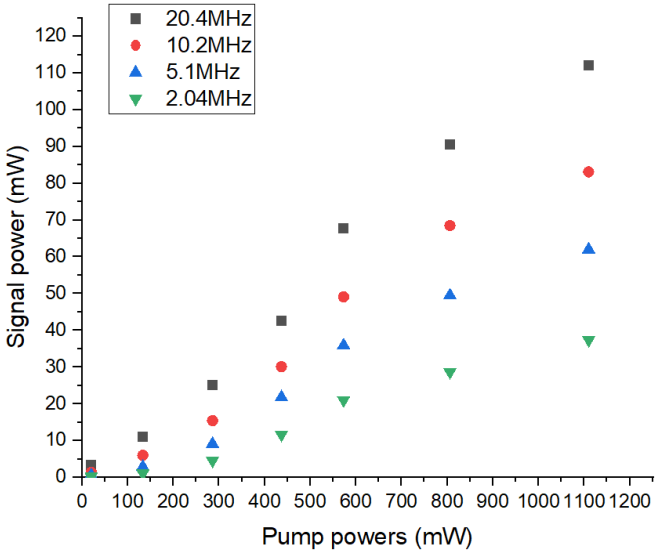

FIGURE 3.9: Second stage amplifier power output at different RRs and pump input.

To eliminate the variation of the average powers when imaging samples operating settings at the fundamental repetition frequency (20.4 MHz) and its divisions (highlighted in Table 3.2), were selected to ensure similar and comparable average powers into the final amplifier.

TABLE 3.2: Second stage amplifier out data used to characterise the later stages.

2^{nd} pump power (mW)	437	573	806	1110
Rep. Rate (MHz)	20.4	10.2	5.1	2.04
Power (mW)	42.5	49.1	49.5	37.4

3.5 Power amplifier and compressor

The final amplifier and compressors are shown in Fig. 3.10. Core pumping is set up by coupling the output of a high-power EDFL to a TDF, which is spliced to a short length of SMF angled patch-cord to minimise Fresnel's reflection when free-space coupling the final output to a dichroic mirror for pump filtering, followed by an ISO before the grating compressor are used to prepare the beam for the microscope.

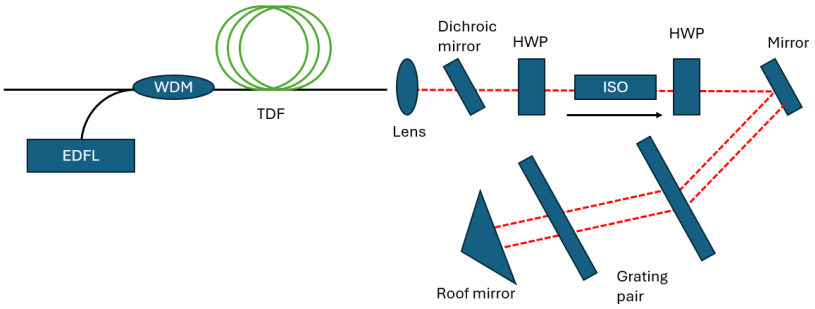

FIGURE 3.10: Final stage amplifier schematics pumped by an erbium-doped fibre laser (EDFL).

Despite the long DCF length lowering the overall peak power propagating in the fibre, spectral broadening was observed at the output of the final amplifier when using a 70 cm long single cladding TDF with 9 μm core and 125 μm cladding (diameters) as shown in Fig. 3.11.

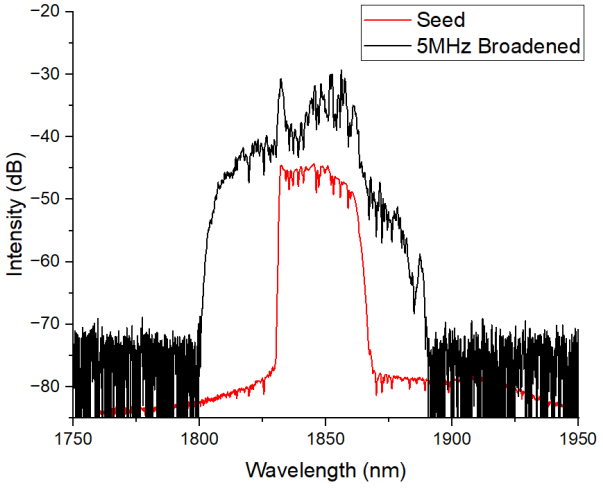

FIGURE 3.11: Pulse spectrum comparison between seed signal and final amplifier.

The onset of nonlinear effects was observed at a RR as low as 5 MHz. This prevented the operation of the laser system at lower RRs. The nonlinearity coefficient in the system is high due to high peak powers, small fibre core, and long fibres, as stated in equation 2.17 and efforts were made to reduce these parameters. Therefore, A "PM-TDF-10P/130-HE" double cladding fibre with 10 μm core diameter and 130 μm outer cladding diameter was used. While using an input signal power of 81.5 mW, a starting fibre length of 40 cm was tested in a cut-back method to find the optimum length where the amplified power was maximum and residual pump power was minimised. The outputs of the different fibre lengths were:

TABLE 3.3: Power output at different lengths of 10/130 μm TDF.

Fibre Length (cm)	signal Av.power(mW)	residual pump power (mW)
40	1883	-
34.5	1955	35
25	2023	33.5
18	1931	42.2

From Table 3.3, it can be seen that highest output power was achieved from a shorter TDF length, due to the increased doping concentration of Tm^{3+} ions. Furthermore, as the length decreased from 40 to 25 cm, the residual pump power increased. However, at 18 cm, the residual pump signal began to increase and the signal power decreased; therefore, the optimum length of 10/130 μm TDF must lie between 25 and 18 cm. In the final amplifier, an 18 cm TDF was used, connected to a 1840/1500 WDM and a short 5 cm SMF28e patch-cord at the output.

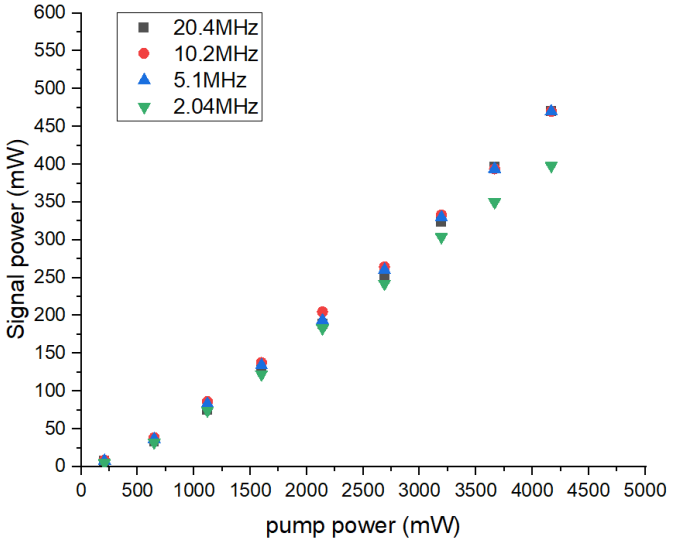

FIGURE 3.12: Power output of the third stage amplifier at different RRs and pump powers.

Using the input power parameters mentioned in Table 3.2 at each RR, the power output after the compressor was measured and the results are plotted in Fig. 3.12. A maximum average power of around 470 mW was measured across all the RRs except at 2 MHz, where it was measured to be around 400 mW. The corresponding output spectrum and compressed pulse duration are shown in Fig. 3.13. Spectral broadening is seen at a lower RR due to the increase in the peak powers. Consequently, a shorter compressed pulse duration was observed. 480 fs (Gaussian) at 20.4 MHz and 380 fs (Gaussian) at 2 MHz were achieved, and their pulse energies were 23 nJ and 156 nJ, respectively.

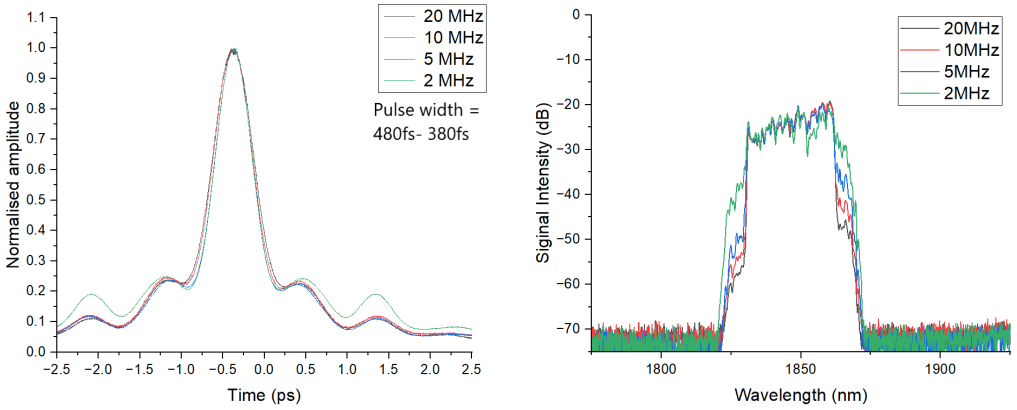

(a) Measured ACF trace, the FWHM = 380 fs.

(b) Pulse spectrum $\lambda_c = 1847\ nm$ and 3 dB bandwidth $\Delta\lambda = 30\ nm$.

FIGURE 3.13: Final pulse characteristics of imaging laser.

Further precautions were taken to minimise the risk of damaging the higher power amplifier by implementing a more stable ML source and sealing it to reduce environmental factors. User guidelines were set up in case of ML instabilities for safely switching off the system, retaining mode-locking, restarting the modulation and resuming the experiment. An inverse electrical trigger was programmed into the PP to allow the AOM to be "opened" if the signal was lost, thus preventing any catastrophic Q-switching in the absence of a signal, which would lead to energy build-up in the amplifiers, which is then suddenly released, damaging the optical components.

3.6 Third-harmonic generation imaging experiment

3.6.1 Experimental set-up

To conduct the imaging experiment, a similar imaging system as the one in the study by *D.Xu et al.* was set up [78], which is illustrated in Fig. 3.14. A custom-built inverted microscope based on a Nikon Ti Eclipse frame, which included a pair of galvanometer mirrors for laser scanning, was used. The output beam from the thulium fibre laser was coupled into the scanner after passing through a pair of lenses. The beam was

reflected by a short-pass dichroic beam splitter and focused on the samples through an infinity-corrected objective.

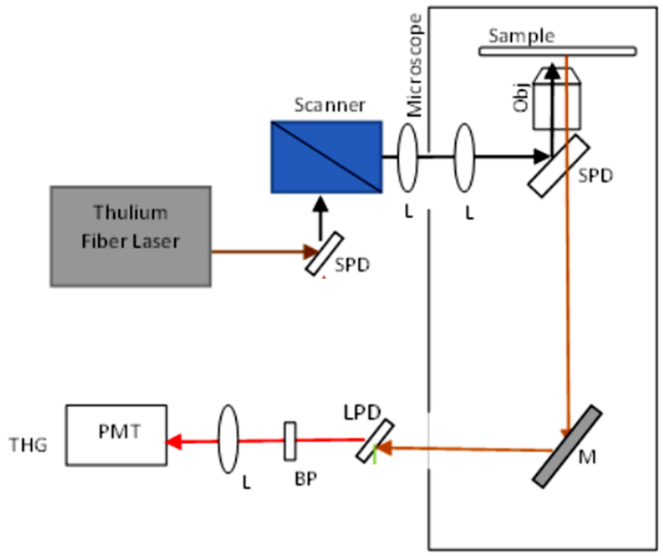

FIGURE 3.14: Schematic diagram of the imaging system. PMT: photo-multiplier tube, L: lens, BP: band-pass filter, M: mirror, LPD: long pass dichroic, SPD: short pass dichroic, Obj: objective lens, THG: third-harmonic generation. This figure was adapted from *Duanyang Xu, 2023* [78].

The THG signal was collected in the back-scattering (epi-detection) geometry using the same objective. This signal was delivered through optics that included the excitation dichroic, mirrors, lenses, and short-pass filters, as well as a narrow band-pass filter, to a photomultiplier tube (PMT) detector. The scanner and detector were interfaced with a DAQ-PCI6110 connected to a desktop computer. Laser scanning and data acquisition were controlled using Scanimage 6.1 (Vidrio Technologies).

All image acquisitions were performed with a 20× objective lens having a numerical aperture (NA) of 0.75. The pixel resolution for each image was 512 × 512 pixels, which corresponded to a field of view of $250 \times 250\ \mu m$, given the objective and scanning settings used. The pixel dwell time was set to 16 μs.

The experiments primarily focused on THG. To separate the SHG signal generated from the sample from the THG signal, a short-pass dichroic beam splitter was employed in the detection branch, reflecting the SHG signal and allowing for effective analysis.

3.6.2 Results

Dry animal horn samples were imaged initially, and the results at 40 μm depth can be seen in Fig. 3.15. At the fundamental RR, the deepest visible layer with meaningful biological details was 40 μm, similar to the study by *D.Xu et al* [78]. However, the

resolution of the acquired images in this experiment were lower. This is owed to the fact that the average power was significantly lower at this RR. However, as RR was reduced, the peak powers increased, resulting in higher resolution and better contrast while maintaining low average powers that would otherwise be detrimental to the biological samples. The increase in the peak power also allowed for deeper penetration. The images acquired at the deepest layer for each of the RRs are shown in Fig. 3.16.

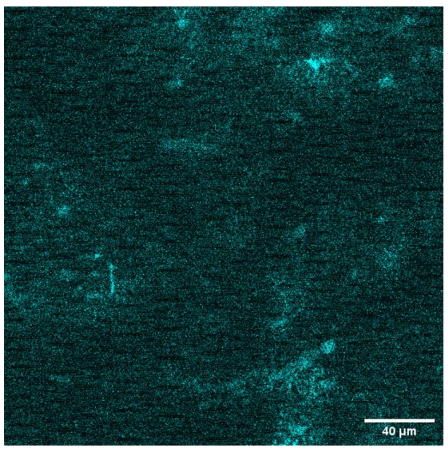

(a) 40 μm depth animal horn tissue using 20 MHz RR.

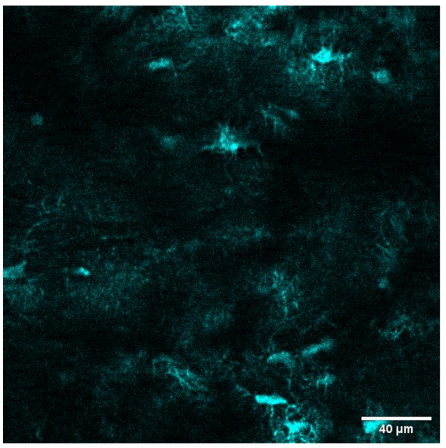

(b) 40 μm depth animal horn tissue using 10 MHz RR.

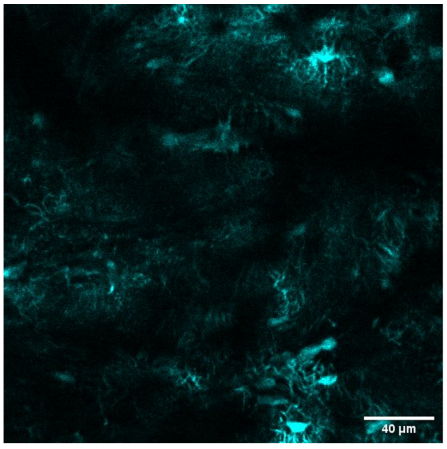

(c) 40 μm depth animal horn tissue using 5 MHz RR.

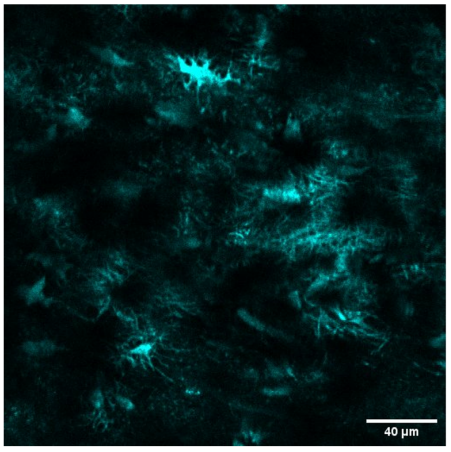

(d) 40 μm depth animal horn tissue using 2 MHz RR.

FIGURE 3.15: 40 μm depth animal horn tissue imaging at different RR.

As expected, the resolution was reduced as the penetration depth increased. However, meaningful biological features were still distinguishable at depths of up to 90 μm in bone tissue at 2 MHz, which was over twice as deep as the penetration depth achieved at the fundamental RR of the laser.

Further testing was carried out using a 2 MHz RR in dry human cancellous bone tissue (shown in Fig. 3.18(a)) since it showed the deepest imaging capabilities in animal horn tissue.

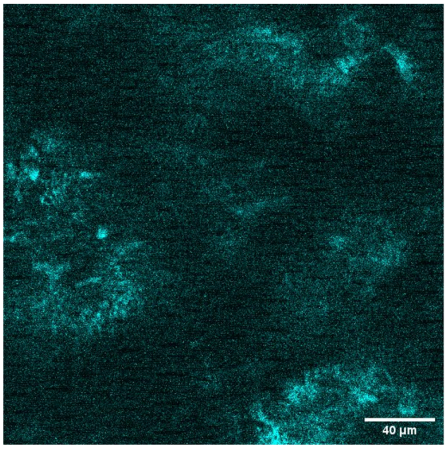

(a) 60 μm depth animal horn tissue using 10 MHz RR.

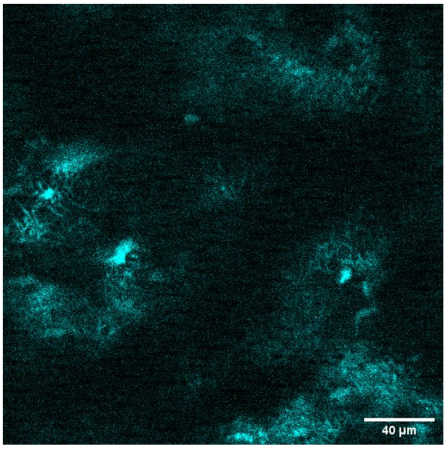

(b) 70 μm depth animal horn tissue using 5 MHz RR.

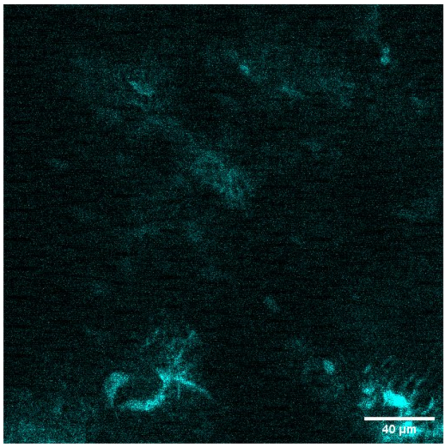

(c) 90 μm depth animal horn tissue using 2 MHz RR.

FIGURE 3.16: Deepest visible layer in animal horn tissue, different RR.

The results presented in Fig. 3.17 showed much higher resolution at 90 μm when compared to the animal sample and a significantly higher penetration depth for up to 310 μm. The higher observable sample depths in cancellous bone tissue were achieved by virtue of its porous structure, unlike the horn samples, which are denser and closely resemble cortical bone tissue. THG imaging is efficient at detecting interfaces [79], and as proven from the acquired imaging results, the detection of those interfaces increases with peak powers.

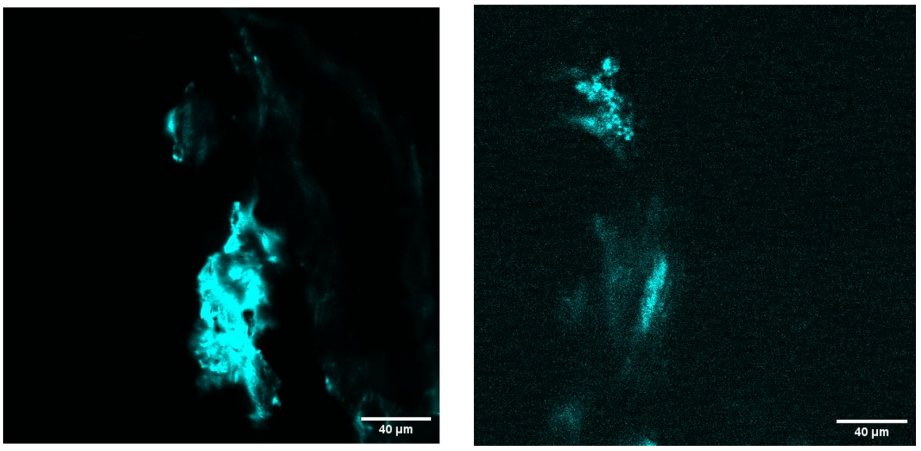

(a) 90 μm depth human bone tissue using 2 MHz RR.

(b) 175 μm depth human bone tissue using 2 MHz RR.

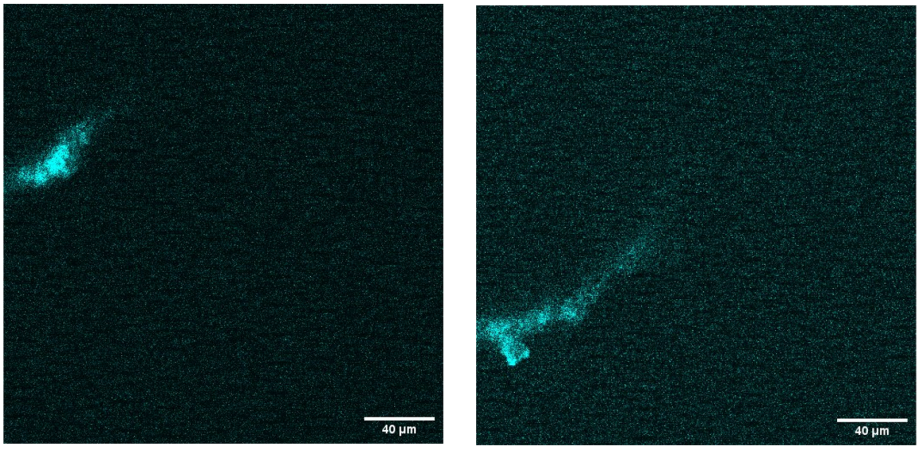

(c) 310 μm depth human bone tissue using 2 MHz RR.

(d) 400 μm depth human bone tissue using 2 MHz RR.

FIGURE 3.17: Imaging results in human cancellous bone sample at increasing depths using 2 MHz RR.

Finally, the stacks of images captured with a laser at different depths can be used to reconstruct a 3D model of the sample, giving an in-depth insight into the structure of the sample. As shown in Fig. 3.18(b), a depth encoded layered image was created, revealing a clear structure of the bone sample, where the bone boundaries are defined. This is a powerful technique for anatomical structural analysis and can be used to create 3D models.

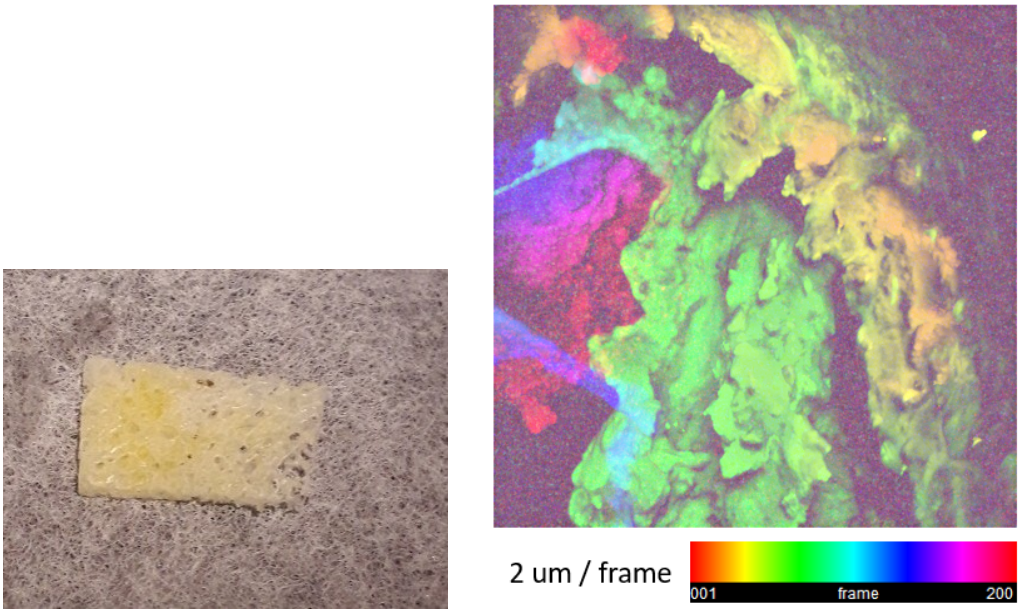

(a) Porous (cancellous) bone sample from Tubercular bone.

(b) Depth encoded reconstructed image stacking all the layers captured up to 200 μm depth.

FIGURE 3.18: The cancellous bone sample and 3D visualisation

Chapter 4

1789 nm femtosecond thulium fibre laser system

The imaging laser, discussed in chapter 3, operated at a wavelength of 1.84 μm. Dr. Hiroki Cook from the IFLS team measured a high-resolution absorption spectrum of articular cartilage (a type of soft tissue), which is illustrated in Fig. 4.1. The results revealed that the current operating wavelength does not operate at the minimum water absorption wavelength, thereby increasing the risk of thermal damage to the tissue and limiting the achievable imaging depth. Notably, the absorption begins to decrease below 1.8 μm, which is more suitable for imaging softer biological tissues with higher water content.

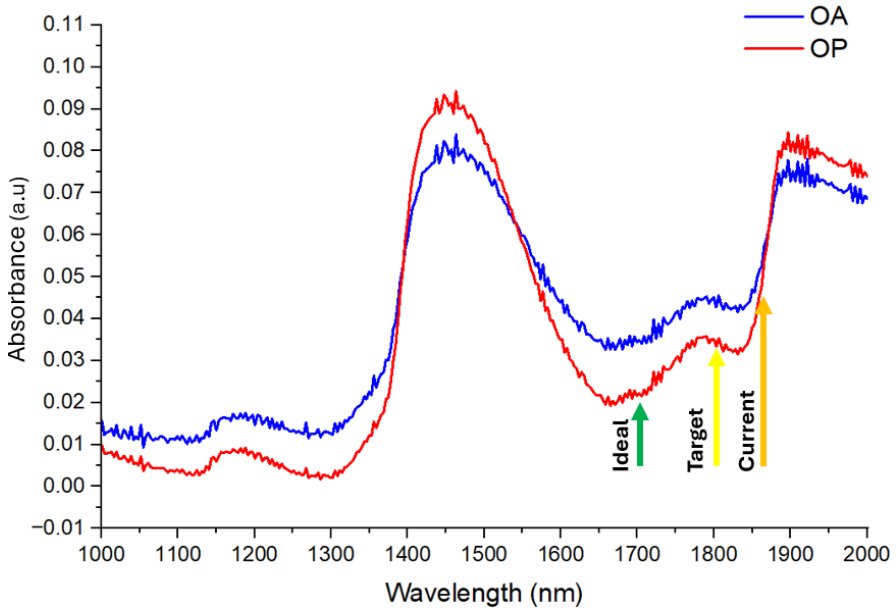

FIGURE 4.1: Absorbance spectra of articular cartilage (soft tissue), measured between 1000-2000 nm; Osteoarthritis (OA, blue), Osteoporotic (OP, red).

The design constraints remain true for developing a cost-effective and compact laser. However, challenges arise in developing a laser source with an operating window < 1.8 μm using thulium due to absorption that overlaps with emission, ranging from 1.5 μm to 1.8 μm and peaking at $\approx$1.6 μm. Furthermore, an appropriate SA is necessary to build a ML laser. Commercially available SESAMs have an operating range exceeding the target wavelength; instead the broad absorption bandwidth of different CNT samples makes them a more suitable SA for shorter wavelength applications. Moreover, it is necessary to add a spectral filter in the cavity to blue shift the favourable lasing wavelength and suppress unwanted emission. The incorporation of such technologies in the laser oscillator may limit the achievable pulse bandwidth and, consequently, the pulse duration and power. There are, however, approaches that can be taken to overcome the effects of these constraints. For example, a fundamental soliton is confined by its energy due to the balance of the nonlinearity and anomalous dispersion, but a DS or SPS can be generated by incorporating a positive dispersion element into the cavity, allowing a higher-energy pulse to circulate within the cavity. This may result in broader pulse bandwidths due to increased nonlinearities.

As demonstrated previously (refer to chapter 3), CPA can be implemented to achieve high powers from an ML system while mitigating nonlinearities that can affect the pulse. Therefore, the compressed pulse duration achieved by this method is limited to the TFL duration of the source pulse. However, if nonlinear pulse compression is implemented, shorter pulses will be achievable [77]. For this technology to be feasible, coherent spectral components need to be generated and optical wave breaking suppressed [80].

The work presented in this chapter discusses the development of a new ML seed laser optimised for short pulse and wavelength emission, where the maximum pulse bandwidth achievable from the cavity was explored. Novel amplification methods that simultaneously promote nonlinear pulse compression via fiberised solutions to overcome the shortcomings of the ML pulse laser output were tested and compared. The four amplification methods tested were chirped pulse amplification, chirp-managed pulse amplification (CMA), chirped pulse amplifier with nonlinear broadening (CPAN), and nonlinear broadening with chirped pulse amplification (NCPA).

The ML laser presented in section 4.1 was presented at the Photonics West conference proceedings [81]. The source was used to develop the novel amplification methods that led to publishing two conference papers on the Chirp-managed amplifier (sections 4.2.1 and 4.2.2) and nonlinear chirped pulse amplifier (section 4.2.4) in CLEO [82] and CLEO-PR [83], respectively.

4.1 All fiberised CNT ML cavity

A schematic of the ML fibre laser cavity is shown in Fig. 4.2. The cavity features unidirectional ring oscillation. A Tm-doped fibre was pumped with a single-mode laser diode (DEI14919, Princeton Lightwave) at 1560 nm through a WDM. Another WDM was placed after the Tm-doped fibre to extract residual pump in the single-pass pumping configuration. A high reflectance (HR) single-mode retroreflector (P5-SMF28ER-P01-1, Thorlabs) was attached to the WDM pump port to recycle the residual pump back into the Tm-doped fibre for double-pass pumping. An OC with 50% coupling ratio was spliced to the WDM signal port to extract the ML signal. An in-house fabricated SWNT polyvinyl alcohol (PVA) composite was inserted between two angled patch-cords to act as an SA. Unidirectional oscillation of the ring cavity was ensured by an ISO that was placed after the SA. Two in-line PC were placed in the cavity to stabilise the ML operation. A DCF (UHNA4, Coherent) was employed to provide a net normal dispersion.

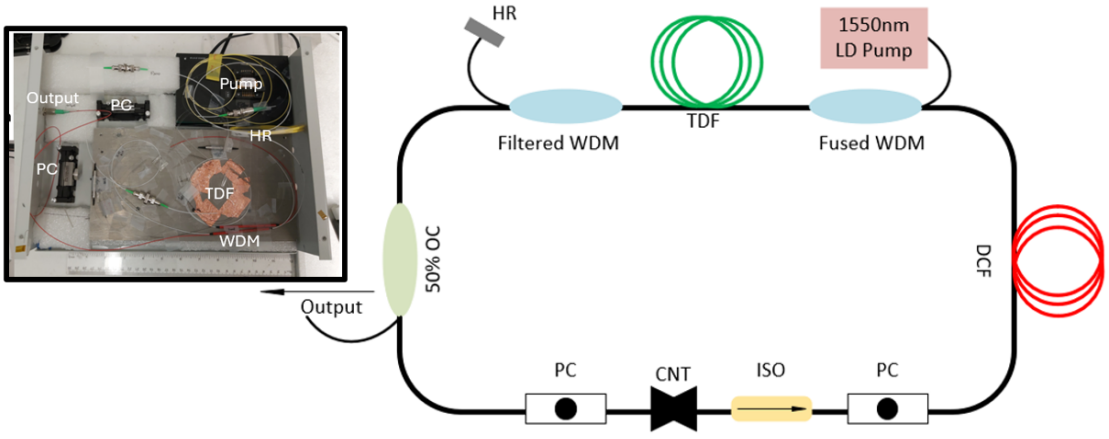

FIGURE 4.2: Schematics of all-fibre mode lock laser; inset photo of the laser mounted in a 28×35 cm box. CNT: carbon nanotube; ISO: Isolator; PC: polarisation controller; OC: output coupler; WDM: wavelength division multiplexer; HR: high reflection mirror; DCF: dispersion compensation fibre.

A short length of 0.3 m was selected for the Tm-doped fibre to realise the short wavelength operation by minimising the signal reabsorption. The length was selected based on the results from characterisation of the ASE output of three different Tm-doped fibres which were: a commercial Tm-doped fibre (OFS, TmDF200), and two in-house fabricated fibres; a Tm 0.2 wt % doped fibre (TDFA1) and a highly doped nested ring fibre (TDFA2) thought to possess relatively low absorption due to small occupied region of the Tm dopant in the core (presented in Fig. 4.3(a)) [84]. Several fibre lengths were core pumped at a power of 860 mW from an in-house built EDFA, and the ASE measurements are shown in Fig. 4.3(b). While increasing the length of TDFA1 by 10 cm,

the ASE profile was maintained, but an increase in the overall gain was observed. On the other hand, the OFS TDF shows higher gain at a comparable length and a higher gain peak at a shorter length. Although an increase in the length resulted in overall higher gain, the gain peak was shifted towards 1850 nm due to the effects of reabsorption of thulium, which would favour mode-locking at longer wavelengths if implemented into the cavity. Lastly, TDFA2 showed a cut-off at ≈1800 nm and an overall lower gain.

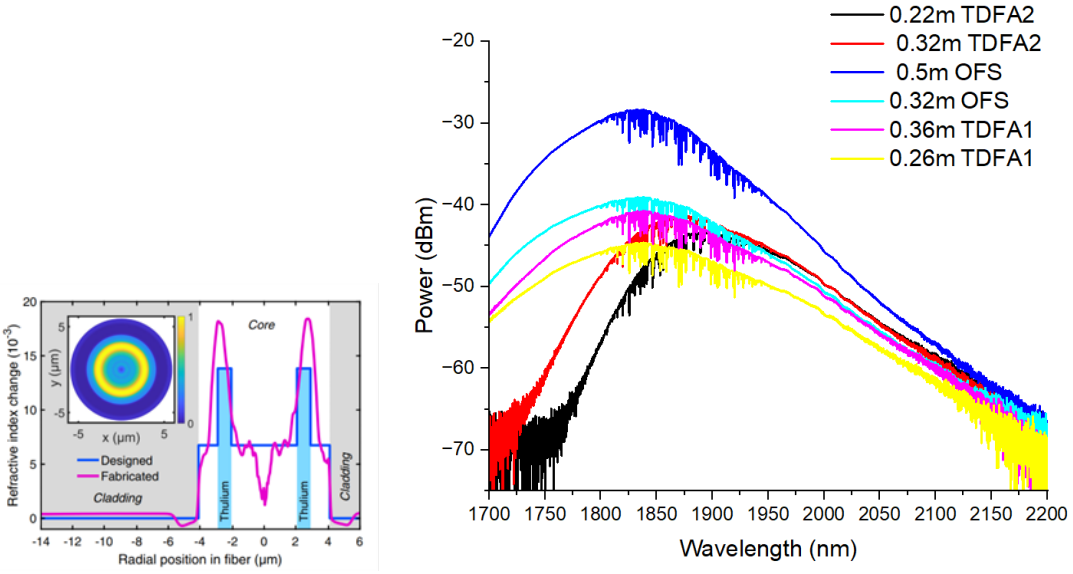

(a) Nested fibre cross-section. This figure was reproduced from [84].

(b) ASE spectrum of different Tm-doped fibre lengths and types.

FIGURE 4.3: Nested fibre cross-section and characterisation of different Tm-doped fibres and lengths.

A fused WDM (WD1525A, Thorlabs) was chosen to facilitate lasing at wavelengths below 1800 nm. The measured transmission spectrum of the fused WDM is shown in Fig. 4.4(a), which exhibits a peak transmission of 90% at 1775 nm. In addition, the WDM also acted as a bandpass filter, providing a Gaussian-like filtering function with a FWHM bandwidth of 60 nm, as required to facilitate the DS generation [85]. In contrast, a filtered WDM (223005, AFR) with a wide and uniform transmission spanning from 1700 nm to 2000 nm was customised to promote a wide spectrum output from the ML cavity. The SWNT-PVA composite SA was designed and fabricated to operate at the short wavelength gain region of the Tm-doped fibre. Fig. 4.4(b) shows a measured transmission spectrum of the SWNT-PVA composite, which exhibits a broad absorption band covering from 1600 nm to 2200 nm. Characterised using an in-house built 1870 nm ultrafast laser, the SWNT-PVA SA provided a modulation depth of 23.1% and a saturation fluence of 56.1 $\mu J/cm^2$.

Once all the components were applied as shown in Fig. 4.2, the intra-cavity dispersion management was carried out by using a cutback method of the DCF to minimise the net dispersion of the cavity, which increases the pulse bandwidth, therefore, shortening the

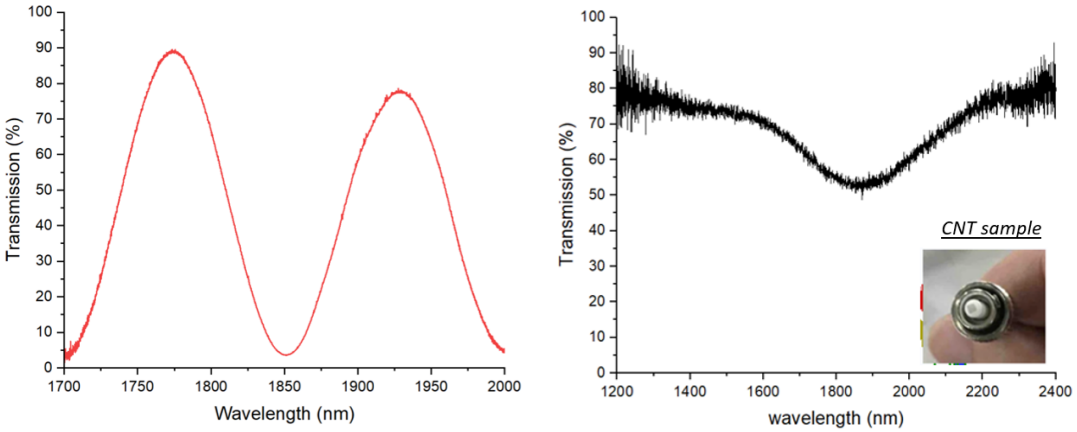

(a) Fused WDM transmission.

(b) CNT transmission.

FIGURE 4.4: Spectral transmission of different components.

compressed pulse duration [13] as explained in Fig. 4.5. The SMF length was shortened by 1 m between measurements, resulting in a broadened spectral output from 18 nm to 35 nm (10 dB bandwidth) and reduced compressed pulse width from 450 fs to 320 fs, while maintaining a net positive dispersion evident by the flat spectral edges.

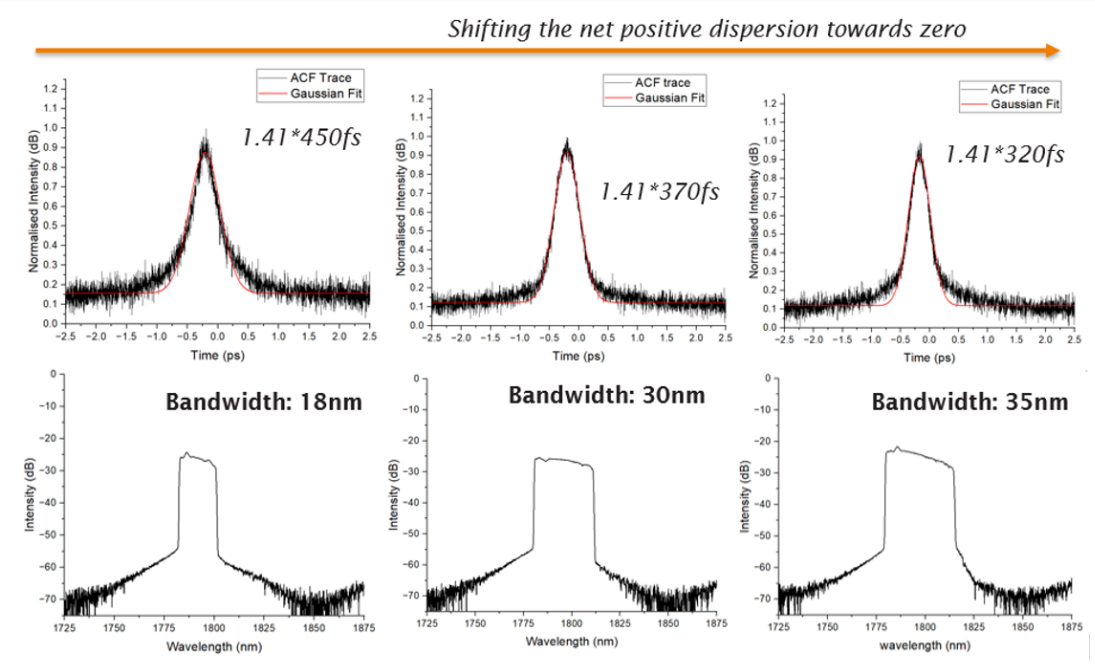

FIGURE 4.5: Spectrum output of the cavity at different net dispersion values and corresponding to the compressed pulse duration separated by a GDD of 0.045 ps^2 between each value.

The GVD of the single-mode fiber (SMF, SMF28e) and Tm fiber are anomalous with an estimated value of -0.045 ps^2m^{-1} and -0.02 ps^2m^{-1} at the laser wavelength, respectively, while the DCF provides a normal dispersion with an estimated value of +0.085 ps^2m^{-1}

[44, 86]. The total lengths of the SMF and DCF were 5.4 m and 3.2 m, respectively, which leads to an estimated net-cavity dispersion of $+0.023\ ps^2$. The resultant output spectrum was found to be a DS pulse as shown in Fig. 4.6, exhibiting typical sharp leading and trailing edges, with a central wavelength of 1789 nm and a 10 dB bandwidth of 47 nm.

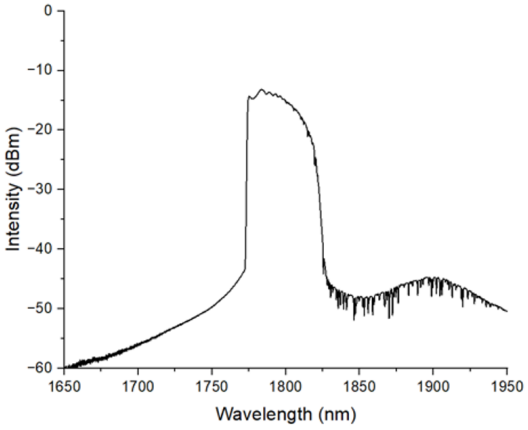

FIGURE 4.6: Final ML output spectrum.

Furthermore, the cavity length resulted in a fundamental repetition frequency of 23.1 MHz as shown by radio frequency (RF) spectrum measurement of the ML pulses in Figs. 4.7(a) and 4.7(b), which exhibit an signal-to-noise ratio (SNR) over 60 dB and 80 dB with and without the mirror coupled, respectively and the wide scanning range RF spectrum confirms stable single-pulse ML operation is maintained in both cases.

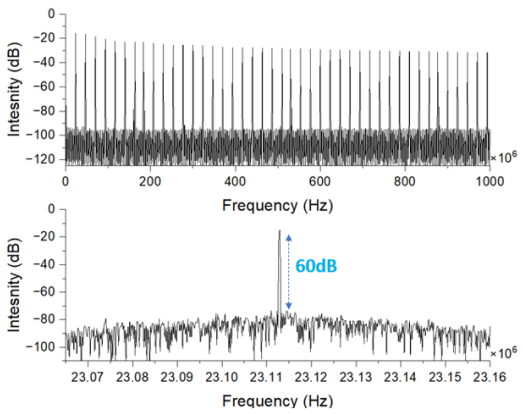

(a) RF spectrum of the cavity spanning 1GHz (top) and 10kHz (bottom) with the mirror.

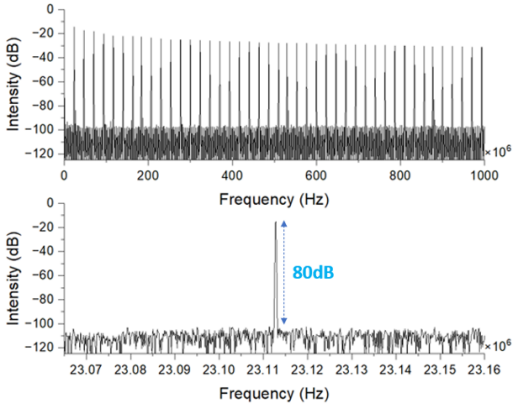

(b) RF spectrum of the cavity spanning 1GHz (top) and 10kHz (bottom) without the mirror.

FIGURE 4.7: Comparison of the cavity performance with and without a fibre-coupled mirror.

Moreover, in the single-pass pumping operation, the ML operation was observed with a pump threshold of 145 mW, and an output power of 10.2 mW was obtained when the pump power was increased to the maximum of 250 mW. In comparison, the mode

locking pump threshold was effectively reduced to 110 mW in the double-pass pumping operation, and the maximum output power was increased to 16.3 mW. Fig. 4.8 shows the power performance of the ML laser in the single-pass and double-pass pumping operations, from which it is seen that the double-pass pumping method enhanced the power performance and efficiency of the laser.

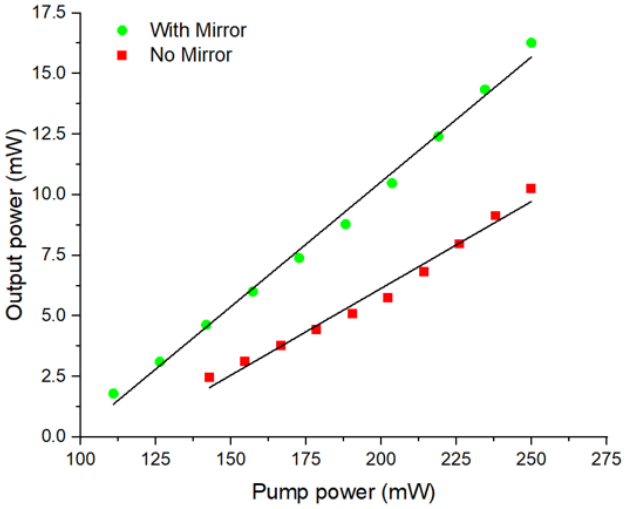

FIGURE 4.8: Relationship between output signal power and input pump power of the ML laser with (green) and without (red) the fibre-coupled mirror.

Further analysis of the pulse output revealed a polarisation exciton ratio (PER) of 14.2 dB at the output, and a positive chirp with a measured duration of 3.2 ps (assuming a Gaussian pulse) was estimated based on the cut-back of a piece of SMF that was employed to compensate for the pulse chirp and compress the pulse. A minimum compressed pulse width of 270 fs was achieved using a SMF length of 4.65 m, as shown in Figs. 4.9(b) and 4.9(a).

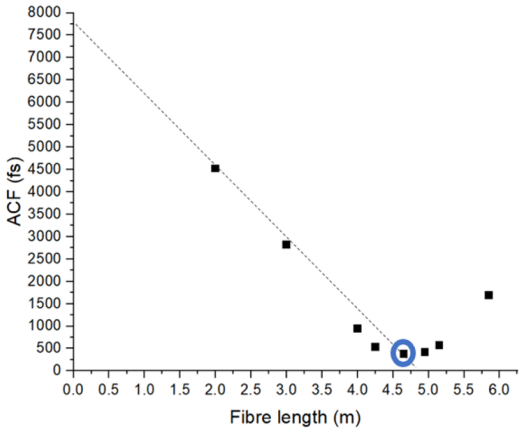

(a) ACF FHWM measurements at different SMF compressor length, the minimum pulse duration highlighted in blue.

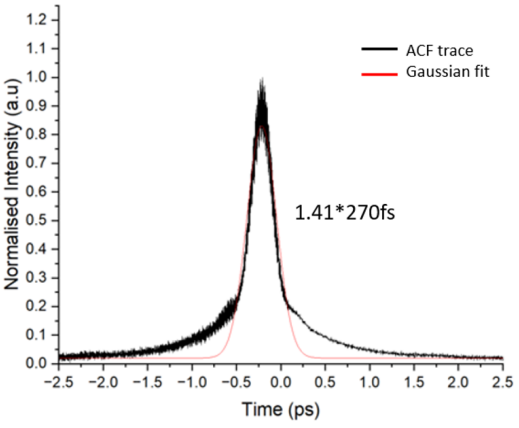

(b) ACF trace of compressed pulse duration.

FIGURE 4.9: ML pulse output and compression results.

4.2 Amplification and compression

4.2.1 Chirped pulse amplification

A single amplifier CPA system, shown in Fig. 4.10, was built to demonstrate the short wavelength amplification in Tm-doped fibres. A 90/10 fibre splitter was connected to the output of the ML cavity to provide a monitoring port (10%) for the mode-locking operation. An ISO was placed after the splitter to prevent backwards-travelling signals that may disturb the mode-locking operation. A 5 m length of DCF was used to stretch the pulse of the ML laser, thereby eliminating the nonlinear effect in the subsequent amplification. To build a Tm-doped fibre amplifier for the CPA, a WDM was used to couple the pump light from an in-house-made 1560 nm EDFL to core-pump a 1 m Tm-doped fibre (TmDF200, OFS). At the output of the amplifier, a pulse compressor comprising a pair of transmission gratings (PCG-550/2000-930, Ibsen photonics) was employed to characterise the pulse compression.

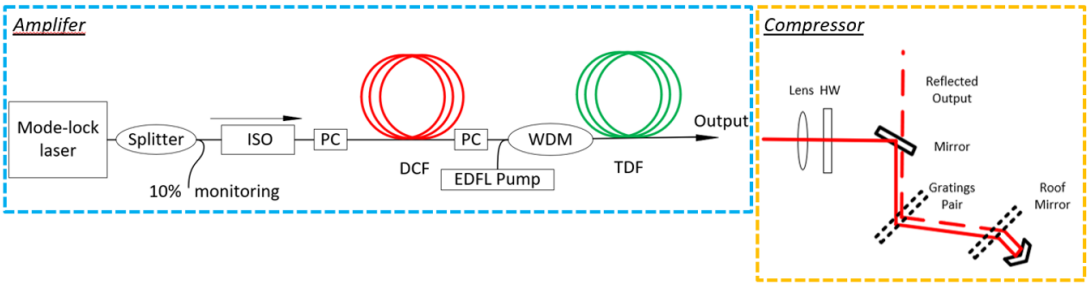

FIGURE 4.10: Schematics of the Tm-doped fibre chirped pulse amplifier (and CMA) and compressor; HW: half wave plate.

The pulse width after amplification using the 5 m DCF was measured to be ≈6.5 ps as shown in Fig. 4.11(a), which reduced the pulse peak power entering the Tm-doped fibre amplifier bellow the threshold for non-linearity. Two PCs were added at the input and output of the DCF to optimise the polarisation of the signal since the DCF has poor PM properties. The PER measured after the DCF was 2.5 dB, but was improved by adding a PC up to 5 dB. The power output of the Tm-doped fibre amplifier is shown in Fig. 4.11(b). A slope efficiency of 34.5% and a maximum output power of 950 mW were achieved when the pump power was increased to the maximum available power of 3 W. The corresponding maximum pulse energy is 41.5 nJ.

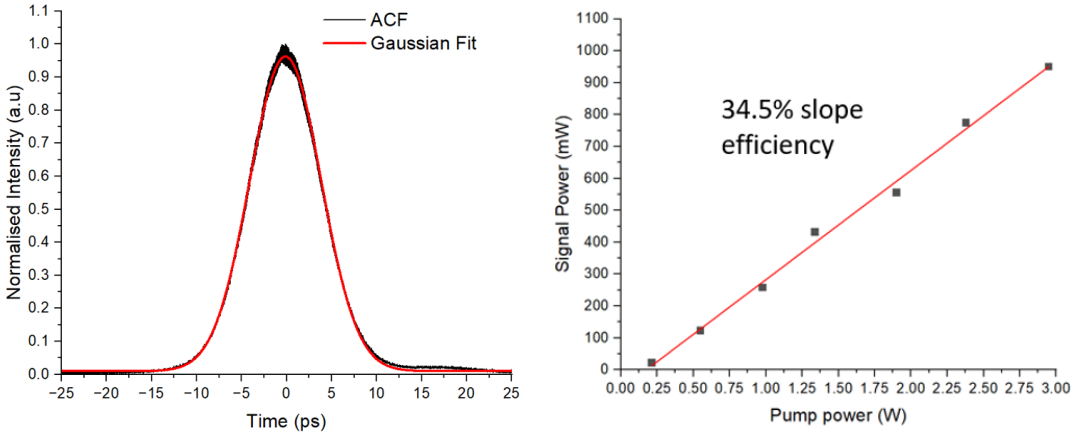

(a) 5m DCF output pulse duration.

(b) Relationship of the input pump power and output signal power.

FIGURE 4.11: CPA input pulse and output power.

Fig. 4.12(a) shows the spectrum of the output pulses at different powers, which indicates no significant nonlinear effects or notable spectral distortions from the amplifier. Autocorrelation measurements for the pulses after compression at different powers were also undertaken and are shown in Fig. 4.12(b), which gives a minimum pulse width of 260 fs as similar to that for the ML laser, due to the absence of nonlinearity affecting the bandwidth of the pulses. The CPA increased the pulse energy from 0.45 nJ to 41.5 nJ, providing a gain of 19.64 dB, while maintaining the pulse compression ability of the ML laser.

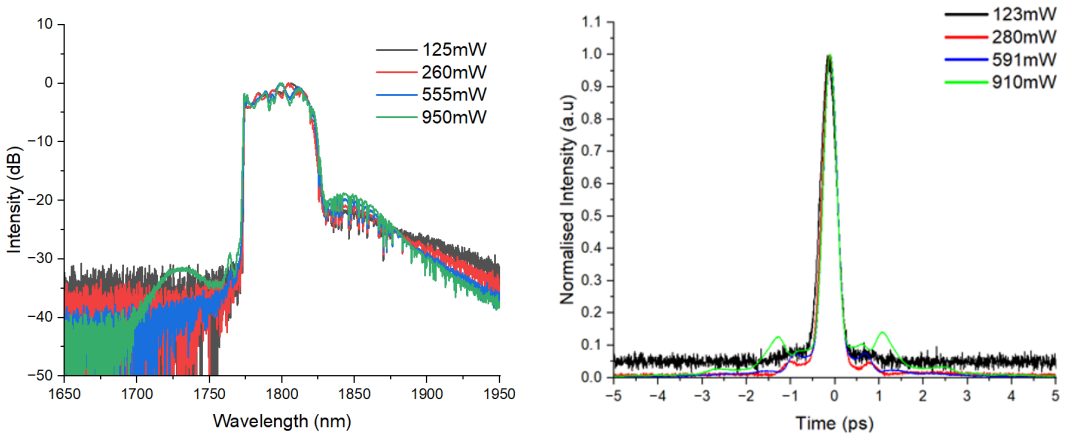

(a) Output spectrum.

(b) ACF trace of the compressed pulses.

FIGURE 4.12: CPA output at different powers.

4.2.2 Chirp-managed pulse amplifier

In order to generate a shorter compressed pulse duration at high powers, the pulse spectrum needs to be broadened before compression. Therefore, using the same amplifier configuration seen in Fig. 4.10, the DCF length was shortened using the cutback method to manage the pulse peak powers, duration and chirp propagating through the fibre, thus managing the rate of spectral broadening in the amplifier via SPM.

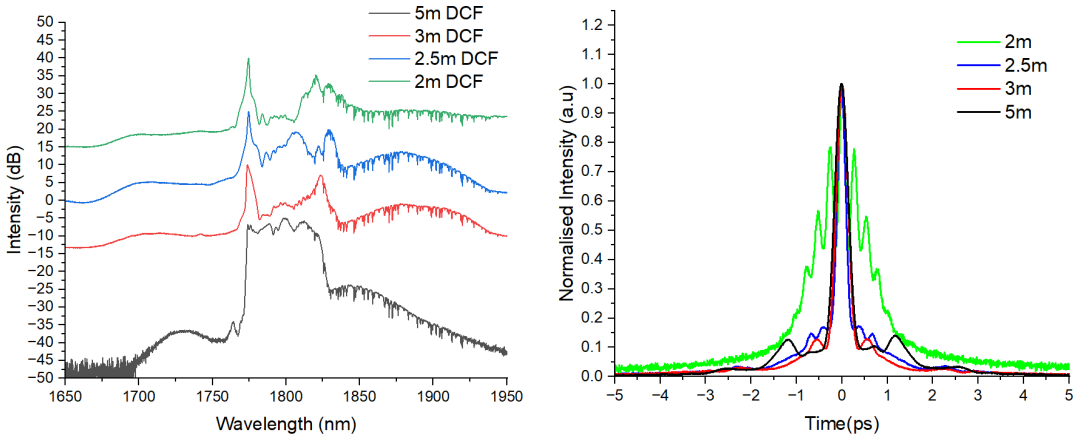

(a) Amplified spectrum output at 950 mW at different DCF lengths offset by 20 dB.

(b) Corresponding compressed pulse autocorrelation.

FIGURE 4.13: Chirp-managed pulse amplifier output at different DCF lengths; 5 m (black), 3 m (red), 2.5 m (blue), 2 m (green).

Fig. 4.13(a) shows the variation of the DCF length with the output spectrum at the highest pump power and the resultant compressed pulse durations. SPM has led to the transfer of energy from the central parts of the pulse spectrum to the sides, which increases at shorter lengths. At a DCF length of 3 m, the onset of spectral broadening appeared during amplification at increased powers. Consequently, the minimum achievable compressed pulse also reduced as the power rose, reaching a measured value of 230 fs at the highest power, shorter than was previously attained from CPA, as seen in Fig. 4.13(b). Next, a length of 2.5 m DCF was tested, and a similar trend is seen where the pulses increase bandwidth with increasing power, resulting in a minimum compressed pulse duration of 180 fs (assuming a Gaussian pulse).

Shortening the fibre length further to 2 m does not continue the pattern of shorter compressed pulse duration, rather it increased the generated pedestal with increased pump power, reaching a multi-peak ACF trace at the highest power. These phenomena can be attributed to the increased nonlinear chirp accumulating from increased SPM, which is not compensated for by the grating pair compressors, thus appearing as temporal pedestals. In extreme cases of high nonlinearity, in an anomalous dispersion fibre, modulation instability arises, which results in the optical pulse breaking up into multiple peaks in the time domain, where the number of pulses equals $(n + 1/2)$, and n is the

number of peaks on the ACF. The time delay between each pulse corresponds to the period of each peak seen on the ACF trace [87].

4.2.3 Chirped pulse amplifier and nonlinear broadening

As seen in Fig. 4.14, the original CPA set-up was modified to add a HNF at the output of the TDFA, to further broaden the spectrum post-amplification in a normal dispersive fibre to avoid the optical wave breaking encountered previously. Therefore, a 2.5 m fixed length of UHNA4 acting as HNF was added following the amplifier, and the DCF length was reverted to 5 m to avoid any nonlinearity during the amplification.

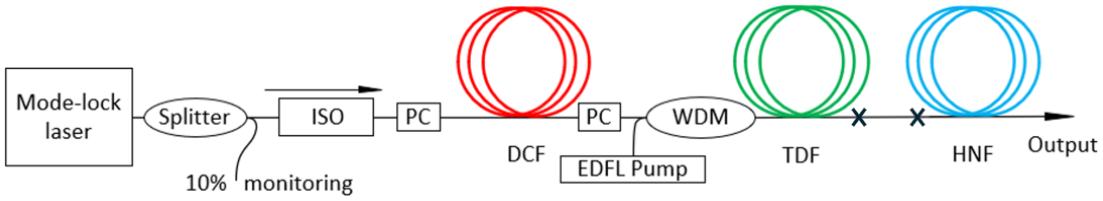

FIGURE 4.14: Schematics of the Tm-doped fibre Chirped pulse amplifier and nonlinear broadening system; HNF: Highly nonlinear fibre.

An SMF was utilised between the TDF and HNF for its negative dispersion to compress the pulse and control peak powers entering the HNF. An initial 1 m length of SMF was used, then shortened to 60 cm, and again to 30 cm. As shown in Fig. 4.15, the SMF spectrum output reveals that the 1 m generated nonlinearity, whereas 60 cm was sufficient to suppress it at the highest output powers.

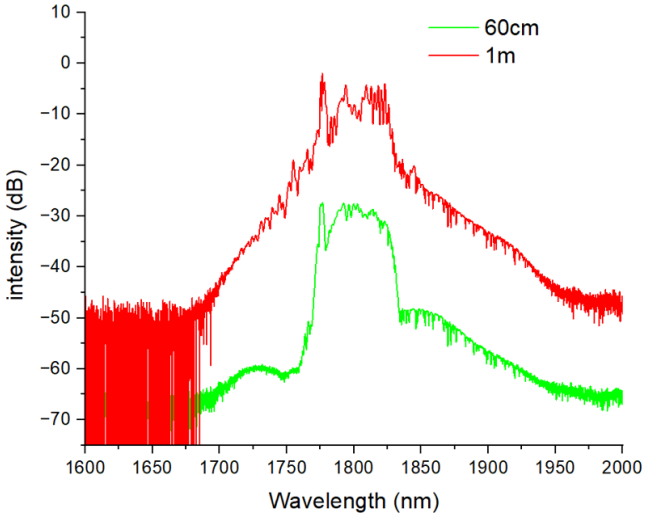

FIGURE 4.15: At 2 W of pump power, the amplified spectrum after different lengths of SMF; 60 cm (green), 1 m (red).

The HNF output spectrum showed broadening of the spectrum as presented in Fig. 4.16(a) regardless of the length of the SMF used. As expected, the 1 m SMF showed

a large pedestal formation after compression due to the modulation instability, whereas the measured compressed pulse revealed durations of 270*1.41 fs and 170*1.41 fs with minimal pedestal formation at lengths of 60 cm and 30 cm, respectively (Fig. 4.16(b)).

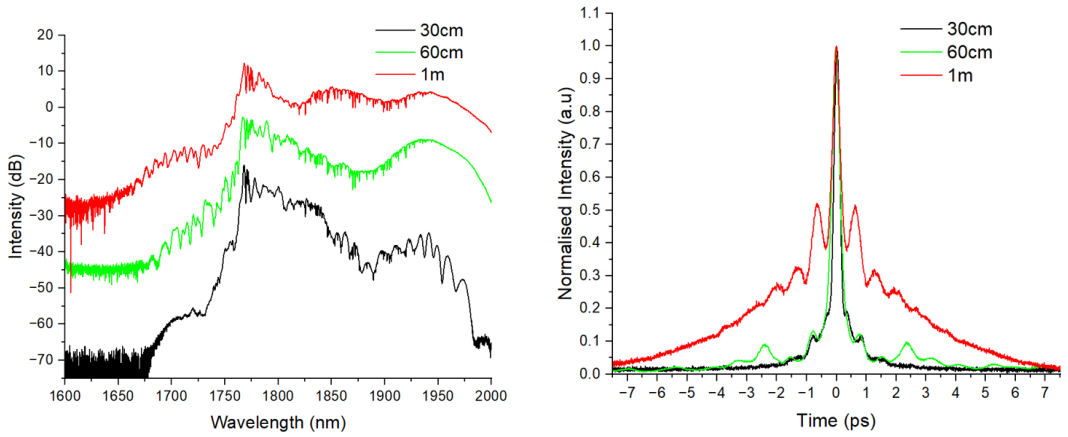

(a) HNF output spectrum.

(b) Compressed pulse duration After HNF.

FIGURE 4.16: CPAN output at different SMF lengths; 30 cm (Black), 60 cm (green), 1 m (red).

The slight improvement in the pulse compression compared to the previous method came at the cost of the output power because the output spectrum seen in Fig. 4.16(a) reveals gain at a peak shifted 13.8 THz away from the central frequency (≈1950 nm), which corresponds to Raman in silica [88]. A non-instantaneous transfer of the energy from the main pulse was caused by the several picoseconds-long pulse propagating in the HNF, resulting in a Raman gain of ≈20 dB, which is detrimental to the main signal pulse. Moreover, a loss in power occurs due to the MFD mismatch of the spliced fibres, SMF and UHNA4. Both factors greatly limit the power scaling and efficiency of this method.

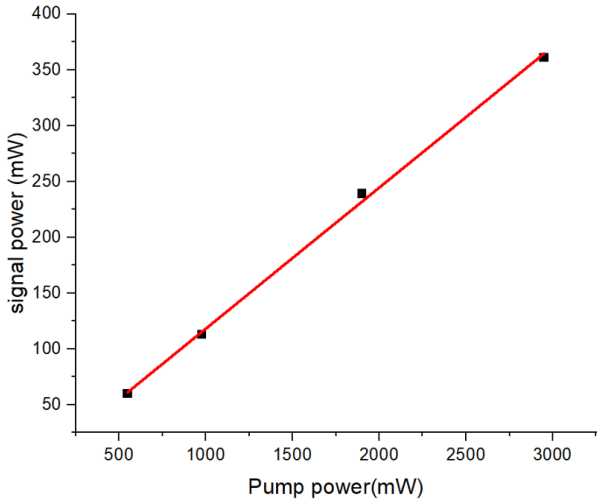

FIGURE 4.17: Output power against pump power after HNF.

As shown in Fig. 4.17, ≈3 dB loss is measured at the output of the HNF, showing that a maximum signal power of 390 mW is achievable compared to the 950 mW signal power expected from the amplifier. Therefore, any tinkering in the pulse compressibility needs to take place on a femtosecond scale to avoid delayed nonlinear effects and needs to take place before the amplifier to maximise the output power.

4.2.4 Nonlinear broadening and chirped pulse amplification

A nonlinear fibre amplification approach was set up as shown in Fig. 4.18 to overcome the limitations of the previous methods. A section of SMF was added before the HNF to compress the pulses to the minimum pulse duration, thus increasing the peak powers passively. Therefore, in accordance with the previous pulse compression characterisation, a total SMF length of 4.65 m was placed between the seed and the HNF.

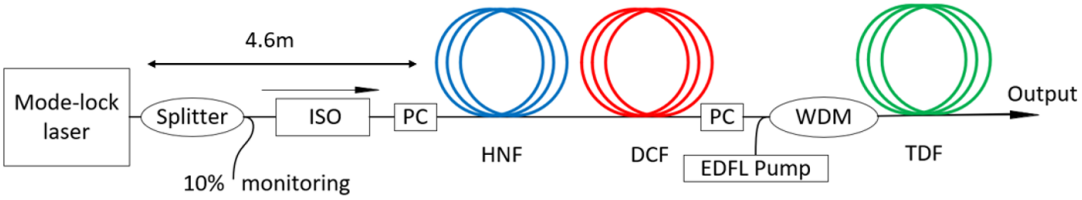

FIGURE 4.18: Schematics of the Tm-doped fibre nonlinear chirped pulse amplifier.

The compressed pulses were then used to assess the nonlinear broadening capabilities of 3 normal dispersion HNF, which were a 50 m UHNA4, 60 m UHNA7 and 10 m HN1550 (refer to Table 2.2 for fibre parameters). As seen in Fig. 4.19, the 10 m HN1550 showed the broadest pulse broadening compared to the other fibres, regardless of having a similar core size.

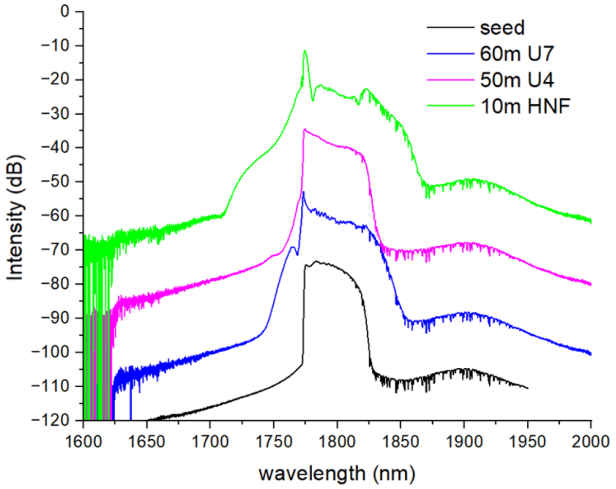

FIGURE 4.19: Spectra of Seed laser (Black) and the output of different HNFs UHNA7 (Blue), UHNA4 (Pink) and HN1550 (green) offset by 20 dB.

Therefore, the 10 m length of HNF (HN1550, Thorlabs) was selected and placed in front of the DCF to provoke SPM for coherent broadening of the pulse spectrum. When comparing the spectrum of the ML laser to the spectrum after the HNF, the spectral broadening was asymmetric. This indicates that the compressed pulse entering the HNF had an asymmetric profile.

The HNF was originally designed to provide near-zero dispersions with a large nonlinear coefficient for wavelengths around 1550 nm. However, it was found that it exhibited a small normal dispersion at the lasing wavelength due to the temporal pulse stretching observed at the output of the HNF. As shown in Fig. 4.20, the pulses were slightly stretched in the HNF to a duration of 2.83 ps. Thus, a GVD of the HNF was later estimated to be $2.75\times10^{-4} ps^2 m^{-1}$ at 1789 nm based on the observation and the available manufacturer data. After passing the pulses from the HNF through the grating-based compressor, a minimum pulse duration of 130 fs was achieved. This indicates that the nonlinear spectral broadening using the HNF provides an effective method for pulse narrowing.

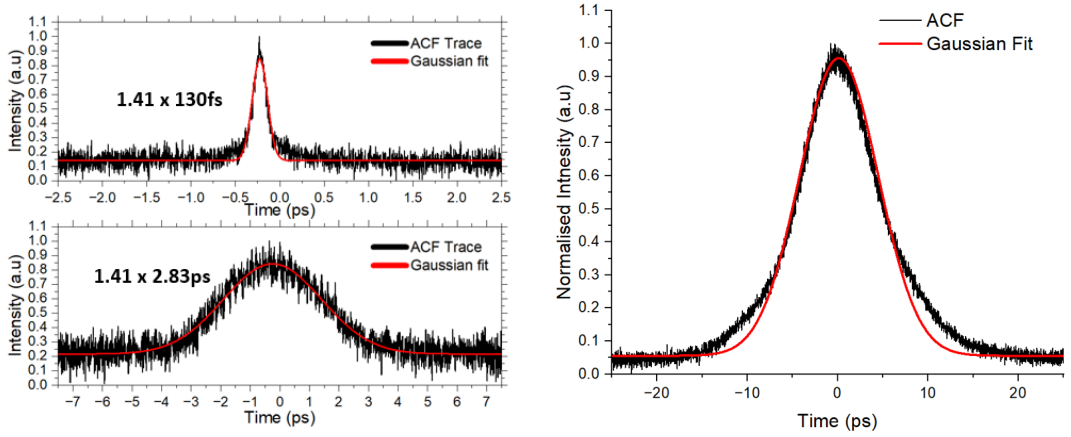

(a) ACF trace of the output of the HNF before (bottom) and after compression (top).

(b) ACF trace of the output of the HNF and DCF.

FIGURE 4.20: Autocorrelation measurements after HNF and DCF.

Furthermore, the 5 m DCF length used further increased the pulse width to 9 ps as shown in Fig. 4.20(b), which ensured that no further nonlinearity distortion occurs during amplification as proven by the measured output spectrum of the amplified pulses seen in Fig. 4.21(a). A minimum pulse duration of 180 fs was measured at the maximum amplifier power, as shown in Fig. 4.21(b), which is longer than the 130 fs output directly from the HNF. This is likely attributed to the gain narrowing of thulium, as the operating wavelength coincides with the high absorption region of thulium.

To summarise, a ML seed laser with a 110 mW pump power mode-locking threshold generating a DS with 0.45 nJ pulse energy at 1.79 μm that can be compressed to 270 fs was developed, and several amplification and pulse-narrowing methods were tested. The CMA approach was capable of generating 180 fs when 2.5 m of DCF was used; however,

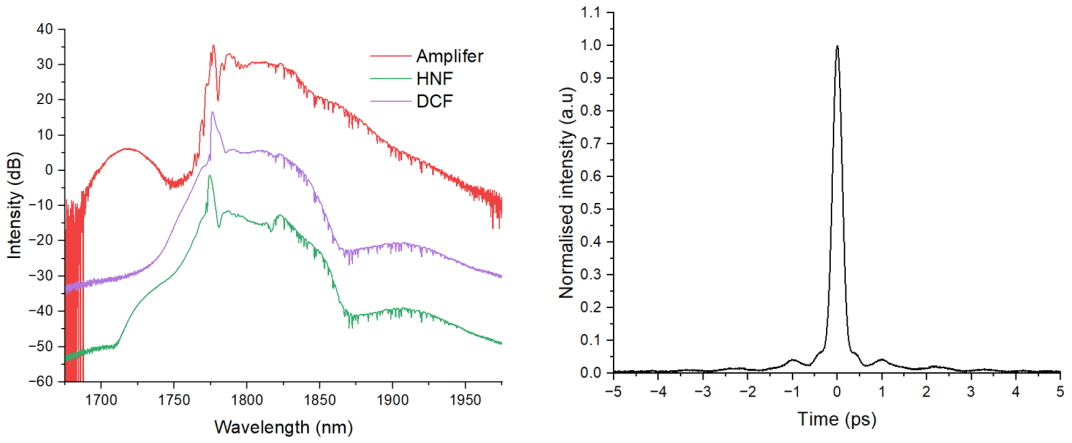

(a) Output spectrum at different sections; (green), 5 m DCF (pink) and amplifier (red).

(b) Final amplified compressed pulse at the highest power.

FIGURE 4.21: NCPA output at different stages.

it generated a pedestal due to the modulation instability caused by the nonlinearity in the anomalous dispersion. Sending a long pulse in an HNF also resulted in unwanted effects in the form of Raman amplification. To solve this, the pulse was first compressed to a near TFL pulse duration before spectrally broadening in a normal dispersion HNF, allowing for newly generated coherent spectral components. The addition of the HNF fibre led to the generation of the smallest pedestal out of the methods evaluated in this chapter for the highest power. The generated pulses had a central peak occupying 76% of the total pulse area, as opposed to only 54% from linear compression in CPA and 49 % from CMA, which produced the highest pedestal as shown in Fig. 4.22, resulting in peak powers of 174 kW, 79 kW and 113 kW, respectively. A factor of 1.44 improvement in the pulse compression, 1.7 in the pulse peak power and an improved pedestal mitigation was obtained by using NCPA over CPA.

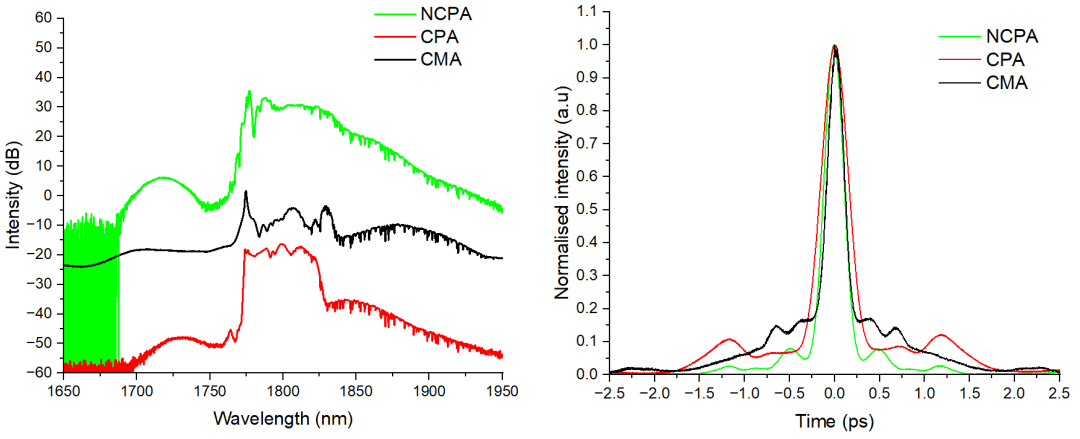

(a) Output spectrum of different amplification methods.

(b) Output ACF of different amplification methods.

FIGURE 4.22: Comparison of the different amplification and compression methods; NCPA (green), CPA (red) and CMA (black).

This compact and efficient fibre laser source and amplifier provides amplification and pulse broadening simultaneously for enhanced peak power output by improved gain and pulse compression. This technology allows for ease of integration into the current imaging laser and holds advancements towards power scaling, wavelength emission and pulse compression over the older technology.

Chapter 5

1740 nm femtosecond thulium fibre laser development

5.1 Background and introduction

Building upon the work presented in the previous chapter 4, this section investigates the development of a ML laser oscillator designed for generating short wavelength pulses below 1.75 μm. This wavelength is hypothesised to be ideal for deep imaging of soft tissue (Fig. 4.1). The investigation involved constructing and testing various cavity designs that utilised different saturable absorption mechanisms. However, this task proved challenging due to the limited availability of commercially compatible components at this wavelength. Consequently, we faced high losses that were difficult to compensate, primarily because of the low gain of thulium, which results from significant absorption at this wavelength.

As well as having high gain at the target wavelength, it is imperative to have a spectral filter to suppress unwanted wavelength emission to promote lasing at the target wavelength. Several tunable laser sources have been demonstrated in the literature which cover the short thulium emission band. The tunable free-space filter elements, such as grating, Fabry-Perot, and acousto-optic tunable filter (AOTF) [89–91], increase the bulkiness of the laser system. On the other hand, fiberised Lyot filters have been used, but they rely on the gain profile of the active fibre to promote lasing and may result in dual-wavelength emission [92]. One work that stands out in particular by S. Chen et al. for using a low-pass filter induced via bending of a specially designed W-type Tm-doped fibre [91]. Although this method is optimised for the suppression of longer wavelengths, the use of specialised fibre limits wide-scale adoption in many applications requiring tunable sources. Therefore, there is still a need for an all-fiberised ML laser source capable of generating short wavelengths below 1.75 μm.

In this work, a linear cavity design is explored first to reduce the number of components used and reduce the overall cavity losses since the gain at the shot wavelengths is low. This design allowed for the testing of multiple SESAM samples for the short wavelength application. Later, several Tm-doped fibres were tested as well as spectral filters to optimise the pulse energy and favour the lasing at the short wavelength. Several forms of solitons were observed throughout the experiments, which were DS, CS, SPS and NLS.

Finally, the limitations and results of various components and techniques applied to different cavities were investigated and discussed to arrive at an optimal cavity design. The final design incorporates a CNT ring cavity, utilising a bending-induced low-pass fibre filter to generate SPS mode-locking. Later, a series of amplifiers, optimised for short wavelength emission, were employed to enhance pulse energy, and the pulse compression was characterised.

5.2 SESAM

The use of a SESAM was investigated as an SA for this application. Two commercially available samples from BATOP Optoelectronics were: SAM-1920-36-10ps-x, and SAM-1960-54-10ps-x. The low-intensity spectral reflectance provided by the supplier for each is shown in Fig. 5.1. The reported modulation depth values were 20% at 1920 nm and 30% at 1960 nm, respectively. The side windows of both SESAMs were targeted for use, which is outside the manufacturer's intended wavelength range, so the actual modulation depth values were unknown. Therefore, to find the appropriate SA, the SESAMs' linear reflectivity was characterised, expanding on the wavelength range of interest from 2000 nm to 1600 nm as shown in Fig. 5.2.

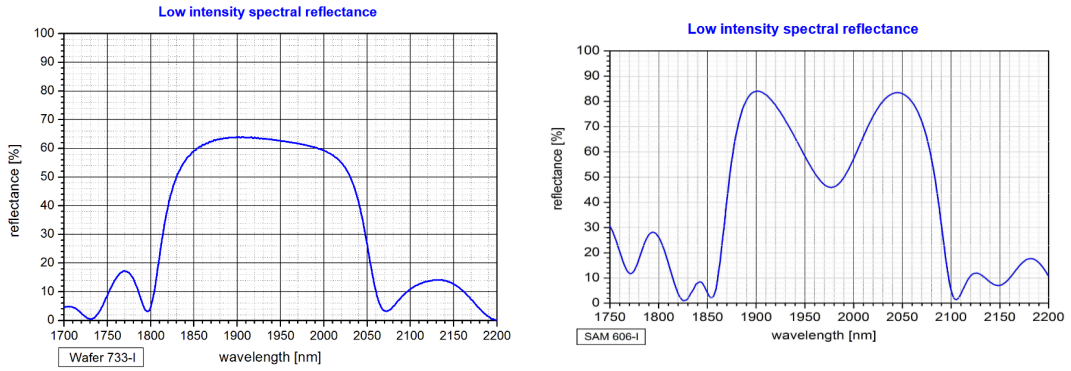

(a) SAM-1920. (b) SAM-1960.

FIGURE 5.1: Low intensity spectral reflectance of different Batop SESAM samples. These figures were reproduced from *BATOP GmbH, 2024* [54], in accordance with their open access policy and terms of use.

Several operation windows can be observed. SAM-1920, provided 2 interesting operational windows between 1700-1780 nm and 1780-1850 nm at the cost of 70% linear losses at the peak reflected windows for each window. SAM-1960 has an operational window between 1800-1720 nm but provides higher linear reflection loss of 85% at the peak reflectivity in that window.

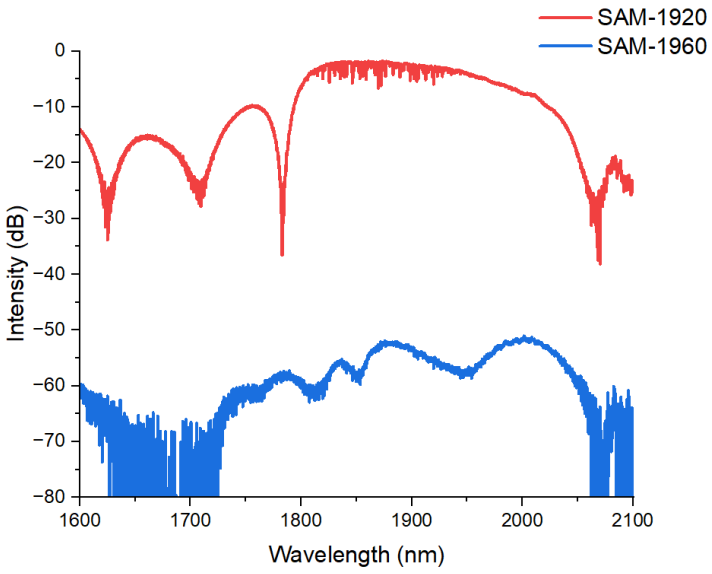

FIGURE 5.2: Characterisation of the linear reflection of the SESAM samples; SAM-1920 (Red), and SAM-1960 (Blue). Offset: 50 dB.

5.2.1 First linear cavity design

A linear cavity was built as shown in Fig. 5.3. On one end, the SESAM sample is wedged tightly against a flat patch cord. On the other end, a 2x2 50/50 OC is used as an output, as well as providing linear reflection back into the cavity by shortening the fibre lengths of 1.6 m and splicing them together to form a linear loop mirror. The linear reflection of the 50/50 coupler is designed at 2 μm and would provide 100% reflection back into the cavity, but since the target wavelength is 1750 nm, it is assumed to have a lower linear reflection value. Two fused WDMs (Thorlabs WD1525A) are similar to the one used in chapter 4 because it has a transmission window that peaks at 1775 nm (refer to Fig. 4.4(a)) for pump coupling and filtering to not damage the SESAM samples from the high pump powers.

Furthermore, based on the data from chapter 4, 15 cm of TDF (OFS TmDF200) was shown to minimise the reabsorption of the short wavelength of thulium. Two in-line PCs are used to tune the mode-locking. This formed an all-anomalous dispersion cavity where all the fibres used were SMF28e for a total length of 9.7 m and an effective length of 21.6 m due to the double pass operation of the linear cavity for 1 round-trip. Moreover, the SMF and the TDF have a GVD of -0.045 ps^2/m and -0.02 ps^2/m, respectively, at

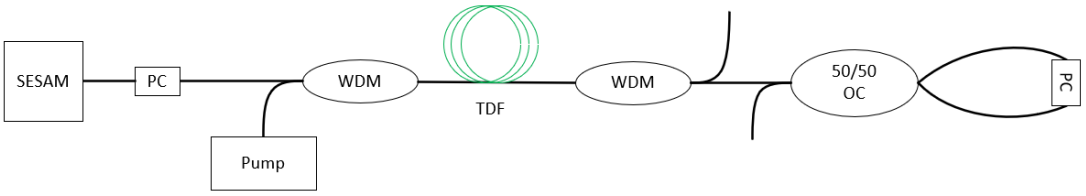

FIGURE 5.3: Schematics of the SESAM-based linear mode-locked cavity.

1750 nm. This leads to a RR of 11.28 MHz and a net cavity GDD of -0.807 ps^2. A 2-stage in-house built EDFA at 1560 nm was used to pump the system, capable of up to 4 W of power. The results of using the different SESAM samples are shown in the following sections.

5.2.1.1 Cavity implementation: SAM-1960

By placing the SESAM with SAM-1960, two CS mode-locking states were found at 1908 nm and 1783 nm as shown in Fig. 5.4. Switching between the two states was realised by tuning the PC in the cavity. This corresponds to the two operational wavelength windows of this SESAM sample. As expected, as a consequence of the high cavity losses and short gain fibre, a high pump threshold of 700 mW was required to initiate pulsing in combination with the low output coupling ratio, making this an inefficient laser.

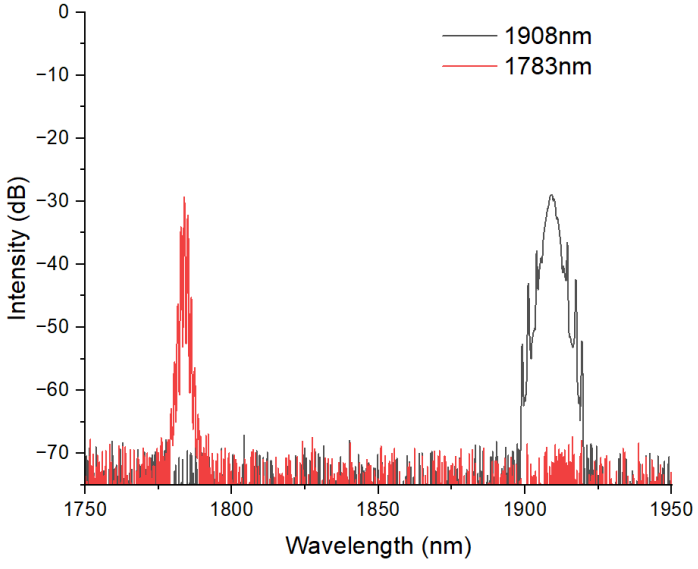

FIGURE 5.4: Spectrum of two CS mode-locked states achieved by SAM-1960.

5.2.1.2 Cavity implementation: SAM-1920

Next, the SA was replaced with SAM-1920 in an attempt to achieve shorter wavelength emission. The results showed mode-locking states at 1764 nm and 1798 nm, which were both CS as evidenced by the Kelly sidebands as seen in Fig. 5.5. The pump threshold for pulsing was much higher, however, at 1.2 W. This also revealed the lower wavelength limit attainable by using these SESAM samples.

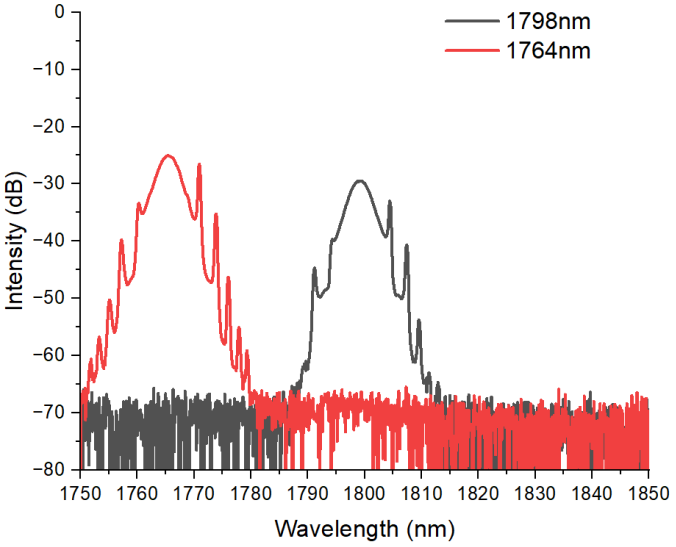

FIGURE 5.5: Spectrum of two CS mode-locked states achieved by SAM-1920.

Nonetheless, to resolve the Kelly's sidebands, 4 m of the normal dispersion UHNA4 was added to manage the dispersion inside the cavity to achieve higher pulse energies.

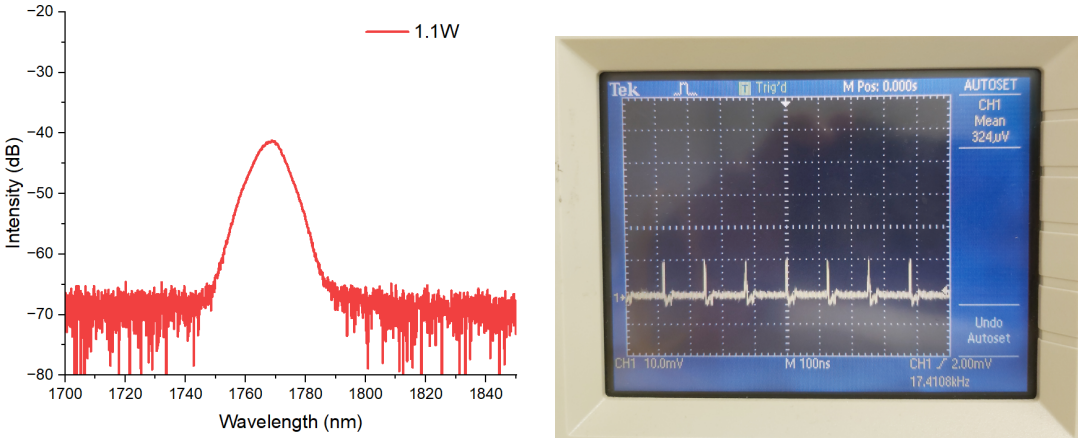

(a) Spectrum of a mode-locked state at 1.1 W pump power

(b) Oscilloscope measurements

FIGURE 5.6: Results of using SAM-1920 on net anomalous dispersion mode-locking

A GVD coefficient of 0.085 ps^2/m at 1750 nm was estimated. The impact of the additional fibre length shifted the net GDD to -0.144 ps^2 and lowered the laser RR to a

stable 7.8 MHz as seen by the oscilloscope measurements in Fig. 5.6(b). The pump threshold for mode-locking at 1.1 W outputs a signal power of 14 mW, and the laser spectrum indicates that a SPS is formed as seen in Fig. 5.6(a).

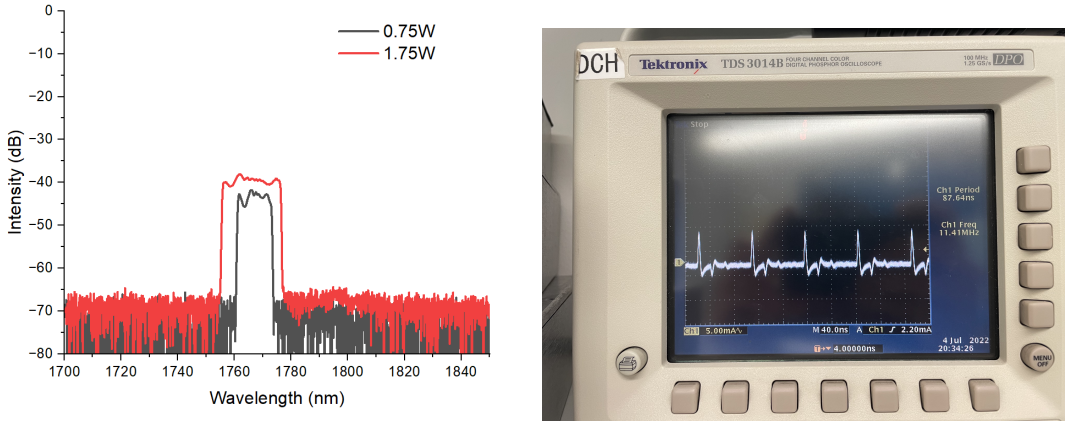

(a) Spectrum of a DS at different pump power.

(b) Oscilloscope measurements.

FIGURE 5.7: Results of using SAM-1920 on net normal dispersion mode-locking.

Next, to generate a DS, 4m of SMF were taken out of the cavity, shifting the net GDD to 0.059 ps^2 at 1750 nm and shifting the RR to 11.4 MHz as shown in Fig. 5.7(b). The results showed a sharp edge spectrum at 1767 nm, indicating a DS at a pump threshold of 0.74 W, as shown in Fig. 5.7(a). By increasing the pump power to 3.15 W, the output power rose from 4 mW to 9.17 mW, and the spectral bandwidth increased from 12 nm to 21 nm.

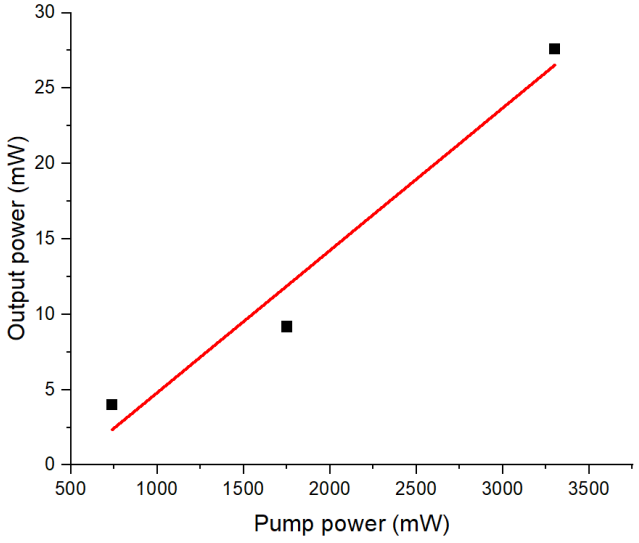

FIGURE 5.8: Output power of the laser at different pump powers.

The poor slope efficiency of 0.92 % and high pumping thresholds are the causes of high losses within the system and the short gain fibre, as shown in Fig. 5.8. To combat this, the TDF fibre was increased to 30 cm, and the WDM filtering of the pump was removed. Since the WDM possess spectral filtering. The results, however, showed an

output power of 0.6 mW at a similar pump threshold pump power of 800 mW as a continuation of the reabsorption of the gain fibre. Further shifting the dispersion closer to zero while maintaining a net normal dispersion did not result in a further increase of the bandwidth, likely due to the strong spectral filtering in the cavity and short fibre lengths, which limit the pulse bandwidth and broadening. Ultimately, DS bandwidth remained capped at ≈20 nm. Therefore, a change of strategy was required to broaden the output spectrum and improve both the pulse energy and efficiency.

5.2.2 Germanium/Tm co-doped fibre

A higher gain is required for higher pulse energy output. Therefore, two Tm-doped fibres were characterised and compared based on their short wavelength emission by pumping both fibres at 1 W of power at 1550 nm and examining the output ASE. The first fibre was the OFS TDF, which was used throughout as it set the standard for high-quality short wavelength performance. The second fibre studied was a Germanium (Ge)/Tm co-doped fibre. According to the literature, this configuration was said to shift the gain peak toward the shorter wavelengths of the thulium emission band, mainly due to the high concentration of Ge and low concentration of Tm [93]. A 3.6 m long Ge/Tm doped fibre was used, which had a low thulium doping concentration of 0.12 % by weight. This fibre was compared to a 0.4 m OFS TDF, as well as a combination of the two fibres. The ASE data showed that both fibres, despite the length difference, perform similarly across the emission band as seen in Fig. 5.9. Therefore, an extra 0.4 m of OFS fibre was added to both fibres, and the data revealed that although there is an increase in the long wavelength emission in both fibres, higher short wavelength gain can still be achieved from a 0.8 m OFS TDF by an extra 8 dB.

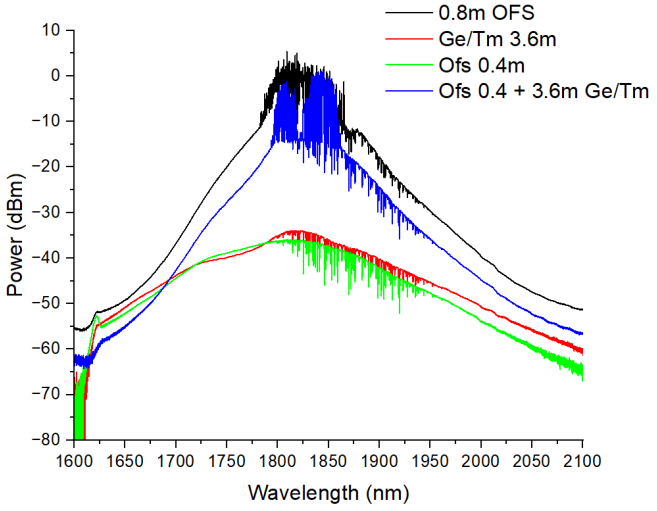

FIGURE 5.9: ASE output of different TDF and lengths; 0.8m OFS (black), 3.6m Ge/Tm (red), 0.4m OFS (green), and 0.4 m OFS 3.6m Ge/Tm.

5.2.3 Second linear cavity design

A new design was adopted to accommodate for the longer fibre and minimising the power onto the SESAM to avoid damage. Fig. 5.10 shows the updated cavity design. The OC is changed to a 25% output with the use of a two-by-two 25/75 fibre coupler. Therefore, the optical loop mirror was replaced with a fiberised mirror (Thorlabs, P5-SMF28ER-P01-1). A 0.8 m OFS TDF was added based on the characterisation, and the secondary WDM was added back into the cavity because in previous experiments with one WDM, the SESAM patch cord was more prone to damage. The total SMF length was increased to 8 m, and 3.4 m of UHNA4 DCF was used. The net GDD was -0.29 ps^2.

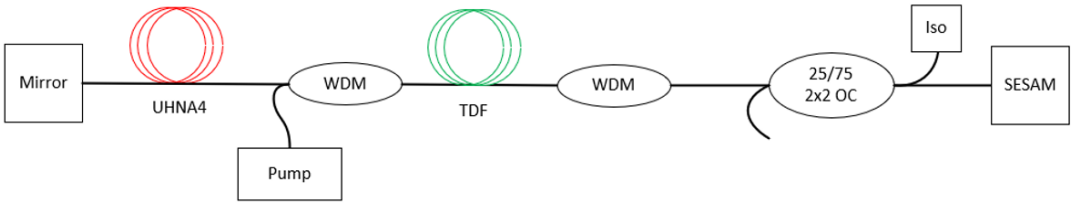

FIGURE 5.10: Schematics of the SESAM-based linear mode-locked cavity.

The RF analyser measurement showed a stable harmonic frequency corresponding to an RR of 8.4 MHz and over 65 dB optical signal-to-noise ratio (OSNR), which initiated at a threshold pump power of 200 mW as depicted in Fig. 5.11.

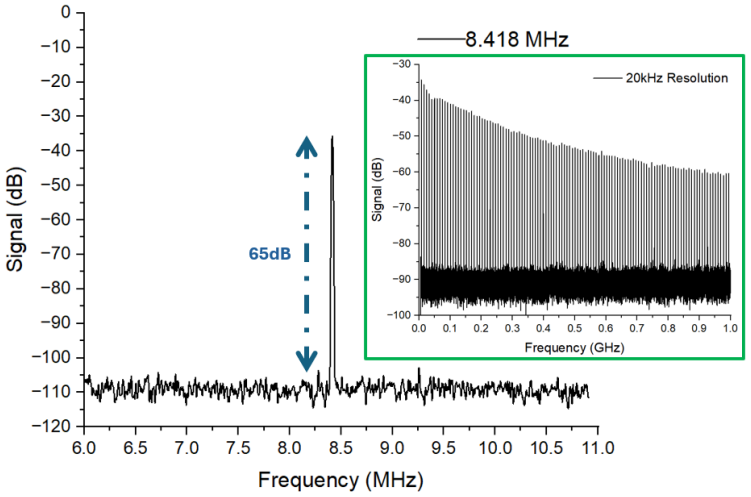

FIGURE 5.11: 1 kHz span range of an RF analyser showing a peak at 8.4 MHz; Inset: 1 GHz scan range.

Successfully lowering the mode-locking threshold and increasing the slope efficiency to 2.1 % courtesy of the longer gain fibre as presented in Fig. 5.12(b). The generated output spectrum is shown in Fig. 5.12(a), which is similar to the observations made in

previous experiments (Fig. 5.6(a)). The generated spectral bandwidth increased with pump power, and a single pulse operation was tolerable up to 2 W of pump power, outputting an average of 38 mW.

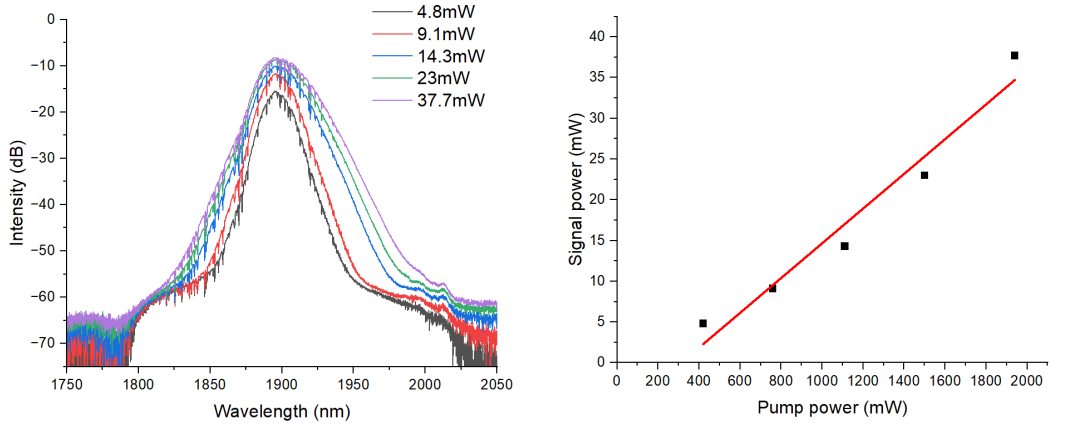

(a) Spectrum of NLS at different pump power.

(b) Cavity output power at different pump powers.

FIGURE 5.12: Results of the mode-locked cavity.

The autocorrelator measurements seen in Fig. 5.13(a) were taken to verify the nature of the soliton generated (whether it is an NLP or an SPS). At 1 W of pump power, the autocorrelator showed a 300 fs peak with a large pedestal being generated that exceeds the scan range of the autocorrelator. Therefore, a fast photodiode and oscilloscope were used to measure the pulse duration, which was shown to increase with pump power as seen in Fig. 5.13(b). At 1 W, the pulse duration was ≈100 ps. The changing of the pulse spectrally and temporally is a key indicator of an NLP [94]. Moreover, the large pedestal on the ACF shows the envelope of the pulses spread in time, where the central peak reveals the average duration of these pulses [95].

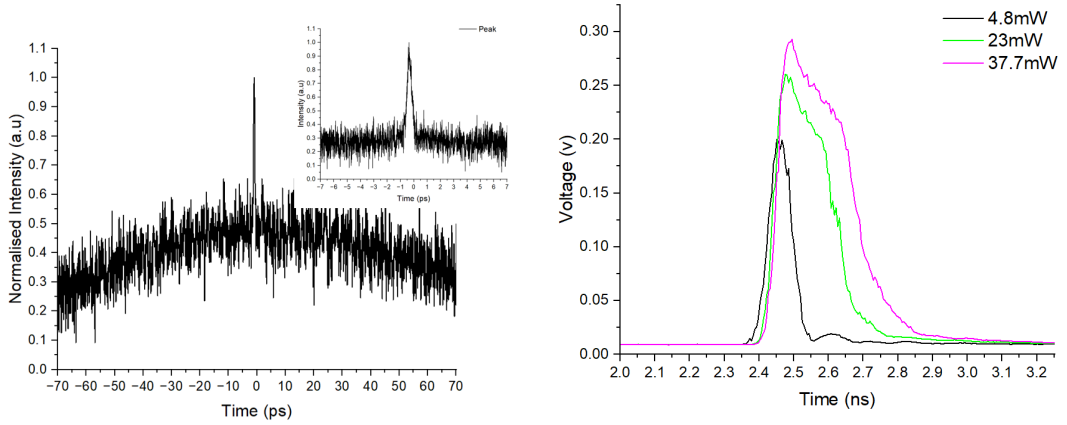

(a) autocorrelation measurement at 1 W pump power; inset short scan range showing a 300 fs peak.

(b) Oscilloscope measurement showing pulse width at different powers.

FIGURE 5.13: Temporal measurements of noise-like pulses.

A noteworthy phenomenon was observed with this NLP mode-locking, which was in the initiation of the pulsing, long-term stability and resistance to environmental factors.

Stable mode-locking was initiated from no signal by tapping the fibre, unlike traditional mode-locking, where noisy pulsing is observed and by fine-tuning the PC, a stable state is reached. Any further tapping of the fibre, changing of the PC position or any mechanical or thermal change to the system did not affect the stable pulsing operation despite being made from all non-PM components. Moreover, the long-term stability of the system was measured where spectral measurements were taken every 10 mins for over an hour while continuously monitoring the output power as demonstrated in Fig. 5.14. A drop in power of less than 0.05 mW of the output was seen across the duration of the recording. The observed stability rivals fully PM systems, which opens the door for many applications that require a high-power, compact and stable source.

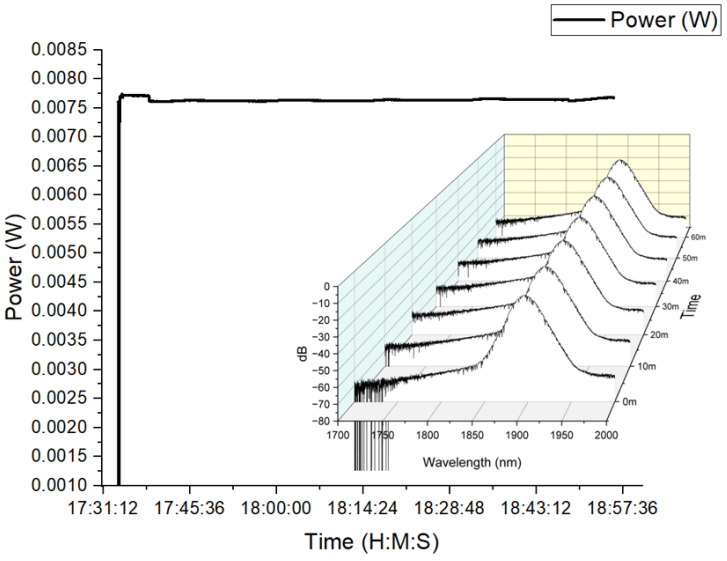

FIGURE 5.14: Power stability of the laser over 1.5 h; inset spectral stability every 10 mins for an hour.

5.3 Fibre spectral filter

Although increasing the TDF length enhanced the gain at shorter wavelengths, it also caused a shift of the gain peak toward longer wavelengths, as shown in Fig. 5.9. Consequently, mode-locking centred around 1900 nm was achieved as shown in Fig. 5.12(a). Therefore, a short-pass filter was proposed by inducing bending losses on a "weakly-guiding" (Low V-number) SMF to suppress the long wavelength emission while taking advantage of the increased gain at the shorter wavelength.

To achieve this, bending losses were purposely introduced in a 1m length of a DCF filter (Corning, optical fibre 003-H5T6 1 10). A supercontinuum source (YSL Photonics) was used to characterise the effects of bending on the wavelength transmission as seen in Fig. 5.15. Whereas the bending radius of the DCF determined the cutoff wavelength, the number of coils influenced the steepness of the cutoff edge; increasing the number

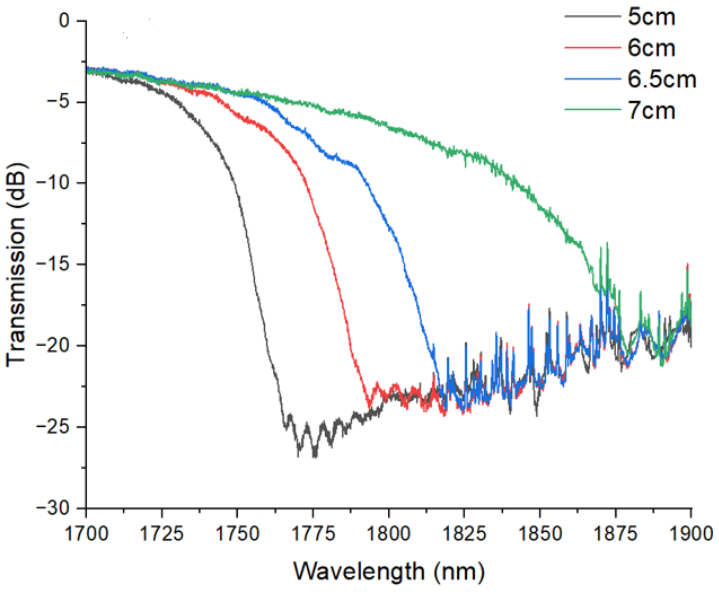

FIGURE 5.15: Spectral transmission of the bending-induced low-pass filter at different bending radii; 5 cm (black), 6 cm (red), 6.5 cm (blue) and 7 cm (green).

of coils resulted in a steeper edge due to the cumulative bending losses. Therefore, by reducing the bending radius of the DCF from 7 cm to 5 cm, the cut-off emission wavelength is shifted from ≈1875 nm to 1760 nm and up to ≈20 dB of extinction ratio of the longer wavelengths with a 5 cm radius looped 3 times. Finally, due to the core mismatch between the DCF filter and SMF, a 1.5 dB loss was measured from splicing the two fibres.

5.4 Ring CNT cavity

Based on the previously mentioned SESAM-based mode-locking experiments, stable broadband pulse operation seems to be unachievable for wavelengths below 1750 nm. On the other hand, the CNT sample used in chapters 3, 4 showed broadband width compatibility. Therefore, a change in strategy was taken, and a deviation from the use of the SESAM in conjunction with the low-pass filter was made.

Fig. 5.16 shows the ML laser oscillator consisting of all-fiberised components with SMF28e fibre pigtails. An OC (THORLABS, TW2000R3A2B) with a 25% output is used. Two inline PCs (THORLABS, CPC250) for tuning the polarisation to achieve a stable ML operation. An ISO (OPTOSUN, PIIS-1750-0-1-1-5) to ensure the unidirectional flow of light. A single-walled CNT (SWNT) sample was placed between two patch cords, providing saturable absorption. The cavity was core pumped at 1560 nm from an in-house built EDFA by using a WDM (OPTOSUN, FWDM-1-1750-0-1-1-5) to couple the pump light into the gain fibre and extract any residual pump at the output of the gain fibre. Two 35 cm sections of TDF (OFS, TmDF200) are used, separated by a short

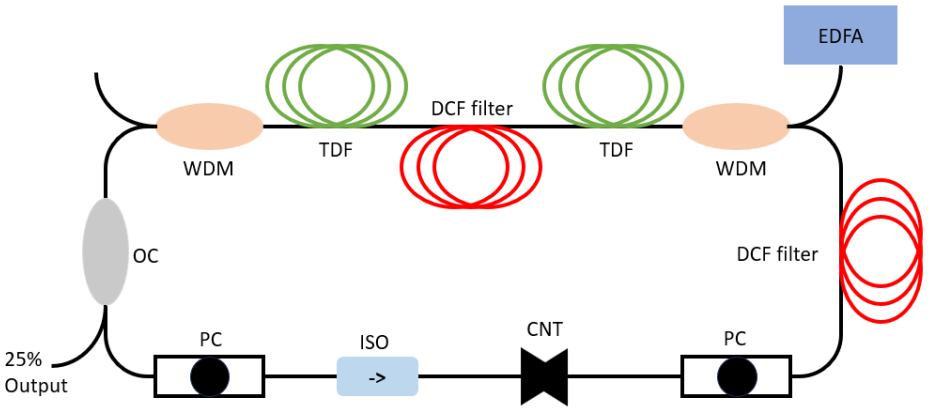

FIGURE 5.16: Schematics of the all-fibre mode lock laser. CNT: carbon nanotube; ISO: Isolator; PC: polarisation controller.

pass filter induced by bending a 1 m length of DCF (Corning, optical fibre 003-H5T6 1 10). Later, another 1 m section of a DCF filter was used to tune the dispersion in the cavity to resolve Kelly's sidebands. The total length of the combined SMFs is 7.2 m.

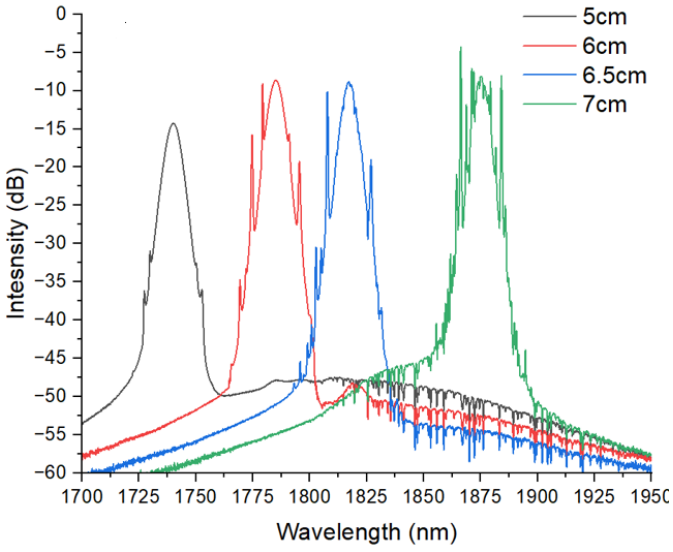

FIGURE 5.17: CS spectrum output at different 1 m long DCF Bending radii; 5 cm (black), 6 cm (red), 6.5 cm (blue), 7 cm (green).

The capabilities of the DCF (Fig. 5.15) were initially tested by adding a 1 m section to the cavity. The effect of changing the bending radius on the model-locking state was carried out while maintaining a fixed input pump power. As shown in Fig. 5.17, a CS at 1860 nm is generated at 7 cm of bending radius. By reducing the bending radius further, mode-locking states were observed, producing 1815 nm, 1775 nm and 1740 nm CS at bending radii of 6.5 cm, 6 cm, and 5 cm, respectively. Reducing the bending radius further resulted in no stable ML output even at increased pump power; thus, a minimum radius of 5 cm was utilised to achieve the shortest wavelength operation from this cavity.

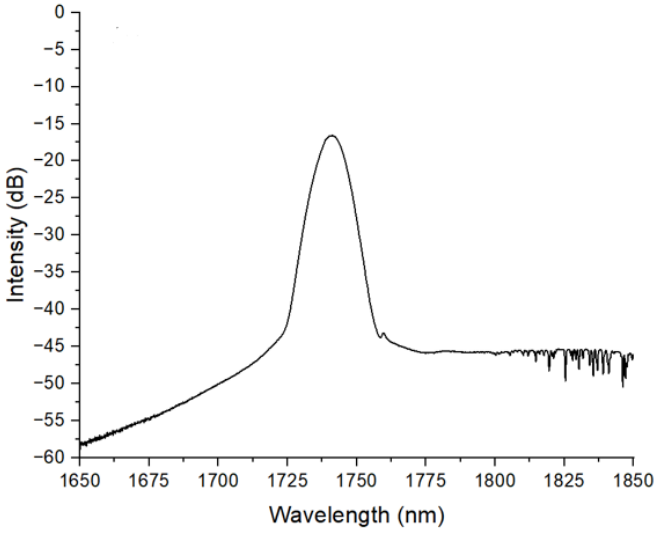

FIGURE 5.18: Stretched pulse mode-locked spectrum at 1740 nm and 17 nm 10 dB bandwidth.

The addition of 1 m DCF (3 loops of 5cm radius) shifted the net dispersion closer to zero and shifted the ML operation from outputting CS to SPS, resolving Kelly's sidebands, making it easier to amplify and compress the pulse. The resultant spectrum is 1740 nm with a 10 dB bandwidth of 17 nm as shown in Fig. 5.18. When compressed, for a chirped pulse duration at the output of the cavity of 2.4 ps, a pulse duration of 320 fs (assuming a $Sech^2$ profile) was attained as represented by the ACF in Fig. 5.19(a) and 5.19(b), respectively.

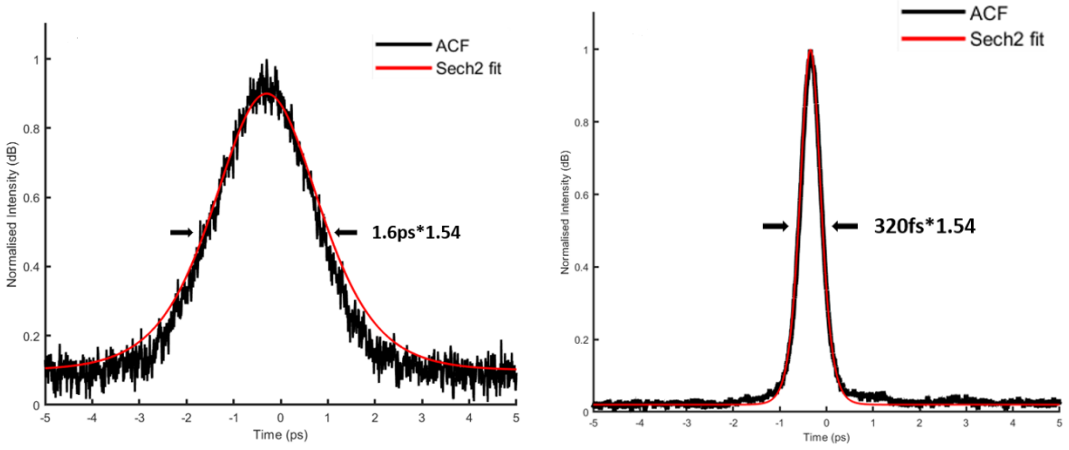

(a) Chirped pulse output ACF trace (black) and $Sech^2$ fitting (red).

(b) Compressed pulse ACF trace (black) and $Sech^2$ fitting (red).

FIGURE 5.19: Mode-locked laser pulse measurements.

The total cavity length resulted in a fundamental RR of 20.66 MHz, which was verified by an RF spectrum analyser as seen in Fig. 5.20. Moreover, the RF measurement shows a stable operation and over 75 dB of OSNR at the fundamental RR. Finally, the cavity output power was measured to be 3.7 mW with an input pump power of 500 mW.

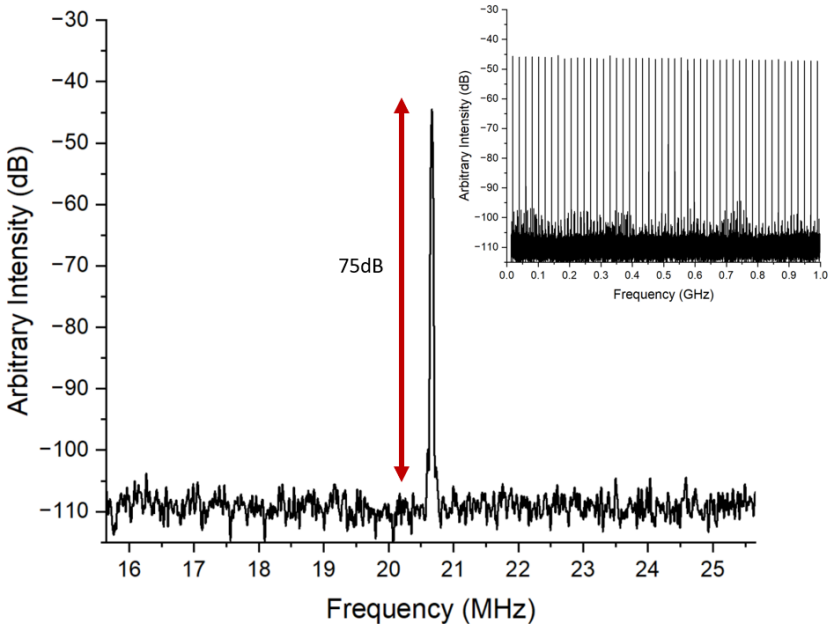

FIGURE 5.20: RF 10 MHz scan range showing over 75 dB OSNR at the fundamental RR of 20.66 MHz; inset: 1 GHz RF scan range.

Since no data is provided on the dispersion of this DCF filter at 1750 nm, the laser output was used to characterise the dispersion of the fibre by fixing the ML state and power by varying the length of the DCF at the output of the laser and feeding the output to a grating pair compressor as shown in Fig. 5.21.

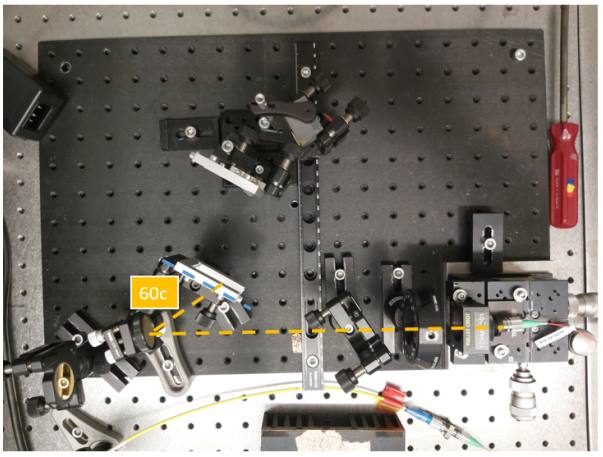

FIGURE 5.21: Transmission grating compressor set-up.

The distance between the gratings needed to achieve the same (minimum) compressed pulse duration is measured, and the results are shown in Fig. 5.22. The GVD of the fibre can be estimated by knowing the angle, grating distance, and properties of the two transmission gratings used to compress the optical pulse (PCG-550/2000-930, Ibsen Photonics). The results of the variation of the change in fibre length with grating distance are shown in Fig. 5.22, and the calculations reveal that a GVD of the DCF at

1750 nm is approximately 0.096 ps^2/m. Therefore, the net GDD of -0.146 ps^2 in the cavity was deduced.

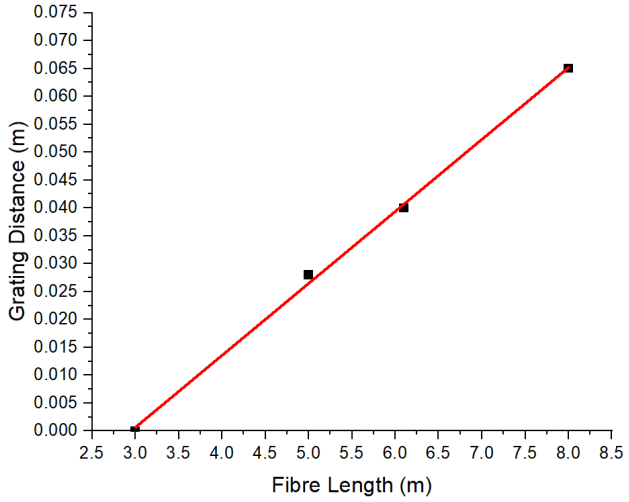

FIGURE 5.22: Change of the compressor gratings separation distance with DCF Length.

5.5 Pulse amplification

The amplifier schematics seen in Fig. 5.23 were built in collaboration with Mr. Matthew Gerard. An ISO was added at the output to prevent any light from flowing back to the cavity, and a 1% tap was used for monitoring the mode-locking. A section of 10 m of UHNA4 DCF was used at the input of the amplifier as a pre-stretcher for CPA instead of the DCF filter to lower the splicing loss to SMF28e to 0.5 dB per splice. Bi-directional pumping was employed by utilising two WDMs and a 3 dB splitter to couple the pump light from a single in-house built EDFA to two sections of TDFs (TmDF200, OFS), which had lengths of 1 m and 0.6 m, respectively. In the 1 m section, over 87% of pump absorption was achieved in a single-pass operation. A 2 m DCF filter with 5 loops of 5.5 cm bending radius was spliced in between the TDF sections. The parameters of the DCF filter were chosen based on the characterisation discussed in section. 5.3. This resulted in over 28 dB suppression of the peak ASE at the longer wavelengths.

The amplifier was designed to maximise gain at short wavelengths by implementing several key features. The first feature is the use of a short-pass DCF filter in front of the longer section of the TDF. This configuration leads to benefiting from the higher gain from the longer TDF length while suppressing the increased ASE associated with longer TDF lengths. Additionally, a shorter TDF length was used to further increase the gain at the short wavelengths with minimal ASE. Moreover, the use of two WDMs along with a bi-directional pumping scheme offers several other advantages. It enhances

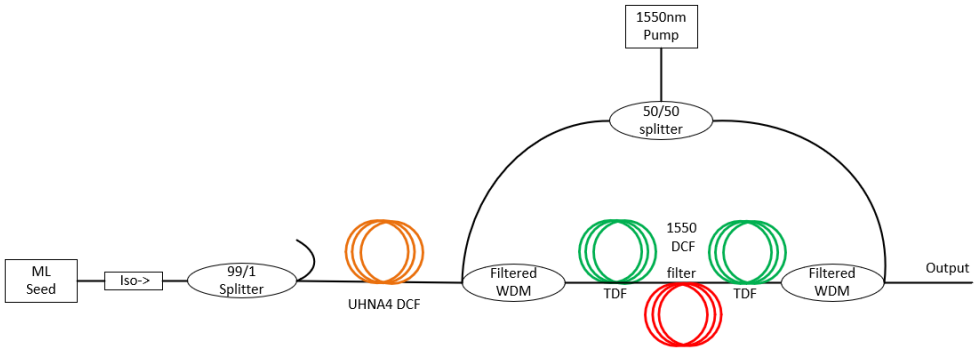

FIGURE 5.23: Schematics of the Tm-doped fibre amplifier optimised for the short wavelength.

pump absorption, thereby increasing pumping efficiency while filtering out any unabsorbed residual pump energy that accompanies the signal. Most importantly, the bi-directional pumping ensures effective pump wavelength absorption, which improves the transparency of the TDF ions at the short wavelength emission of thulium. Thus, minimising the effects of reabsorption while maximising the gain at the laser wavelength. The result of this implementation was a slope efficiency of 12% was measured, and a maximum signal output power of 273 mW was measured at the highest available pump power of 2.25 W, as shown in Fig. 5.24. Therefore, a maximum pulse energy of 13.2 nJ was achieved.

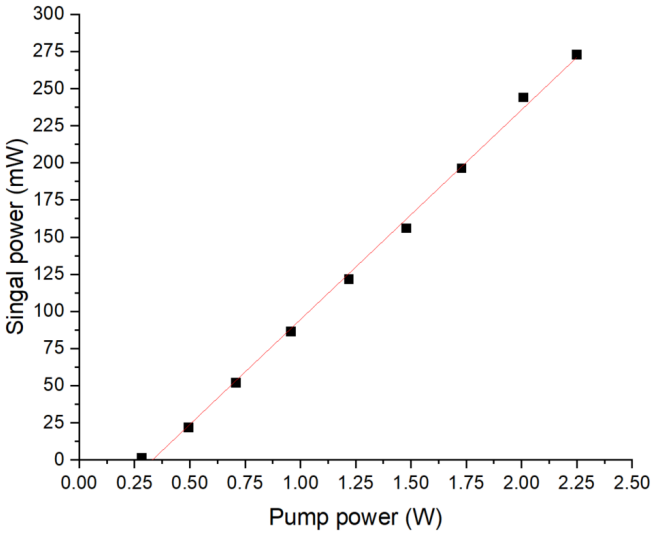

FIGURE 5.24: Amplifier output power at different pump powers.

Furthermore, the amplified pulse spectra were characterised and plotted as seen in Fig. 5.25(a). Minimal distortion due to nonlinearity is observed at high powers, akin to the addition of the long DCF pre-stretcher as shown in Fig. 5.25(b). However, a dip is observed 15 dB below the signal peak at the long wavelength side of the spectrum, which is created as a result of a slight mismatch in the bending diameter of the short pass filter in the amplifier, compared to the ML source intentionally made to avoid losses

at the laser wavelength. Furthermore, the ASE from the second TDF was shown to be a further ≈12 dB below the ASE level of the first TDF.

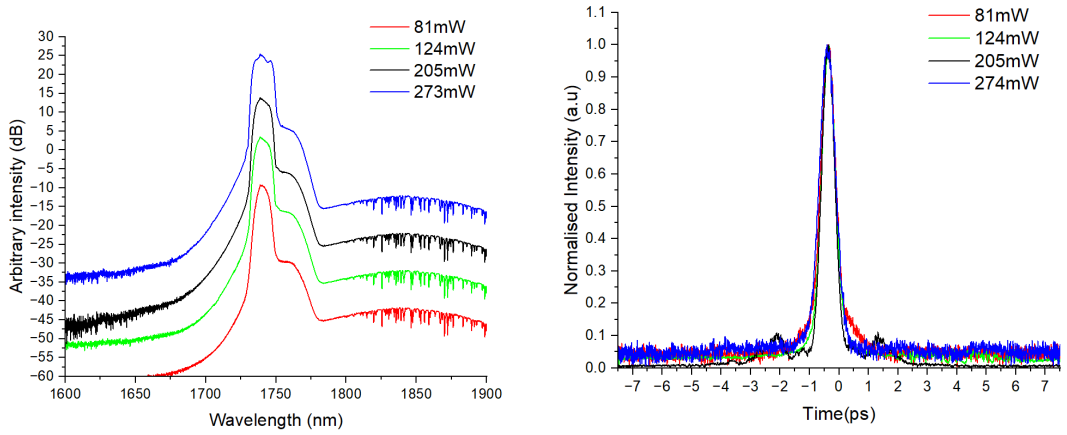

(a) Amplified spectrum output.

(b) Compressed pulse ACF trace.

FIGURE 5.25: Amplifier output power at different powers; 81 mW (red), 124 mW (green), 205 mW (black), 273 mW (blue).

A deeper insight into the amplified pulse spectrum in the linear scale as seen in Fig. 5.26(a), reveals that this amplification method results in 98% of the total amplified pulse energy contained within the 15 dB bandwidth. In addition, the 3 dB bandwidth of the amplified signal is 10 nm, which corresponds to a TFL pulse duration of ≈320 fs assuming a $Sech^2$ Pulse profile. Furthermore, a close inspection of the autocorrelation of the pulses with the highest energy, as seen in Fig. 5.26(b), shows a 366 fs minimum compressed pulse duration with a good $Sech^2$ fit. This equates to a peak power of 36 kW being generated from a single amplifier at 1740 nm.

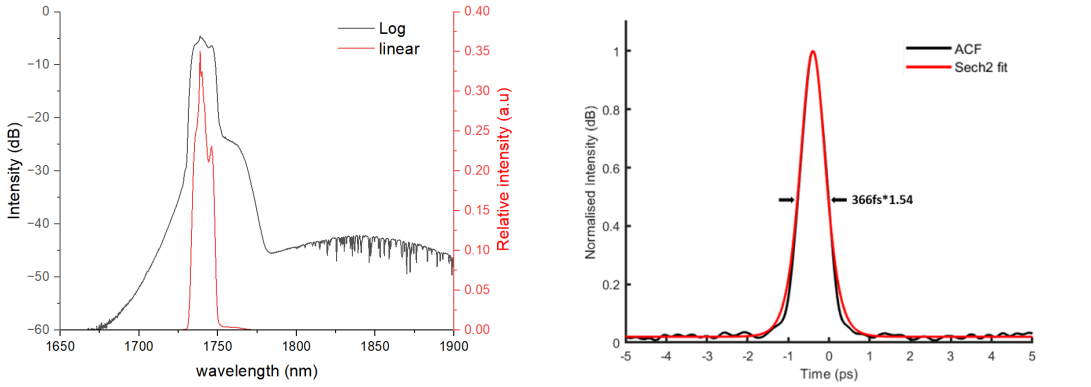

(a) Log scale (black) and linear scale (red) spectrum.

(b) Compressed pulse ACF trace (black) and $Sech^2$ fitting (red).

FIGURE 5.26: Amplified spectrum at 273 mW.

To summarise, a tunable seed and amplifier optimised for the short wavelength amplification were built generating high energy pulse at wavelength as low as 1740 nm realised by short pass filter of a bending fibre. High quality pulse compression with low pedestal

pulse was achieved by managing the cavity dispersion to generate SPS and suppressing the nonlinearities in the amplifier via the implementation of CPA.

Chapter 6

Beyond mode-locking: ultrafast pulse generation

6.1 Background and introduction

The work thus far has revolved around the generation of ultrafast pulses from ML lasers, whereby balancing the dispersion, nonlinearity, cavity length, and gain dynamics enables a pulse with a fixed bandwidth, RR, and energy to be generated. Changing these parameters requires the use of external systems such as nonlinear broadening, modulators or amplifiers, respectively, as demonstrated in previous chapters. This is both a time and component-consuming process producing a laser cavity that is appropriate for a limited number of applications and is often sensitive to environmental factors, which limit its stability [59].

Gain-switched laser diode are commonly used for communication, optical storage, multiphoton and time-resolved spectroscopy [96]. They offer answers to many of the problems associated with ML fibre lasers since they are a single low-cost optical component with a small footprint relative to ML lasers. Pulse parameters such as energy, RR and wavelength can be controlled electronically alongside the operational stability, which is controlled by managing the temperature of the laser diode. However, laser diodes suffer from intra-pulse amplitude and phase noise since the pulses are generated from noise by a slower process [97], which limits the applications that they can be used for unless techniques such as self-seeding and external cavity injections to reduce pulse-to-pulse fluctuation, are implemented [98]. For multiphoton imaging applications, these fluctuations don't pose a problem, and the electronically tunable RR means that the scanning speed of the microscope can be synchronised with the pulse output. State-of-the-art laser diode systems can only generate a chirped pulses with durations of $<$10 ps with a narrow spectral bandwidth. This, alongside the degeneration of the side mode suppression ratio [98] that results in a temporal pedestal, makes achieving a TFL compressed

pulse duration challenging, and limits their usefulness in ultrafast pulse generation applications.

To understand the operational principles of gain-switching in laser diodes, firstly, we need to consider that the change in the current applied to the laser diode during gain-switching causes a change in the carrier density affecting the effective refractive index and thus cavity properties, which determines the chirp of the pulse generated. The change in the carrier density erupts at the start of the pulse, leading to relaxation oscillations, that result in an up chirp at the start of the pulse, followed by a nonlinear down chirp towards the end [96]. This relaxation period adds a quasi-CW (steady state) component to the gain switch pulse, which, in combination with the nonlinear chirp, results in the temporal pedestal. The key factors to consider when operating a GSLD are that the over-pumping (magnitude of the voltage applied) of the laser diode results in a broader bandwidth signal and a steeper chirp, whereas the period in which the electrical pulse is applied controls the optical pulse width in time by generating more CW components in the pulse. The former needs to be maximised while the latter needs to be minimised to achieve a short compressed pulse output.

Furthermore, two key techniques are needed to convert and compress GSLD pulses to femtosecond pulses. The first is to broaden the spectrum to reduce the TFL pulse duration, and the second is to remove the nonlinear chirp and pedestal. The former can be achieved by imposing spectral broadening in the pulse via a nonlinear process such as SPM. Therefore, the peak powers of the laser diode must first cross the threshold value for nonlinear spectral broadening. The latter can be achieved by either a spectral filter (SF) or an SA to keep the linear chirp part of the pulse and remove both the nonlinear phase and steady-state components. The advantage of using an SA is the transmission of the high-intensity part of the pulse while suppressing/absorbing the low-intensity pedestal.

Fast artificial SA, such as NPR or NALM, possess an oscillatory response that can shape the pulse over time, where material SA has a low power operating threshold, thermal stability issues, and relatively low modulation depth. Proposing a MR as a pulse cleaning method overcomes many of the challenges associated with other SAs, since it provides a strong and uniform suppression of the pedestal. The operating principle of an MR is based on the peak power, which is dependent on SPM-induced spectral broadening, so the newly generated spectral component corresponds to the pulse peak. By applying a SF to select these newly generated components, a robust artificial SA effect is achieved [59].

As for the compression methods, after cleaning the pulse chirp, the pulse bandwidth needs to be sufficiently broad to achieve a femtosecond pulse regime. After this, conventional compression methods such as a grating pair or fibre compressors can be used. However, using a fibre compressor may result in further nonlinearity, which may affect

the output pulse depending on the dispersion regime. For example, for positive dispersion, if gain is present, the pulse forms a parabolic pulse shape without a nonlinear phase, and pulse compression is near TFL as demonstrated by W. Fu et.al [59]. On the other hand, using an anomalous dispersion fibre for pulse compression, the presence of strong nonlinearity may result in optical wave breaking that will result in the break-up of the pulse into multiple pulses as encountered in chapter 4, unless the dispersion and nonlinearity are balanced, such that a soliton is formed. If a fundamental soliton is formed, the pulse propagates in a near TFL state at the cost of the pulse energy in the order of pico-joules [59]. In work by *T. Heuermann et al.*, 250 nJ, 50 fs pulses were produced in a thulium fibre amplifier using an adiabatic-compression method that forms CS for pulse compression. Furthermore, higher-order solitons can also be generated and utilised for pulse compression. They may result in higher pulse energy but require careful management of the fibre length due to the periodic evolution of the pulse from a single compressed state to a higher-order chirped state [99].

In this chapter, a GSLD is employed to generate ultrafast pulses. The process begins with broadening the spectrum of the pulse, followed by the use of an offset filter. This creates a MR condition that acts as an SA for pulse cleaning. Subsequently, various compression regimes and spectral filtering methods are explored. The results showed that the addition of a bandpass filter was essential for removing the temporal pedestal. A two-stage compression method composed of an initial linear part followed by nonlinear compression in an amplifier increased the pulse bandwidth while simultaneously amplifying and compressing the pulse by a soliton effect, generating a high-energy femtosecond pulse. The results shown in section 6.2.4.5 were published in the Optics Letters journal [100].

6.2 System Building

6.2.1 Gain-switched Laser diode

A fibre-coupled GSLD (EP1854 Eblana Photonics) was used to seed the system. Several operating parameters and pulse settings were tested and compared to CW operation as shown in Fig. 6.1. The voltage bias was set just below the pumping threshold to 20 mV, and the magnitude of the electrical pulse was set to 3 V. The temperature can be used to control the emission wavelength of the LD, where the wavelength would decrease with decreasing temperature. A wavelength of 1875 nm was tuned by setting the temperature to 20 ^oC. The electrical pulse width was set to an optimum value of 250 ps since increasing this further would increase the steady-state component, while reducing it would reduce the amplitude of the optical pulse. Maximising the pulse peak power from amplification was limited by the minimum RR of the pulse generator, which

was set to a minimum value of 32 MHz. The resultant average power of the GSLD using these settings was measured to be 12.3 μW.

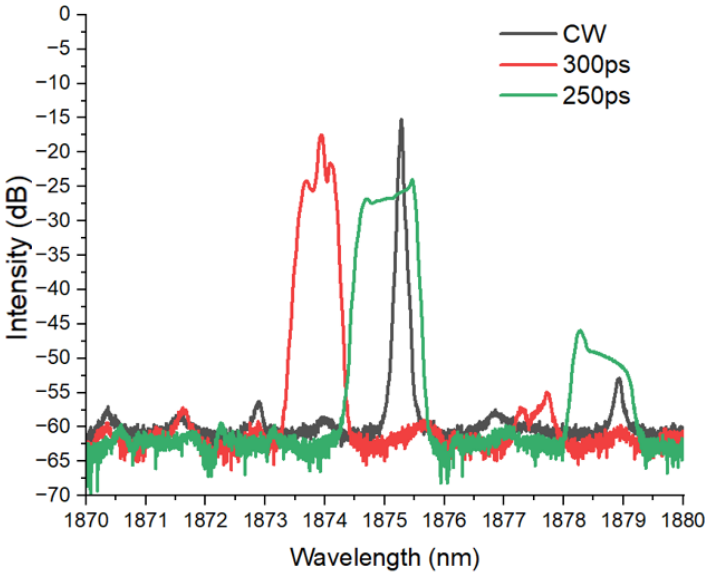

FIGURE 6.1: Laser diode spectral output at various operating conditions.

Using a fast photodiode (10GHz-InGaAs ET-5000F, EOT) and oscilloscope (10GHz-CSA 808A, Tektronix), the output optical pulse duration was measured to be 59 ps as shown in Fig. 6.2(a). Since the measured data coincides with the limit of the photodiode data sheet, stating a 28 ps rise and fall time, the optical pulse was amplified to verify the measured pulse duration against an autocorrelator. This has a faster scan rate, revealing an ACF width of 56 ps as shown in Fig. 6.2(b), which is shorter than the oscilloscope measurement.

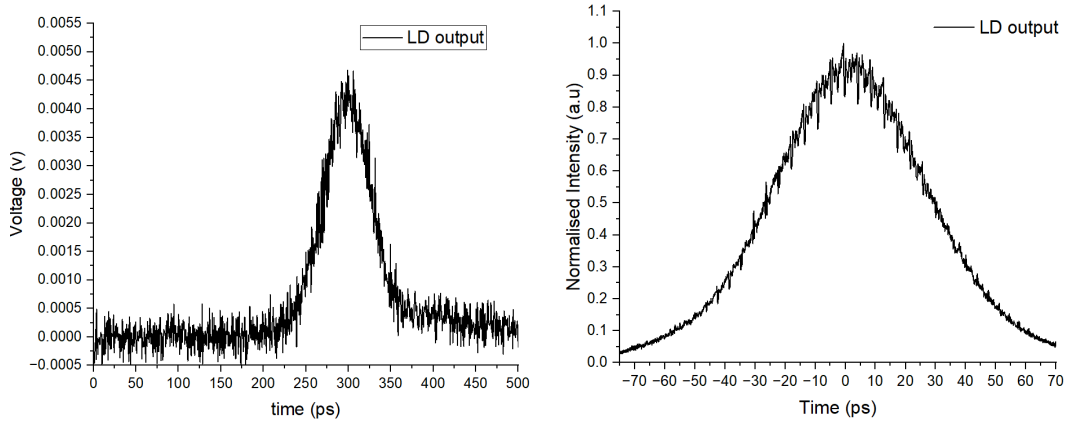

(a) Oscilloscope measurement of the LD output optical pulse.

(b) Autocorrelation measurement of the LD output optical pulse.

FIGURE 6.2: Temporal analysis of the laser diode output.

To compress the pulse, calculations were carried out based on the measured 10dB pulse bandwidth of the pulse using the following formula [101]:

$$\tau(z)^2 = \tau_0^2 \left(1 + \frac{z^2}{z_c^2}\right) \tag{6.1}$$

$$\text{where,} \quad z_c = \frac{\tau_0^2}{2\beta_2} \tag{6.2}$$

Where τ is the pulse width, τ_0 is the TFL pulse width, z is the propagation distance, z_c is the chirp length, and β_2 is the GVD of the fibre. This revealed a GDD value of ≈180 ps^2 required to compress the pulses to the TFL duration of 3.7 ps. This equates to an SMF length of ≈4 km.

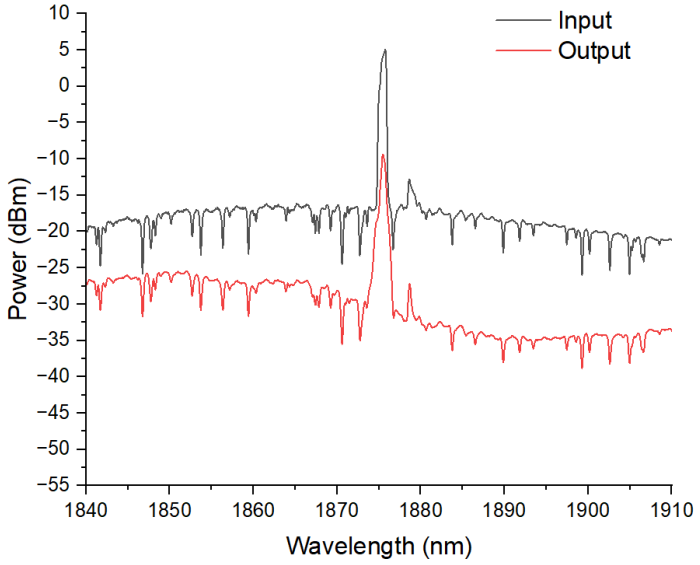

FIGURE 6.3: Input (black) and output (red) spectrum after propagating 1km of SMF.

However, the required length of the fibre was not available. Instead, several long sections of SMF (that were available), 2 km, 1.35 km and 1 km, were used to observe the change of pulse width and the GDD. The pulse was amplified after the fibre compressor to enable measurement in an autocorrelator. Despite no nonlinearity in the fibre compressor, as indicated by the unchanged input and output spectrums shown in Fig. 6.3, the compressed pulses showed the formation of a large pedestal that started as a multi-peak after propagating through a 1km fibre. Then increased with increased fibre length while maintaining a constant central peak ACF width of ≈4.9 ps. This confirmed the original hypothesis of having a nonlinear chirp component as shown in Fig. 6.4.

The long length required to compress the pulses comes from the short pulse bandwidths and is impractical due not only to the cost of fibre but also the compactness, propagation losses and nonlinearities that arise from long propagation distances. A nonlinear process is required to change the output spectrum of the pulses since it is not possible to achieve

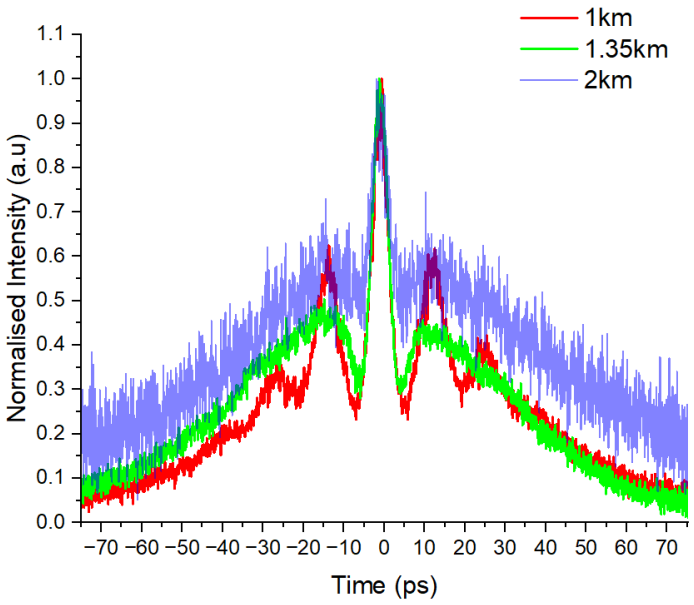

FIGURE 6.4: Autocorrelation measurement of the compressed pulses after propagation of different SMF lengths; 2 km (blue), 1.35 km (green) and 1 km (red).

the TFL pulse duration by directly compressing the GSLD pulse, and the long fibre requirement to observe any changes in the pulse shape.

6.2.2 Amplifiers

A fibre amplifier was constructed to enhance peak power beyond the nonlinear threshold, thus broadening the spectrum and shortening the fibre length needed to observe the desired effects. As shown in Fig. 6.5, a WDM in the first amplification stage was used to core pump a 90 cm in-house fabricated single-mode TDF, followed by an ISO preventing backwards reflection.

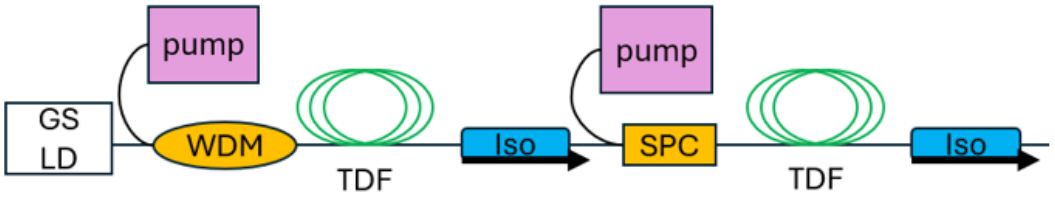

FIGURE 6.5: First two amplification stages schematics; inset functional schematics. GSLD: Gain-switched laser diode; WDM. Wave division multiplexer: TDF(A), Tm-doped fibre (amplifier), ISO: Isolator; SPC: Signal pump combiner.

An purpose built EDFA (seeded at a wavelength of 1565 nm), achieving a maximum output of 1.8 W was used to pump the first amplifier resulting in a maximum output

signal power of 75 mW, with a threshold for amplification occurring at a pump power of 1.1 W. This resulted in a lasing efficiency of ≈ 10%, as shown in Fig. 6.6(a). The poor slope efficiency was due to the low duty cycle of the signal pulse train. However, no parasitic lasing was observed in the spectrum, a high OSNR of 27 dB was attained at the maximum power, and a low residual pump power of 45 dB below the signal power was measured as seen in Fig. 6.6(b).

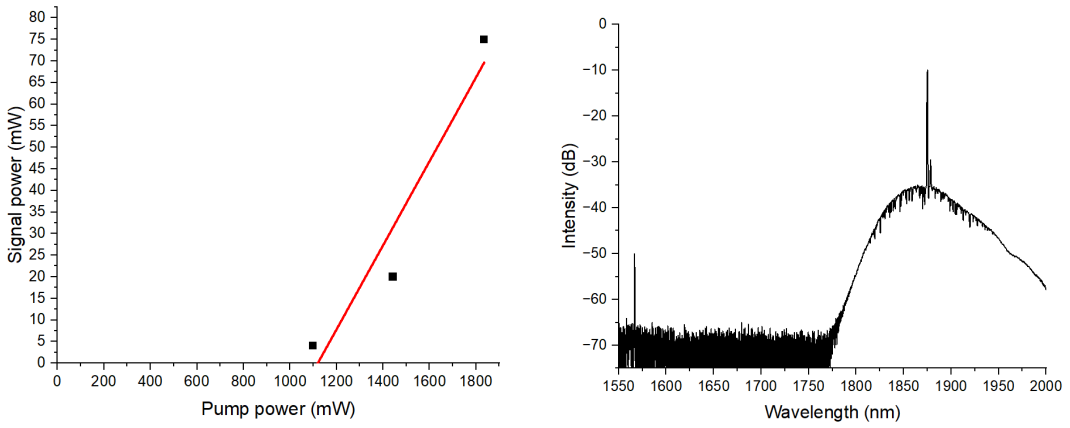

(a) first stage amplifier signal power at different pump power.

(b) output spectrum of the amplified signal at the highest pump power.

FIGURE 6.6: First stage amplifier output.

Following the amplified signal power, an 8 m HNF (HN1550) was used to broaden the GSLD spectrum. This showed significant spectral broadening in the previous experiment (see chapter 4). A 3 dB splice loss in the power was measured due to a mismatch between the core sizes of the HNF and SMF. The output spectrum also showed no obvious change compared to the input. Therefore, another amplification stage was needed.

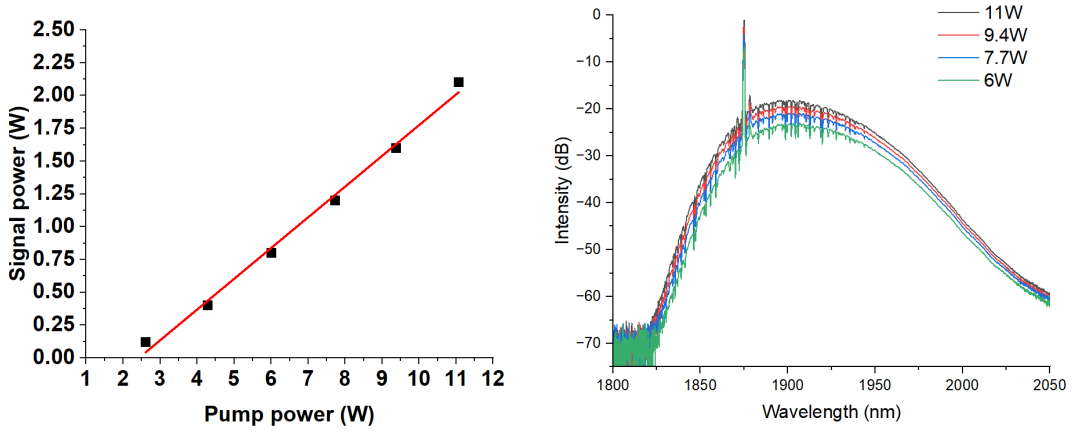

(a) Second stage amplifier at different pump power.

(b) Output spectrum of the amplified signal at increasing pump power.

FIGURE 6.7: Second stage amplifier output.

The second stage amplifier, as shown in Fig. 6.5, comprised a 1.6 m double-cladding single-mode Tm-doped fibre (SM-TDF-10P/130-M, Coherent) that was cladding-pumped

by a 790 nm Laser diode (LD, e03.0150793105 nlight), which was coupled in using a signal pump combiner (SPC, lightcomm) followed by another ISO. A low-index coating polymer was used to cover the input splice point at the input of the double-cladding gain fibre to ensure the pump light propagates in the cladding, while the output splice point was covered with a high-index polymer coating to ensure any residual pump power escaped, thus filtering the pump power from the amplified signal output.

A 23% slope efficiency was achieved after amplification, attaining a 2.1 W maximum average power at a pump power of 11 W as seen in Fig. 6.7(a). The total energy in the main peak of the pulse was found to be 43.2% by analysing the spectrum in the linear scale, leading to maximum peak powers of 475 W. The OSNR was reduced to 18 dB at the highest output power. The increased ASE levels are likely attributed to a combination of having multiple stages of amplification, low duty cycle, the high doping concentrations associated with cladding pumped fibres and the high input pump powers [102]. Amplification was carried out successfully while avoiding any spectral broadening as a result of the increased peak powers, as seen from the Fig. 6.7(b).

6.2.3 HNFs

For short pulse generation the pulse spectrum needs to be broadened to reduce the TFL pulse duration and to clean the pulse chirp by selecting linear components of the spectrum for compression. Therefore, to elicit the spectral broadening, a HNF was spliced at the output of the fibre amplifier as shown in Fig. 6.8. The theory discussed in equation 2.16 shows that the nonlinear length L_{NL} is proportional to the core size and inversely proportional to the peak power. The peak powers were fixed to the maximum achievable level from the amplifiers used. Therefore, effects from small core sizes and long fibre lengths were prioritised in testing different fibres for spectral broadening. In this section, the results from characterising several fibres for SPM are described.

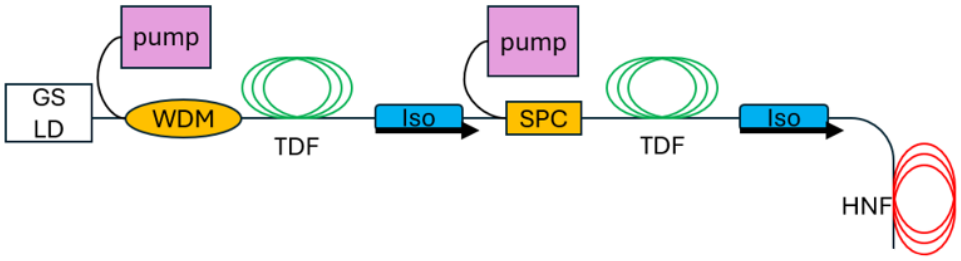

FIGURE 6.8: First two amplification stages schematics; inset functional schematics. HNF: Highly nonlinear fibre.

6.2.3.1 HN1550

As presented in Fig. 6.9, the results measured at the output of HNF did not display any SPM but rather two side peaks 4 nm away from the central peak, associated with FWM [103]. A phase-matching condition is required for FWM to manifest (see section 2.4.1.3). Based on the previous characterisation of this fibre, the near-zero dispersion at this wavelength is the most likely cause of phase matching. The peak powers achieved from the 2-stage amplification have overcome the nonlinear threshold; however, a different HNF with a dispersion coefficient shifted away from zero is needed for spectral broadening.

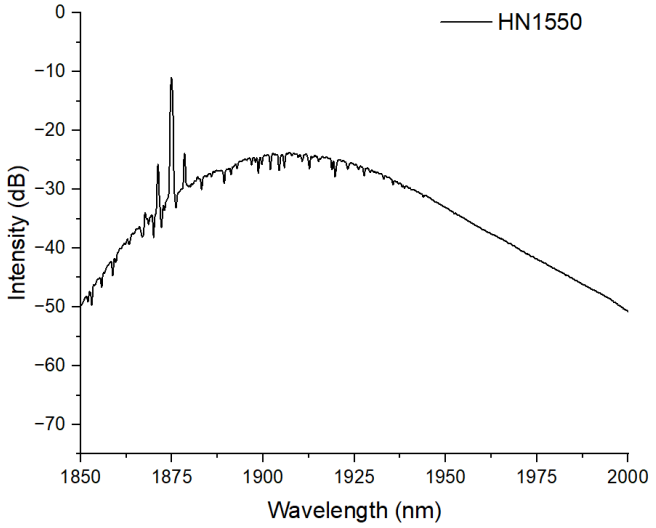

FIGURE 6.9: Output spectrum after 8 m of HN1550 at 2.1 W input power.

6.2.3.2 PM1550

A 300 m long piece of PM1550 fibre was tested next, having a similar value of GVD at the lasing wavelength and a fibre core diameter to SMF28e, with the added benefit of polarisation maintenance, thus minimising the deterioration of the pulse quality. To take advantage of the PM capabilities of the fibre, the input ISO was replaced with a fast-axis blocked PM-isolator emitting a linearly polarised light. A PC at the input of the ISO was used to optimise the transmitted power, which resulted in an overall 4 dB loss. Nonetheless, the HNF transmitted spectrum showed a successful increase of the 10 dB bandwidth of the pulse to 8 nm as seen in Fig. 6.10(a).

The ACF trace of the broadened pulse was also investigated. A 2.8 ps peak duration accompanied by a large pedestal spanning 75 ps was measured on the autocorrelator as seen in Fig. 6.10(b). The shape of the ACF resembles a NLS pulse, which indicates a pulse breakup due to modulation instability (MI) as a result of large nonlinearity in the

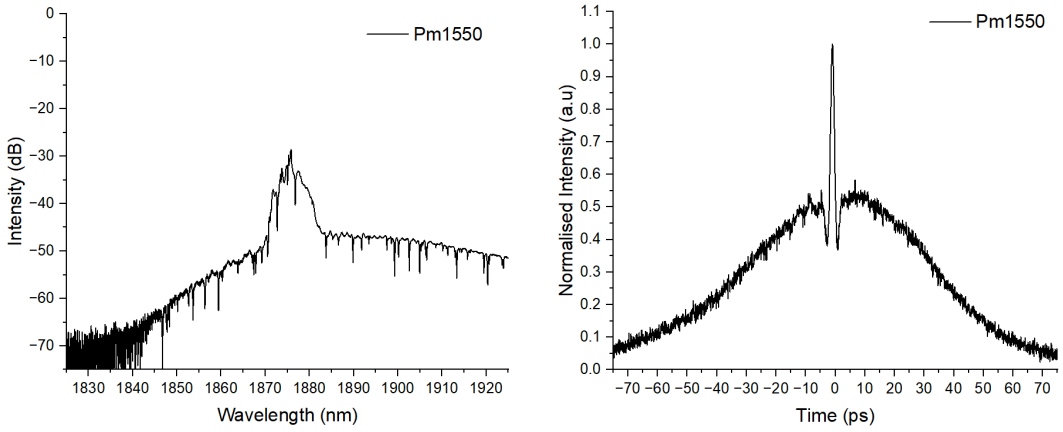

(a) Spectrum output of a 300 m Pm1550 fibre. (b) Corresponding autocorrelation measurement.

FIGURE 6.10: Output of PM1550 as HNF.

presence of anomalous dispersion in the fibre. Therefore, a normal dispersive fibre is required to achieve coherent pulse broadening.

6.2.3.3 PM2000D

To investigate the generation of coherent pulse broadening, a 50 m of PM2000D with a normal GVD at the lasing wavelength with a value of $\approx 0.095\ ps^2/m$, replaced the previously used PM1550 as HNF [104]. Although a shorter length of PM2000D fibre was used, the core size of the fibre was much smaller, measuring at 2.1 μm.

As presented in Fig. 6.11(a), nonlinearity was observed at the output of the fibre as evident from the spectral distortion that was measured by the OSA. Interestingly, the results showed two distinct features in the output spectrum. They were the FWM lines and the broadening of peaks present on the spectrum. The broadening due to SPM shows that fibre parameters and power levels exceed the threshold value. However, the FWM lines prove that there is a phase-matching condition being met despite the normal dispersion of the fibre. This is further supported by a larger separation gap between the central and side peaks of 24 nm.

From experience of using the PM2000D, it became apparent that the fibre has poor PM capability, especially at increased fibre length, due to irregularities in the manufacturing process, leading to the formation of an elliptical core. The effects can be mitigated by careful splicing recipes and fibre management (e.g environmentally, such as thermal or mechanical stress). This has also been observed by other research groups [69, 104]. With this information, it was suspected that the cause of phase matching was achieved due to the propagation of the pulse in a birefringent normal dispersion fibre offset to the principal axis of the fibre [103]. To test this theory, a PC was added at the input of the HNF to optimise the polarisation alignment to the principal axis of the fibre. The

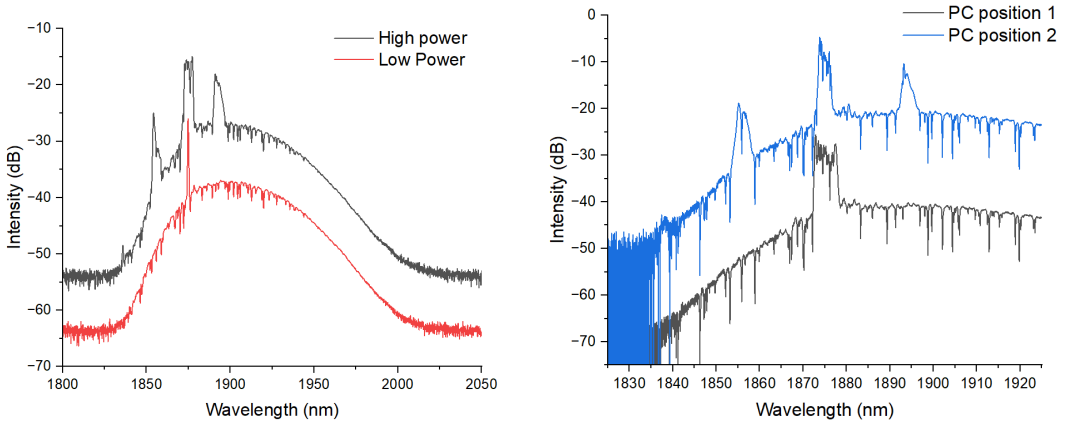

(a) Spectrum output of the PM2000D at low input power (red) and high amplifier power (black).

(b) Same input power at different PC (after the PM-isolator) orientations.

FIGURE 6.11: Output of PM2000D as HNF; offset by 20 dB for visualisation.

results proved that the output spectrum can switch from a "pure" SPM effect to an optimised/maximised FWM state as seen in Fig. 6.11(b).

A review of the literature revealed four different possibilities for FWM to occur in a birefringent fibre, two of which result from normal dispersion [103] (Table 2.3). To identify which of the effects caused the FWM, an experiment was set up by optimising the PC position for maximised FWM, then feeding the output of the fibre to a collimating lens into a free-space polariser. This was aligned to a focusing lens for collection by a large-core multimode fibre that is fed into an OSA for analysis as depicted in Fig. 6.12.

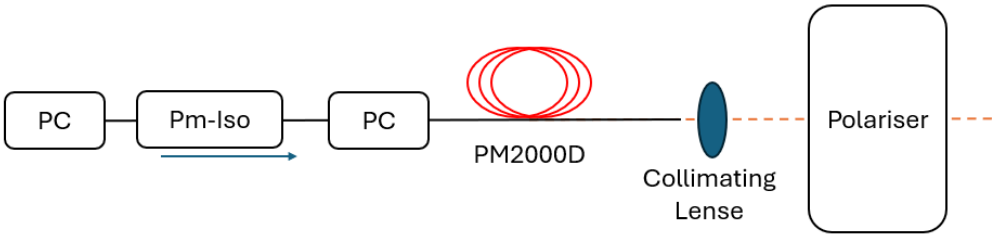

FIGURE 6.12: Experimental set-up for testing the polarisation of the FWM.

As shown in Fig. 6.13, at any given polariser angular position, the central peak was always present at the output (with slight variation in intensity), showing the existence of a proportion of the central peak in both axes, while the magnitude of the side peaks' intensities varied oppositely to each other and relative to the central peak. The maximum anti-Stokes (blue shift) peak intensity was found at the same position where the Stokes peak (red shift) was minimised at 210^o and vice versa at 310^o, which are approximately π radians out of phase. Slight deviations in the angular measurements are likely due to the drift in the polarisation over the long measurement period of the experiment.

Since the FWM process is coherent [49, 103] and peak power dependent, it shows great potential to be used as a SA. To investigate this further, a free-space filter was set up by

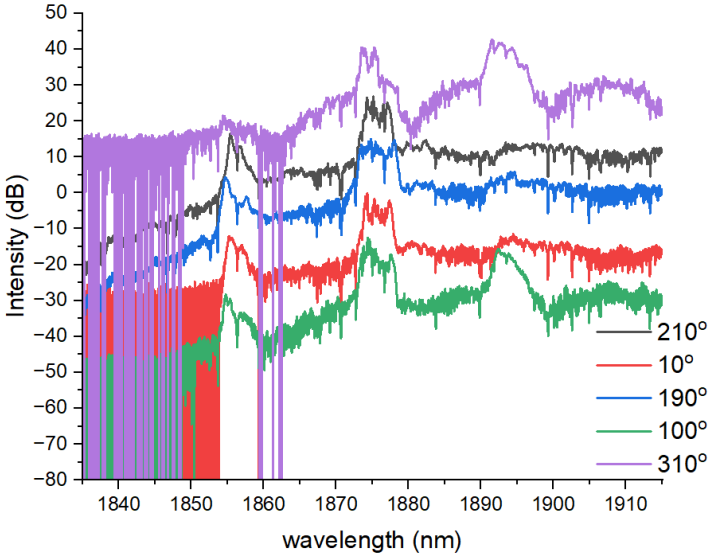

FIGURE 6.13: Output spectrum at different polariser angles.

using a pair of transmission gratings and a beam block to separate each of the distinct spectral components of the spectrum, which were represented as separate spot sizes on the IR card as seen in Fig. 6.14.

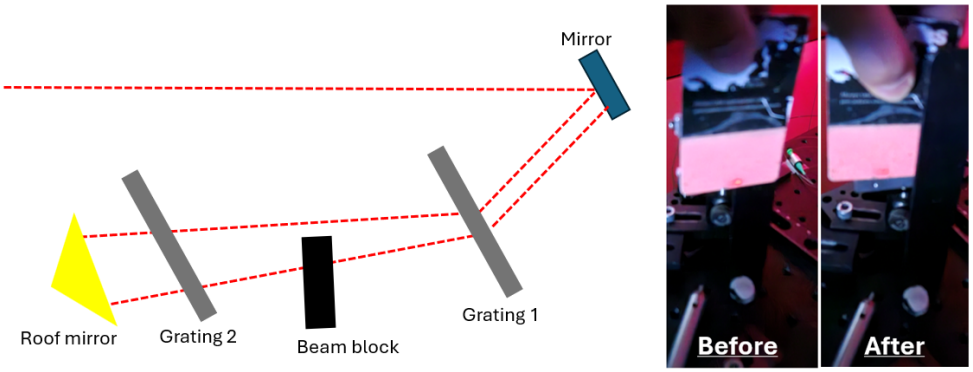

FIGURE 6.14: Free-space filter schematics and beam intensity before and after beam block.

The central and the Stokes peaks were measured, while the power in the anti-Stokes peak was too low to measure. A large grating distance of 46 cm was required to compress each peak to the minimum pulse duration, equating to a GDD of -0.397 ps^2 and an SMF fibre length of the order of ≈100 m. From Fig. 6.15, the autocorrelation of the compressed peaks both showed a pedestal being generated, with the central peak having a longer duration of 50 ps compared to the 24 ps measured at the redshifted peak.

Due to the high losses associated with free-space compressors, an alternative method of quantifying the compression of the side peaks was required. A fibre-coupled tunable SF (Agiltron FOTF-020121131) was used to freely select and control the selected spectral

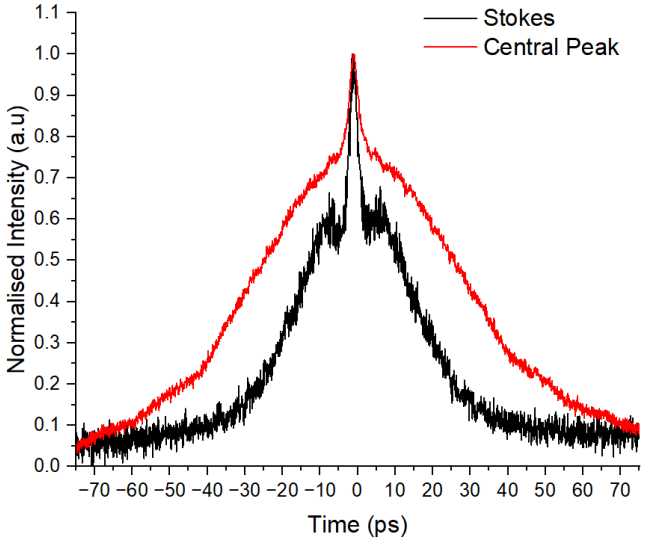

FIGURE 6.15: Autocorrelation measurement of the compressed, filtered Stokes (black) and central spectrum peak (Red).

components as seen in Fig. 6.16(a) showing the filter transmission function. A power loss of ≈12 dB was measured at 1875 nm, and spectral transmission at 3 dB and 10 dB bandwidths of 3.6 nm and 5.2 nm, respectively. The selected Stokes and anti-Stokes side peaks in Fig. 6.16(b) were selected to propagate in a 1 km long SM, then they were amplified to be measured by the autocorrelator.

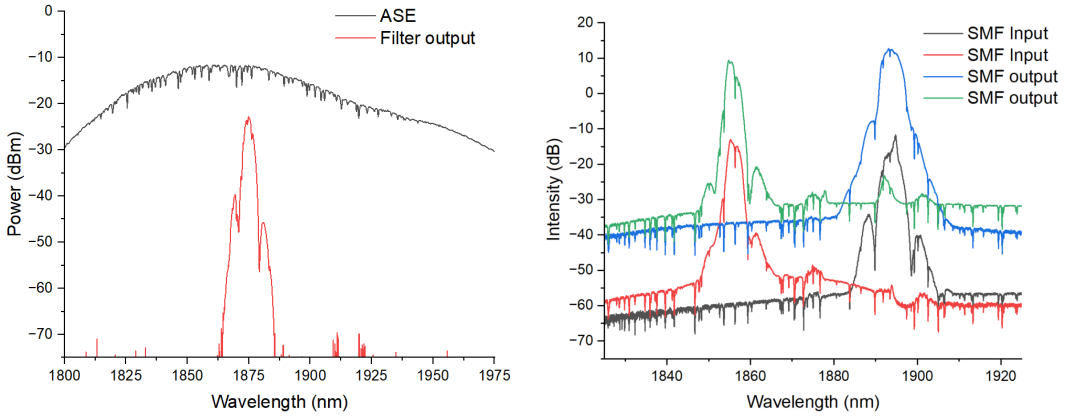

(a) Spectrum power transmission of the tuneable gratings at 1875 nm.

(b) Selected spectrum at the input and output of 1 km SMF offset by 20 dB for visualisation.

FIGURE 6.16: The transmission of the fiberised tunable filter at different positions.

In order to observe the change in each spectral component and reveal information about the nature of the chirp in each peak. The filter output showed an anti-Stokes pulse duration of 22 ps, whereas the Stokes output measured 35 ps. Negligible change in the spectra at input and output of the fibre compressor and amplifier as shown in Fig. 6.16(b) and the autocorrelator measurements showed a similar pulse shape of a large pedestal with a 4 ps peak duration in both instances as seen in Fig. 6.17.

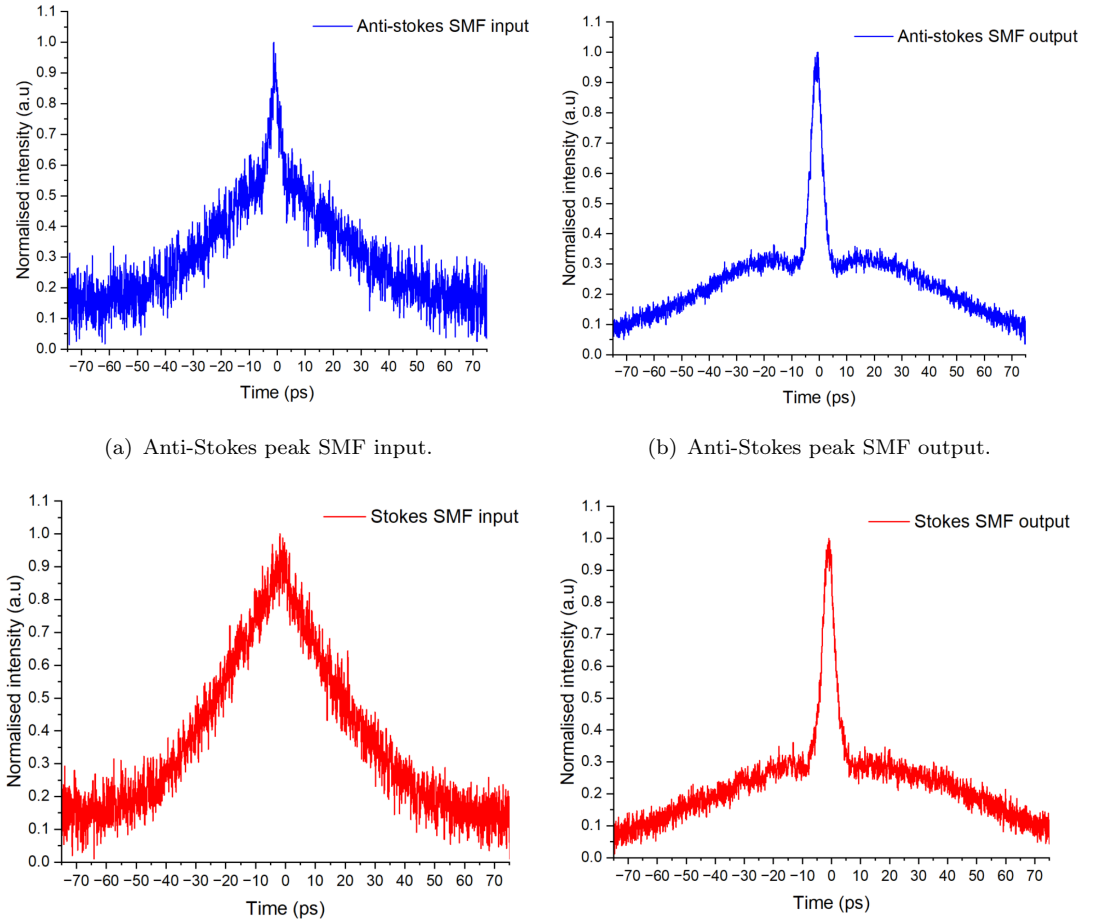

(a) Anti-Stokes peak SMF input.

(b) Anti-Stokes peak SMF output.

(c) Stokes peak SMF input.

(d) Stokes peak SMF output.

FIGURE 6.17: Autocorrelation measurement of different filtered peaks.

Since compression was observed in both peaks and a similar change was measured, it is assumed that the chirp in each peak is similar, as seen in SPM, but at the cost of a lower efficiency. The edges of the SPM central peak were also selected as shown in Fig. 6.18, which led to a compression of the pulse width to an ACF duration of 30 ps pedestal-free.

Furthermore, the results of 1 km pulse propagation were used to compare two scenarios where SPM was maximised and FWM was maximised without the use of the filter. The input of the fibre was attenuated to minimise further nonlinearities, and the results of the autocorrelation measurement showed that both cases behaved similarly, generating a 3.5 ps pulse peak. However, the FWM process showed a larger pedestal being generated, likely due to the presence of the Stokes and anti-Stokes pulses propagating with the main pulse as seen in Fig. 6.19.

The following conclusions on the use of this process as an SA were drawn based on the measured results. The FWM is inefficient in the fibre used and outputs very low-energy pulses. After traversing a long fibre, both peaks show similar behaviour to the central

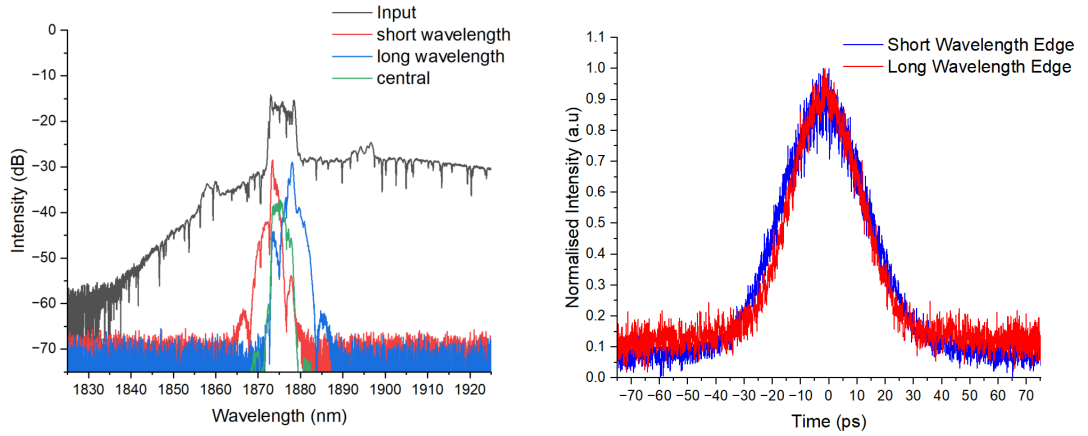

(a) SF output spectrum of the selected edges compared to the SPM broadened input.

(b) Output ACF measurement.

FIGURE 6.18: SPM edge filtering; short (red) and long (blue) wavelength.

(pump) peak, thus a similar chirp, which resulted in a large pedestal being generated at the output. Therefore, this technique is adequate to be used as an SA. The SPM effect has higher efficiency, and filtering the selected components can result in a pedestal-free output, making it ideal for pulse cleaning.

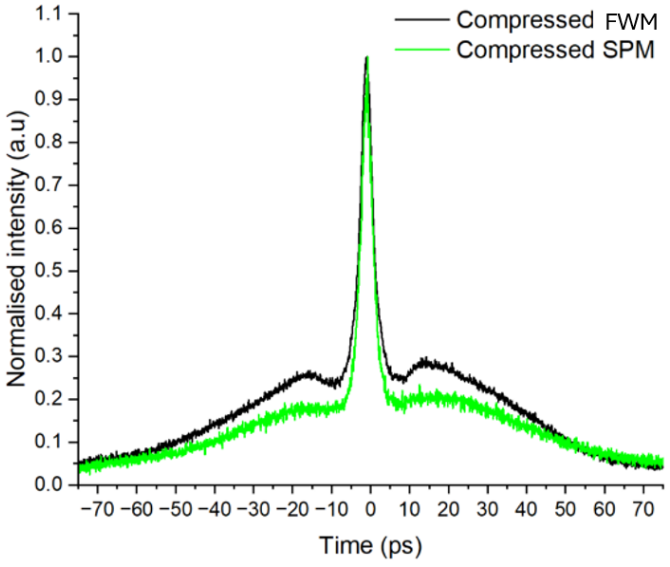

FIGURE 6.19: 1 km autocorrelation compressed pulse measurement of both SPM (green) and FWM (black).

6.2.3.4 UHNA4

To elicit solely SPM in the HNF, a 40 m UHNA4 fibre was used to replace the previous HNFs. Following the first two amplification stages, the output power after the UHNA4 showed a 2.4 dB loss. Both the autocorrelation and the spectrum were measured at the

output of the HNF, and the change in the power was investigated as shown in Fig. 6.20.

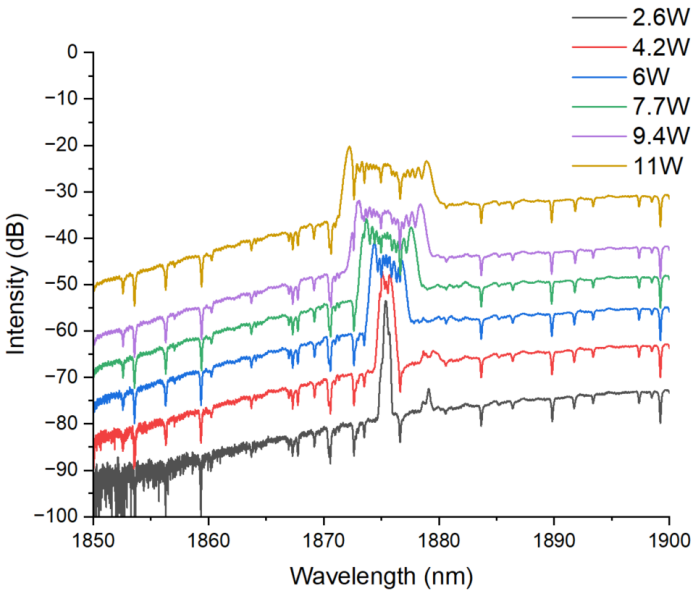

FIGURE 6.20: HNF spectrum output at different pump powers offset by 10 dB.

As the power increased, the output 10 dB bandwidth of the pulses increased to a maximum of 8.1 nm; however, the OSNR was reduced to 13 dB. The autocorrelation, on the other hand, showed an initial increase in the pulse width from 57 ps at the lowest pump power to a maximum of 69 ps at 1.6 W of power, after which the pulse width was reduced to 63 ps at the highest pump power, as shown in Fig. 6.21.

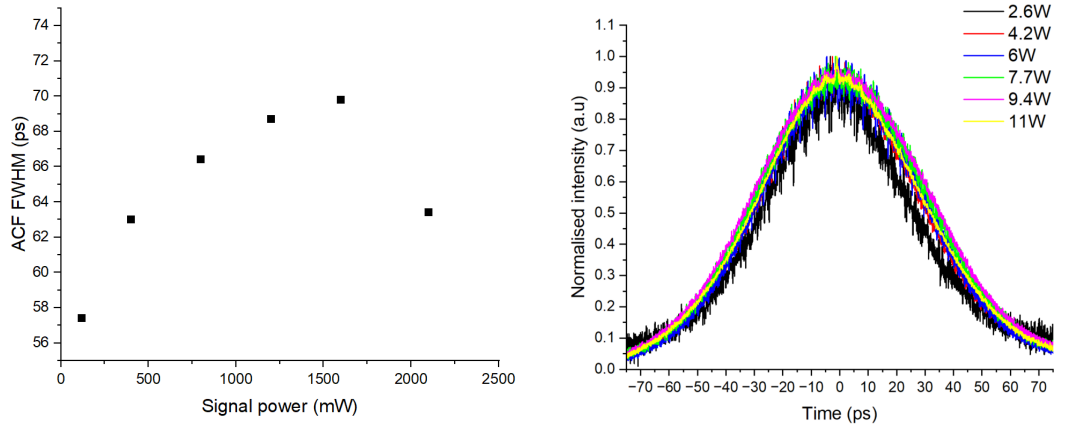

(a) HNF output ACF pulse width at different power. (b) Pulse autocorrelation at different pump powers.

FIGURE 6.21: The HNF output autocorrelation measurement at different powers.

The initial increase in the pulse width can be explained by the positive chirp imposed on the pulse by the nonlinearity, which is the dominant effect. The HNF has a positive dispersion at the lasing wavelength, and since the pulse starts to reduce, it indicates the

existence of a down chirp in the pulse. This phenomenon supports our initial hypothesis of having 2 chirps in the pulse as a result of the gain switching, which was further added on by the nonlinear chirp imposed on the pulse by SPM. Therefore, novel compression and pulse cleaning methods are needed.

6.2.4 Compression methods

Various compression methods were evaluated on the broadened spectrum resulting from the implementation of the HNF in the system. This analysis identified the optimal pulse compression and the shortest achievable compressed pulse duration.

6.2.4.1 Linear compression

Initially, an experiment was set up as shown in Fig. 6.22 using various lengths of anomalous dispersion SMF fibre compressor without the use of a filter to see the impact on the compressed pulse shape. The tested fibre lengths were in increments of 25 m from 25 m to 175 m. 2.1 W of power was used during the experiment, as it gave rise to the broadest pulse spectrum. This meant that the input to the fibre compressor was attenuated to ensure no further nonlinearity impacted the compression and the compressor output spectra.

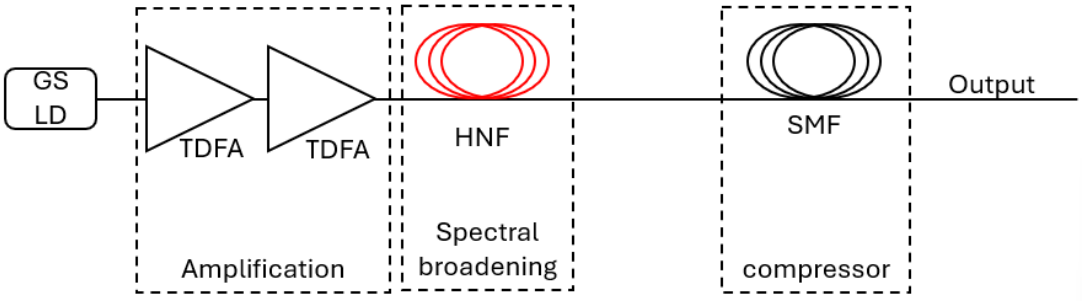

FIGURE 6.22: Compression experimental set-up schematics.

As described in Fig. 6.23(a), as the length of the fibre increased, the pulse width decreased to a minimum value at 150 m of SMF; and further increasing the fibre length did not result in any further change in the pulse width but rather a change in the shape caused by an increase in the pulse pedestal as seen in Fig. 6.23(b). The minimum pulse ACF width achieved was 1.7 ps with a noticeable pedestal. As expected, the minimum compressed pulse duration achieved via linear compression far exceeds the TFL pulse width value of 650 fs based on the bandwidth of the pulse, assuming a $Sech^2$ pulse shape.

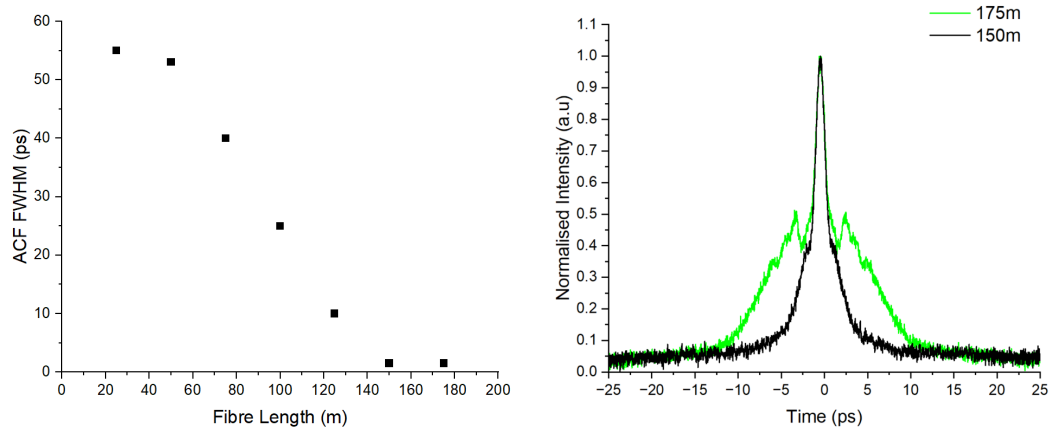

(a) SMF compressor output ACF pulse width at different lengths.

(b) ACF at 175 m (green) and 150 m (black) of compressor length.

FIGURE 6.23: The autocorrelation measured linear compression results.

6.2.4.2 Nonlinear compression

A nonlinear compression approach was tested next by not attenuating the input power to the fibre compressor with a similar experimental set-up as illustrated in Fig. 6.22. As seen in Fig. 6.24(b), a pulse ACF peak with a width of ≈700 fs was generated, but a large pedestal accompanied, which seems to reduce from 60 ps to 40 ps as the fibre compressor length increased at the maximum input power. The autocorrelator shape is indicative of pulse break up due to MI in the anomalous dispersion fibre, whereby the peak duration represents the average pulse durations of the pulses, and the envelope shows the spread of the pulses in time, similar to noise-like pulses. Additionally, the pulse spectrum indicates that the main pulse features appear to broaden, ultimately becoming indistinguishable from the ASE, as illustrated in Fig. 6.24(a). This overlap is a result of the high levels of ASE and energy transfer due to the broadening.

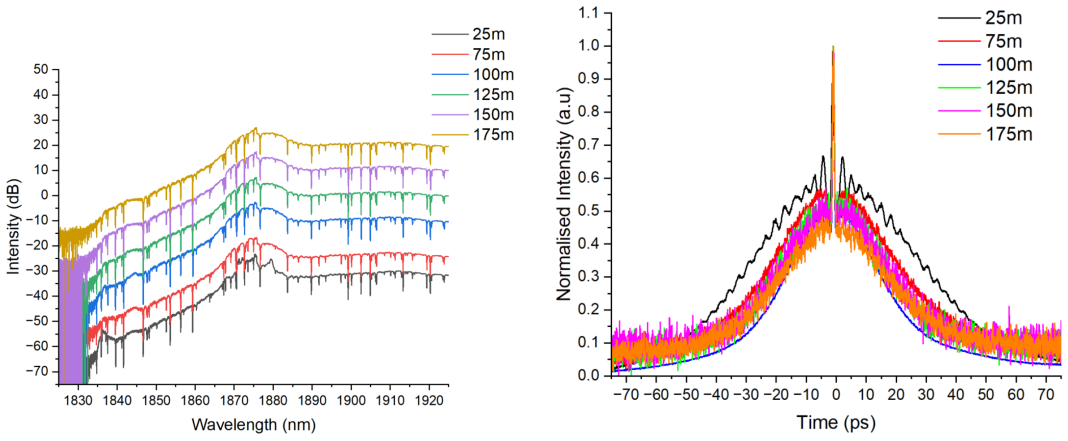

(a) Spectrum at different lengths.

(b) ACF measurements at different lengths.

FIGURE 6.24: The output of different SMF compressor lengths.

6.2.4.3 Spectral filter

In theory, adding an SF at the input of the SMF compressor, as shown in Fig. 6.25, should overcome the limitations of the previous compression methods by selecting spectral components of the pulse with a linear chirp that best complements the compression.

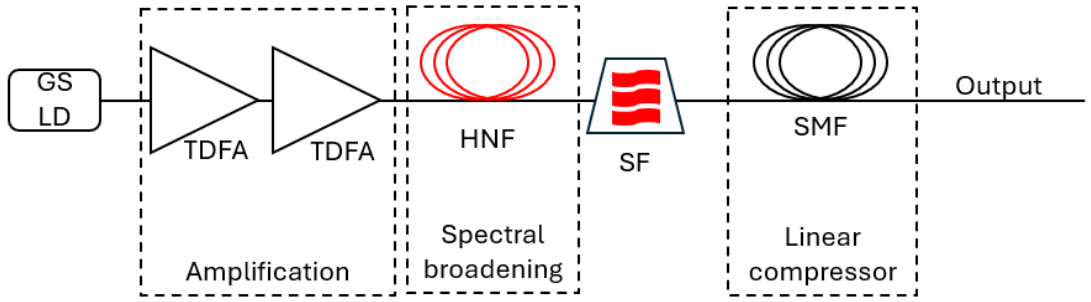

FIGURE 6.25: Compression using a spectral filter experimental set-up schematics.

The output power of the filter was measured to be 51 mW. Pulse compression experiments were carried out by finding the optimum spectrum components by monitoring the final compressed pulse output and tuning the filter position simultaneously for a given fibre length. The selected spectral components seen in Fig. 6.26(a) were optimised for the pulse compression, and the corresponding pulse duration directly after the SF showed a compression to an ACF width of 23 ps, accompanied by a pedestal as shown in Fig. 6.26(b), likely due to the overlap of the filter spectrum with the original GLSD spectrum.

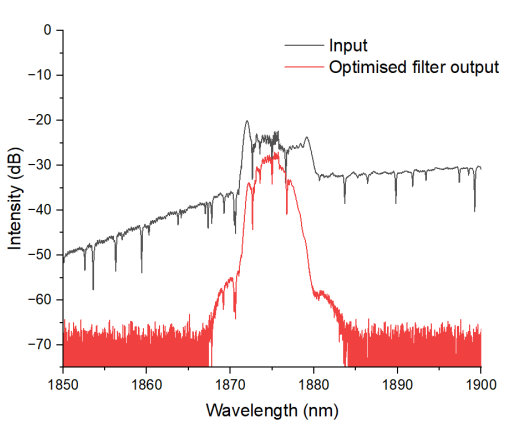

(a) Selected spectrum for optimised linear pulse compression.

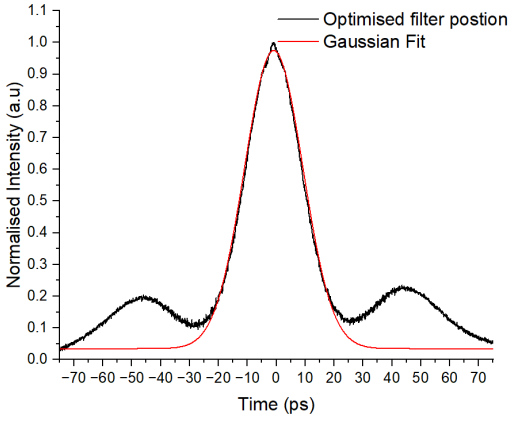

(b) ACF measurement of the filter output.

FIGURE 6.26: Optimum spectral filter output.

The autocorrelation results of the compression is shown in Fig. 6.27. No spectral broadening was seen during propagation in the SMF fibre compressor, and the required fibre compression length seems to be shortened due to the initial compression caused by the filter reaching a minimum compressed ACF duration of 1.6 ps at 75 m SMF fibre.

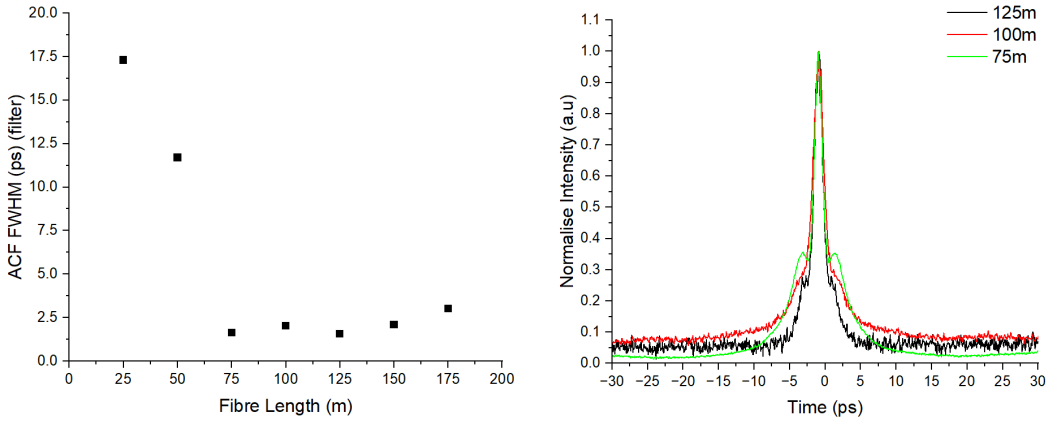

(a) SMF compressor output ACF pulse width at different lengths.

(b) ACF at 75 m (green), 100 m (red) and 125 m (black) of compressor length.

FIGURE 6.27: The autocorrelation measured linear compression results.

Increasing the fibre length further showed a similar pulse duration but an increase in the pulse pedestal until 125 m, then the pulse peak starts to broaden again, indicating a flip in the pulse chirp. Comparing the autocorrelation of the minimum pulse duration

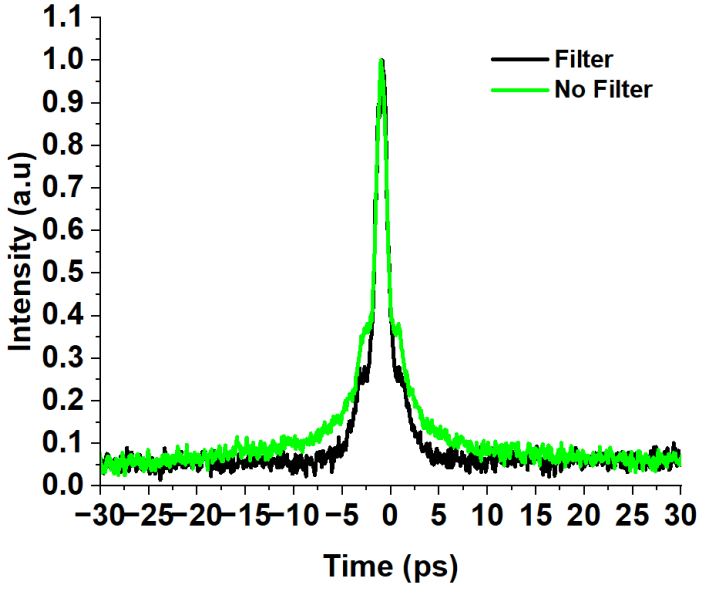

FIGURE 6.28: ACF measurement of the minimum compression with (black) and without filter (green).

at the compressor output with and without the use of the filter clearly shows an improvement in the pedestal suppression when the filter was used (Fig. 6.28). However,

some pedestals can still be seen, which is a result of the broad transmission window of the filter. Therefore, the pulse compression would benefit from a narrower SF.

6.2.4.4 Nonlinear compression on filtered spectrum

Nonlinear pulse compression is introduced to the filtered pulse to investigate the possibility of achieving even shorter pulse durations. This was carried out by adding an amplifier between the SF and fibre compressor as shown in Fig. 6.29.

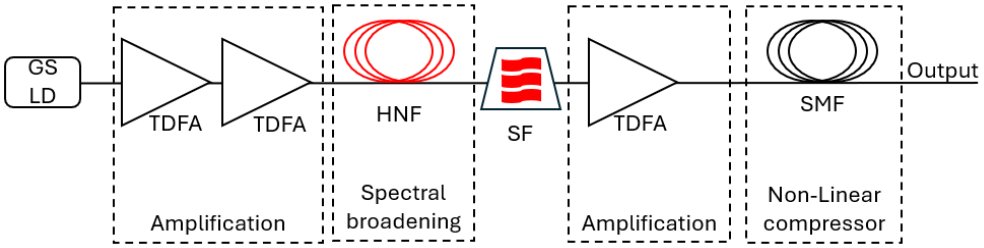

FIGURE 6.29: Nonlinear compression experimental set-up schematics.

The newly added amplifier was core pumped by a commercial EDFA (Amonics, AEDFA-33-b-FA) operating at 1560 nm, and was made with a 1.3 m in-house fabricated TDF and had a total SMF length of 4.1m. The amplification was characterised, showing a 20% slope efficiency with a maximum available pump power of 1 W as seen in Fig. 6.30, giving an output signal power of 200 mW with over 60 dB of OSNR and negligible residual pump, while negligible spectral distortion in the amplifier was observed as shown in Fig. 6.31.

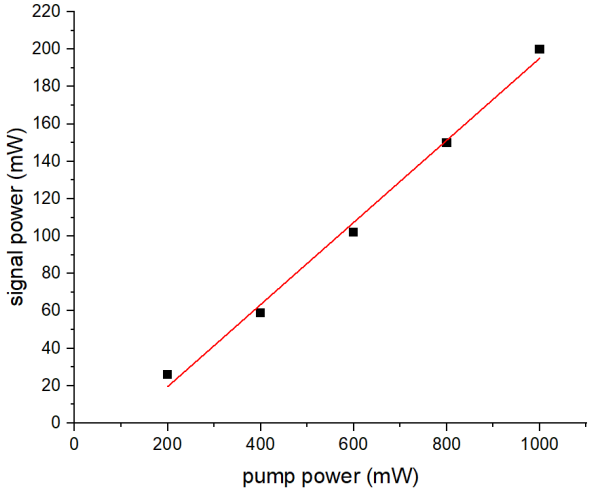

FIGURE 6.30: Amplified signal power at different input pump power.

A similar technique of working backwards to characterise the pulse compression was adopted while initially fixing the pump power to 1 W and varying the SMF length.

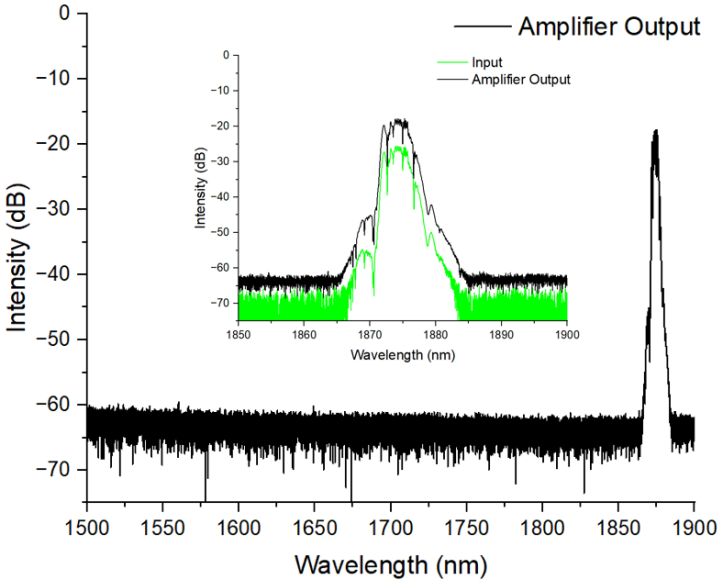

FIGURE 6.31: Amplified output spectrum; Inset: zoomed in amplified output (black) and input (green) spectrum.

The spectrum measurements seen in Fig. 6.32 shows a signal more distinguishable from the background ASE after nonlinear broadening compared to the previous nonlinear experiment (refer to Fig. 6.24(a)) since the ASE was suppressed using the SF. The powers used for the input were also much lower than the initial nonlinear experiment, which allowed for a more "controlled" nonlinear pulse evolution. As the fibre compressor length increased, the pulse bandwidth also increased.

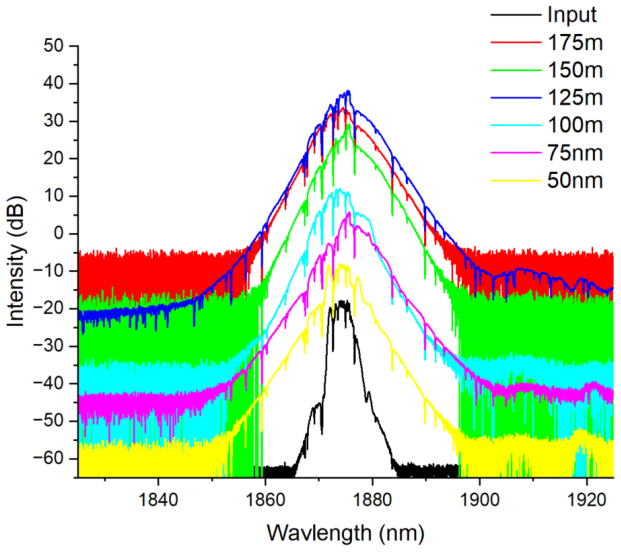

FIGURE 6.32: Nonlinear SMF compressor output spectrum at different lengths; offset by 10 dB.

Similarly, a fixed pulse peak width was generated despite the fibre compression length, with a minimum value of 545 fs (assuming a $sech^2$ pulse shape) at 100 m. Furthermore,

the pedestal generated was much lower than the SF and lower signal power. The minimum pulse pedestals were seen at 25 m and 100 m of SMF length. However, at 25 m, distinct side peaks were generated, showing clearly the onset of the pulse break-up due to MI as seen in Fig. 6.33.

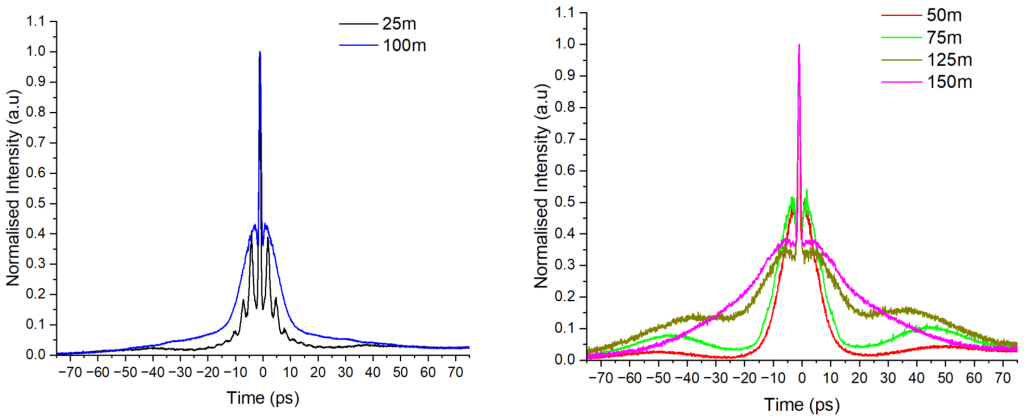

(a) SMF compressor lengths: 25 m (black), 100 m (blue).

(b) SMF compressor lengths: 50 m (red), 75 m (green), 125 m (brown), 150 m (pink).

FIGURE 6.33: ACF measurements at different fibre compressor lengths.

After investigating the effect of the fibre length on compression, the input power was varied while fixing the length at 100 m, which gave the shortest pulse duration. The result presented in Fig. 6.34 showed a decrease in the pulse width at 1 W. However, the pedestal area was shown to increase with pump power. Varying the length while fixing the power and varying the power while fixing the length gives a qualitative compression between a GVD and SPM dominant propagation comparison for pulse compression.

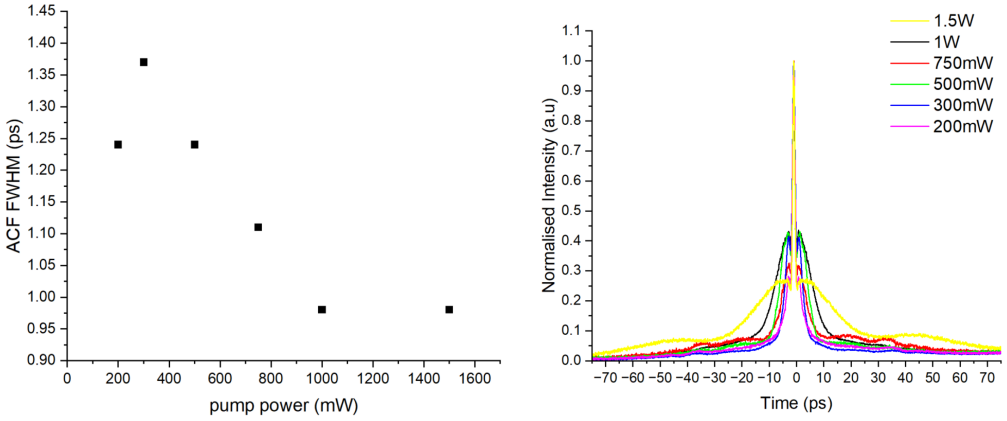

(a) ACF pulse width at different powers after 100 m SMF compression.

(b) ACF traces at different pump powers.

FIGURE 6.34: ACF pulse ACF measurements at different powers after 100 m of SMF compressor.

To summarise, SPM is necessary for nonlinear pulse compression to achieve sub-picosecond pulse compression. However, it needs to be balanced with the effects of GVD (according to equation 2.50) while compressing the pulse, in order to suppress the pedestal, while varying the fibre length does not control the pulse duration. These factors were taken into consideration when implementing the next compression method.

6.2.4.5 2-stage compression

The final experiment set-up was compiled based on the conclusions from the previous experiments, which aimed to magnify the desired effects while suppressing the unwanted effects that would negatively affect the pulse shape after compression. The experimental set-up is shown in Fig. 6.35. It was arranged such that, after the HNF, a SF is added directly to the output, and then the output is attenuated to ensure no nonlinearity occurs in the next stage, which is a fibre linear compressor of a 100 m SMF, which is then fed into a final non-linear compression stage comprised of an additional TDFA.

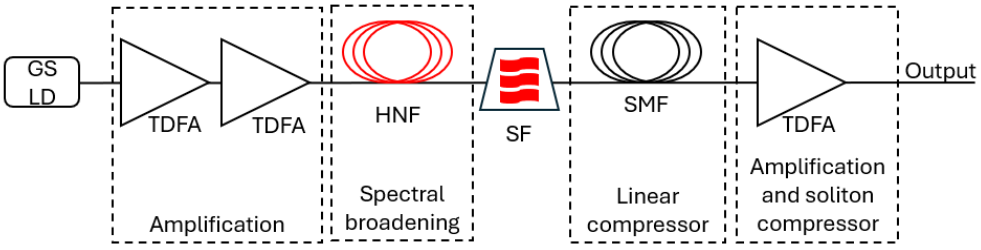

FIGURE 6.35: 2-stage compression experimental set-up schematics.

The linear compressor did not compress the pulse to the minimum duration to allow for further compression in the next stage, thus passively increasing the peak powers and pulse envelope slope into the final stage while not over compressing the pulse.

This stage focuses on linear compression while minimising the nonlinearity of the system, which is proven by maintaining the same spectrum at the input and output of the compressor as seen in Fig. 6.36(a). The linear compression associated with the use of the filter is shown in Fig. 6.36(b). The results from 100 m of SMF compressor show a significant improvement in the pulse shape and pedestal suppression with the use of the filter. This is beneficial for the next compression which aims to maximise the effects of the high peak power with minimal side pedestals. To achieve this, a third amplifier which focuses on energy scaling and nonlinear pulse compression by maximising SPM while minimising the effects of GVD was added after the linear compressor.

The spectrum at output shows an increase at the base, both in amplitude and width. This effect was larger than the previous case of nonlinear compression (refer to Fig. 6.32) due to having a higher peak power during propagation despite the short fibre length.

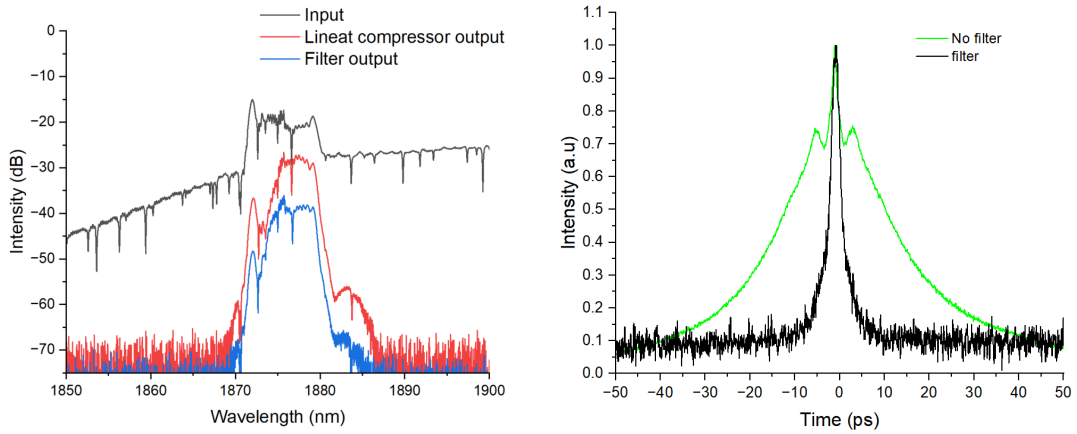

(a) Selected spectrum for optimised pulse before (red) and after (Blue) linear pulse compression compared to the SF input (Black) offset by 5 dB.

(b) ACF measurement after 100 m with and without a filter (green) at the input (black.)

FIGURE 6.36: Final amplifier input pulse parameters.

Autocorrelation measurements for the output pulses revealed pulse self-compression during the amplification. The pulses narrowed when the output power was increased up to 150 mW; however, further increases in the output power resulted in a slightly broader pulse with a higher pedestal shown on the ACF trace, as presented in Fig. 6.37(b). At an output power of 150 mW, self-compressed pulses with high contrast and a pulse width of 509 fs were obtained. With a 10 dB bandwidth of 7.4 nm, the pulses exhibited a TBP of 0.321, which is close to the TBP value of 0.315 for a $sech^2$ pulse, confirming the soliton formation caused by the interplay between the anomalous dispersion and SPM in the fibre. The corresponding pulse energy and peak power are therefore 4.7 nJ and 8.52 kW, respectively; Where $\approx$ 40% of the total pulse energy is concentrated in the central peak.

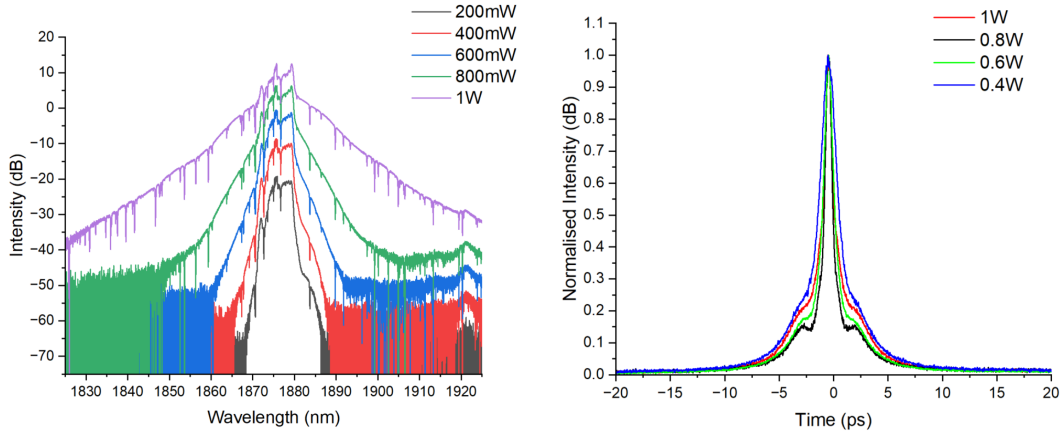

(a) Amplified spectrum at different pump powers, offset by 5 dB.

(b) Corresponding compressed autocorrelation.

FIGURE 6.37: Final amplifier output measurements.

To test the extent of the soliton compression in the amplifier, 10 m of SMF was added to

the output of the amplifier. A similar trend is seen in the change of the spectrum with power as shown in Fig. 6.38(a). However, with increased fibre length, more nonlinearity and dispersion are experienced by the pulse, causing the narrow pulse width to stretch to 0.9 ps at 800 mW as seen in Fig. 6.38(b) compared to 0.5ps at the same similar power at the output of the amplifer (Fig. 6.37). Furthermore, side peaks start to appear for pump powers over 400 mW, showing signs of pulse break-up.

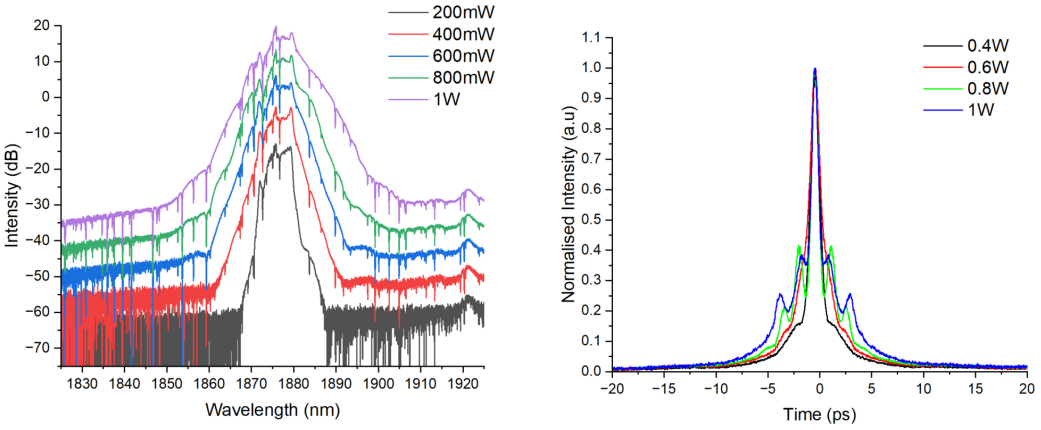

(a) Amplified spectrum at different pump powers after 10 m SMF Offset by 5 dB.

(b) Corresponding compressed autocorrelation measurement.

FIGURE 6.38: Output of the 10 m SMF after the final amplifier.

To summarise, a soltion is formed showing a near TFL pulse duration at the output of the amplifier, further increasing the compressor length results in over compression of the pulse leading to a wider output pulse duration and eventually pulse break up at higher powers.

Chapter 7

Burst-mode pulse shaping

This chapter presents investigations into a novel technique for selective imaging, which will be incorporated into the modulation capabilities of the imaging laser discussed in chapter 3. As the imaging laser was being used by IFLS, a separate system was built, primarily focusing on optimising the adaptive imaging methodology.

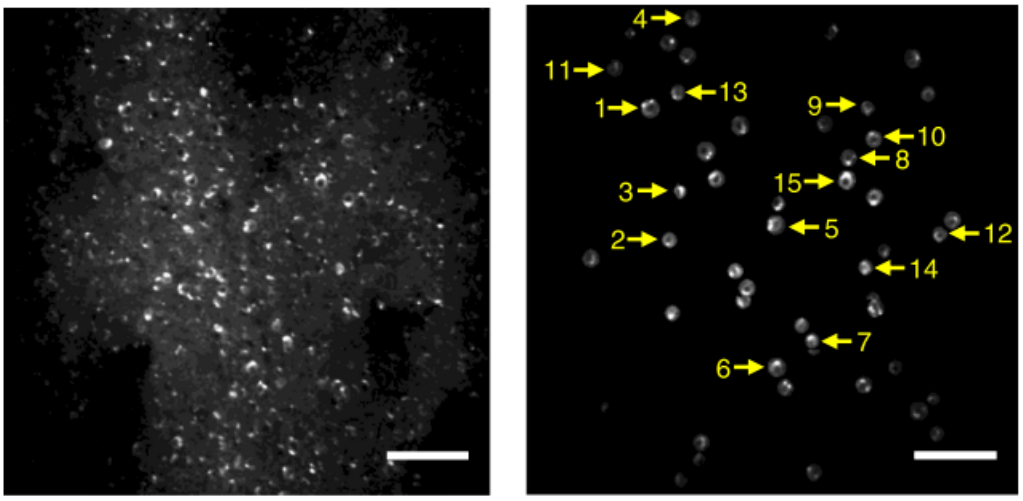

(a) Neurons of mouse brain without APC

(b) Neurons of mouse brain with APC

FIGURE 7.1: Image of neurons of the mouse brain with (a) and without (b) adaptive pulse control (APC). The images have a field of view (FOV) of $620 \times 620 \mu m$, 512×512 pixels, and a scale bar of 100 μm. These figures were reproduced from *Bo Li, 2020* [6].

This technique involves generating non-uniform bursts that temporally align with the distribution of the ROI on biological samples. The calculations for the target experimental parameters are based on the work conducted by *Li et al.*, where a 30 Hz frame rate is used for imaging a 512×512 pixel, $620 \times 620 \mu m$ field of view (FOV) image, as reported in [6]. This results in a scanning time of 33.3 ms per frame. From Fig. 7.1, one ROI can be estimated to be ≈ 20 μm across, which equates to a 2 μs time period, and one line of pixels can be imaged in 0.5 ms. While this may not accurately represent

the experimental conditions that will be used during the actual testing of the system, it serves as a starting point for developing an appropriate methodology to address such issues.

Additionally, burst generation causes non-uniform amplification of the pulses due to gain saturation effects within the amplifier. As a result, the theory of pulse shaping was originally developed to address gain saturation for a single burst to produce uniform pulse waveform. This theory was later adapted to accommodate more complex, non-uniform multi-burst signals.

7.1 Uniform Burst window shaping

In this section, the laser system designed to investigate the effects of gain saturation is presented, along with the techniques applied to compensate for gain saturation and produce a uniform burst output for adaptive imaging of ROIs.

7.1.1 Experimental set up

The system built to emulate the gain saturation in amplifying bursts of pulses is illustrated in Fig. 7.2. The key operational conditions established to observe significant saturation effects were a low RR and an extended burst window. The seed was a GSLD with a central wavelength of 1875 nm (EP1854 Eblana Photonics) modulated by a PG (8133a Agilent) to operate in pulsed mode.

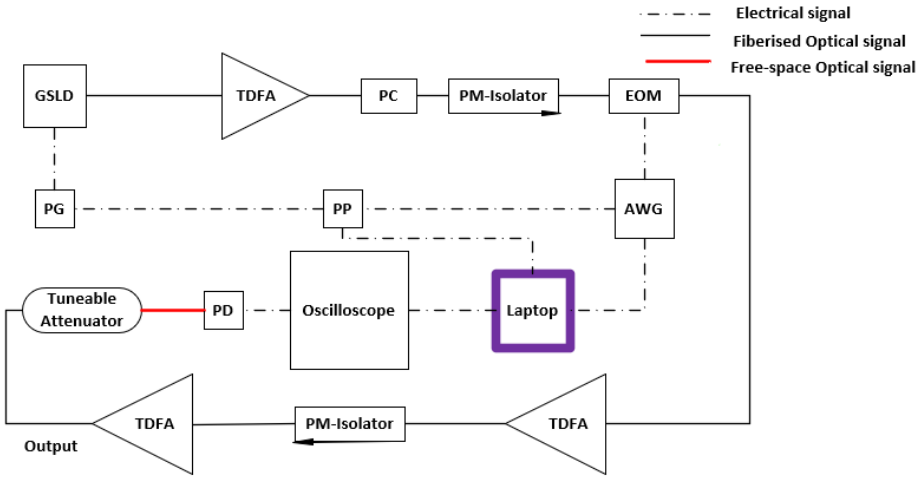

FIGURE 7.2: GSLD-driven MOPA system for burst shaping. EOM: electro-optic modulator; AWG: arbitrary waveform generator; PP: pulse picker; PG: pulse generator; PD: photodiode.

The pulse parameters were chosen based on convenient experimental conditions from a maximum EOM excitation ratio to a high OSNR, while avoiding parasitic lasing in the following amplifier stages; a 3 ns electrical signal at 100 MHz of repetition frequency was used to trigger the LD, generating an average power of 0.33 mW. The optical output spectrum and 100 MHz train are shown in Fig. 7.3. A single peak at 1875 nm was expected from the GSLD; however, an additional side peak in the spectrum at 1879 nm indicates 50 dB of longitudinal cavity mode suppression, likely due to over-pumping of the laser diode. Furthermore, the narrow spectral line observed in the main peak represents the steady state component of gain switching as a result of the the extended trigger period.

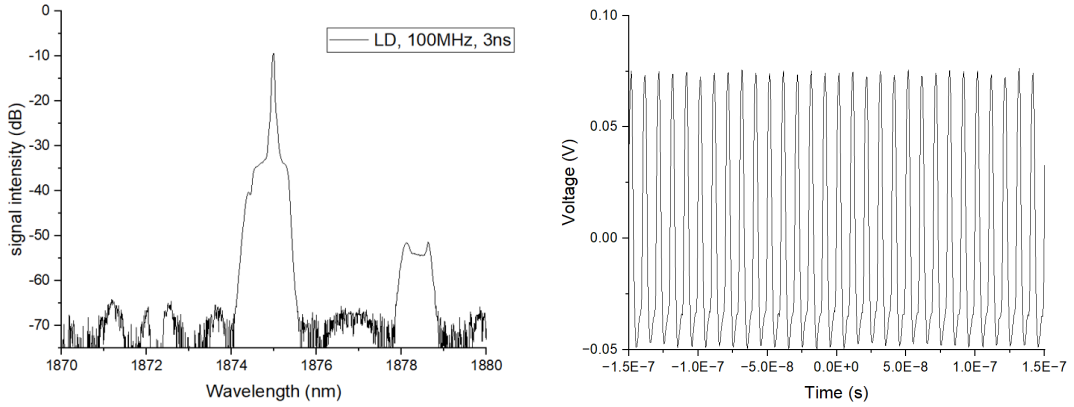

(a) Output spectrum of GSLD at 3 ns and 100 MHz. The operating wavelength is 1875 nm.

(b) 100 MHz pulse repetition frequency.

FIGURE 7.3: Output characteristics of GSLD.

The output trigger signal of the pulse generator (PG) was used to synchronise sub-electronic components of the system. A PP (OMBAK/AERO-DIODE V2.7") was introduced between the AWG (AFG3102C) and the PG to produce frequencies that are lower than the PG's standard capabilities. The EOM gating functionality was managed by the AWG, which has limited built-in waveform functions, such as square and sinusoidal waveforms. A laptop was employed to control the AWG and generate more complex waveforms.

Additionally, a laptop was also used to control the PP and relay information to and from the oscilloscope ("Agilent Technologies, MSO7104A", 1 GS/s). The software utilised for the pulse picker (PP) was "ALPhANOV Control Software," while MATLAB was used for both the oscilloscope and the AWG, as it allows for efficient script development with extensive online support and resources available. Finally, an attenuator was placed at the output of the final stage to prevent saturation of the photodiode used to measure the signal.

7.1.1.1 First amplifier

Since the power output of the LD was small, an amplifier was needed to raise the power and overcome the losses of the EOM. Therefore, a pre-amplifier was built and pumped by an EDFL as shown in Fig. 7.4.

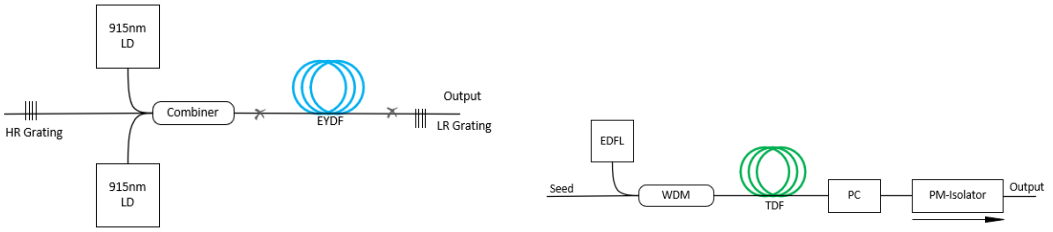

(a) Schematics of the first stage EDFL pump; HR: high reflecting, LR: low reflecting.

(b) Schematics of the first stage TDFA; EDFL: erbium-doped fibre laser.

FIGURE 7.4: First stage EDFL pump and TDFA amplifier schematics.

A 4 m TDF was used as the gain medium, a WDM for combining the signal and the pump light, and a PM-isolator (slow axis blocked), because a polarised input is required for the EOM. In addition, a PC was inserted at the input fibre to maximise the power output through the ISO. According to the manufacturer's specification of the EOM, the maximum handling optical input power was 100 mW. Therefore, a fixed input power of 78 mW at a 592 mW pump power was maintained at this stage throughout the experiment. As illustrated in Fig. 7.5, the spectrum of the amplified pulse shows an OSNR of around 40 dB, showing that most of the power resides in the signal peak with negligible power in the ASE.

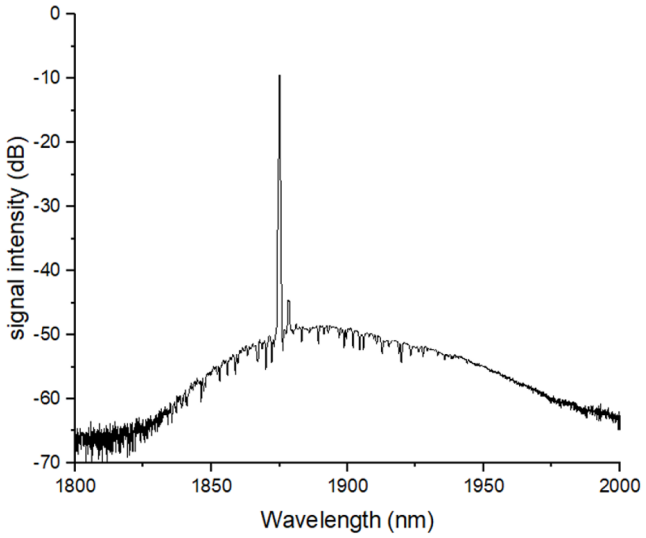

FIGURE 7.5: Spectrum of the amplified 1875 nm, 3ns and 100MHz gain-switched pulse.

7.1.1.2 EOM

The extinction ratio of the EOM was found to be 14.6 dB by examining the oscilloscope trace when a square electrical signal was applied, as shown in Fig. 7.6. The amplitude of the electrical signal for maximum signal transmission occurs at V_π, which was experimentally found to be 5.5 V.

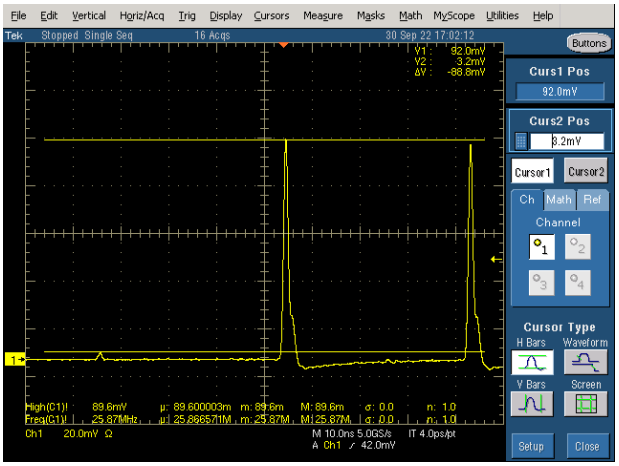

FIGURE 7.6: Extinction ratio of the EOM for a square electrical pulse; $V_\pi = 5.5V$.

The EOM was set to modulate at a fixed uniform burst train of 100 kHz (inter-burst) RR As shown in Fig. 7.7. To observe saturation effects post modulation three burst windows of 50 ns,100 ns, and 200 ns were set as seen in Fig. 7.8. A long inter-burst window allows enough time for the pump energy to build up in the gain fibre before the next burst is amplified to observe the saturation effects clearly. Whereas, the burst window was varied to test the effectiveness of saturation correction under different magnitudes of saturation at burst parameters.

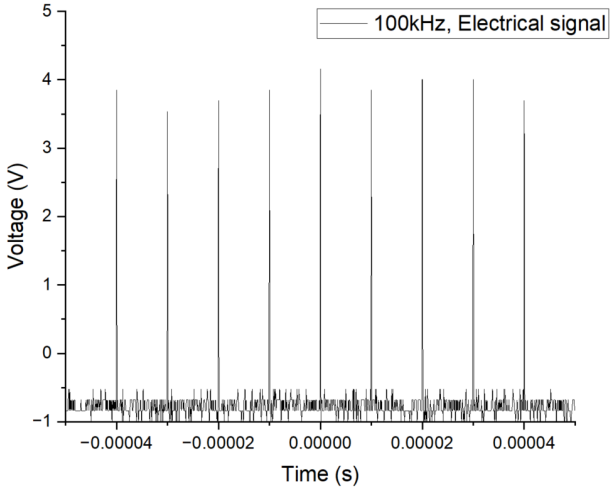

FIGURE 7.7: 100 kHz RR electrical signal applied to the EOM.

The uniform burst shapes observed at the EOM also serve to be the target shape for correction at the output of the final amplifier. Note that the electrical signal shown in Fig. 7.8 is not perfectly uniform as a result of both the speed of the oscilloscope and signal noise.

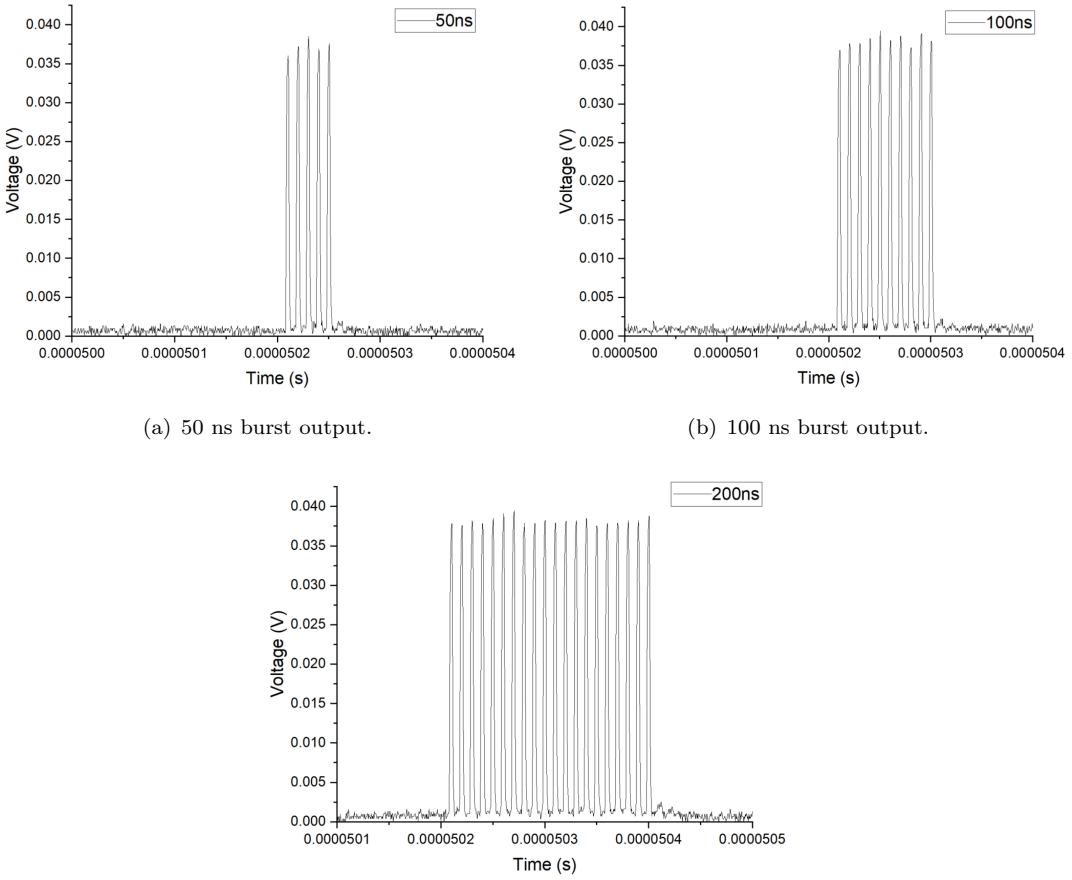

(a) 50 ns burst output.

(b) 100 ns burst output.

(c) 200 ns burst output.

FIGURE 7.8: Output of an EOM operating at 100 kHz RR and square electrical signal.

Finally, the EOM output powers and operating losses were quantified and are presented in Table 7.1. Higher losses at the shorter burst widths (BW) were measured due to a larger number of pulses being suppressed to achieved a smaller burst width.

TABLE 7.1: Insertion losses and output powers of the EOM at 3 different BW.

Burst width (ns)	Av. Power(mW)	Loss (dB)
50	1.42	16.16
100	2.77	13.25
200	5.67	10.14

7.1.1.3 Second amplifier

The schematics are given in Fig. 7.9(b) for the second amplifier, as shown a PM-WDM and 0.7 m PM-TDF, followed by an ISO. The amplifier was pumped with higher power EDFL than the previous stage, utilising six laser diodes (LD) as shown in Fig. 7.9(a). The pump was characterised at different input currents, and the results show a linear increase in power output, reaching an average power of 4.95 W at a current of 4 A, as represented in Fig. 7.10.

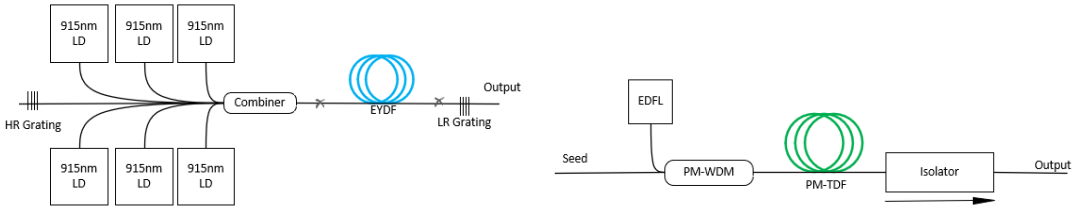

(a) Schematics of the second stage EDFL pump. (b) Schematics of the second stage TDFA.

FIGURE 7.9: Second stage pump and amplifier schematics.

The amplifier output power was also characterised at the three working burst widths. Note that there were no pump filtering components in the final system between the second and final amplifying stages. A WDM was used for characterising the output powers, showing the actual signal power as presented in Fig. 7.11(a). The power is increased for a higher burst window due to the higher input powers at the larger burst window.

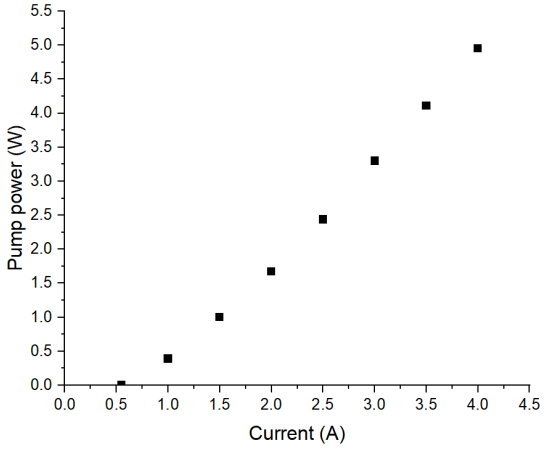

FIGURE 7.10: Six LD pumped EDFL characterisation.

The oscilloscope trace was examined at maximum power for each of the BW for any saturation. As seen in Fig. 7.11, a linear decrease in the peak intensities across the three burst windows shows minimal gain saturation independent of the BW parameters. Thus, it became apparent that another amplification stage was needed, introducing more gain and exaggerating the desired effects.

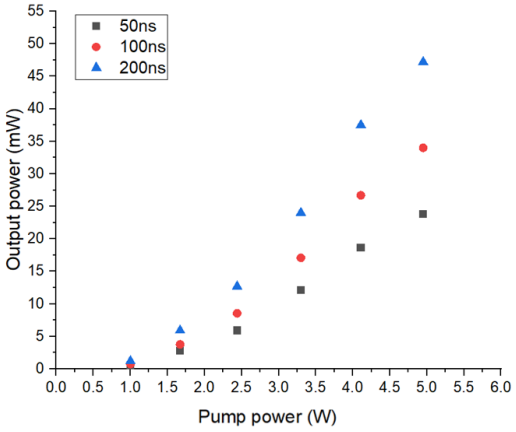

(a) Output power of the second stage amplifier filtered using a WDM at 50 ns,100 ns, and 200 ns BW.

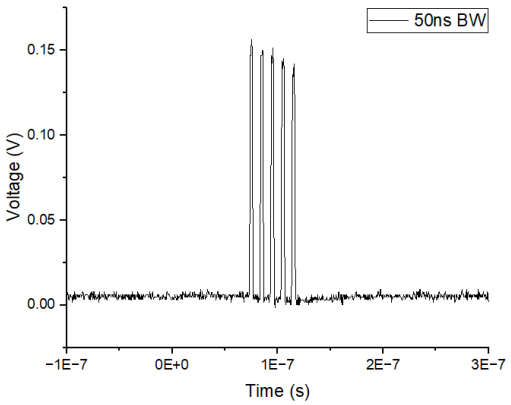

(b) 50 ns BW after the second amplifier.

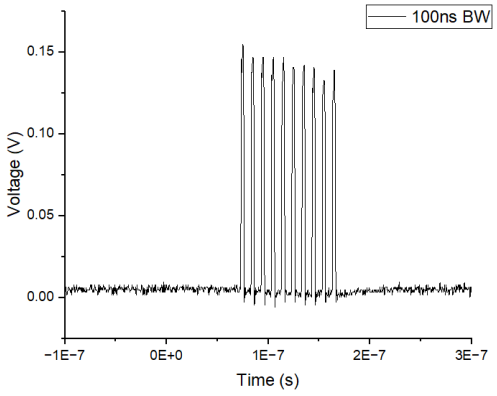

(c) 100 ns BW after the second amplifier.

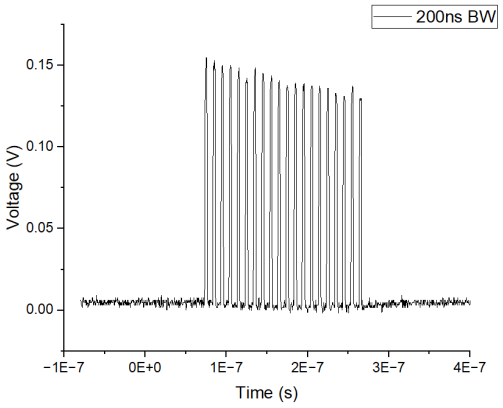

(d) 200 ns BW after the second amplifier.

FIGURE 7.11: Output power and burst profile of the second stage amplifier.

7.1.1.4 Final amplifier

Unlike the previous amplifier stage, the final stage amplifier was cladding pumped by a 790 nm LD for higher output power as shown in Fig. 7.12. The pump was delivered into the amplifier via a signal pump combiner (SPC). The LD was mounted on a cooling plate, and the temperature was controlled by temperature control (Oven Industries, 5C7-362) and set to 20 ^oC.

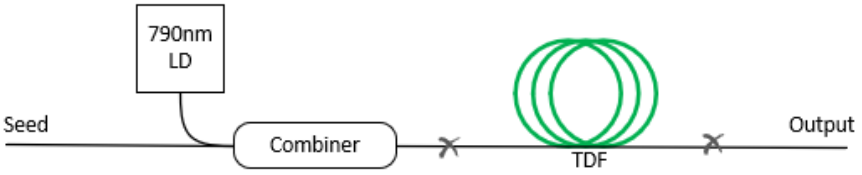

FIGURE 7.12: Third stage TDFA amplifier pumped by a 790 nm LD.

The output power of the laser diode was measured before splicing it to the amplifier, and the results showed up to 14.1 W of power with slight shifting in the pump wavelength due to the heating of the LD at high supply current, as seen in Fig. 7.13.

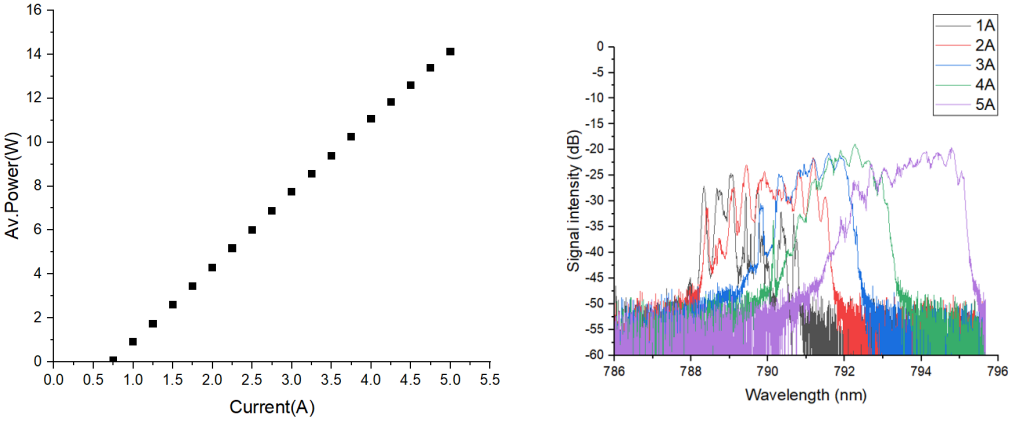

(a) The output power of the 790 nm LD at different supply currents.

(b) The spectral shift in the output of the 790 nm pump laser diode at different currents.

FIGURE 7.13: Laser diode spectral and power characterisation.

For the maximum output power from the previous stage, the output power of the final amplifier was later tested and shown in Fig. 7.14(a); the maximum average powers of up to 4.4 W, 4.7 W, and 4.9 W were achieved at 50 ns, 100 ns, and 200 ns, respectively. Since the amplifier was cladding pumped and the output splice point was submerged in high index coating (filtering the pump wavelength), the output power is expected to be purely the amplified signal. Moreover, investigating the spectrum of the output showed no parasitic lasing and an OSNR of 27 dB as seen in Fig. 7.14(b).

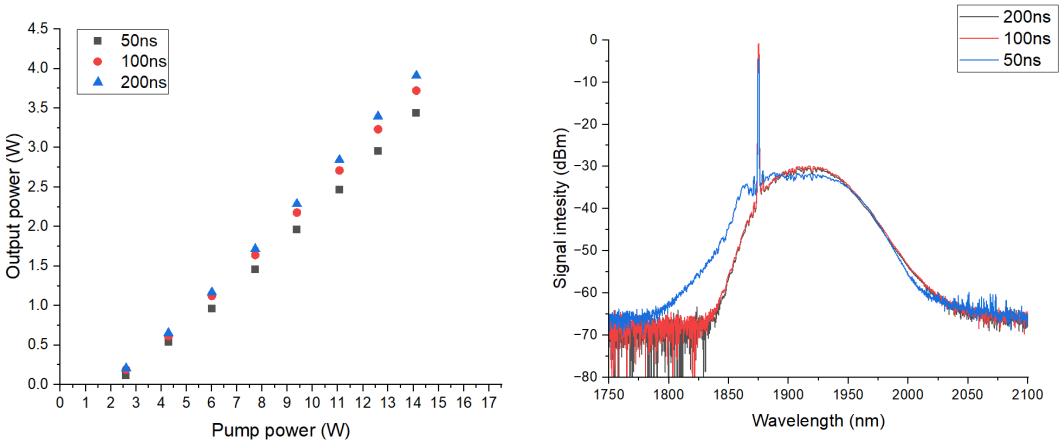

(a) The output powers of the final stage amplifier at different pump powers.

(b) Spectrum at 11 W pump power of the 50 ns, 100 ns and 200 ns BW.

FIGURE 7.14: Final amplifier spectral and power characterisation.

The bursts began to exhibit signs of nonlinear gain saturation at pump powers of 7 W, but became more apparent at 11 W of pump power as shown in Fig. 7.15. Therefore, 11 W pump power was fixed for the rest of the study. Two methods will be discussed in the

following section. Initially, an analytical approach was taken into consideration for the prediction of the shape of the input bursts (after EOM) to achieve flat gain across the burst width. However, it became apparent that exact knowledge of various experimental parameters, such as burst energy, gain, amplifier saturation energy, as well as the input and output intensity profiles of the burst, is required for this method. Therefore, an algorithmic approach was adopted instead, which only required knowledge of the input, output, and target burst shape.

As shown in Fig. 7.15, the gain saturation causes the pulse intensities in the burst to fall nonlinearly to 35%, 50%, and 55% of the initial peak intensity for 200 ns, 100 ns, and 50 ns, respectively.

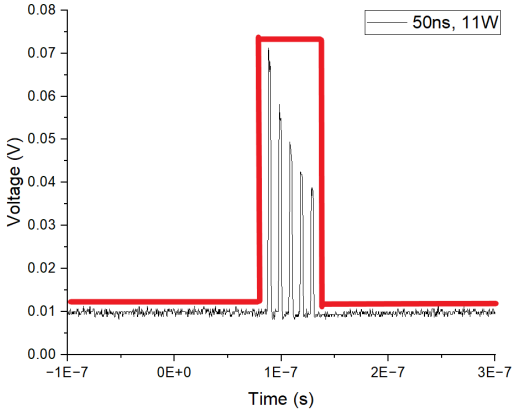

(a) 50 ns BW after the third amplifier.

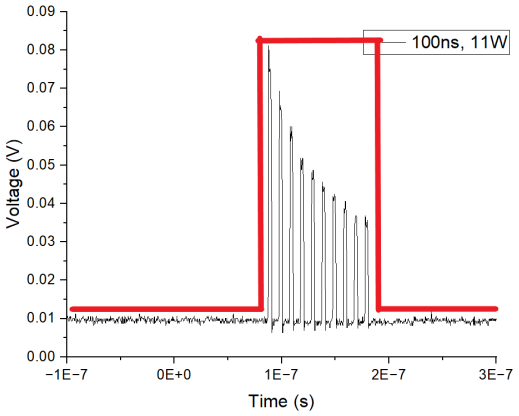

(b) 100 ns BW after the third amplifier.

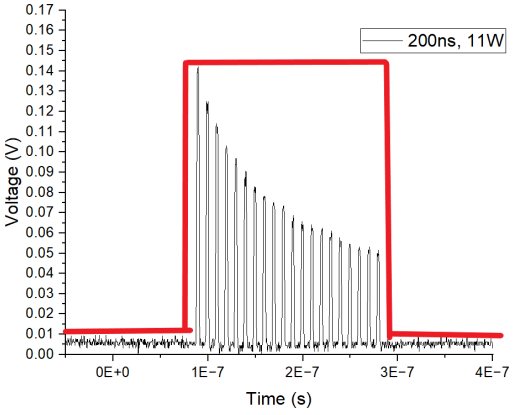

(c) 200 ns BW after the third amplifier.

FIGURE 7.15: Saturated amplified burst profile. A top-hat target envelope is illustrated in red.

7.1.2 Analytical method

All the computations were done in MATLAB, and some assumptions were made to simplify the problem for modelling. The last two amplifiers were treated as one amplifier,

and energy is assumed to be a continuous burst profile rather than in discrete peaks. The full code can be found in Appendix:A for reference.

Firstly, the oscilloscope traces of each burst were imported into MATLAB, and the peaks and their temporal coordinates were extracted into a new array, then normalised. Their actual values were later calculated using known experimental parameters.

Using equation 2.12, the optical input burst profile ($I(t)_{in}$) can be predicted if all the other terms in the equations are known, where t is the intra-burst time. $I(t)_{out}$ is measured at the output of the final stage amplifier and shown in Fig. 7.15; it can be used to calculate $E(t)_{out}$ if both input and output average powers are known. Firstly, the total pulse energy was calculated where $E_{total} = P_{av}/f$. Then, the energy distribution in the burst was found by calculating the area under the normalised burst profile; this was done for both actual and normalised input and output bursts. Unlike the output intensity, where the actual measured data were used, the square input intensity profile was used for the input.

The conversion ratio of the total burst energy to the total normalised burst energy was then used to calculate the actual peak powers in the pulse $P(t)$. This allowed the gain of the amplifier chain to be calculated where $G(t) = I(t)_{out}/I(t)_{in}$. Therefore, by rearranging equation 2.12, plotting the results, and fitting the left-hand side of the equation, G_0 and E_{sat} can be determined. Table 7.2 includes all the relevant measured and calculated parameters mentioned.

TABLE 7.2: Gain, burst energies at 50 ns, 100 ns and 200 ns BW.

BW (ns)	50	100	200
$E_{in}(uJ)$	0.24	0.34	0.47
$E_{out}(uJ)$	24.65	27.10	28.44
Amplifier gain (G) (dB)	20.12	19.01	18.97

This approach assumes nothing about the actual amplifier design parameters but depends on the input and output powers in the system and a goodness-of-fit (GOF) parameter. Apart from the $G(t)$ for which the fitting was tailored for the last step. The MATLAB built-in *"fit"* function *"exp1"* and *"exp2"* that correspond to $a \times e^{bx}$ and $(a \times e^{bx}) + (c \times e^{dx})$, respectively were compared, where a, b, c, d were coefficients to be determined by the fitting. The quality of the fitting increases more with added terms; however, it decreases for a smaller number of peaks.

Since the fitting isn't a reliable approach to modelling the peak powers, a point-wise (PW) approach was adopted instead (i.e using the peaks as discrete points for analysis). All the calculated coefficients were inserted back into the original equation 2.12 to work out a value for the normalised input optical intensity $NI(t)_{in}$.

The transmissivity T of an EOM as a function of the applied voltage can be described as:

$$T = \frac{I_{in}}{I_{out}} = sin^2(\frac{\pi V}{2V_\pi})$$
$$Where,\ V_\pi = \frac{d\lambda}{2Ln_0^3\gamma} \tag{7.1}$$

Due to the sinusoidal response of the EOM to the electrical signal, equation 7.1 was rearranged to make V the subject and was applied to $NI(t)_{in}$ to achieve the desired outcome. The results of using the GOF for the different BW are shown in Fig. 7.16 for comparison.

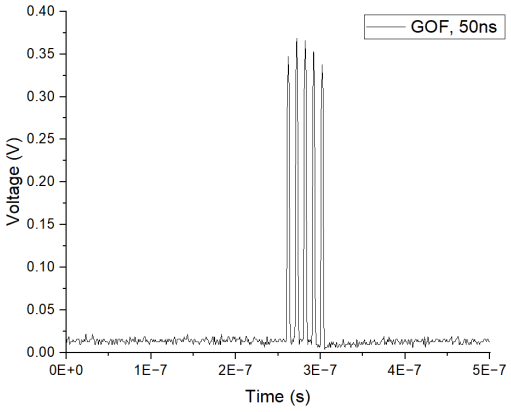

(a) 50 ns BW after the third amplifier.

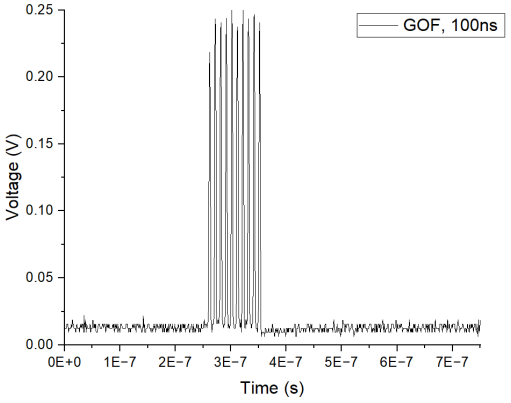

(b) 100 ns BW after the third amplifier.

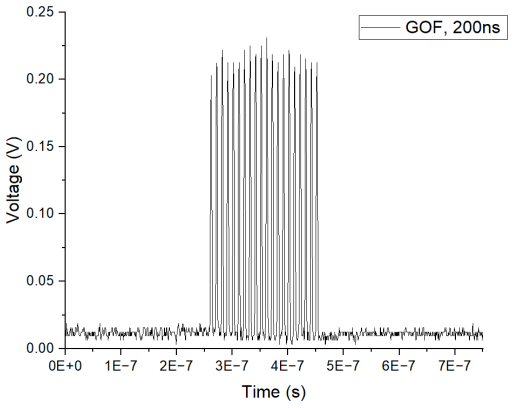

(c) 200 ns BW after the third amplifier.

FIGURE 7.16: Corrected amplified burst profile for 50 ns, 100 ns and 200 ns BW using the GOF method.

The results show an arched burst envelope and the accuracy of the correction seemed to decrease as the number of peaks decreased. The GOF method does not account for instabilities/ noise in the measured data. The results of the predicted input shape for the different burst widths and the corrected output using the point-wise method are shown in Fig. 7.17.

Overall, the correction provided better results when using the PW approach over the GOF one, since it doesn't assume a continuous flow of energy. The pulse outputs shown

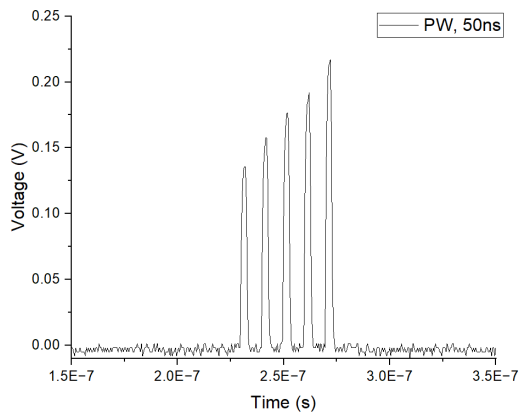

(a) 50 ns BW after the EOM, correction applied.

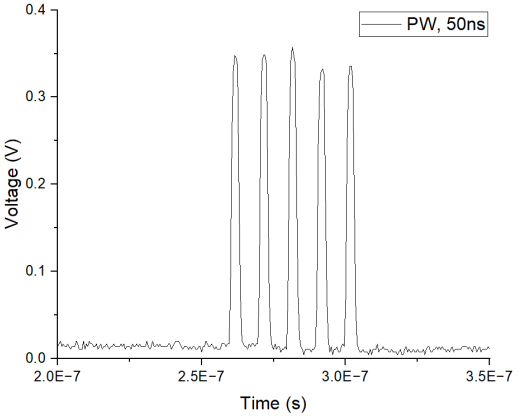

(b) 50 ns BW after the final amplifer, correction applied.

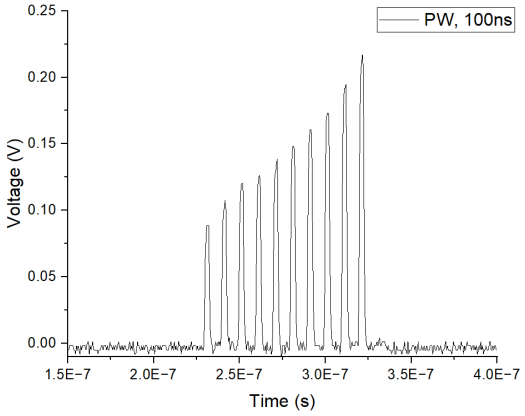

(c) 100 ns BW after the EOM, correction applied.

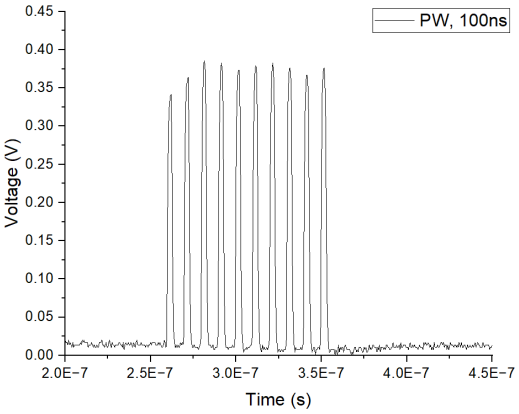

(d) 100 ns BW after the final amplifer, correction applied.

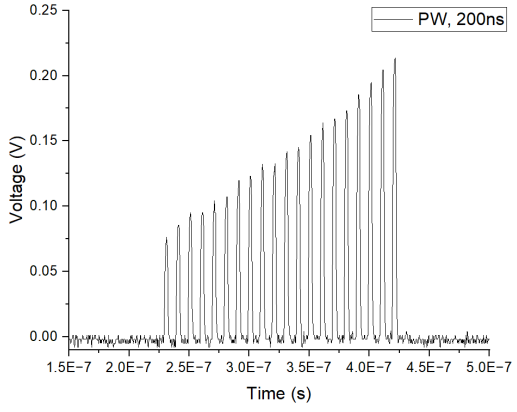

(e) 200 ns BW after the EOM, correction applied.

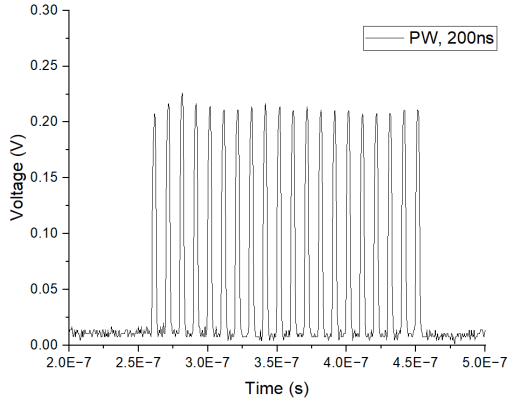

(f) 200 ns BW after the final amplifer, correction applied.

FIGURE 7.17: Before and after corrected amplified burst shape using PW method.

in Fig. 7.17 closely resemble the input pulses before the saturation in the amplifiers. Some modulation is seen in the oscilloscope function for reasons that have already been discussed, but the initial peaks were also lower than expected, which is due to the rise time from the AWG, which is 5 ns for a pulse period of 10 ns.

The correction method was challenged applying it to two burst; however, after closer examination, the complexity of the problem and the computation time increased with the additional bursts using this method. Therefore, a new method to undertake a multi-burst problem is needed.

7.1.3 Algorithmic method

The idea for an iterative method, as proposed by *Li et al.* [6], was adopted. The advantage of this method over the analytical one is its flexibility. No prior knowledge of the experimental parameters was needed, only the saturated output burst envelope profile, which changes with each iteration. During the correction process, the laser will be continuously running. Therefore, the experimental procedure needs to be updated to account for the closing of the EOM and resetting of the AWG for each updated loop. To do this, a voltage offset of 1 V was set in the AWG, maintaining the same $Vpk - pk = V_\pi$ of 5.5 V. To compensate for the change, the DC was adjusted to a fixed value that does not change each loop. Therefore, the EOM doesn't fully close during each reset. The EOM output power was measured when the adjusted DC bias was applied in the absence of the AWG signal, showing an average power of 5.75 mW. This will feed into the later amplifier stages during reset to avoid damage due to the absence of a signal in the amplifier.

The laser was safe for continuous operation. The next step was to set up communication between the AWG, oscilloscope, and laptop. The instrument control toolbox is a built-in feature that allows MATLAB to connect and exchange Standard Commands for Programmable Instruments (SCPI) information using Virtual Instrument Software Architecture (VISA). The source code for initiating the connection with the instrumentation was obtained from the MATLAB File Exchange, where community members upload example codes. However, the remaining code for controlling the instrumentation was developed from scratch using the programming guide provided by the manufacturer. Two original scripts were written for communicating with the AWG and oscilloscope separately, and their functions were called in the main script, where the synchronisation and calculations are done. I devised an algorithmic mathematical model for iteratively correcting the saturation in the amplifier. The formula states:

$$\begin{aligned} f_i\tilde{(t)}_n &= f_i\tilde{(t)}_{n-1} + [f_o\tilde{(t)}_{n-1} - f_T\tilde{(t)}] \\ Where, f\tilde{(t)} &= \frac{f(t)}{|f(t)|} \end{aligned} \tag{7.2}$$

Where $f_i(t)$ and $f_o(t)$ are functions that describes the envelope of the amplifier input and output respectively, n indicates the loop iteration number and $f_T\tilde{(t)}$ is the target envelope function, which resembles the initial observed signal at the output of the EOM

as seen in Fig. 7.8. Equation 7.2 takes the difference between the current output and the target shape and adds it to the input from the previous loop, and the function is normalised to create the input for the next loop. The process is repeated until the target shape is reached. The condition for meeting the target shape was defined later in the code by working out the difference between the mean of the peaks of the current output to the previous output, whereby if the $1.001 \leq f_o(t)_{n-1}/f_o(t)_n \leq 0.999$, the loop would stop. A sinusoidal transformation was finally applied to $f_i(t)_n$, similar to the previous method. The results with and without this condition proved to be very similar when the loop was manually or automatically terminated. The analysis is done by PW since it represents the problem more accurately.

Two methods, fitting and interpolation, were compared at the final output of the amplifiers in order to increase the number of data points beyond the number of peaks (e.g 20 peaks, 20 points in a 200 ns burst) to 1000 points for a higher shaping waveform resolution from AWG. The comparison for the output function can be seen in Fig. 7.18. Interpolation better addresses the imperfections in the signal due to noise and amplifier instabilities.

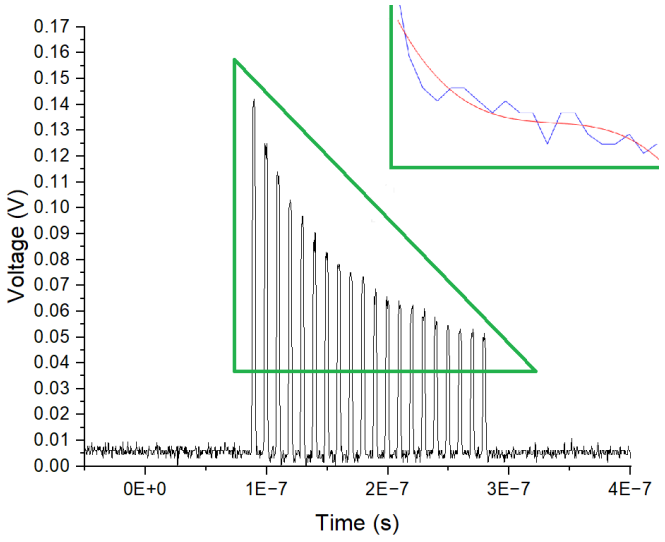

FIGURE 7.18: Interpolation (blue) vs fitting (red) of a 200 ns burst peaks points.

Only a 200 ns burst window was tested using this approach, and the results showed that saturation correction for a signal burst can be achieved within 10 iterations, as shown in Fig. 7.19.

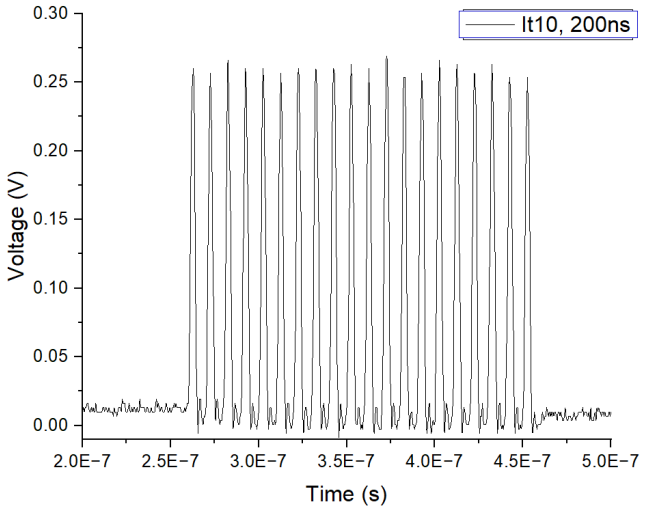

FIGURE 7.19: Corrected amplified 200 ns burst width after 10 iterations.

The flexibility and other applications of this method have been explored. Various target shapes can be set for different applications, delivering burst energies at different rates. Here, 2 different "h" shapes have been demonstrated, and the results seen in Fig. 7.20 were achieved after 9 to 10 iterations. Starting from Fig. 7.15(c) with 200 ns BW, for demonstration purposes, the target shape is highlighted in red, where 2 flat steps from 50% to 100% intensities each 100 ns long were set.

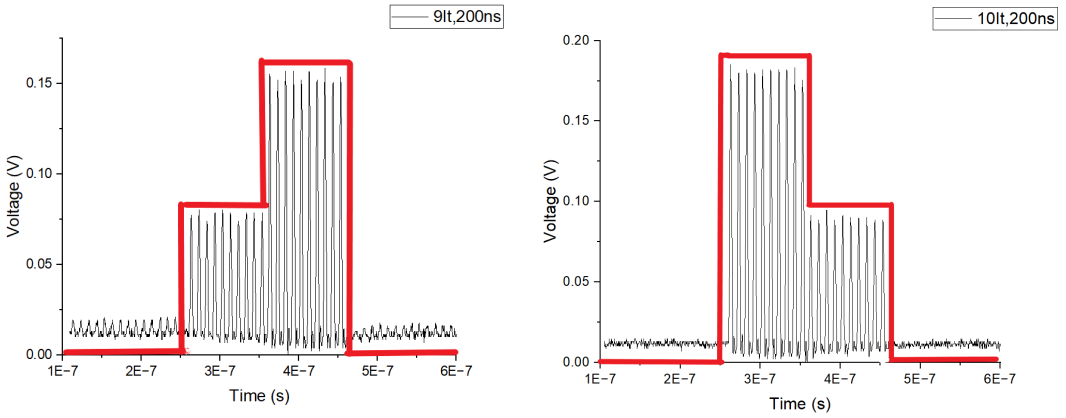

(a) a reverse "h" shape achieved as after 9 iterations

(b) an "h" shaped achieved as after 9 iterations

FIGURE 7.20: Non-uniform burst target shapes achieved using the iterative method. Red lines show the target envelope shape; 100 ns steps from 50%to 100% were set.

7.2 Non-uniform burst window shaping

The algorithmic method was carried out to achieve a long signal correction due to its flexibility and capabilities of simplifying an otherwise complicated mathematical problem. The development of saturation correction over a multi-burst signal was carried out

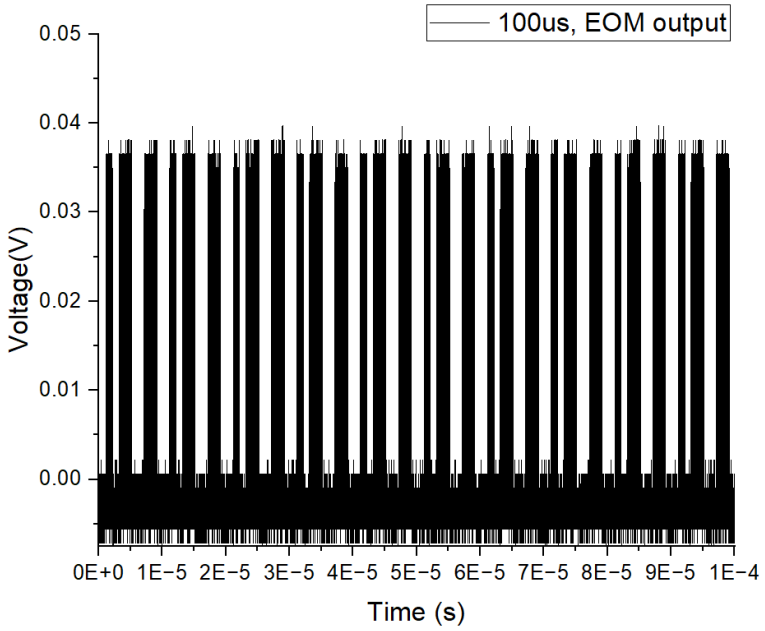

FIGURE 7.21: 100 μs non-uniform signal. 10:1 data points to peak ratio extracted from oscilloscope.

at 100 μs to reduce the data size, increase computational speed, and for ease of visualisation of the changes. The approach was later tested up to 1 ms. Firstly, a 100-point random binary array was created in MATLAB and exported to the AWG to create a non-uniform burst train. 1 point equates to 1 μs and translates to opening or closing the EOM. The optical signal after EOM is represented in Fig. 7.21. This also serves to create the target shape (more on this later).

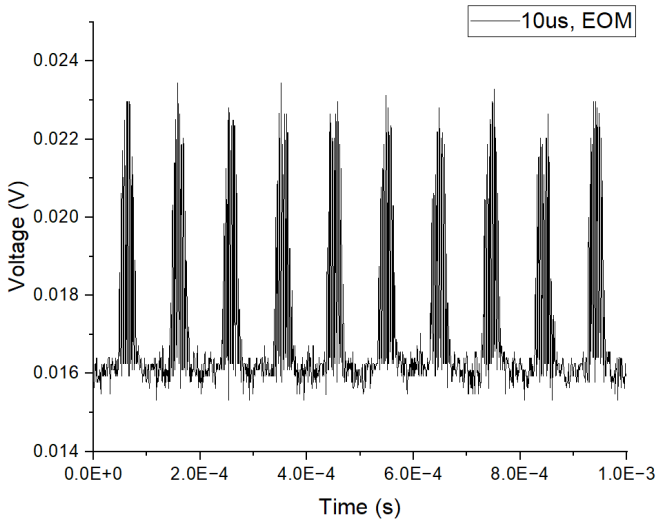

FIGURE 7.22: 10 μs non-uniform signal. 1:1 data points to peak ratio extracted from oscilloscope.

10,000 peaks exist in a 100 μs period of a 100 MHz RR signal. The number of data

points in Fig. 7.21 is 100,000, which is 10 times the number of peaks. This is the minimum number of points that can be extracted from the oscilloscope to get an accurate representation of the signal. Features are lost when fewer data points were extracted, as shown in Fig. 7.22 where a 1:1 peak to data point ratio was exported (same pattern, zoomed in). The maximum number of data points that can be extracted from the oscilloscope used in this study was determined experimentally to be 1 million points. It should also be noted that a maximum of 100,000 points array can be imported into the AWG.

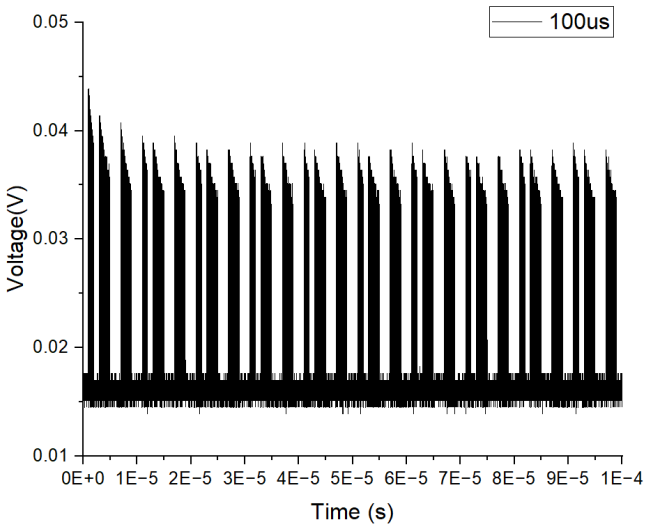

FIGURE 7.23: Amplified saturated output of 100 μs non-uniform signal.

At 11 W of pumping power, the saturated output was measured, and the results are represented in Fig. 7.23. It is seen that noise and instabilities can be observed in the signal. The use of a high-pass filter was tested; however, no significant improvements have been observed. Instead, filtering was carried out computationally after importing the signal. Firstly, all the amplitude values that fall below 40% of the maximum were set to zero, removing all the ground-level noise and maintaining the array pattern. Secondly, any point that falls outside 2 standard deviations (σ) of the mean was initially set to zero and then replaced with an average value between the leading and trailing non-zero values to reduce the noise in the peaks of the signal. The peak location is then extracted using the "findpeaks" function in MATLAB (See Fig. 7.24).

A new and reduced array size equal to the total number of pulses is created. For every 10 peaks, 1 peak represents a pulse, assuming that there can only exist 1 peak per 1 pulse. The total array number corresponding to each amplitude value is divided by the number of the expected/ reduced array size and rounded to the nearest integer. This creates a scenario where the location of the data point is the same for the product of *(oscilloscope array size/ reduced array size)*. The maximum value is extracted from each set, assuming it corresponds to the actual peak. The temporal, peak and new array number properties were inserted into a new array where all the non-peak values were set

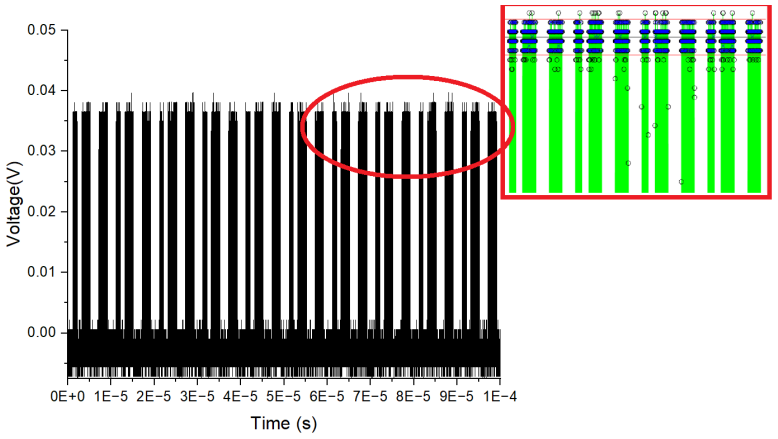

FIGURE 7.24: A snapshot of peak filtering in MATLAB. Oscilloscope trace (green) is imported, the peaks were identified (black circles) and filtered (blue), horizontal lines showing mean, upper and lower limits.

to zero. All these pre-processing steps were taken to ensure signal properties (pattern) are maintained while eliminating noise that interferes with the calculations and is in an appropriate format for the equipment to handle. During the first loop only, based on the pre-processing, the target frame is also created at the reduced array size, which was sent into the AWG, and no further analyses were done. These are common principles used in imaging analysis that have been adapted to deal with this problem.

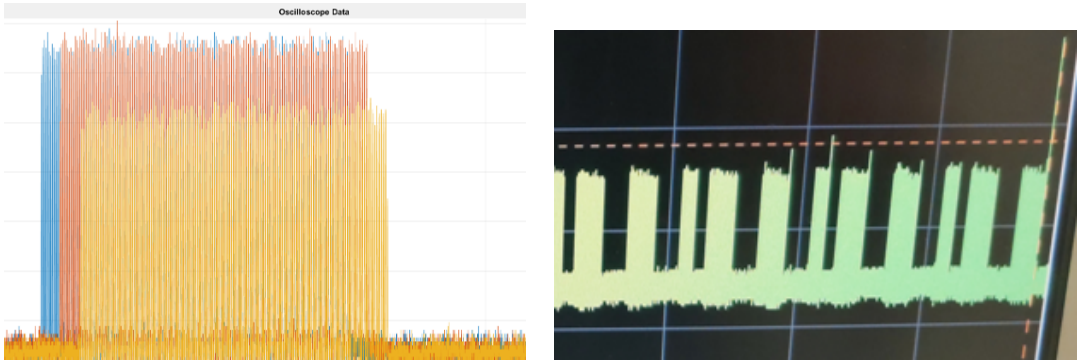

(a) Delay in the imported oscilloscope signal in MATLAB between each loop.

(b) A snap shot from the oscilloscope showing the evolution of optical noise after a number of iteration.

FIGURE 7.25: Common issues encountered during development such as delay and noise.

As for the following loop iterations, the remaining steps were repeated using the reduced array size as a frame instead of the initial 100-point array. Equation 7.2 is applied on the non-zero values in each array while accounting for the delay in-between each oscilloscope reading as seen in Fig. 7.25(a). This was carried out by finding the start of each non-zero value and carrying out the calculation. Finally, post-filtering is applied to the data again, setting any data point that falls outside 2 σ to zero if it is at the edge of the burst or to an average of the two neighbouring peaks. This is found to reduce an effect that has been observed to parasitically grow any unfiltered noise peaks in each loop, as shown in Fig. 7.25(b).

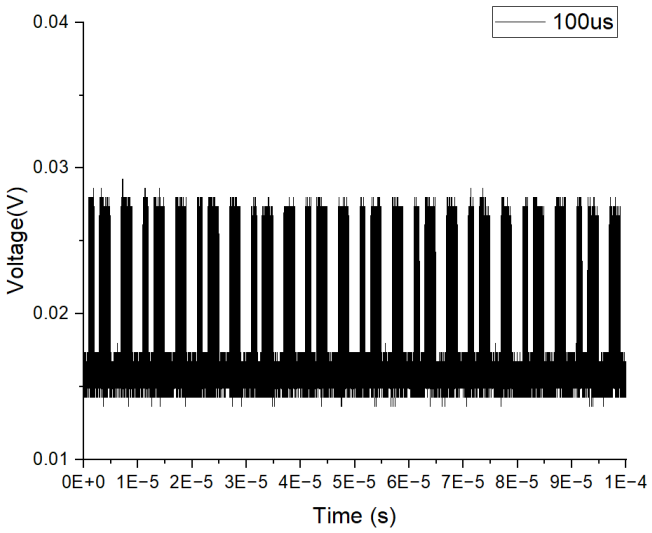

FIGURE 7.26: Amplifier output after 3 correction loop runs for a 100 μs signal.

The results are represented in Fig. 7.27; they suggest that correction of the output can be achieved after 3-5 iterations for both 100 μs and 1 ms signals, as shown in Fig. 7.26. The equipment was pushed to the maximum number of data points at 1 ms for a 100 MHz frequency. A further time window can be achieved at a lower intra-burst RR.

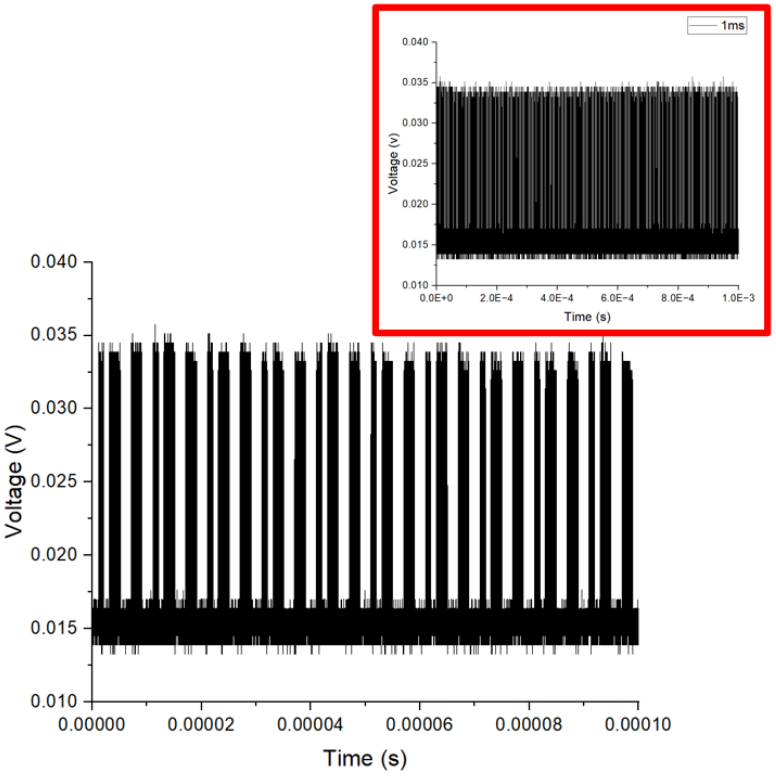

FIGURE 7.27: 1 ms non-uniform signal zoomed to 100 μs; Inset: Flat peaks from 4 loop iterations for a 1 ms non-uniform signal.

Although gain-saturation correction and flat burst outputs were achieved for durations

up to 1 ms, the speed of the electronics imposes a limit on the amount of data and correction that can be processed at one time. Consequently, in a practical experimental environment, the program would need to be executed multiple times for different pixel lines, followed by separate loops applied to smaller data segments to achieve low noise and accurate correction. Further work is also required to synchronise the microscope with the laser system.

Moreover, the principles used here form the basis of several machine-learning approaches, suggesting that the development of a machine-learning model could be beneficial for handling this type of correction in order to achieve higher complexity levels of correction at faster rates.

Chapter 8

Conclusions and Future work

8.1 Conclusions

To summarise, I have presented the development of various fibre-laser technologies for multiphoton imaging applications. Different thulium fibres (both commercial and purpose-developed) were used as gain media to generate laser output within the optical transparency window of 1600–1850 nm. An emphasis on the development of novel pulse compression and short thulium wavelength tuning techniques was investigated with the purpose of generating more adaptive pulses for deep-tissue biological imaging.

A robust mode-locked fibre laser operating at 1845 nm, capable of producing compressed pulse outputs of 380 fs, was developed using entirely non-PM components. The laser relied on a CNT for saturable absorption to achieve mode-locking. The polarisation-insensitive nature of the mode-locked laser cavity enhanced its stability and made it resistant to small environmental changes, such as temperature fluctuations and vibrations. The peak power performance was improved through CPA, which incorporated a DCF for pulse stretching, along with a series of thulium-doped amplifiers. A modulator was placed before the second stage of amplification to reduce the RR, thereby increasing the pulse energy per pulse while keeping the average power relatively low to avoid thermal damage to biological samples.

This system was sent to IFLS, and it showed an increase in the penetration depth from 40 μm at the fundamental RR to 90 μm, in a similar sample, at the lowest RR of 2 MHz. However, several limitations on the maximum attainable depths for imaging were identified. Although reducing the RR increased the peak power and allowed for greater penetration depths, excessively lowering the RR could lead to complications such as increased ASE and parasitic lasing that give rise to photon shot noise during imaging. Therefore, alternative methods for scaling peak powers while maintaining low average power are necessary. Additionally, the operating wavelength of the laser was not at the minimum water absorption, which increased the risk of thermal damage to the tissue.

Therefore, the next work was carried out to develop novel ways of increasing the peak power without RR manipulation but rather by enhanced pulse compression. Simultaneously, the operating wavelength of the laser was shifted to be shorter for lower biological attenuation. These systems featured a short length of TDF, which minimised the reabsorption of the signal at the short wavelength, resulting in a 1789 nm laser output. The net dispersion of the laser of the mode-locked cavity was shifted towards zero, ensuring maximum laser output and bandwidth were emitted. This gave a TFL pulse duration of 270 fs, which was much shorter than any of the previously developed ML lasers in this project.

A novel amplifier design was adopted to achieve an even shorter compressed pulse duration. Two nonlinear compression methods were explored. The first involved the management of the input chirp into the final amplifier by controlling the input pulse width, dependant upon the length of the DCF used, which resulted in a 180 fs although pulse with significant pedestal generation. The second method that was explored also resulted in a 180 fs compressed pulse duration, but the generated pedestal was much lower. This was due to the generation of a coherent pulse broadening of the pulse in a positive near-zero dispersion, HNF before CPA. Both techniques, however, involved the use of a free-space compressor grating to compress the pulse due to the high peak powers traversing the fibre.

Another mode-locked fibre laser was built, exploring the limit of the short wavelength emission. Bending-induced losses of a low V-number DCF were used, creating a short pass filter with a strong suppression of the long wavelengths and a tunable cut-off wavelength dependent on the bending diameter. The strong suppression allowed the use of longer TDF in the mode-locking cavity, thus increasing the output pulse energy. Furthermore, a tunable mode-locked cavity emitting pulses from 1900-1725 nm, makes it ideal for many applications requiring wavelength specific outputs. The ML laser used CNT as a SA, and the dispersion managed to ensure a net negative dispersion yet close to zero, creating a stretch-pulse soliton with a Gaussian-like spectrum, which is better for pulse compression than a dissipative soliton. This resulted in a 320 fs compressed pulse duration with no observable pedestal. The laser output was enhanced using a novel amplification method utilising a short pass filter for enhanced ASE suppression.

Initially in the project (Chapters 3-5), the ultrafast pulses were generated from mode-locked cavities. This proved to be a challenging and time-consuming task throughout the PhD as it requires careful cavity design to ensure balanced gain, losses, dispersion and nonlinear management. An alternative laser source was proposed for the ultrafast pulse generation as it is an off-the-shelf, cheap, environmentally stable and electrically tunable source. Laser diodes, however, output low-power, picosecond pulses with a narrow bandwidth and nonlinear chirp, making it challenging to compress them into femtosecond pulses. To enhance the pulse energy, a series of amplifiers was built and the higher peak power was used to broaden the pulse spectrum in an HNF fibre. Various

compression methods were tested in the later stages, and it was found that the use of a spectral filter was necessary for pedestal suppression. Whereas a two-stage compression method involving an initial linear compression and nonlinear compression by soliton formation in an amplifier was found to output pulse durations down to 560 fs, proving great potential for biological imaging applications.

Moreover, it should be highlighted that the two-stage nonlinear compression method was featured in both chapter 4 as NCPA and chapter 6 as soliton compression. The former caused coherent pulse broadening in a normal dispersion HNF, whereas the latter showed coherent pulse broadening and compression in an anomalous dispersion amplifier. The common dominator is the linear pulse compression at the input of the nonlinear stages, which results in an "exaggeration" of the wanted nonlinear effects that lead to coherent pulse broadening over the unwanted nonlinear effects that lead to optical pulse breaking or Raman. This is because, the linear part of the SPM induced positive nonlinear chirp, which scales with the "steepness" of the optical pulse. This technique holds exciting potential in ultrafast pulse generation in the anomalous dispersion region where parabolic pulse shaping is not possible.

Finally, the LD source was used in conjunction with an AOM, AWG, PG and assisted computational programming to simulate an arbitrary spread of ROI by an arbitrary pulse train made up of optical bursts of pulses. Two methods for pre-shaping the optical signal into an amplifier chain to correct for gain saturation effects during amplification of a non-uniform burst signal have been demonstrated on a single burst as short as 50 ns, which was adapted to a multi-burst signal up to 1 ms.

8.2 Future work

8.2.1 Upgrading current imaging technology

Throughout the project, several innovative systems were built featuring novel techniques for pulse generation and compression separately. These techniques should be combined into a single optimum system for multiphoton imaging as proposed in Fig. 8.1. Furthermore, the effects of the shorter wavelength and compressed pulse duration on the deep-tissue imaging need to be investigated, and the limitations for deeper imaging need to be identified to build a laser capable of overcoming them. The first step would be replacing the source of the current imaging laser with the 1789 nm ML laser and adding the HNF fibre directly at the output of the fibre to produce a broad coherent spectrum, as mentioned in chapter 4. With the incorporation of the amplifier stage post modulation as used in the current imaging laser. Higher peak powers will be achieved, at the lower RRs, due to the enhanced pulse compression detailed in chapter 4. This gives 2 initial metrics for deep-tissue imaging investigation, capitalising on enhanced compressed pulse

and shorter wavelength. The initial stages of the amplifier have already been tested and characterised as seen in chapter 4; however, the rest of the system and incorporation of the optical modulators still need to be developed, optimised, and characterised before for nonlinear imaging. Alternatively, the tunable ML seed laser presented in chapter 5 can be incorporated into the imaging laser, along with the nonlinear pulse amplification and compression detailed in the same chapter. This would allow for the simultaneous investigation of the effect of different wavelength emissions on deep-tissue imaging. The challenge of this approach would be in the amplification, since the thulium gain profile is not flat; therefore, different wavelengths would experience different powers and pulse evolution in the system and may result in unexpected outcomes. To make this possible, investigations need to be taken into developing a flat gain profile thulium amplifier similar to the ones seen in telecom applications.

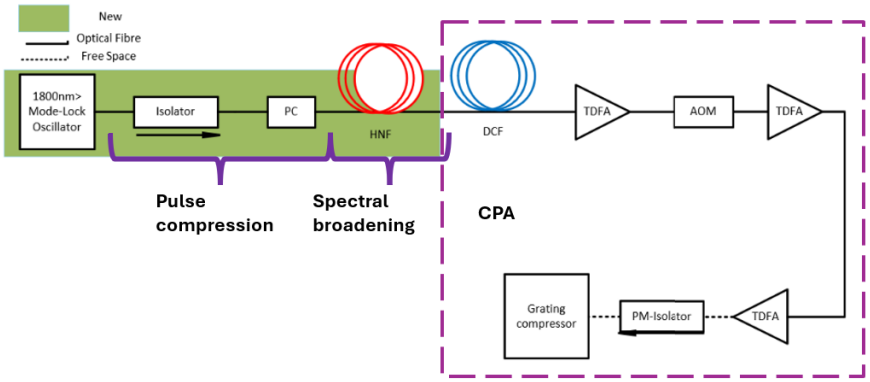

FIGURE 8.1: Schematics of the imaging laser incorporating NCPA and operating at the short wavelength of thulium.

Nonetheless, the expected imaging results from the updated laser system would suggest the next steps to be taken are to aim to refine those techniques demonstrated thus far for achieving higher pulse energies and shorter compressed pulse durations below 100 fs. Both can be done with careful management of the pulse evolution and amplification while accounting, and compensating for, higher-order dispersion effects. Whereas, the optimum wavelength for imaging would be identified and tested since the shortest achievable wavelength from thulium fibre is very close to the shortest wavelength feasible, as demonstrated in chapter 5.

8.2.2 Alternative to mode-locked systems

In chapter 7, the usability and potential of a GSLD as an alternative pulsed laser source to mode-locking were demonstrated. Computer integration, electronically controlled thermal stability, complex waveform generation and femtosecond pulse generation were shown. This provides a compact, cost and time-effective solution for multiphoton imaging sources. Many readily available components that emit various wavelengths can be

easily purchased and integrated into a laser system, addressing the critical issue of short wavelength emission in thulium-based mode-locked lasers. The caveat, however, is the pulse-to-pulse jitter (or fluctuation) and degradation of the side mode suppression ratio as a result of electronically driven emission and voltage-dependent refractive index in the diode laser cavity. Future work, with these sources, should include careful monitoring and control of the pulse-to-pulse jitter and aim to mitigate this. Methods in literature that have been shown to reduce this effect include injection of CW light into the laser cavity or self-seeding.

Another improvement that can be used in the system presented in chapter 6 is in the pulse compression. The first limitation is believed to come from the bandwidth of the spectral filter, as it was too broad for the generated spectrum, allowing some nonlinear chirp to transmit to the subsequent stage of compression and manifesting as a pedestal. This can be improved by a SPM-induced spectral broadening or via the use of a narrower spectral filter. Aside from the offset filter induced saturable absorption, other artificial saturable absorption mechanisms, such a NALM/NOLM, can be integrated into the system to improve the pedestal suppression and overall pulse coherence for compression.

Furthermore, the pulse compression demonstrated great benefits from the anomalous dispersion of the fibres used at this lasing wavelength. However, a deeper understanding of the compression method is needed by investigating the generation of higher-order solitons or adiabatic pulse compression in the final stages, and their effects on the final pulse output. More sophisticated measuring equipment, such as FROG, if available, can be used to reveal a more in-depth insight into the compressed pulse chirp. Thus enabling prediction of the pulse evolution in the system can be made thus improving the overall pulse compression by applying methods to reduce/ compensate for higher-order dispersion effects, such as specialised fibres with waveguide shifted dispersion design.

Finally, the arbitrary pulse train generation and gain compensation technology should be combined with the ultrafast GSLD work (or with mode-locked systems) for selective imaging of biological samples. Before applying this for real-world uses, the technology developed should be applied using a shorter-wavelength laser diode, as it will benefit from deeper tissue penetration. Furthermore, fine-tuning parameters of the method to solidify the usability of the system includes the use of faster driving electronics, allowing a shorter initial pulse generation and lower RR. There would be a rise in the risk of generating higher levels of ASE as a result of the reduced duty cycle. To prevent this, an additional pre-amplification stage should be added or a spectral filter. Alternatively, a high RR could be set from the initial laser diode driver, and after the initial pre-amp stages, an optical modulator can be used to lower the RR.

8.2.3 Mamyshev oscillator

As depicted in Fig. 8.2, a Mamyshev oscillator (MO) consists of two MRs. The work carried out in chapter 6 can be expanded and steered in the direction of forming an MO, which would be capable of producing very high output pulse energies and femtosecond pulse durations. Two potential architectures can be adopted to achieve this, either by means of building a linear or circular cavity. A linear cavity would require a reflective grating filter at either end of the amplifier chain, whereas the circular cavity would use two bandpass filters separating the amplifiers and spectral broadening sections. The filter used would also need to be offset from the central peak of the seed pulse, as well as being both blue and red-shifted. The separation distance of the spectral filters also plays a role in the output pulse bandwidth, energy and overall compression; therefore, a tunable filter should be used to identify the optimum operational parameter of the oscillator. A tunable filter source would have the added benefits of creating a starting mechanism since such lasers often struggle with self-starting. Another major issue with such a mode-locked cavity at the anomalous dispersion wavelength is the soliton formation, which greatly limits the pulse energy formed from such cavities and may result in optical wave-breaking as a result of the high power used to drive the system. Throughout the thesis, several techniques mitigating these effects have been discussed, and studies can be applied and tested in this laser format.

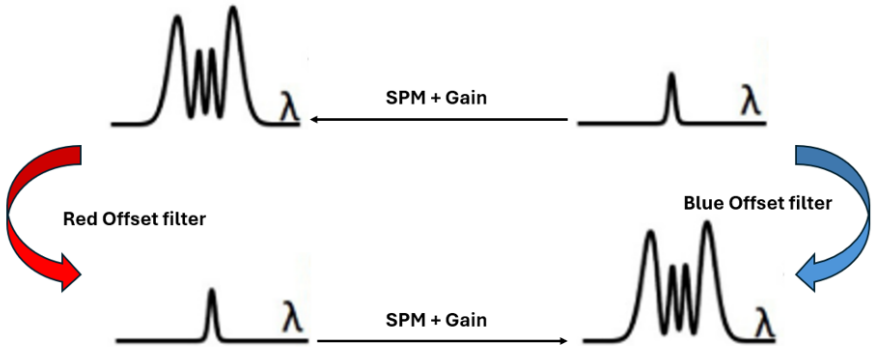

FIGURE 8.2: Schematics of the Mamyshev oscillator.

8.2.4 Novel thulium-doped fibres

Several thulium-doped fibres were tested through this project and were used in different applications. However, all the active fibres tested have an anomalous dispersion. There have been reports in literature of normal dispersion thulium-doped fibre, such as soft glass fibres (ZBLAN) and the W-type fibre made in-house at Nanyang Technological

University. Such fibres allow parabolic pulse propagation and are of great interest in nonlinear applications and pulse compression since the phase function as a result of the nonlinearity in such a pulse is largely linear across the pulse shape. Therefore, they allow for high pulse energy and broad pulse bandwidth, mitigate optical wave-breaking effects, and provide excellent pulse compression with suppressed pedestal formation. To date, no report of parabolic pulse formation in silica-based thulium fibres has been mentioned. These fibres have great potential to achieve this, either by integrating them into amplifiers or mode-locked cavities.

8.3 Publication list

8.3.1 Conferences

1. Lin Xu, Duanyang Xu, Konstantinos N. Bourdakos, Peter B. Johnson, Anna Crisford, **Ibrahim Abughazaleh**, Panuwat Srisamran, Qiang Fu, Sumeet Mahajan, and David J. Richardson, "1840 nm femtosecond thulium fiber laser system for label-free third-harmonic generation microscopy," in *Conference on Lasers and Electro-Optics (CLEO)*, Technical Digest Series (Optica Publishing Group), paper JM4E.5 (2022).

2. Konstantinos N. Bourdakos, Lin Xu, Duanyang Xu, Peter B. Johnson, Anna Crisford, **Ibrahim Abughazaleh**, Panuwat Srisamran, Qiang Fu, Richard O. C. Oreffo, David J. Richardson, and Sumeet Mahajan, "Third harmonic generation deep-tissue imaging with a thulium fiber laser at 1840 nm," *CLEO AT*, 10.1364/JM4E.5 (2022).

3. Panuwat Srisamran, Duanyang Xu, **Ibrahim Abughazaleh**, Matthew Gerard, Sijing Liang, David Richardson, and Lin Xu, "1875-nm high-energy mode-locked thulium fiber laser," *EPJ Web of Conferences (EuroPhoton)* 267, 02013 (2022).

4. Konstantinos N. Bourdakos, Lin Xu, Anna Crisford, Duanyang Xu, **Ibrahim Abughazaleh**, Peter B. Johnson, Hiroki Cook, Panuwat Srisamran, Richard O. C. Oreffo, David J. Richardson, and Sumeet Mahajan, "deep-tissue imaging with multiphoton microscopy in the short wavelength infrared windows," *Proc. SPIE* 123330E (2023).

5. **Ibrahim H. Abughazaleh**, Panuwat Srisamran, Matthew D. Gerard, Duanyang Xu, Yongmin Jung, David J. Richardson, and Lin Xu, "Compact 1790-nm dissipative-soliton mode-locked thulium fibre laser," *SPIE 2024*, LA304.

6. **Ibrahim H. Abughazaleh**, Panuwat Srisamran, Duanyang Xu, Yongmin Jung, Richardson, and Lin Xu, "Pre-chirp managed thulium fibre amplifier for 1.8 µm ultrashort pulse generation," *CLEO 2024*, JW2A.38.

7. **Ibrahim H. Abughazaleh**, Panuwat Srisamran, Duanyang Xu, Yongmin Jung, Richardson, and Lin Xu, "Efficient pulse amplification and temporal compression in a 1790 nm femtosecond thulium fibre amplifier," *CLEO-PR 2024*, 60912X.

8. Panuwat Srisamran, **Ibrahim Abughazaleh**, Matthew Gerard, Duanyang Xu, Yongmin Jung, Jing He, Jeremiah Marcellino, Boyang Mao, Andrea Ferrari, David Richardson, and Lin Xu, "All-polarization-maintaining dissipative-soliton mode-locked thulium fiber laser at 1876 nm," *Proc. SPIE*, PC12865G (2024).

9. Panuwat Srisamran, **Ibrahim Abughazaleh**, Duanyang Xu, Matthew Gerard, Sijing Liang, David Richardson, and Lin Xu, *et al.*, "Polarization-Maintaining Dissipative Soliton Mode-Locked Thulium Fiber Laser with a NALM cavity," *CLEO 2025*

10. Konstantinos N. Bourdakos, Lin Xu, Duanyang Xu, Peter B. Johnson, Anna Crisford, **Ibrahim Abughazaleh**, Panuwat Srisamran, Qiang Fu, Richard O. C. Oreffo, David J. Richardson, and Sumeet Mahajan *et al.*, "Nonlinear Optical Microscopy in the short wavelength Infrared Windows for deep-tissue Imaging," *mmc2025* (submitted).

11. Matthew D. Gerard, **Ibrahim H. Abughazaleh**, Panuwat Srisamran, Duanyang Xu, David J. Richardson, and Lin Xu, "All-fiberised picosecond 1.7 μm thulium fibre laser," *Europe-EQEC*, CJ-3.4 (2025).

8.3.2 Journals (Published)

1. Duanyang Xu, Konstantinos N. Bourdakos, Anna Crisford, Peter Johnson, **Ibrahim Abughazaleh**, Panuwat Srisamran, Richard O. C. Oreffo, Sumeet Mahajan, David J. Richardson, and Lin Xu, "All-fiberized 1840-nm femtosecond thulium fiber laser for label-free nonlinear microscopy," *Biomed. Opt. Express* 14, 4520–4530 (2023).

2. Matthew Gerard, Hiroki Cook, James Read, **Ibrahim Abughazaleh**, Panuwat Srisamran, Siddhi Chugh, Sijing Liang, Qiang Fu, Richard O. Oreffo, David Richardson, Sumeet Mahajan, and Lin Xu, "Single-cell high-precision ablation using nanosecond pulsed thulium-doped fiber laser," *Opt. Eng.* 63(8), 086102 (2024).

3. **Ibrahim H. Abughazaleh**, Matthew D. Gerard, Panuwat Srisamran, Duanyang Xu, Yongmin Jung, and Lin Xu, "Femtosecond thulium fiber laser utilizing a gain-switched laser diode," *Opt. Lett.* 50, 3636–3639 (2025).

4. Panuwat Srisamran, **Ibrahim H. Abughazaleh**, Matthew D. Gerard, Duanyang Xu, Yongmin Jung, Jing He, Jeremiah Marcellino, Boyang Mao, Andrea Ferrari, David J. Richardson, and Lin Xu, "Nanojoule-energy-level, polarization-maintaining, dissipative-soliton mode-locked thulium fiber laser at 1876 nm," *Optics & Laser Technology*, 10.1016/j.optlastec.2025.112978 (2025).

5. Panuwat Srisamran, **Ibrahim H. Abughazaleh**, Matthew D. Gerard, Duanyang Xu, Yongmin Jung, David J. Richardson, and Lin Xu, "Polarization-maintaining dissipative-soliton mode-locked thulium fiber laser with a nonlinear-amplifying-loop-mirror cavity operating at 1860 nm", *Optics Express* pp. 1094–4087, 10.1364/OE.559358 (2025).

6. Matthew D. Gerard, **Ibrahim H. Abughazaleh**, Panuwat Srisamran, Duanyang Xu, Yongmin Jung, and Lin Xu, " 1.75-μm multi-watt picosecond-pulsed all-fiberised thulium fibre system seeded by gain-switched laser diode" ,*Optics & Laser Technology*, 10.1016/j.optlastec.2025.112978 (2025).

8.3.3 Journals (In Progress)

1. **Ibrahim H. Abughazaleh** *et al.*, "Power-efficient mode-locked thulium fiber oscillator and nonlinear chirped pulse amplifier for 1789 nm ultrashort pulse generation," (submitted).

2. **Ibrahim H. Abughazaleh** *et al.*, "1740 nm stretch-pulse mode-locked thulium fibre laser by bending-induced short pass filter," *Opt. Express* (to be submitted).

Bibliography

[1] P. Brisset and J. Thereska. Radioactive tracers. In Franco Bassani, Gerald L. Liedl, and Peter Wyder, editors, *Encyclopedia of Condensed Matter Physics*, pages 101–106. Elsevier, Oxford, 2005. URL: https://www.sciencedirect.com/science/article/pii/B0123694019007257, doi:10.1016/B0-12-369401-9/00725-7.

[2] Physiopedia. Mri scans physiopedia,, 2022. [Online; accessed 1-June-2022]. URL: https://www.physio-pedia.com/index.php?title=MRI_Scans&oldid=290333.

[3] Carlo Giussani, Frank-Emmanuel Roux, Jeffrey Ojemann, Erik Sganzerla, David Pirillo, and Costanza Papagno. Is preoperative functional magnetic resonance imaging reliable for language areas mapping in brain tumor surgery? Review of language functional magnetic resonance imaging and direct cortical stimulation correlation studies. *Neurosurgery*, 66:113–20, 11 2009. doi:10.1227/01.NEU.0000360392.15450.C9.

[4] Adam M. Larson. Multiphoton microscopy. *Nature Photonics*, 5(1):1–1, 2010. doi:10.1038/nphoton.an.2010.2.

[5] Sergii Golovynskyi, Iuliia Golovynska, Ludmila I. Stepanova, Oleksandr I. Datsenko, Liwei Liu, Junle Qu, and Tymish Y. Ohulchanskyy. Optical windows for head tissues in near-infrared and short-wave infrared regions: Approaching transcranial light applications. *Journal of Biophotonics*, 11(12):e201800141, 2018. URL: https://onlinelibrary.wiley.com/doi/abs/10.1002/jbio.201800141, arXiv:https://onlinelibrary.wiley.com/doi/pdf/10.1002/jbio.201800141, doi:10.1002/jbio.201800141.

[6] Bo Li, Chunyan Wu, Mengran Wang, Kriti Charan, and Chris Xu. An adaptive excitation source for high-speed multiphoton microscopy. *Nature methods*, 17(2):163–166, 2020.

[7] Evangelia Gavgiotaki, George Filippidis, Vassilis Tsafas, Savvas Bovasianos, George Kenanakis, Vasilios Georgoulias, Maria Tzardi, Sofia Agelaki, and Irene Athanassakis. Third harmonic generation microscopy distinguishes malignant cell grade in human breast tissue biopsies. *Scientific Reports*, 10(1), 2020. doi:10.1038/s41598-020-67857-y.

[8] Claudia Florindo. Overcoming photobleaching and phototoxicity in imaging, 2019. URL: https://www.oxinst.com/learning/view/article/how-to-overcome-photobleaching-and-phototoxicity-in-live-cell-imaging.

[9] Eva Hemmer, Antonio Benayas, Francois Legare, and Fiorenzo Vetrone. Exploiting the biological windows: Current perspectives on fluorescent bioprobes emitting above 1000 nm. *Nanoscale Horizons*, 1, 01 2016. doi:10.1039/C5NH00073D.

[10] K. Yelen, L.M.B. Hickey, and M.N. Zervas. Experimentally verified modeling of erbium-ytterbium co-doped DFB fiber lasers. *Journal of Lightwave Technology*, 23(3):1380–1392, 2005. doi:10.1109/jlt.2005.843477.

[11] Søren Dyøe Agger and Jørn Hedegaard Povlsen. Emission and absorption cross section of thulium doped silica fibers. *Opt. Express*, 14(1):50–57, Jan 2006. URL: http://opg.optica.org/oe/abstract.cfm?URI=oe-14-1-50, doi:10.1364/OPEX.14.000050.

[12] Michael J. Redlich, Brad Prall, Edesly Canto-Said, Yevgeniy Busarov, Lilit Shirinyan-Tuka, Arafat Meah, and Hyungsik Lim. High-pulse-energy multiphoton imaging of neurons and oligodendrocytes in deep murine brain with a fiber laser. *Scientific Reports*, 11(1):1–12, 2021. doi:10.1038/s41598-021-86924-6.

[13] R. Gumenyuk, I. Vartiainen, H. Tuovinen, and O. G. Okhotnikov. Dissipative dispersion-managed soliton 2 μm Tm-Ho fiber laser. *2011 Conference on Lasers and Electro-Optics Europe and 12th European Quantum Electronics Conference, CLEO Europe 2011*, 36(5):609–611, 2011. doi:10.1109/CLEOE.2011.5943010.

[14] Zhengqi Ren, Qiang Fu, Lin Xu, Jonathan H. V. Price, Shaif ul Alam, and David J. Richardson. Compact, high repetition rate, 4.2 MW peak power, 1925 nm, thulium-doped fiber chirped-pulse amplification system with dissipative soliton seed laser. *Opt. Express*, 27(25):36741–36749, Dec 2019. URL: http://opg.optica.org/oe/abstract.cfm?URI=oe-27-25-36741, doi:10.1364/OE.27.036741.

[15] C. Lefort. Jablonski diagram of one, two and three photon fluorescence and second and third harmonic generation. Report in the Optical Microscopy for Nanotechnology course Microscopy 2020, 2017. https://www.researchgate.net/publication/342304496_Jablonski_diagram_of_one_two_and_three_photon_fluorescence_and_second_and_third_harmonic_generation.

[16] Youbo Zhao and Nicusor V. Iftimia. 13 - overview of supercontinuum sources for multiphoton microscopy and optical biopsy. In Robert R. Alfano and Lingyan Shi, editors, *Neurophotonics and Biomedical Spectroscopy*, Nanophotonics, pages 329–351. Elsevier, 2019. URL: https://www.sciencedirect.com/science/article/pii/B9780323480673000135, doi:10.1016/B978-0-323-48067-3.00013-5.

[17] Hye Jin Cho, Hoon Jai Chun, Eun Sun Kim, and Bong Rae Cho. Multiphoton microscopy: an introduction to gastroenterologists. *World Journal of Gastroenterology: WJG*, 17(40):4456, 2011.

[18] Class 5 Photonics. Multiphoton microscopy, 2025. Accessed: 2025-08-16. URL: https://www.class5photonics.com/applications/multi-photon-microscopy/.

[19] Henry Pinkard, Hratch Baghdassarian, Adriana Mujal, Ed Roberts, Kenneth H Hu, Daniel Haim Friedman, Ivana Malenica, Taylor Shagam, Adam Fries, Kaitlin Corbin, et al. Learned adaptive multiphoton illumination microscopy for large-scale immune response imaging. *Nature communications*, 12(1):1–14, 2021.

[20] Ilze Oshina and Janis Spigulis. Beer–lambert law for optical tissue diagnostics: current state of the art and the main limitations. *Journal of Biomedical Optics*, 26(10):100901, 2021.

[21] A.E. Siegman. *Lasers*. University Science Books, 1986. URL: https://books.google.co.uk/books?id=1BZVwUZLTkAC.

[22] Paul McManamon. *Three-Level and Four-Level Lasers*, pages 63–64. SPIE Press, 2015. https://www.spiedigitallibrary.org/ebooks/FG/Field-Guide-to-Lidar/Three-Level-and-Four-Level-Lasers/Three-Level-and-Four-Level-Lasers/10.1117/3.2186106.ch63. URL: https://lens.org/030-977-857-266-48X, doi:10.1117/3.2186106.ch63.

[23] Andrew Malinowski, Khu Tri Vu, Kang Kang Chen, Johan Nilsson, Yoonchan Jeong, Shaiful Alam, Dejiao Lin, and David J. Richardson. High power pulsed fiber mopa system incorporating electro-optic modulator based adaptive pulse shaping. *Optics Express*, 17(23):20927, 2009. doi:10.1364/oe.17.020927.

[24] Michael R Vastag. Mode field diameter and effective area white paper optical fiber. pages 3–4, 2001. URL: www.corning.com/opticalfiber.

[25] Hongxing Shi, Fangzhou Tan, Yi Cao, Peng Wang, and Pu Wang. High-power diode-seeded thulium-doped fiber mopa incorporating active pulse shaping. *Applied Physics B: Lasers and Optics*, 122(10):1–8, 2016. doi:10.1007/s00340-016-6543-4.

[26] Xuan He, Bin Zhang, Shuailin Liu, Linyong Yang, Jinmei Yao, Qilin Wu, Yuxin Zhao, Tao Xun, and Jing Hou. High-power linear-polarization burst-mode all-fibre laser and generation of frequency-adjustable microwave signal. *High Power Laser Science and Engineering*, 9:1–7, 2021. doi:10.1017/hpl.2021.11.

[27] Parviz Elahi, Hamit Kalaycioğlu, Önder Akçaalan, Çağri Şenel, and F. Ömer Ilday. Burst-mode thulium all-fiber laser delivering femtosecond pulses at a 1 GHz intra-burst repetition rate. *Optics Letters*, 42(19):3808, 2017. doi:10.1364/ol.42.003808.

[28] Eoin Russell, Niamh Kavanagh, Kevin Shortiss, and Fatima C Garcia Gunning. Development of thulium-doped fibre amplifiers for the 2um waveband. In *Fiber Lasers and Glass Photonics: Materials through Applications*, volume 10683, page 106832Q. International Society for Optics and Photonics, 2018.

[29] Bernard Dussardier, Wilfried Blanc, and P. Peterka. Tailoring of the luminescent ions local environment in optical fibers, and applications, 2012. URL: https://arxiv.org/abs/1201.1113, arXiv:1201.1113.

[30] Shaghayegh Mirhosseini, Payman Kazemikhah, Hossein Aghababa, and Mohammadreza Kolahdouz. Fabrication of an erbium – ytterbium - doped waveguide amplifier at communication wavelengths for integrated optics applications. *SN Applied Sciences*, (December), 2022. doi:10.1007/s42452-022-05258-8.

[31] Yue Cheng, Hehe Dong, Chunlei Yu, Qiubai Yang, Yan Jiao, Shikai Wang, Chongyun Shao, Lili Hu, and Ye Dai. Temperature dependence of absorption and energy transfer efficiency of Er^{3+} Yb^{3+} P^{5+} co-doped silica fiber core glasses. *Materials*, 15(3), 2022. URL: https://www.mdpi.com/1996-1944/15/3/996, doi:10.3390/ma15030996.

[32] Xin Cheng, Zhiquan Lin, Xuezong Yang, Shuizhen Cui, Xin Zeng, Huawei Jiang, and Yan Feng. High-power 1560 nm single-frequency erbium fiber amplifier core-pumped at 1480 nm. *High Power Laser Science and Engineering*, 10:E3, 2023. doi:10.1017/hpl.2023.6.

[33] Anna Mauro, Valentina Serafini, Chiara Bellezza Prinsi, Matteo Cavagnetto, Luca Maggio Tanasi, Sabina Zaimovic, José Maria Blanco Triana, Gabriella Motta, and Guido Perrone. Theoretical and experimental comparison of three pumping methods for thulium fiber lasers for low-output power (<10 W). *Photonics*, 12(4):328, 2025. doi:10.3390/photonics12040328.

[34] Mathias Lenski, Tobias Heuermann, Martin Gebhardt, Ziyao Wang, Christian Gaida, César Jauregui, and Jens Limpert. Inband-pumped, high-power thulium-doped fiber amplifiers for an ultrafast pulsed operation. *Optics Express*, 30(24):44270–44282, 2022. Open Access. doi:10.1364/OE.476160.

[35] Kanwal, Ahmad Atieh, Salman Ghafoor, Muhammad Sajid, and Jawad Mirza. Pumping scheme for holmium-doped fiber amplifiers using traditional 1480 nm pumps exploiting cascaded lasers implemented using fiber bragg gratings. *Microwave and Optical Technology Letters*, 66, September 2023. doi:10.1002/mop.33899.

[36] Maryam Eilchi and Parviz Parvin. Gain saturation in optical fiber laser amplifiers. In Mukul Chandra Paul, editor, *Fiber Laser*, chapter 13. IntechOpen, London, 2016. doi:10.5772/62136.

[37] Søren Dyøe Agger and Jorn Hedegaard Povlsen. Emission and absorption cross section of thulium doped silica fibers. *Optics Express*, 14(1):50, 2006. doi:10.1364/opex.14.000050.

[38] D. J. Richardson, J. Nilsson, and W. A. Clarkson. High power fiber lasers: current status and future perspectives [invited]. *Journal of the Optical Society of America B*, 27(11):B63, 2010. doi:10.1364/josab.27.000b63.

[39] Govind P. Agrawal. *Introduction*, pages 1–27. Academic Press, 3rd edition, 1995. doi:10.1016/B978-0-12-045142-5.50007-6.

[40] Govind P. Agrawal. *Chapter 5 – Optical Solitons*, pages 129–191. Academic Press, 5th edition, 2013. doi:10.1016/B978-0-12-397023-7.50011-8.

[41] Govind P. Agrawal. *Wave Propagation in Optical Fibers*, pages 28–59. Academic Press, 3rd edition, 1995. doi:10.1016/B978-0-12-045142-5.50008-8.

[42] Dirk-Mathys Spangenberg, Anupamaa Rampur, Grzegorz Stepaniewski, Tomasz M. Kardas, Dominik Dobrakowski, Thomas Feurer, Alexander Heidt, and Mariusz Klimczak. Ultra-low-noise coherent supercontinuum amplification and compression below 100 fs in an all-fiber polarization-maintaining thulium fiber amplifier. *Optics Express*, 27(24):35041–35051, 2019. doi:10.1364/OE.27.035041.

[43] Piotr C. Iacka, Nupamaa R. Ampur, Alexander H. Eidt, Thomas Homas, Florian Eurer, and Mariusz K. Limczak. Dispersion measurement of ultra-high numerical aperture fibers covering thulium, holmium, and erbium emission wavelengths. *arXiv preprint*, pages 2–7, 2017. arXiv:1712.02100.

[44] Yuxing Tang, Andy Chong, and Frank W. Wise. Generation of 8 nJ pulses from a normal-dispersion thulium fiber laser. *Optics Letters*, 40(10):2361, 2015. doi:10.1364/ol.40.002361.

[45] Fosco Connect. Dispersion in fibers, Mar 2023. URL: https://www.fiberoptics4sale.com/blogs/wave-optics/dispersion-in-fibers.

[46] Liang Chen, Meisong Liao, Wanjun Bi, Fei Yu, Tianxing Wang, Weiqing Gao, and Lili Hu. Coherent supercontinuum generation in step-index heavily ge-doped silica fibers with all normal dispersion. *IEEE Photonics Journal*, 14(4):1–6, 2022. doi:10.1109/JPHOT.2022.3177945.

[47] Govind P. Agrawal. *Introduction*, pages 1–25. Academic Press, 6th edition, 2019. doi:10.1016/B978-0-12-817042-7.00008-7.

[48] Govind P. Agrawal. *Group-Velocity Dispersion*, pages 60–88. Academic Press, 3rd edition, 1995. doi:10.1016/B978-0-12-045142-5.50009-X.

[49] Govind P. Agrawal. *Self-Phase Modulation*, pages 89–132. Academic Press, 3rd edition, 1995. doi:10.1016/B978-0-12-045142-5.50010-6.

[50] Govind P. Agrawal. *Parametric Processes*, pages 404–470. Academic Press, 3rd edition, 1995. doi:10.1016/B978-0-12-045142-5.50016-7.

[51] P. Mouchel, M. Kemel, G. Semaan, M. Salhi, M. Le Flohic, and F. Sanchez. Limitations of graphene nanocoated optical tapers for high-power nonlinear applications. *Optical Materials: X*, 1(December 2018):100003, 2019. doi:10.1016/j.omx.2018.100003.

[52] John J. Zayhowski. *Microchip lasers*. Woodhead Publishing Limited, 2013. URL: http://dx.doi.org/10.1533/9780857097507.2.359, doi:10.1533/9780857097507.2.359.

[53] D. Kopf, K. J. Weingarten, G. Zhang, M. Moser, M. A. Emanuel, R. J. Beach, J. A. Skidmore, and U. Keller. High-average-power diode-pumped femtosecond Cr:LiSAF lasers. *Applied Physics B: Lasers and Optics*, 65(2):235–243, 1997. doi:10.1007/s003400050269.

[54] BATOP GmbH. Saturable absorber mirror 2000nm - batop, 2024. Accessed: 2025-06-16. URL: https://www.batop.de/products/saturable-absorber/saturable-absorber-mirror/saturable-absorber-mirror-2000nm.html.

[55] Grzegorz Sobon, Anna Duzynska, Michaa Swiniarski, Jarosaaw Judek, Jarosaaw Sotor, and Mariusz Zdrojek. CNT-based saturable absorbers with scalable modulation depth for thulium-doped fiber lasers operating at 1.9 μm. *Scientific Reports*, 7(April):1–9, 2017. doi:10.1038/srep45491.

[56] Franz X. Kärtner, Juerg Aus Der Au, and Ursula Keller. Mode-locking with slow and fast saturable absorbers - what's the difference? *IEEE Journal on Selected Topics in Quantum Electronics*, 4(2):159–168, 1998. doi:10.1109/2944.686719.

[57] Dr. Rüdiger Paschotta. Saturable absorbers, Mar 2023. URL: https://www.rp-photonics.com/saturable_absorbers.html.

[58] Michel Olivier, Marc Daniel Gagnon, and Joé Habel. Automation of mode locking in a nonlinear polarization rotation fiber laser through output polarization measurements. *Journal of Visualized Experiments*, 2016(108), 2016. doi:10.3791/53679.

[59] Walter Fu, Logan G. Wright, and Frank W. Wise. High-power femtosecond pulses without a modelocked laser. *Optica*, 4(7):831, 2017. arXiv:1705.03940, doi:10.1364/optica.4.000831.

[60] Shaoxiang Chen, Yuhao Chen, Raghuraman Sidharthan, Kun Liu, Chen Jian Chang, Qi Jie Wang, Dingyuan Tang, and Seongwoo Yoo. All-fiber short-wavelength mode-locked fiber laser and amplifier using normal dispersion thulium-doped fiber. *Optics InfoBase Conference Papers*, Part F183-(12):17570–17580, 2020. doi:10.1364/CLEO_SI.2020.STh1P.3.

[61] RP Photonics. Fiber loop mirrors, 2024. Accessed: 2025-06-17. URL: https://www.rp-photonics.com/fiber_loop_mirrors.html.

[62] Ahmed Nady, F. H. Mathkoor, and Sulaiman Wadi Harun. Theoretical study on passively mode-locked fiber lasers with saturable absorber. *Fiber and Integrated Optics*, 38(1):76–89, 2019. doi:10.1080/01468030.2018.1527417.

[63] Wenle Weng, Romain Bouchand, Erwan Lucas, Ewelina Obrzud, Tobias Herr, and Tobias J. Kippenberg. Heteronuclear soliton molecules in optical microresonators. *Nature Communications*, 11(1):1–9, 2020. URL: http://dx.doi.org/10.1038/s41467-020-15720-z, arXiv:1901.04026, doi:10.1038/s41467-020-15720-z.

[64] Zhihua Shao, Xueguang Qiao, Qiangzhou Rong, and Dan Su. Observation of the evolution of mode-locked solitons in different dispersion regimes of fiber lasers. *Optics Communications*, 345:105–110, 2015. URL: http://dx.doi.org/10.1016/j.optcom.2015.02.004, doi:10.1016/j.optcom.2015.02.004.

[65] Junsong Peng, Mariia Sorokina, Srikanth Sugavanam, Nikita Tarasov, Dmitry V. Churkin, Sergei K. Turitsyn, and Heping Zeng. Real-time observation of dissipative soliton formation in nonlinear polarization rotation mode-locked fibre lasers. *Communications Physics*, 1(1):1–8, 2018. URL: http://dx.doi.org/10.1038/s42005-018-0022-7, doi:10.1038/s42005-018-0022-7.

[66] Shutao Xu, Ahmet Turnali, and Michelle Y. Sander. Group-velocity-locked vector solitons and dissipative solitons in a single fiber laser with net-anomalous dispersion. *Scientific Reports*, 12(1):1–8, 2022. doi:10.1038/s41598-022-10818-4.

[67] S. M.J. Kelly. Characteristic sideband instability of periodically amplified average soliton. *Electronics Letters*, 28(8):806–807, 1992. doi:10.1049/el:19920508.

[68] Moritz Bartnick, Gayathri Bharathan, Thorsten A. Goebel, Ria G. Krämer, Stefan Nolte, and Camille-Sophie Brès. Wavelength-stabilized tunable mode-locked thulium-doped fiber laser beyond 2μm. *Opt. Lett.*, 47(8):2085–2088, Apr 2022. URL: https://opg.optica.org/ol/abstract.cfm?URI=ol-47-8-2085, doi:10.1364/OL.453936.

[69] Nanz Hang, Weiqi J. Jiang, Yafei M. Eng, and Fengqiu W. Ang. All-polarization-maintaining mode-locked thulium-doped femtosecond laser at 1.7 μm. *Optics Continuum*, 2(5):1013–1019, 2023. doi:10.1364/optcon.487127.

[70] Y. S. U. Alam Wang, E. D. Obraztsova, S. Y. Set, and S. Yamashita. Generation of stretched pulses and dissipative solitons at 2 μm from an all-fiber mode-locked laser using carbon nanotube saturable absorbers. *Optics Letters*, 41(17):3864–3867, 2016. doi:10.1364/OL.41.003864.

[71] Tohoku University Nakazawa Lab of RIEC. Research activities — Ultrahigh-speed optical soliton transmission and nonlinear optics in optical fibers. https://www.nakazawa.riec.tohoku.ac.jp/English/reserch/re01.html. Accessed: 2025-08-16.

[72] Xinyang Liu, Jayanta K. Sahu, and Regina Gumenyuk. Tunable dissipative soliton Tm-doped fiber laser operating from 1700 nm to 1900 nm. *Optics Letters*, 48(3):612, 2023. doi:10.1364/ol.478838.

[73] J. Jeon, J. Lee, and J. H. Lee. Numerical study on the minimum modulation depth of a saturable absorber for stable fiber laser mode locking. *J. Opt. Soc. Am. B*, 32:31, 2015.

[74] Dr. Rüdiger Paschotta. Time–bandwidth product, Apr 2023. URL: https://www.rp-photonics.com/time_bandwidth_product.html#:~:text=The%20minimum%20possible%20time%E2%80%93bandwidth,0.44%20for%20Gaussian%2Dshaped%20pulses.

[75] M. Gebhardt, C. Gaida, T. Heuermann, F. Stutzki, C. Jauregui, J. Antonio-Lopez, A. Schulzgen, R. Amezcua-Correa, J. Limpert, and A. Tünnermann. Nonlinear pulse compression to 43 W GW-class few-cycle pulses at 2 μm wavelength. *Optics Letters*, 42(20):4179, 2017. doi:10.1364/ol.42.004179.

[76] J. A. Garza-Reyes. Pulse stretching and compressing using grating pairs. *European University Institute*, (2):2–5, 2012. URL: https://eur-lex.europa.eu/legal-content/PT/TXT/PDF/?uri=CELEX:32016R0679&from=PT%0Ahttp://eur-lex.europa.eu/LexUriServ/LexUriServ.do?uri=CELEX:52012PC0011:pt:NOT.

[77] Jinzhang Wang, Weiyu Lai, Kun Wei, Kuilei Yang, Huiye Zhu, Zhijian Zheng, Chunyu Guo, Shuangchen Ruan, and Peiguang Yan. Generation of few-cycle pulses from a mode-locked Tm-doped fiber laser. *Optics Letters*, 46(10):2445, 2021. doi:10.1364/ol.420379.

[78] Duanyang Xu, Konstantinos N. Bourdakos, Anna Crisford, Peter Johnson, Ibrahim Abughazaleh, Panuwat Srisamran, Richard O. C. Oreffo, Sumeet Mahajan, David J. Richardson, and Lin Xu. All-fiberized 1840-nm femtosecond thulium fiber laser for label-free nonlinear microscopy. *Biomed. Opt. Express*, 14(9):4520–4530, Sep 2023. URL: https://opg.optica.org/boe/abstract.cfm?URI=boe-14-9-4520, doi:10.1364/BOE.495879.

[79] Ke Wang, Yu Du, Hongji Liu, Mengyao Gan, Shen Tong, Wenhui Wen, Ziwei Zhuang, and Ping Qiu. Visualizing the "sandwich" structure of osteocytes in their native environment deep in bone in vivo. *Journal of Biophotonics*, 12, 11 2018. doi:10.1002/jbio.201800360.

[80] W J Tomlinson, R H Stolen, and A M Johnson. Optical wave breaking of pulses in nonlinear optical fibers. 10(9):457–459, 1985.

[81] Ibrahim Abughazaleh, Panuwat Srisamran, Matthew Gerard, Duanyang Xu, Yongmin Jung, Jing He, Jeremiah Marcellino, Boyang Mao, Andrea C. Ferrari, David Richardson, and Lin Xu. Compact 1790-nm dissipative-soliton mode-locked thulium fiber laser. In Peter R. Herman, Roberto Osellame, and Adela Ben-Yakar, editors, *Frontiers in Ultrafast Optics: Biomedical, Scientific, and Industrial Applications XXIV*, volume PC12875, page PC1287501. International Society for Optics and Photonics, SPIE, 2024. doi:10.1117/12.3000615.

[82] Ibrahim Abughazaleh, Panuwat Srisamran, Matthew Gerard, Duanyang Xu, Yongmin Jung, David Richardson, and Lin Xu. Pre-chirp managed thulium fiber amplifier for 1.8μm ultrashort pulse generation. In *CLEO 2024*, page JW2A.38. Optica Publishing Group, 2024. doi:10.1364/CLEO_AT.2024.JW2A.38.

[83] Ibrahim H. Abughazaleh, Panuwat Srisamran, Matthew D. Gerard, Duanyang Xu, Yongmin Jung, David J. Richardson, and Lin Xu. Efficient pulse amplification and temporal compression in a 1790 nm femtosecond thulium fiber amplifier. In *2024 Conference on Lasers and Electro-Optics Pacific Rim (CLEO-PR)*, page P1 049. Optica Publishing Group, 2024.

[84] Matthew J. Barber, Peter C. Shardlow, Pranabesh Barua, Jayanta K. Sahu, and W. Andrew Clarkson. Nested-ring doping for highly efficient 1907 nm short-wavelength cladding-pumped thulium fiber lasers. *Optics Letters*, 45(19):5542, 2020. doi:10.1364/ol.401228.

[85] Hussein E Kotb, Mohamed A Abdelalim, and Hanan Anis. Effect of mode locking technique on the filtering bandwidth limitation in all normal dispersion femtosecond fiber laser. 8961(2157):1–11, 2014. doi:10.1117/12.2038248.

[86] Shaoxiang Chen, Yuhao Chen, Kun Liu, Raghuraman Sidharthan, Huizi Li, Chen Jian Chang, Qi Jie Wang, Dingyuan Tang, and Seongwoo Yoo. W-type normal dispersion thulium-doped fiber-based high-energy all-fiber femtosecond laser at 1.7um. *Optics Letters*, 46(15):3637–3640, 2021. doi:10.1364/OL.431023.

[87] R. Trebino, R. Jafari, S. A. Akturk, P. Bowlan, Z. Guang, P. Zhu, E. Escoto, and G. Steinmeyer. Highly reliable measurement of ultrashort laser pulses. *Journal of Applied Physics*, 128(17), 2020. doi:10.1063/5.0022552.

[88] Stimulated Raman. Chapter 8 stimulated Raman scattering. pages 316–369. doi:10.1016/B978-0-12-045142-5.50014-3.

[89] Y. Mashiko, E. Fujita, and M. Tokurakawa. Tunable noise-like pulse generation in mode-locked Tm fiber laser with a SESAM. *Opt. Express*, 24:26515, 2016.

[90] T. Noronen, O. Okhotnikov, and R. Gumenyuk. Electronically tunable thulium-holmium mode-locked fiber laser for the 1700-1800 nm wavelength band. *Opt. Express*, 24:14703, 2016.

[91] Shaoxiang Chen, Yuhao Chen, Kun Liu, Raghuraman Sidharthan, Huizi Li, Chen Jian Chang, Qi Jie Wang, Dingyuan Tang, and Seongwoo Yoo. All-fiber short-wavelength tunable mode-locked fiber laser using normal dispersion thulium-doped fiber. *Opt. Express*, 28(12):17570–17580, Jun 2020. URL: https://opg.optica.org/oe/abstract.cfm?URI=oe-28-12-17570, doi:10.1364/OE.395167.

[92] Y. Zhu, F. Xiang, L. Jin, S. Y. Set, and S. Yamashita. All-fiber dual-wavelength mode-locked laser using a bend-induced-birefringence lyot-filter as gain-tilt equalizer. *IEEE Photonics J.*, 11:1–7, 2019.

[93] Ahmet Turnali, Shutao Xu, and Michelle Y. Sander. Noise-like pulse generation and amplification from soliton pulses. *Optics Express*, 30(9):13977, 2022. doi:10.1364/oe.453946.

[94] M. A. Chernysheva, A. A. Krylov, P. G. Kryukov, N. R. Arutyunyan, A. S. Pozharov, E. D. Obraztsova, and E. M. Dianov. Thulium-doped mode-locked all-fiber laser based on nalm and carbon nanotube saturable absorber. *Eur. Conf. Opt. Commun. ECOC*, 20:124–130, 2012.

[95] Y. U. Z. Hou, X. I. C. Hu, Y. I. Q. Ian, C. H. L. Iang, A. N. K. Omarov, X. I. T. Ang, M. I. N. G. T. Ang, H. A. Z. Hu, and L. U. Z. Hao. Investigation of noise-like pulse evolution in normal dispersion fiber lasers mode-locked by nonlinear polarization rotation. *Opt. Express*, 30:35041–35049, 2022.

[96] Shaoqiang Chen, Masahiro Yoshita, Aya Sato, Takashi Ito, Hidefumi Akiyama, and Hiroyuki Yokoyama. Dynamics of short-pulse generation via spectral filtering from intensely excited gain-switched 1.55μ m distributed-feedback laser diodes. 21(9):2377–2379, 2013. doi:10.1364/OE.21.010597.

[97] W F U Alter, L Ogan G W Right, P Avel S Idorenko, S Terling, B Ackus, and F Rank W W Ise. Several new directions for ultrafast fiber lasers [invited]. 26(8):9432–9463, 2018. arXiv:arXiv:1802.08879.

[98] David Méchin, Elodie Le Cren, Douglas A. Reid, Doh Kyeong Lee, Benn C. Thomsen, and John D. Harvey. Generation of a 2.5ps pedestal-free optical

pulse using a 10ghz gain-switched laser and a compressing nonlinear amplifying loop mirror. *Conference on Lasers and Electro-Optics and 2006 Quantum Electronics and Laser Science Conference, CLEO/QELS 2006*, pages 1–2, 2006. doi:10.1109/CLEO.2006.4628027.

[99] Tobias Heuermann, Christian Gaida, Martin Gebhardt, and Jens Limpert. 50 fs-pulses emitted by a Tm-doped nonlinear fiber amplifier at 20 W of average power. *Optics InfoBase Conference Papers*, Part F121-(18):4441–4444, 2018. doi:10.1364/ASSL.2018.AM5A.8.

[100] Ibrahim H. Abughazaleh, Matthew D. Gerard, Panuwat Srisamran, Duanyang Xu, Yongmin Jung, and Lin Xu. Femtosecond thulium fiber laser utilizing a gain-switched laser diode. *Opt. Lett.*, 50(11):3636–3639, Jun 2025. doi:10.1364/OL.564071.

[101] Bahaa E. A. Saleh and Malvin C. Teich. *Fundamentals of Photonics*. Wiley, Hoboken, NJ, 3rd edition, 2019.

[102] R. Paschotta. Amplified spontaneous emission. https://www.rp-photonics.com/amplified_spontaneous_emission.html, 2024. Accessed: 2025-06-17.

[103] Govind P. Agrawal. *Parametric Processes*, pages 404–470. Academic Press, 3rd edition, 1995. doi:10.1016/B978-0-12-045142-5.50016-7.

[104] Piotr Ciacka, Anupamaa Rampur, Alexander Heidt, Thomas Feurer, and Mariusz Klimczak. Dispersion measurement of ultra-high numerical aperture fibers covering thulium, holmium, and erbium emission wavelengths. *Journal of the Optical Society of America B*, 35(6):1301–1308, 2018. doi:10.1364/JOSAB.35.001301.

Appendix: A

8.4 MATLAB CODE

8.4.1 Correction script

```
dir = 'C:\Users\......';
seedfreq = 100000000; % hz
minperiod = 1/seedfreq;
count = 1;
inu = 0;
pat_one = [0 1 0 1 1 0 0 1 1 0] ; %%% this can be flipped
roi = 1us aim for 1ms
pat_ten = [pat_one pat_one pat_one pat_one pat_one pat_one
   pat_one pat_one pat_one pat_one];% 100us
pat_ten pat_ten pat_ten pat_ten pat_ten]; % 1ms
frame = [0 pat_ten pat_ten pat_ten pat_ten pat_ten pat_ten
   pat_ten pat_ten pat_ten pat_ten 0]; % 1ms
vt_vpi = frame; % pick the snap shot i am doing the analysis
    on
xAWGtime = 1:100000; % to be put in AWG time scale test
Pat2pnts = length(xAWGtime)/length(pat_ten);
talktoAWGlong;
pause(2) % AWG too slow at reseting give time to read scope

while count ~= inu
    inu = count;
    sprintf('itt no = %d ', inu-1)
    readingscopefunlong;
%% load File and data
    filtered = [waveform.XData' waveform.YData];
    filteredcell{inu,1} = filtered;
```

```
    filename = sprintf('ItterationNumber%d.csv', (inu-1));

    fullFileName = fullfile(dir, filename);
    writematrix(filtered,filename);

    % find peak
    pkstime = [];
    pks= [];
    pkslocst = [];

    maxval = max(filtered(:,2));
    minval = min(filtered(:,2));
    midval = ((maxval - minval)/2.5) + minval; % the bigger
   the divisioon the smaller the center
    arr1arr2 = length(filtered(:,2))/length(xAWGtime);

     for i = 1:length(filtered(:,2))
        if filtered(i,2) <= (midval)
            filtered(i,2) = 0;

        else
            filtered(i,2) = filtered(i,2);
        end
     end


    [pks, locs] = findpeaks(filtered(:,2));
    for x = 1:length(locs)
        pkslocst(x) = filtered(locs(x),1);
    end
stpks = std(pks);
avpks = mean(pks);
upst = avpks + 2*stpks;
lowst = avpks - 2*stpks;

    figure(6)
    hold on
plot(filtered(:,2),'g')
plot(locs,pks,'ok')

% plot(filtered(:,2),'ob')
```

```
yline(lowst,'r')
yline(upst,'r')
yline(avpks,'k')

    if pks(k) < lowst
        pks(k) = 0;
        %locs(k) = 0;
    end
end

plot(locs,pks,'xb')
    hold off

%% filtering extra peaks out

knt = 1;
%method of find the highest point
while knt <= length(locs10k)-1
if locs10k(knt) == locs10k(knt+1)
     if pks(knt)>= pks(knt+1)
         pks(knt+1) = [];
         locs10k(knt+1) = [];
         pkslocst(knt+1) = [];
      elseif pks(knt) < pks(knt+1)
          locs10k(knt) = [];
          pks(knt) = [];
          pkslocst(knt) = [];
     end
else
  locs10k(knt) = locs10k(knt);
  pks(knt) = pks(knt);
  pkslocst(knt) = pkslocst(knt);
  knt = knt + 1;
    end
end

%% interoplation
%     % there used to be a -1 here (length(xAWGtime)-1)
     stepdiv = (max(filtered(:,1))-min(filtered(:,1)))/(
   length(xAWGtime)-1);% convert from 400k to 10k in time
length(filtered(:,1))/(length(xAWGtime)-1);
```

```
    stepdiv1 = (max(locs)-min(locs))/(length(xAWGtime)-1); %
    convert from 400k to 10k in loaction

temp10k = zeros(1,length(xAWGtime));

for n = 1: length(locs10k) % adding true values
    temp10k(locs10k(n)) = pks(n); % +1 to adjust for
   rounding error
    inpkstime(locs10k(n)) =  pkslocst(n);
end


for n = 2: length(temp10k) -1
    if temp10k(n) == 0 && temp10k(n+1) ~= 0 && temp10k(n-1)
   ~= 0
        temp10k(n) = (temp10k(n+1) + temp10k(n-1))/ 2 ;
    end
end
    figure(1)
    hold on
    plot(filtered(:,1),filtered(:,2),'g')
    plot(inpkstime,temp10k,'r')
    plot(inpkstime,temp10k,'o')
    plot(pkslocst,pks,'x')
    yline(lowst)
    yline(upst)
    yline(avpks)

    pkstime = inpkstime; % or locs ?
    pks = temp10k;
    % make sure peaks are the same number
    figure(2)
    hold on
    plot(filtered(:,1),filtered(:,2),'g')
    plot(pkstime,pks,'k')
    hold off
%% normalising pk (0-1) and time (0-bw)
    npks = pks/max(pks);
    npkstime = pkstime- min(pkstime);
    normpkarr = [npks; npkstime];
    figure(3)
```

```
    hold on
    plot(npkstime,npks)
%% shape target
    if inu == 1 % itt 1 is just to creat a new sqaure pulse
   with new time shift

        for i = 1:length(pks)
            if pks(i) == 0
           nfi(i) = 0;
            else
            nfi(i) = 1;
            end  % code line for square shape
            nfi_square = nfi; % this fixes target to
   correction function
            sqnfitime = npkstime;

        end

    end

%% Avarage / median / mode saturated
    meanpks = mean(npks);
    midpks = median(npks);
    yline(meanpks, 'r')
    yline(midpks,'b')
    hold off
 %% moving points
    figure(4)
    hold on
    plot(npkstime,nfi_square,'x')
    plot(npkstime,nfi,'.')

%% correct for time delay

    if inu ~= 1 % itt 1 is just to creat a new sqaure pulse
   with new time shift

allonessquare = find(nfi_square == 1);
firstone = allonessquare(1);
lastone = allonessquare(end);
allnonzeroks = find(npks ~= 0);
```

```
firstnonzero = allnonzeroks(1);
lastnonzero = allnonzeroks(end);
arrdiffitt = firstone - firstnonzero;
 still appropreiat
% NEEDS TO ADD A SHIFT IN TIME
    nfi = nfi/max(nfi);
    nfi  = real(nfi);


    plot(npkstime,nfi)
%% Avarage / median / mode for correction input
    meanpks1(inu) = mean(nfi);
    midpks1(inu) = median(nfi);
    yline(meanpks1(inu), 'g')
    yline(midpks1(inu),'y')
    hold off
%% normalising Prediction for LabView
    auc = (length(xAWGtime)-0)/(max(pkstime)-min(pkstime));
   % coneversion constant
    arbtime = auc*npkstime;% time 0-500
%% EOM Response
    vt_vpi = (acos(1-(2*nfi)))/pi;
vt_vpi = vt_vpi/ max(vt_vpi);

nonzerovt = vt_vpi(vt_vpi ~=0);
stvt = std(nonzerovt);
avvt = mean(nonzerovt);

vtupst = avvt + 2.5*stvt;
vtlowst = avvt - 3.5*stvt;

% get rid of side peaks only make them zero
for k = 2: length(vt_vpi) - 1

    if vt_vpi(k) < vtlowst
        pks(k) = 0;
        %locs(k) = 0;
    end
end

    figure(5)
```

```
    hold on
    plot(arbtime,vt_vpi,'x')
    yline(avvt,'r')
    yline(vtupst,'k')
    yline(vtlowst,'k')
    hold off

talktoAWGlong;

vt_vpi = [];

count = count + 1;

    pause(5)
    %count = count +1;
end
```

8.4.2 AWG communication

```
awgwaveform = vt_vpi;% depends on the snap shot i am doing
   the analysis on
awgwaveform = awgwaveform / max(awgwaveform);
timeVec = 1:length(vt_vpi);
%% links to AWG
interfaceObj = instrfind('Type', 'visa-usb', 'RsrcName', '
   USB0::0x0699::0x034C::C012545::0::INSTR', 'Tag', '');
% Create the VISA-USB object if it does not exist
% otherwise use the object that was found.
if isempty(interfaceObj)
    interfaceObj = visa('NI', 'USB0::0x0699::0x034C::C012545
   ::0::INSTR');
else
    fclose(interfaceObj);
    interfaceObj = interfaceObj(1);
end

interfaceObj.OutputBufferSize = 5120000;
% Set the |ByteOrder| to match the requirement of the
   instrument
```

```
interfaceObj.ByteOrder = 'littleEndian';% this sets it to
   the lowest order of bytes
% Open the connection to the function generator
fopen(interfaceObj);
% Reset the function generator to a know state ..... this
   shuts AWG
fprintf(interfaceObj, '*RST');
fprintf(interfaceObj, '*CLS;');% with is one it helps reduce
    the delay between traces
%% arb wavform stuff dont understand
awgwaveform =  round((awgwaveform*2)*8191);
awgwaveformLength = length(awgwaveform);
% Encode variable 'awgwaveform' into binary awgwaveform data
    for AFG.  This is the
% same as AWG5000B but marker bits are ignored. Refer to
   AWG5000B series
% programmer manual for bit definitions.
binblock = zeros(2 * awgwaveformLength, 1);
binblock(2:2:end) = bitand(awgwaveform, 255);
binblock(1:2:end) = bitshift(awgwaveform, -8);
binblock = binblock';
% Build binary block header
bytes = num2str(length(binblock));
header = ['#' num2str(length(bytes)) bytes];
% Resets the contents of edit memory and define the length
   of signal
fprintf(interfaceObj, ['DATA:DEF EMEM, ' num2str(length(
   timeVec)) ';']); %1001
% Transfer the custom awgwaveform from MATLAB to edit memory
    of instrument
fwrite(interfaceObj, [':TRACE EMEM, ' header binblock ';'],
   'uint8');
% Associate the awgwaveform in edit memory to channel 1
fprintf(interfaceObj, 'SOUR1:FUNC EMEM');
%% my settings burst
fprintf(interfaceObj, 'TRIGger:SEQuence:SOURce EXTernal');
fprintf(interfaceObj, 'SOURce1:BURSt:STATe ON');
fprintf(interfaceObj, 'SOURce1:BURSt:MODE TRIGgered');
fprintf(interfaceObj, 'SOURce1:BURSt:NCYCles 1');
fprintf(interfaceObj, 'SOURce1:VOLTage:LEVel:IMMediate:HIGH
   6.5V');
```

```
fprintf(interfaceObj, 'SOURce1:VOLTage:LEVel:IMMediate:LOW 1
    V');
fprintf(interfaceObj, 'SOUR1:FREQ:FIXed 10kHz'); % 33Hz = 30
    ms time width
% % Resets the contents of edit memory and define the length
     of signal
fprintf(interfaceObj, ':OUTP1 ON');
```

8.4.3 Oscilloscope communication

```
%% Interface configuration and instrument connection
% The second argument to the VISA function is the resource
    string for your
% instrument
visaObj = instrfind('Type', 'visa-usb', 'RsrcName', 'USB0::0
    x0957::0x1755::MY48260183::0::INSTR', 'Tag', '');

if isempty(visaObj)
    visaObj = visa('NI','USB0::0x0957::0x1755::MY48260183
    ::0::INSTR');
else
     fclose(visaObj);
     visaObj =  visaObj(1);
end


% Set the buffer size
visaObj.InputBufferSize = 100000000;% 10x bigger than
    wavepoints
% Set the timeout value
visaObj.Timeout = 10;
% Set the Byte order
visaObj.ByteOrder = 'littleEndian';
% Open the connection
fopen(visaObj);

%% Instrument control and data retreival
% Now control the instrument using SCPI commands. refer to
    the instrument
% programming manual for your instrument for the correct
    SCPI commands for
```

```
% your instrument.
% Reset the instrument and autoscale and stop
% fprintf(visaObj,'*RST; :AUTOSCALE');
fprintf(visaObj,':STOP');
% Specify data from Channel 1
fprintf(visaObj,':WAVEFORM:SOURCE CHAN2');
% Set timebase to main
fprintf(visaObj,':TIMEBASE:MODE MAIN');
% Set up acquisition type and count.
%fprintf(visaObj,':SYSTem:PRECision on');
% fprintf(visaObj,':ACQUIRE:TYPE NORMAL');
fprintf(visaObj,':ACQUIRE:COUNT 1');
% Specify 5000 points at a time by :WAV:DATA?
fprintf(visaObj,':WAV:POINTS:MODE raw');
fprintf(visaObj,':WAV:POINTS 100000');% 100,000 (10ns) in a
   ms 1 point = 1 pk
% Now tell the instrument to digitize channel1
fprintf(visaObj,':DIGITIZE CHAN2');
% Wait till complete
operationComplete = str2double(query(visaObj,'*OPC?'));
while ~operationComplete
    operationComplete = str2double(query(visaObj,'*OPC?'));
end
% Get the data back as a WORD (i.e., INT16), other options
   are ASCII and BYTE
fprintf(visaObj,':WAVEFORM:FORMAT WORD');
% Set the byte order on the instrument as well
fprintf(visaObj,':WAVEFORM:BYTEORDER LSBFirst');
% Get the preamble block
preambleBlock = query(visaObj,':WAVEFORM:PREAMBLE?');

% Now send commmand to read data
fprintf(visaObj,':WAV:DATA?');
% read back the BINBLOCK with the data in specified format
   and store it in
% the waveform structure. FREAD removes the extra terminator
    in the buffer
waveform.RawData = binblockread(visaObj,'uint16'); fread(
   visaObj,1);
% Read back the error queue on the instrument
instrumentError = query(visaObj,':SYSTEM:ERR?');
```

```
while ~isequal(instrumentError,['+0, ''No Error'' ' char(10)
    ])
     disp(['Instrument Error: ' instrumentError]);
     instrumentError = query(visaObj,':SYSTEM:ERR?');
end
% Close the VISA connection.
fclose(visaObj);
%% Data processing: Post process the data retreived from the
     scope
% Extract the X, Y data and plot it
% Maximum value storable in a INT16
maxVal = 2^16;
%  split the preambleBlock into individual pieces of info
preambleBlock = regexp(preambleBlock,',','split');
% store all this information into a waveform structure for
    later use
waveform.Format = str2double(preambleBlock{1});     % This
    should be 1, since we're specifying INT16 output
waveform.Type = str2double(preambleBlock{2});
waveform.Points = str2double(preambleBlock{3});
waveform.Count = str2double(preambleBlock{4});      % This
    is always 1
waveform.XIncrement = str2double(preambleBlock{5}); % in
    seconds
waveform.XOrigin = str2double(preambleBlock{6});    % in
    seconds
waveform.XReference = str2double(preambleBlock{7});
waveform.YIncrement = str2double(preambleBlock{8}); % V
waveform.YOrigin = str2double(preambleBlock{9});
waveform.YReference = str2double(preambleBlock{10});
waveform.VoltsPerDiv = (maxVal * waveform.YIncrement / 8);
       % V
waveform.Offset = ((maxVal/2 - waveform.YReference) *
    waveform.YIncrement + waveform.YOrigin);         % V
waveform.SecPerDiv = waveform.Points * waveform.XIncrement
    /10 ; % seconds
waveform.Delay = ((waveform.Points/2 - waveform.XReference)
    * waveform.XIncrement + waveform.XOrigin); % seconds
% Generate X & Y Data
waveform.XData = (waveform.XIncrement.*(1:length(waveform.
    RawData))) - waveform.XIncrement;
```

```
waveform.YData = (waveform.YIncrement.*(waveform.RawData -
    waveform.YReference)) + waveform.YOrigin;
% Plot it
figure(7)
hold on
plot(waveform.XData,waveform.YData);
set(gca,'XTick',(min(waveform.XData):waveform.SecPerDiv:max(
    waveform.XData)))
xlabel('Time (s)');
ylabel('Volts (V)');
title('Oscilloscope Data');
grid on;
hold off
```